

DOCTORAL THESIS

Fabrication of In-Situ Alloyed Ti-Nb via Selective Laser Melting for Orthopedic Applications

Shangavi Subramanian

TALLINN UNIVERSITY OF TECHNOLOGY
DOCTORAL THESIS
33/2026

**Fabrication of *In-Situ* Alloyed Ti-Nb via
Selective Laser Melting for Orthopedic
Applications**

SHANGAVI SUBRAMANIAN



TALLINN UNIVERSITY OF TECHNOLOGY

School of Engineering

Department of Mechanical and Industrial Engineering

This dissertation was accepted for the defense of the degree 18/05/2026

Supervisor:

Prof. Prashanth Konda Gokuldoss
Department of Mechanical and Industrial Engineering
Tallinn University of Technology
Tallinn, Estonia.

Co-supervisor:

Assoc. Prof. Jayaraj Jayamani
Department of Mechanical and Materials Engineering
Karlstad University, Karlstad, Sweden.
Department of Mechanical Engineering
Dalarna University, Falun, Sweden.

Opponents:

Prof Marek Kazimierz Hebda
Department of Materials Engineering
Cracow University of Technology
Cracow, Poland.

Prof Kateřina Skotnicová
Department of Materials Science and Technology
VSB - Technical University of Ostrava
Ostrava, Czech Republic.

Defense of the thesis: 16/06/2026, Tallinn

Declaration:

Hereby, I declare that this doctoral thesis, my original investigation and achievement, submitted for the doctoral degree at Tallinn University of Technology, has not been submitted for a doctoral or equivalent academic degree.

Shangavi Subramanian

signature



European Union
European Regional
Development Fund



Investing
in your future

Copyright: Shangavi Subramanian, 2026

ISSN 2585-6898 (publication)

ISBN 978-9916-80-505-3 (publication)

ISSN 2585-6901 (PDF)

ISBN 978-9916-80-506-0 (PDF)

<https://doi.org/10.23658/taltech.33/2026>

Subramanian, S. (2026). *Fabrication of In-Situ Alloyed Ti-Nb via Selective Laser Melting for Orthopedic Applications* [TalTech Press]. <https://doi.org/10.23658/taltech.33/2026>

TALLINNA TEHNIKAÜLIKOO
DOKTORITÖÖ
33/2026

***In-situ* legeritud Ti–Nb sulamite
valmistamine selektiivse lasersulatamise abil
ortopeedilisteks rakendusteks**

SHANGAVI SUBRAMANIAN



Contents

| | |
|--|----|
| Contents | 5 |
| List of publications | 7 |
| Author's contribution to the publications | 8 |
| Introduction | 9 |
| Abbreviations | 12 |
| 1 Literature review | 13 |
| 1.1 Biomaterials for orthopedic applications | 13 |
| 1.1.1 Metallic implant materials | 13 |
| 1.1.2 β -Ti alloys for implant applications | 15 |
| 1.2 Selective laser melting of β -Ti alloys | 18 |
| 1.2.1 Selective laser melting of β -Ti-Nb alloy | 19 |
| 1.2.2 Mechanical properties of SLM-fabricated β -Ti-Nb-based alloys | 21 |
| 1.2.3 Passivation behavior of SLM-fabricated β -Ti-Nb alloys in physiological environments | 23 |
| 1.3 Surface modification of SLM-fabricated β -Ti-Nb alloy | 25 |
| 2 Materials and methods | 28 |
| 2.1 SLM fabrication | 28 |
| 2.2 Structural and microstructural characterization | 29 |
| 2.3 Mechanical testing | 29 |
| 2.4 Passivation studies | 30 |
| 2.5 Surface modification and its characterization | 30 |
| 2.6 <i>In-vitro</i> cell viability studies | 31 |
| 3 Results and discussion | 33 |
| 3.1 Powder characterization | 33 |
| 3.2 Effect of remelting on SLM-fabricated Ti-Nb alloy | 33 |
| 3.2.1 Phase analysis | 33 |
| 3.2.2 Relative density analysis | 34 |
| 3.2.3 Microstructural analysis | 35 |
| 3.2.4 Microhardness distribution | 36 |
| 3.2.5 Influence of remelting | 37 |
| 3.3 Effect of Fe addition on the SLM-fabricated Ti-Nb alloy | 38 |
| 3.3.1 Phase analysis | 38 |
| 3.3.2 Microstructural analysis | 39 |
| 3.3.3 Mechanical properties | 40 |
| 3.3.4 Passivation behavior | 41 |
| 3.4 Effect of surface modification on SLM-fabricated Ti-Nb alloy | 44 |
| 3.4.1 Phase analysis of PEO coatings | 44 |
| 3.4.2 Surface morphology of PEO coatings | 45 |
| 3.4.3 Surface wettability | 46 |
| 3.4.4 Cell-viability evaluation | 47 |
| 4 Conclusion | 49 |
| 5 Future work | 50 |
| References | 51 |

| | |
|------------------------|-----|
| Acknowledgement | 61 |
| Abstract | 62 |
| Lühikokkuvõte | 64 |
| Appendix | 67 |
| Curriculum vitae | 129 |
| Elulookirjeldus | 130 |

List of publications

The list of author's publications based on which the thesis has been prepared:

- I. **S. Subramanian, S.**, Mohanty, S., & Prashanth, K. G. (2023). Effect of process parameters on the properties of β -Ti-Nb-based alloys fabricated by selective laser melting: A review. *Materials Today: Proceedings*. <https://doi.org/10.1016/j.matpr.2023.03.461>
- II. **Subramanian, S.**, Yadav, M. K., Jayaraj, J., Yangyang, Xi, L., & Prashanth, K. G. (2025). Microstructural homogenization through laser remelting in an additively manufactured Ti-40Nb sample from elemental feedstock powders. *Journal of Materials Research and Technology*, 38, 4305–4320. <https://doi.org/10.1016/j.jmrt.2025.08.203>
- III. **Subramanian, S.**, Praveenkumar, K., Rameshbabu, N., Lokeshraj, K., Raheem, A., Jayaraj, J., & Prashanth, K. G. (2026). Biofunctionalization of SLM Ti-40Nb alloy through hydroxyapatite-modified plasma electrolytic oxidation coating. *Applied Surface Science Advances*, 31, 100917. <https://doi.org/10.1016/j.apsadv.2025.100917>
- IV. **Subramanian, S.**, Manivasagam, G., Jayaraj, J., & Prashanth, K. G. (2026). Microstructural refinement, mechanical enhancement, and superior passivation of SLM Ti-Nb-Fe fabricated through insitu alloying. *Journal of Alloys and Compounds*, 187930. <https://doi.org/10.1016/j.jallcom.2026.187930>

Author's contribution to the publications

Contributions to the papers in this thesis are:

Paper I First author - Conceptualization, Formal analysis, Writing - original draft

Paper II First author - Methodology, Data curation, Formal analysis, Investigation, Writing - original draft

Paper III First author - Methodology, Data curation, Formal analysis, Investigation, Writing - original draft

Paper IV First author - Methodology, Data curation, Formal analysis, Investigation, Writing - original draft

Introduction

The demand for implantable biomaterials is increasing due to advances in healthcare and the rising life expectancy. Bioimplants are designed to interact with biological systems for therapeutic, diagnostic, or regenerative purposes (Geetha et al., 2009). Among the available biomaterials, metallic implants remain essential in orthopedic applications due to their high mechanical strength, fracture toughness, and wear resistance. Traditionally, stainless steel and cobalt-chromium alloys served as the primary choices due to their strength and manufacturability (Al-Shalawi et al., 2023; Chen et al., 2015). However, these materials exhibit high elastic modulus, susceptibility to corrosion, and limited biocompatibility. On the other hand, Ti-based alloys are gaining importance due to their excellent biocompatibility, mechanical strength, and superior corrosion resistance (Jakubowicz, 2020). Nevertheless, the commonly used Ti-6Al-4V implants raise concerns related to the release of vanadium (V) and aluminium (Al) ions, which are associated with cytotoxic and neurological effects. In addition, Ti-6Al-4V implants exhibit a relatively higher elastic modulus (~110 GPa) than that of cortical bone (10-30 GPa). This modulus mismatch causes stress shielding, where the stiffer implant carries most of the load, leading to bone resorption, implant loosening, and eventual long-term failure. These limitations have motivated the development of low-modulus β -Ti alloys using non-toxic elements such as niobium (Nb), tantalum (Ta), molybdenum (Mo), iron (Fe), and copper (Cu) (Bălăţatu et al., 2015; Ji et al., 2020; Yılmaz et al., 2018).

Among different β -Ti alloys, Ti-Nb alloy has received significant attention due to its low elastic modulus, excellent biocompatibility, and high corrosion resistance owing to the protective Nb₂O₅ surface film. Literature based on the molybdenum equivalence (Moeq) indicates that β -phase stabilization is achieved at Nb content of approximately 40 wt.% or higher (Wang et al., 2017). Consequently, the β -phase stabilized Ti-Nb alloy exhibits an elastic modulus of 57-116 GPa, resulting in reduced stiffness. Thus, the Ti-Nb alloy has evolved as a promising choice for orthopedic applications (Chang et al., 2016; N. Singh et al., 2024). Similar to Nb, Fe is an effective β -phase stabilizer in Ti-alloys. However, its usage should be limited to 5 wt.% to avoid intermetallic phase formation (Kim et al., 2024). Studies on Fe-modified Ti-Nb cast and spark plasma sintered alloys reported favorable β -phase formation with desirable mechanical and corrosion properties (Ehtemam-Haghighi et al., 2016; Haq et al., 2024; Lopes et al., 2016). However, conventional manufacturing methods offer limited geometric flexibility for implant design and limit the fabrication of patient-specific implants (Ahmad et al., 2024; Balasubramani et al., 2025).

In this regard, selective laser melting (SLM), a laser-based powder bed fusion technique, offers an effective alternative for the fabrication of patient-specific implants. Despite its advantages, the SLM technique for implant fabrication is constrained by its dependence on prealloyed powders. In general, gas-atomized pre-alloyed powders are expensive and offer limited compositional flexibility. In addition, processing elements with vast differences in melting point pose challenges during atomization (Feng et al., 2024; Zerwas et al., 2024). Therefore, the use of elemental powders has emerged as a cost-effective alternative, offering greater compositional flexibility and facilitating in-situ alloying (Sharkeev et al., 2016; Subramanian et al., 2023). In the case of SLM fabrication of Ti-Nb alloy using elemental powders, challenges arise due to the higher melting point of Nb (2460 °C) than Ti (1680 °C).

Previous studies on SLM fabrication of Ti-10-30Nb, Ti-35Nb, Ti-41Nb, and Ti-40.5Nb (in wt.%) alloys from elemental powders have reported incomplete melting and segregation of Nb particles, resulting in microstructural heterogeneity and anisotropic mechanical properties (Borgman et al., 2021; Fischer et al., 2016; S. Huang et al., 2022; J. Wang et al., 2021). Thus, achieving homogeneous, low-modulus β -Ti alloys via elemental-powder-based SLM remains challenging. Furthermore, Ti-Nb-based implants are inherently bioinert and require surface modification to improve osteointegration (Cardoso et al., 2024; Molaei et al., 2022). Among the available surface modification techniques, plasma electrolytic oxidation (PEO) is particularly attractive for biomedical applications. The substrate-integrated oxide layer formed during the PEO process promotes early-stage cell attachment, improving osteointegration (Ni et al., 2008; Nisar et al., 2024; Yao et al., 2019). PEO coatings on conventionally processed Ti-Nb alloy have been investigated (Lokeshkumar et al., 2023; Maciej et al., 2023). However, investigations on the PEO coating behavior of SLM-fabricated Ti-Nb alloys have not yet been reported. Based on the current state-of-the-art, several research gaps were identified and are stated below.

1. Studies showing SLM of Ti-Nb from elemental powders have not reported the complete melting and alloying of Nb with a homogeneous microstructure.
2. Investigations on the SLM fabrication of Fe-incorporated Ti-Nb (Ti-35Nb-5Fe) alloy from elemental powders and the role of Fe on the β -stability, mechanical properties, and passive film stability remain unexplored.
3. Surface modification and its influence on osseointegration of SLM-produced Ti-Nb alloys have not been reported.

Thus, the goal of this thesis is to develop a low-modulus β -TiNb-based alloy from elemental powder using SLM with improved properties for orthopedic applications. This study focuses on achieving microstructural homogenization, improving mechanical and passivation behavior, and enhancing bioactivity. To achieve these goals, it is hypothesized that a remelting strategy during SLM will promote complete melting and diffusion of Nb particles, resulting in microstructural homogeneity. The addition of 5 wt.% Fe (Ti-35Nb-5Fe) is expected to enhance β -phase stability, decrease elastic modulus, and reduce feedstock cost by partially replacing the costlier Nb. Alloying with Fe is also expected to modify the passive film chemistry and improve passivation stability in a simulated physiological environment. Furthermore, PEO-based surface modification with hydroxyapatite (HAp) is expected to improve *in-vitro* cell viability. Thus, the goal of this thesis work can be achieved by following specific objectives.

1. Investigate the effect of SLM remelting strategy on the complete melting of Nb particles in Ti-40Nb alloy and evaluate the microstructural homogenization.
2. Evaluate the influence of 5 wt.% Fe addition on β -phase stability of Ti-Nb (Ti-35Nb-5Fe) and compare its mechanical properties with Ti-40Nb alloy.
3. Compare the passivation behavior of Ti-40Nb and Ti-35Nb-5Fe alloys in simulated physiological conditions.
4. Develop PEO coating on SLM fabricated Ti-40Nb alloy and assess the influence of HAp addition on *in-vitro* cell viability.

To achieve the specific objectives outlined above, the following methodology was adopted. For objective 1, single- and triple-melting strategies are used in SLM

fabrication of Ti-40Nb from elemental powders. Phase constituent is analyzed using X-ray diffraction. Microstructural homogenization and elemental distribution are characterized using SEM and EDS. Defect reduction, particularly porosity, is quantified using microCT analysis. Hardness distribution across the sample surface is evaluated using Vickers microhardness. For objective 2, microstructural evaluation was done by SEM and EBSD. Mechanical behavior is assessed using compression testing. Passivation stability is evaluated using electrochemical studies in a simulated physiological environment. For objective 3, surface modification is performed using the PEO process with and without HAp addition. Coating morphology and composition are characterized using SEM and EDX analysis. The cellular response on the coated sample is evaluated through in-vitro Alamar blue assay cell viability studies.

The novelty of the thesis lies in the use of elemental powder and a remelting strategy for SLM fabrication of a low-modulus β -TiNb-based alloy. In addition, it signifies the role of Fe incorporation in improving β -phase stability, mechanical performance, and passive film behavior. Overall, this work establishes a process-microstructure-property relationship for the development of Ti-Nb-based alloys for long-term orthopedic applications. The thesis is organized as follows. Chapter 1 presents a detailed literature review on the topic, followed by Chapter 2, presenting the materials and methods used in the thesis work. Chapter 3 is divided into three sections. Section 3.1 discusses the effect of remelting on the microstructural homogenization of Ti-Nb alloy. Section 3.2 discusses the effect of Fe addition on the mechanical properties and electrochemical passivation behavior in a simulated physiological environment. Section 3.3 discusses the effect of surface modification on coating characteristics and in-vitro cell viability. Chapter 4 provides the conclusion, summarizing the major findings, and Chapter 5 outlines the future scope of the work.

Abbreviations

| | |
|--------|--|
| AM | Additive Manufacturing |
| ASTM | American Society for Testing and Materials |
| BJT | Binder Jetting |
| CAD | Computer-Aided Design |
| CVD | Chemical Vapor Deposition |
| DED | Direct Energy Deposition |
| EBM | Electron Beam Melting |
| EDX | Energy Dispersive X-Ray Spectroscopy |
| EIS | Electrochemical Impedance Spectroscopy |
| FBS | Fetal Bovine Serum |
| FWHM | Full Width at Half Maximum |
| HAADF | High-Angle Annular Dark-Field |
| ICPOES | Inductively Coupled Plasma Optical Emission Spectroscopy |
| IFFT | Inverse Fast Fourier Transform |
| LPBF | Laser Powder Bed Fusion |
| MEX | Material Extrusion |
| MJT | Material Jetting |
| OCP | Open Circuit Potential |
| OM | Optical Microscopy |
| PBF | Powder Bed Fusion |
| PDP | Potentiodynamic Polarization |
| PEO | Plasma Electrolytic Oxidation |
| PS | Phosphate-Silicate |
| PSHA | Phosphate-Silicate-Hydroxyapatite |
| PVD | Physical Vapor Deposition |
| SBF | Simulated Body Fluid |
| SCE | Saturated Calomel Electrode |
| SEM | Scanning Electron Microscopy |
| SHL | Sheet Lamination |
| SIM | Stress-Induced Martensite |
| SLM | Selective Laser Melting |
| SM | Single Melting |
| SS | Stainless Steel |
| TEM | Transmission Electron Microscopy |
| TM | Triple Melting |
| VPP | Vat Photopolymerization |
| WEDM | Wire Electrical Discharge Machining |
| XPS | X-Ray Photoelectron Spectroscopy |
| XRD | X-Ray Diffraction Patterns |

1 Literature review

1.1 Biomaterials for orthopedic applications

Biomaterials are essential for the repair and replacement of damaged musculoskeletal tissues. In particular, orthopedic implants are designed to restore structural stability and functional mobility of the skeletal system. These implants function as long-term load-bearing structures and must maintain mechanical integrity while remaining compatible with surrounding biological tissues (Marin et al., 2025). For reliable in-vivo performance, materials selected for orthopedic applications must meet stringent mechanical and biological criteria. They should withstand cyclic physiological loading, exhibit wear resistance, and remain stable against corrosion in the physiological environment. In addition, the material must be biocompatible, ensuring that implants do not trigger inflammation, cytotoxicity, or immune responses (Choi et al., 2023; Sidambe, 2014). Depending on the clinical requirements, implants are fabricated from metals, polymers, ceramics, and composite systems, each offering specific advantages and inherent limitations (Lele et al., 2024). Among available biomaterials, metallic materials remain the primary choice for load-bearing orthopedic applications. Their high strength, biocompatibility, and long-term structural stability make them suitable for implants such as fixation plates, intramedullary nails, spinal rods, and joint replacements. Metals offer higher strength and fatigue resistance than polymers and ceramics under cyclic loading. Consequently, metallic biomaterials continue to play a dominant role in the development of long-term orthopedic implants (Fan et al., 2024; Marin et al., 2025).

1.1.1 Metallic implant materials

The metallic materials commonly used in orthopedic implants include medical-grade stainless steels (SS), cobalt-chromium (Co-Cr), titanium (Ti) and its alloys, and magnesium-based degradable alloys (Nakano, 2010). Figure 1.1 shows a schematic of commonly used metallic implants in orthopedic applications.

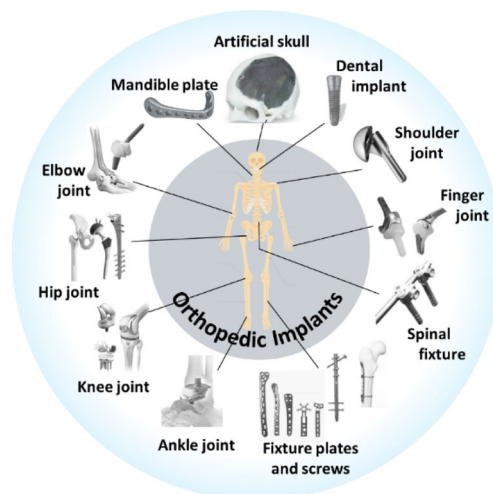


Figure 1.1. Schematic representation of the metallic implants utilized in orthopedic applications, adapted from (Nakano, 2010).

Table 1.1 provides a comparative overview of the advantages and disadvantages of widely used metallic biomaterials for orthopedic applications. These materials often incorporate elements such as cobalt (Co), chromium (Cr), nickel (Ni), and vanadium (V). The release of these metallic ions due to corrosion in physiological environments may lead to hypersensitivity reactions, cytotoxic effects, or adverse tissue responses. For instance, SS316L and Co-Cr alloys are susceptible to dissolution in physiological fluids, releasing Ni, Co, and Cr ions that have been associated with dermatitis, carcinogenic risks, or local inflammatory responses (Yi et al., 2025). In addition to biological concerns, the high elastic modulus of SS316L and Co-Cr alloys relative to that of natural bone (~30 GPa) can lead to stress shielding (Arabnejad et al., 2017). Moreover, SS316L exhibits limited fatigue strength and wear resistance, limiting its long-term use in orthopedics. These limitations led to the development of Ti and Ti-based alloys that provide mechanical stability, biocompatibility, and excellent corrosion resistance. In addition, their elastic modulus is lower than that of SS316L and Co-Cr alloys, thereby reducing stress shielding (Niinomi et al., 2011)

Table 1.1. Advantages and disadvantages of common metallic biomaterials used in orthopedic implants, adapted from (Chen et al., 2015).

| Material | Advantages | Disadvantages | Elastic modulus (GPa) | Density (g.cm⁻³) |
|-------------------------------|---|---|------------------------------|------------------------------------|
| Co-Cr | Excellent wear resistance, high strength and fatigue resistance, stable passive film. | Very high stiffness, potential Co/Cr ion release and associated biological risks, expensive, and difficult to machine. | ~240 | 8.5 |
| SS316L | Low cost, good corrosion resistance, good strength for temporary implants, availability, and easy fabrication. | High elastic modulus leading to stress shielding effect, release of Ni and Cr ions, susceptibility to pitting and fatigue corrosion, and limited long-term performance. | ~200 | 8 |
| Ti and Ti-based alloys | Excellent biocompatibility, forming a stable TiO ₂ passive layer; low modulus, low density, and excellent corrosion resistance in saline environments. | Lower wear resistance, may deform under high load, still stiffer than bone, relatively high material cost | ~110 | 4.4 |
| Mg and Mg-based alloys | Biodegradable, modulus like natural bone, potential to eliminate revision surgery, and lightweight. | Rapid corrosion in physiological environments, insufficient mechanical strength for major load-bearing sites, and hydrogen gas evolution during degradation. | ~40-50 | 2 |

1.1.2 β -Ti alloys for implant applications

Ti and its alloys are widely used in implants owing to their combination of strength, corrosion resistance, and excellent biocompatibility (Elias et al., 2008). Pure Ti exhibits allotropic behavior, with a hexagonal close-packed (hcp) α -phase at room temperature that transforms to a body-centered cubic (bcc) β -phase above 882 °C. The $\alpha \leftrightarrow \beta$ phase transformation plays a key role in controlling the microstructure and mechanical behavior of Ti alloys. Alloying elements modify the β -transus temperature, enabling control of room-temperature phase stability. Based on their effect on phase stability, alloying elements are classified as α -stabilizers, β -stabilizers, and neutral elements. Figure 1.2 represents the effect of the alloying element on the phase stability of the Ti alloy. α -stabilizers such as aluminium (Al), nitrogen (N), carbon (C), and oxygen (O) increase the β -transus temperature by enhancing the thermodynamic stability of the hcp structure, enabling the formation of the α -phase at room temperature. The β -stabilizers decrease the β -transus temperature and extend the stability of the bcc β -phase. The β -stabilizers are further divided into β -isomorphous elements (Niobium (Nb), Tantalum (Ta), Vanadium (V), Molybdenum (Mo)), which have high solubility in Ti, and β -eutectoid elements (Iron (Fe), Copper (Cu), Manganese (Mn), Chromium (Cr), Nickel (Ni), Silicon (Si)), which have limited solubility and may form intermetallic phases. The neutral elements like Sn, Zr, and Hf have a weaker effect on the α/β phase boundary. However, they are generally used along with β -stabilizer, as it contributes to the reduction of ω -phase formation (Banerjee et al., 2013).

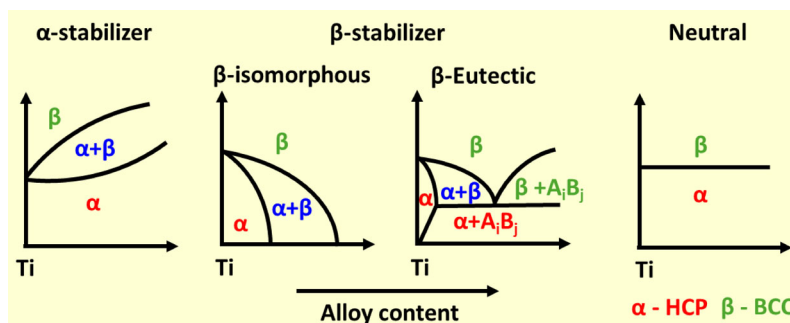


Figure 1.2. Schematic illustration of the effect of alloying elements on the phase stability of the Ti alloys, adapted from (Banerjee et al., 2013).

Depending on the relative proportions of the α and β -phases at room temperature, Ti alloys are classified as α , $\alpha+\beta$, or β alloys. A further subdivision of near- α , near- β , and metastable β alloys is also reported in the literature (Jackson et al., 2016). The $\alpha \leftrightarrow \beta$ transformation is highly sensitive to thermal gradients, alloying additions, and the cooling rate imposed during the processing. Figure 1.3 displays a schematic representation of the stability of different Ti phases as a function of β -stabilizer concentration.

Based on the concentration of β -stabilizer and processing conditions, the β -phase may persist in a metastable or stable form at room temperature. When the concentration of β -stabilizer is low, rapid cooling promotes the formation of hcp α' martensite or orthorhombic α'' . The martensite start temperature (M_s), which increases with decreases in concentration of β -stabilizer, explains whether the

quenched microstructure is fully or partially martensitic (Bignon et al., 2021). At higher concentrations of β -stabilizer, the metastable β matrix may transform to the ω -phase, which can nucleate athermally during quenching or evolve isothermally during low-temperature aging. Although controlled ω formation can enhance strength, excessive ω precipitation reduces ductility and impairs formability (Dobromyslov et al., 2001). The mechanical properties of Ti alloys, particularly their elastic modulus, are strongly influenced by the dominant phase fraction. The increasing trend of the elastic modulus of different phases of Ti is $\omega > \alpha > \alpha' > \alpha'' > \beta$. The β -phase exhibits the lowest elastic modulus and provides improved mechanical compatibility with bone. Consequently, extensive research has focused on developing metastable β -Ti alloys in which the high-temperature β or $\beta+\alpha'$ microstructure is preserved at room temperature. Properly tuned β alloys not only mitigate stress shielding but also provide favorable strength-to-modulus ratios, making them highly attractive for orthopedic applications (Qazi et al., 2005).

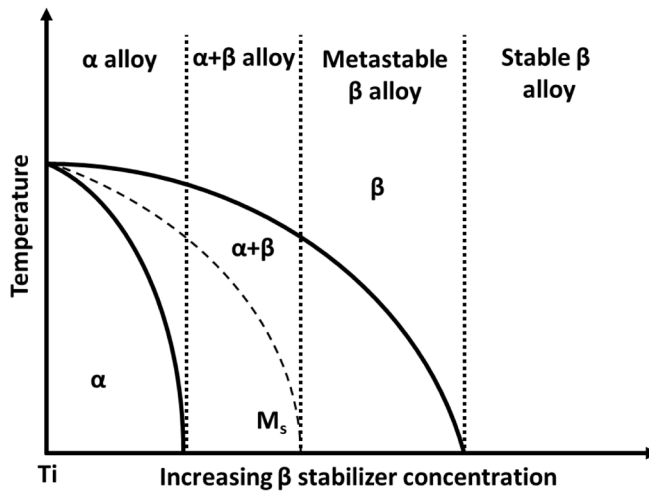


Figure 1.3. Schematic representation of the stability of phases of Ti with respect to the concentration of the β -stabilizer, adapted from (Jackson et al., 2016).

The retention of the β -phase at room temperature is achieved by adding β -stabilizing elements such as Nb, Ta, Fe, Co, V, Cr, Mn, Mo, Cu, Ni, and Sn. The electron-to-atom (e/a) ratio is commonly used to predict phase stability and elastic modulus of the β -Ti alloy. The e/a is the ratio of the average number of valence electrons per atom. The predicted critical value of e/a that retains a complete β -phase at room temperature is approximately 4.20. An e/a value above 4.20 could result in a complete β -phase, thereby achieving a low elastic modulus in the β -Ti alloy. Figure 1.4 shows the relation between the e/a ratio, elastic modulus, and β -phase stability in the Ti alloys. Lower e/a values may promote α'' martensite formation, while intermediate values may lead to ω -phase formation, which increases stiffness (Liang, 2020).

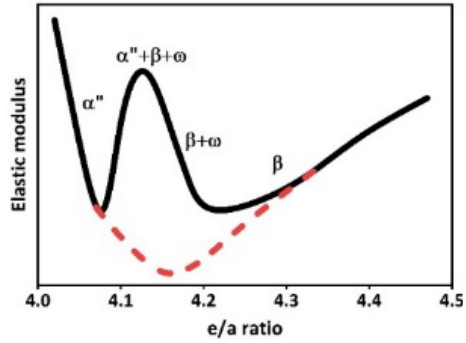


Figure 1.4. Schematic representation of the e/a ratio in Ti alloys, adapted from (Liang, 2020).

Another important and widely used parameter for predicting β -phase stability at room temperature is the molybdenum equivalence (Mo_{eq}), in wt.%, as shown in the relation (Zhou et al., 2018).

$$Mo_{eq} = Mo + 1.25 V + 0.59 W + 0.28 Nb + 0.22 Ta + 1.93 Fe + 1.84 Cr + 1.51 Cu + 2.46 Ni + 2.67 Co + 2.26 Mn + 0.3 Sn + 0.47 Zr + 3.01 Si - 1.47 Al \quad (1)$$

Several works have reported that Mo_{eq} above 10 results in metastable β -phase at room temperature. This relation is commonly used to design a β -Ti alloy with a low elastic modulus. Although appropriate alloy design can reduce the elastic modulus, implant performance also depends on biocompatibility and corrosion resistance. Some β -stabilizing elements may exhibit cytotoxicity or adverse biological effects. The biocompatibility and toxicity of commonly used alloying elements are summarized in Figure 1.5 (Banerjee et al., 2013).

| Element | Biocompatibility | Cytotoxic | Genotoxic | Carcinogenic | Mutagenic | Corrosion prone |
|---------|------------------|-----------|-----------|--------------|-----------|-----------------|
| Ti | Yes | Mild | No | No | No | No |
| Cu | No | High | Yes | No | Yes | Yes |
| Co | No | High | Yes | Yes | Yes | Yes |
| Cr | No | High | Yes | Disputed | Yes | No |
| Fe | Yes | Mild | Yes | No | Disputed | No |
| Mn | No | High | Yes | No | No | No |
| Ni | No | High | Yes | Yes | Yes | Yes |
| Mo | No | Low | Yes | Disputed | Yes | Yes |
| Nb | Yes | Low | No | No | No | No |
| Sn | Yes | Low | No | No | No | No |
| V | No | High | Yes | Yes | Yes | No |
| Ta | Yes | Low | No | No | No | No |

Figure 2.5. Biocompatibility and toxicity of different β -stabilizers in Ti alloys, adapted from (Banerjee et al., 2013).

Considering biocompatibility and toxicity, Nb, Sn, Ta, and Fe are the preferred alloying elements. Among these, Nb is particularly attractive for biomedical applications due to its non-toxicity and ability to enhance mechanical properties without compromising biocompatibility. Nb promotes the development of stable passive films enriched in Nb_2O_5 , which enhances corrosion resistance (Woldemedhin

et al., 2012). Ti alloys containing approximately 35-45Nb (wt.%) typically retain a metastable β -phase at room temperature. It exhibits a significantly lower elastic modulus than conventional Ti alloys. In addition to Nb, Fe is also investigated as a cost-effective β -stabilizing element. Fe is a β -eutectoid stabilizer that enhances β -phase stability when added in small amounts. However, excessive Fe addition may lead to intermetallic phase formation and deterioration of mechanical properties. Therefore, Fe is generally limited to low concentration (<5 wt.%), where it contributes to β -phase stabilization while maintaining favorable mechanical and corrosion performance (Kim et al., 2024).

1.2 Selective laser melting of β -Ti alloys

Selective laser melting (SLM) has emerged as an advanced manufacturing technique for producing complex and patient-specific Ti alloy implants. The advantages of SLM are minimal material waste, high powder utilization efficiency, and unrestricted geometric freedom, attributes that are not feasible through traditional manufacturing routes (Zhou et al., 2019). The schematic representation of the SLM setup is presented in Figure 1.6.

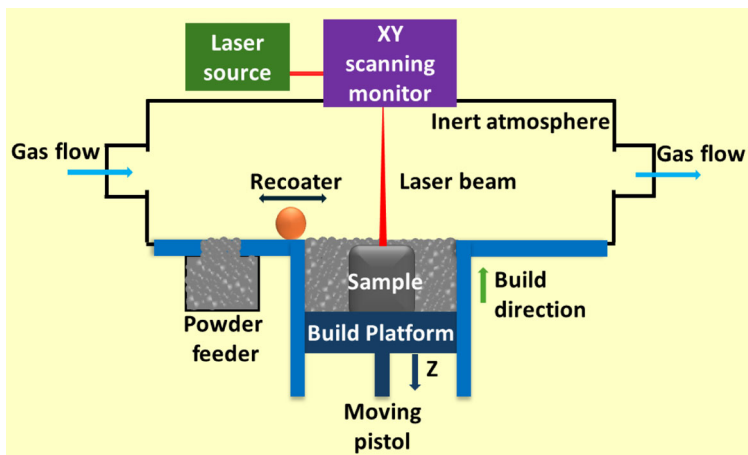


Figure 1.6. Schematic representation of the basic components of an SLM machine, adapted from paper 1.

The SLM process fabricates components directly from computer-aided design (CAD) models by selectively melting thin layers of metallic powder under an inert atmosphere. During fabrication, a thin layer of powder is spread over the build platform using a recoating system. A focused laser beam selectively scans and melts regions defined by the CAD model, producing localized melting followed by rapid solidification. After completing each layer, the platform lowers by a predefined distance, and a new powder layer is deposited on the previously melted surface. This sequence of powder deposition, selective melting, and platform displacement is repeated until the entire part is printed. Upon completion of the printing, the fabricated part is separated from the build substrate by mechanical cutting or the wire electrical discharge machining process (Subramanian et al., 2023).

One of the key characteristics of the SLM process is the extremely high cooling rate ($10^3 - 10^6 \text{ K}\cdot\text{s}^{-1}$) that promotes refined microstructures and metastable phase formation. However, the rapid melting and solidification inherent to the SLM process generate steep thermal gradients within the melt pool. Instability in melt-pool dynamics can lead to defects such as porosity, lack-of-fusion regions, keyhole cavities, and residual thermal stresses. These defects affect the mechanical performance and long-term reliability of the implant. Consequently, the microstructure and properties of SLM-fabricated implants are highly sensitive to processing parameters (Subramanian et al., 2023). The critical parameters, including laser power (P), scanning speed (v), layer thickness (t), and hatch spacing (s), are typically explained by the volumetric energy density ($\text{J}\cdot\text{mm}^{-3}$) expression as provided in paper II,

$$E = \frac{P}{v \cdot t \cdot s} \quad (2)$$

Thus, achieving high-quality parts requires an optimal energy density tailored to the specific alloy system. In addition to SLM process parameters, feedstock powder characteristics strongly influence build quality. Particle morphology, size distribution, flowability, purity, and packing density affect the powder spreading behavior and energy absorption during SLM fabrication (Lewis, 2022). Among available powder production methods, gas atomization is the most widely used due to its mass producibility, reproducibility, reliability, and ability to produce spherical, high-purity particles with homogeneous microstructure (Popovich et al., 2016). Despite their reliability, pre-alloyed powders present several limitations. The production cost is high due to the requirement for sophisticated atomization systems, high-purity inert gases, and energy-intensive processing (Feng et al., 2024). Gas atomization of alloys containing high-melting-point elements is challenging due to reduced melt flow, high viscosity, and the risk of nozzle clogging. (Feng et al., 2024). Gas entrapment during atomization may produce hollow particles or satellite structures, which reduce the packing density of the powder layer (Soong et al., 2023). The limited kinetic energy of the high-pressure gas used to disperse the molten stream influences the efficiency of melt fragmentation, often resulting in reduced powder yield (Feng et al., 2024). Producing powders with desired size ranges and morphologies requires process control and operational expertise, posing additional barriers.

To overcome the drawbacks of pre-alloyed powders, researchers have focused on *in-situ* alloying using blended elemental powders. Notably, *in-situ* alloying enables direct mixing of elemental powders, thereby reducing material costs relative to pre-alloyed powders. This approach is beneficial for alloys containing refractory elements such as Nb, Ta, or Mo, whose high melting points make conventional powder production economically and technically challenging (Mosallanejad et al., 2021). Furthermore, it provides compositional flexibility, allowing alloy composition to be varied by adjusting powder ratios. It enables rapid screening of composition-property relationships and accelerates the development of novel biomedical alloys.

1.2.1 Selective laser melting of β -Ti-Nb alloy

Among the available β -Ti alloys, Ti-Nb systems are widely explored as Nb acts as a strong β -phase stabilizer in Ti alloys. Stabilization of the β -phase is particularly desirable for biomedical implants, as it enables a reduced elastic modulus that is closer to that of cortical bone (Prashanth et al., 2017). Earlier studies on the SLM

fabrication of β -Ti-Nb alloys have primarily employed pre-alloyed powders. Investigations on compositions such as Ti-41Nb (wt.%) (Xu et al., 2022), Ti-42Nb (wt.%) (Qiu et al., 2022), Ti-42Nb (wt.%) (Pilz et al., 2024), and Ti-45Nb (wt.%) (Akman et al., 2024) reported the formation of relatively dense samples with minimal processing defects. Due to the rapid solidification associated with SLM, the alloys predominantly exhibited a β -phase with refined and relatively homogeneous microstructures. These findings demonstrate that SLM is capable of fabricating β -Ti-Nb alloys with stable β -phase microstructures over a wide range of Nb compositions. Figure 1.7 presents the scanning electron microscopy image of the Ti-41Nb alloy fabricated by SLM, highlighting the relatively homogeneous microstructure as reported by (Xu et al., 2022).

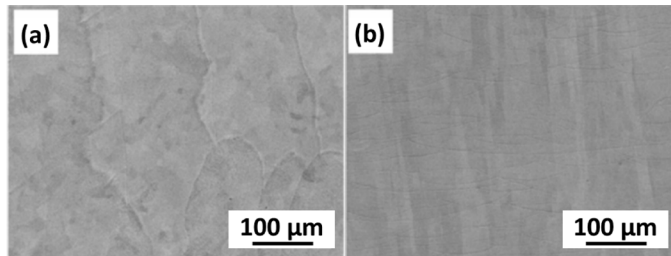


Figure 1.7. SEM images of SLM-fabricated Ti-41Nb alloy using pre-alloyed powder, highlighting the homogeneous β -phase microstructure in (a) normal direction and (b) build direction, reproduced with permission from (Xu et al., 2022).

Owing to the earlier mentioned limitations and difficulties associated with the pre-alloyed powders, the use of elemental powders has emerged as a promising alternative for producing low-modulus β -Ti-Nb alloy. Several studies have investigated the *in-situ* alloying of β -Ti-Nb alloys using elemental powders via SLM fabrication. It includes different compositions such as Ti-40.5Nb (wt.%) (Fischer et al., 2016), Ti-15, 25, and 45Nb (at.%) (Wang et al., 2017), Ti-35Nb (wt.%) (Wang et al., 2019), Ti-25Nb (wt.%) (Zhao et al., 2020), Ti-35Nb (wt.%) (Wang et al., 2021), Ti-10-30Nb (wt.%) (Borgman et al., 2021), Ti-34Nb (wt.%) (S. Huang et al., 2021), Ti-41Nb (wt.%) (S. Huang et al., 2022), and Ti-28.5Nb and Ti-40Nb (wt.%) (Singh et al., 2024). Microstructural analyses consistently report partially melted or unmelted Nb particles in the Ti matrix due to the large difference in melting temperature and density between Ti and Nb. Increasing energy density improves Nb dissolution but promotes porosity, whereas lower energy density reduces porosity but increases the fraction of unmelted Nb. Therefore, only a narrow processing window exists for balancing Nb dissolution and defect formation. Consequently, achieving chemically homogeneous β -Ti-Nb alloys through single-pass *in-situ* SLM processing remains challenging. Figure 1.8. presents the scanning electron microscopy images of SLM-fabricated (a) CP-Ti, (b) Ti-15Nb, (c) Ti-25Nb, and (d) Ti-45Nb alloys, highlighting the presence of unmelted Nb and pores. The fraction of unmelted Nb particles increases with an increase in Nb wt.% in the alloy.

The homogeneity of *in-situ* alloyed β -Ti-Nb alloys is sensitive to powder characteristics such as particle size distribution, morphology, density, and flowability. These factors influence powder spreading behavior and local energy absorption during SLM processes. In addition to physical characteristics, differences in melting

temperature, specific heat capacity, latent heat of fusion, thermal conductivity, and laser reflectivity among alloying elements strongly influence melting and dissolution dynamics. In the case of β -Ti-Nb alloy, the vast difference in melting temperature and density between Ti and Nb presents a major challenge. The larger Nb particles often remain partially unmelted under single laser exposure, leading to chemical heterogeneity and elemental segregation. While finer Nb particles improve dissolution kinetics, excessive refinement can adversely affect powder flowability and increase the risk of powder bed instability. Although Marangoni convection within the melt pool promotes solute mixing, its effectiveness is constrained by differences in liquid-state density and viscosity of the alloying elements (Tang et al., 2025).

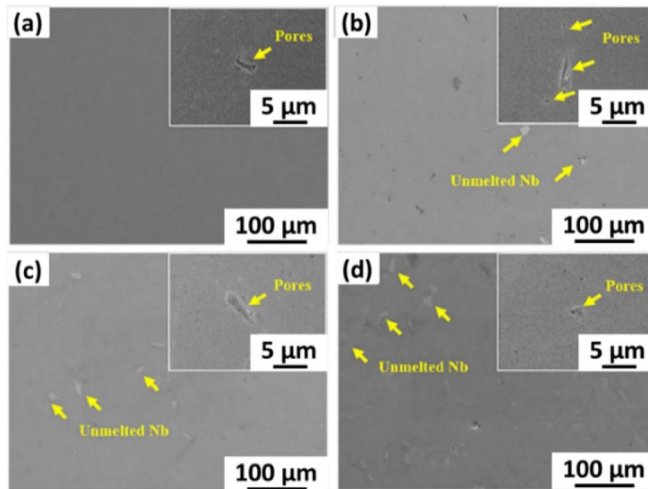


Figure 1.8. SEM images of SLM-fabricated (a) CP-Ti, (b) Ti-15Nb, (c) Ti-25Nb, and (d) Ti-45Nb alloy, highlighting the presence of unmelted Nb and pores (yellow arrows), reproduced with permission from (Wang et al., 2017).

To address the limitations associated with incomplete Nb dissolution and microstructural heterogeneity, laser remelting strategies have been explored as an alternative approach. Similar studies on Ti-25Ta (wt.%) (Brodie et al., 2020), Ti-12Mo (wt.%) (Duan et al., 2021) and Ti-10Ta-5Cu, Ti-15Ta-5Cu, and Ti-20Ta-5Cu (wt.%) (Polozov et al., 2024) demonstrated that repeated laser exposure increases melt-pool lifetime and enhances Marangoni convection. This promotes improved diffusion of refractory elements and better chemical homogenization. Although these studies suggest that remelting reduces the fraction of unmelted particles and improves densification, complete dissolution of high-melting-point elements such as Nb remains challenging (S. Huang et al., 2019).

1.2.2 Mechanical properties of SLM-fabricated β -Ti-Nb-based alloys

The phase stability and mechanical properties of the SLM-fabricated β -Ti-Nb-based alloys are strongly influenced by the alloying elements. A summary of the phase constitution and mechanical properties of these alloys is presented in Table 1.2.

Table 3.2. Comparison of phase constitution and mechanical properties of the SLM-fabricated β -Ti-Nb-based alloys. *H* represents hardness, *E* represents elastic modulus, *Y* represents yield strength, *T* represents tensile testing, and *C* represents compression testing methods.

| Composition (wt.%) | Powder | Phase | H (HV) | E (GPa) | Y (MPa) | Reference |
|---------------------------|------------------------------------|---|---------------|----------------|----------------|----------------------------|
| Ti-35Nb | Prealloyed | α, α'', β | 174 | 72 | 485 (T) | (Wang et al., 2022) |
| Ti-41Nb | Prealloyed | β | - | - | 504 (C) | (Xu, et al., 2022) |
| Ti-42Nb | Prealloyed | β | - | 65 | 701 (C) | (Pilz et al., 2024) |
| Ti-45Nb | Prealloyed | β | 257 | 50 | 380 (C) | (Schwab et al., 2015) |
| Ti-25Nb | Elemental – <i>in-situ</i> alloyed | $\alpha', \beta, \text{unmelted Nb}$ | 264 | 83 | 645 (T) | (Zhao et al., 2020) |
| Ti-30Nb | Elemental – <i>in-situ</i> alloyed | $\alpha'', \beta, \text{unmelted Nb}$ | - | 84 | 769 (C) | (Borgman et al., 2021) |
| Ti-35Nb | Elemental – <i>in-situ</i> alloyed | $\alpha, \alpha'', \beta, \text{unmelted Nb}$ | 274 | 84 | 648 (T) | (Wang et al., 2021) |
| Ti-40Nb | Elemental – <i>in-situ</i> alloyed | $\beta, \text{unmelted Nb}$ | 278 | 81 | 344 (T) | (Singh et al., 2024) |
| Ti-48Nb | Elemental – <i>in-situ</i> alloyed | $\alpha'', \beta, \text{unmelted Nb}$ | - | 82 | - | (Sharkeev et al., 2017) |
| Ti-25Nb-5Sn | Elemental – <i>in-situ</i> alloyed | $\alpha'', \beta, \text{unmelted Nb}$ | - | 92 | 579-648 (T) | (Palaniappan et al., 2025) |
| Ti-35Nb-1Cu | Elemental – <i>in-situ</i> alloyed | $\alpha, \beta, \text{unmelted Nb}$ | 259 | 49 | 729 (T) | (Jin et al., 2024) |
| Ti-35Nb-3Cu | Elemental – <i>in-situ</i> alloyed | $\alpha, \beta, \text{Ti}_2\text{Cu}, \text{unmelted Nb}$ | 253 | 51 | 772 (T) | |
| Ti-35Nb-5Cu | Elemental – <i>in-situ</i> alloyed | $\alpha, \beta, \text{Ti}_2\text{Cu}, \text{unmelted Nb}$ | 289 | 65 | 836 (T) | |
| Ti-34Nb-13Ta | Elemental – <i>in-situ</i> alloyed | $\alpha, \beta, \text{unmelted Nb}$ | 208 | 52 | 610 (T) | (Kong et al., 2021) |
| Ti-34Nb-13Ta-5Zr | Elemental – <i>in-situ</i> alloyed | $\alpha, \beta, \text{unmelted Nb}$ | 232 | 57 | 650 (T) | |
| Ti-34Nb-13Ta-9Zr | Elemental – <i>in-situ</i> alloyed | $\alpha, \beta, \text{unmelted Nb}$ | 259 | 66 | 741 (T) | |

SLM-fabricated β -Ti-Nb-based alloys from pre-alloyed powder show Nb wt.% dependent phase stability. The Ti-35Nb alloy exhibits a mixed $\alpha+\alpha''+\beta$ phase, while the Ti-41Nb, Ti-42Nb, and Ti-45Nb alloys exhibit a predominant β -phase. The enhanced β stability due to uniform and complete dissolution of Nb leads to a decreasing trend in elastic modulus and compressive yield strength. In contrast, phase stability in the SLM-fabricated β -Ti-Nb-based alloys from elemental powders is influenced by the incomplete melting and dissolution of Nb particles. The insufficient dissolution of Nb reduces effective β -phase stabilization during the *in-situ* alloying. As a result, Ti-25Nb, Ti-30Nb, and Ti-35Nb alloys form α'/α'' martensitic along with β phases and unmelted Nb particles, leading to increased elastic modulus and strength. Though Ti-40Nb alloy exhibits a predominant β -phase, complete dissolution of Nb was not achieved. The stabilization of β -phase resulted in reduced elastic modulus and tensile yield strength of the Ti-40Nb alloy. In addition to the Nb, the incorporation of other β -stabilizers like Sn, Cu, Ta, and Zr in the SLM-fabricated β -Ti-Nb alloys further influences the phase stability and mechanical properties. In Ti-25Nb-5Sn alloy, Sn suppresses the ω phase precipitation and retains $\alpha''+\beta$ phases, resulting in increased tensile yield strength. In Ti-35Nb-Cu alloys, Cu promotes β -phase stabilization and precipitation of Ti_2Cu intermetallic phases. Increasing Cu content raises yield strength and modulus, demonstrating precipitation-strengthening effects. In Ti-Nb-Ta alloys, Ta stabilizes the β phase, resulting in reduced elastic modulus, while Zr promotes grain refinement, thereby improving the strength of the alloy. Regardless of different alloy additions, unmelted Nb particles persist in all β -Ti-Nb-based alloys fabricated from elemental powder, leading to anisotropic mechanical behavior.

1.2.3 Passivation behavior of SLM-fabricated β -Ti-Nb alloys in physiological environments

The passivation behavior of SLM-fabricated Ti-Nb-based alloys was investigated using electrochemical methods in simulated physiological environments. The electrochemical methods used in the literature are potentiodynamic polarization (PDP) and electrochemical impedance spectroscopy (EIS). In general, the passivation behavior of β -Ti-Nb-based alloys is typically characterized by low corrosion current density (I_{corr}) from PDP and high polarization resistance (R_p) from EIS, indicating the formation of a stable passive film. The SLM-fabricated Ti-35Nb alloy produced from pre-alloyed powder and tested in Hank's solution at 37 °C exhibited high passive behavior with a low I_{corr} ($0.13 \mu\text{A}\cdot\text{cm}^{-2}$) and high R_p values ($2.70 \text{M}\Omega\cdot\text{cm}^2$). TEM-EDS analysis revealed that the passive film mainly consisted of Ti- and Nb-oxides, indicating the formation of a stable mixed oxide passive film on SLM-fabricated Ti-35Nb. The Ti-42Nb alloy fabricated from pre-alloyed powder and tested in phosphate-buffered saline (PBS) exhibited an I_{corr} of $0.53 \mu\text{A}\cdot\text{cm}^{-2}$ and R_p of $0.14 \text{M}\Omega\cdot\text{cm}^2$, suggesting that β -phase stability influences the passive film stability and passivation behavior. Ti-35Nb alloys fabricated from elemental powder and tested in Hank's solution showed a low I_{corr} ($0.15 \mu\text{A}\cdot\text{cm}^{-2}$) and high R_p ($2.88 \text{M}\Omega\cdot\text{cm}^2$). The results indicate that the Ti-Nb oxide passive film provides effective passivation behavior despite microstructural heterogeneity. Ti-25Nb-5Sn alloy tested in simulated body fluid (SBF) showed a relatively high I_{corr} ($6.90 \mu\text{A}\cdot\text{cm}^{-2}$). The alloy contained $\alpha''+\beta$ phases with unmelted Nb particles, suggesting that microstructural heterogeneity and alloying additions influenced the passive film

stability. The Ti-35Nb-7Zr-5Ta (Ummethala et al., 2021) tested in PBS, exhibited a stable passivation behaviour. PDP analysis revealed a low I_{corr} ($0.23 \mu\text{A.cm}^{-2}$), in physiological media. Surface analysis carried out by Auger Electron Spectroscopy (AES) indicated that the passive layer mainly consisted of Ti-rich and Nb-rich oxides (TiO_2 and Nb_2O_5), while the contributions of Zr and Ta were relatively small. Ti-34.5Nb-6.9Zr-4.9Ta-1.4Si alloy exhibited excellent passivation behaviour in PBS, as the alloy showed a lower I_{corr} of $0.28 \mu\text{A.cm}^{-2}$. EIS analysis revealed the formation of a two-layer passive film, consisting of a dense inner barrier layer and a porous outer layer. The results show that the addition of Si improved passive film stability by increasing the barrier layer resistance. Overall, SLM-fabricated β -Ti-Nb-based alloys exhibit stable passivation characterized by low I_{corr} and high R_p due to the formation of Ti- and Nb-oxide passive films. The passivation behavior is strongly influenced by alloy composition, phase stability, and microstructural homogeneity. Table 1.3 presents a comparison of the electrochemical properties of β -Ti-Nb-based alloys.

Table 4.3. Comparison of the electrochemical properties of SLM-fabricated β -Ti-based alloys. *M* represents the medium, *I*_{corr} represents corrosion current density, *R*_p represents polarization resistance, and *PC* represents passive film chemistry.

| Alloy (wt.%) | Phase | M | <i>I</i>_{corr} (PDP) ($\mu\text{A.cm}^{-2}$) | <i>R</i>_p (EIS) ($M\Omega.cm^2$) | PC | Referenc e |
|---|---|-------------------------------|---|---|---|-----------------------------------|
| Ti-35Nb Pre-alloyed | α, α'', β | Hank's solution at 37°C | 0.13 | 2.70 | TEM-EDS analysis Ti- and Nb- oxide based passive film | (Qin et al., 2021) |
| Ti-42Nb Pre-alloyed | β | PBS at RT | 0.53 | 0.14 | - | (Akman et al., 2024) |
| Ti-35Nb Elemental – in-situ alloyed | α, α'', β , unmelted Nb | Hank's solution at 37°C | 0.15 | 2.88 | - | (Qin et al., 2021) |
| Ti-25Nb- 5Sn Elemental – in-situ alloyed | α'', β , unmelted Nb | SBF at 37°C | 6.90 | - | - | (Palaniap pan et al., 2025) |
| Ti-35Nb- 7Zr-5Ta Prealloyed | β | PBS at 37°C | 0.18 | 0.025 | AES analysis Ti- and Nb- oxide based passive film | (Ummet hala et al., 2021) |
| Ti-35Nb- 7Zr-5Ta Prealloyed | β , | PBS at RT | 0.35 | 1.02 | - | (Luo et al., 2025) |
| Ti-34.5Nb- 6.9Zr-4.9Ta- 1.4Si Prealloyed | β | PBS at RT | 0.28 | 1.42 | - | |

1.3 Surface modification of SLM-fabricated β -Ti-Nb alloy

Surface engineering of β -Ti-Nb alloys aims to improve osseointegration and bone-implant interfacial bonding without compromising mechanical integrity or corrosion resistance. β -Ti-Nb alloys are inherently bioinert, which limits interaction with surrounding tissues and affects long-term implant fixation. Consequently, surface modification is required to enhance biological performance (Cardoso et al., 2024). Conventional coating techniques often face limitations such as high cost, slow growth rate, thin coatings, weak interfacial bonding, and difficulty in coating complex geometries (Lokeshkumar et al., 2023). In this regard, plasma electrolytic oxidation (PEO) has emerged as an effective surface engineering technique for β -Ti-Nb alloys. PEO is an electrochemical process that forms thick, ceramic-like oxide coatings strongly bonded to the metallic substrate. The schematic representation of the PEO setup is shown in Figure 1.9.

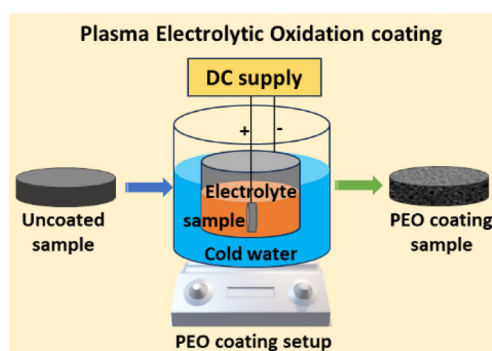


Figure 1.9. Schematic representation of PEO setup.

Unlike conventional anodization, PEO operates at high applied voltages, generating localized plasma micro-discharges that facilitate the incorporation of electrolyte-derived species into the growing oxide layer. The PEO process generally proceeds through three stages of oxide growth. Stage I corresponds to initial anodic oxidation, where a thin and compact oxide layer forms on the surface as the voltage increases. Stage II begins at the dielectric breakdown voltage, where plasma micro-discharges appear across the surface. These discharges cause localized melting of the oxide layer and substrate, followed by rapid quenching in the electrolyte, which promotes coating growth and densification. Stage III, often referred to as the micro-arc stage, is characterized by continued oxide growth and increasing electrical resistance of the coating (Ikonopisov, 1977). The key parameters governing the PEO process include applied voltage, current density, electrolyte composition, and treatment time. These parameters control plasma discharge intensity and influence coating morphology. Higher voltage and current density generally produce thicker and more porous oxide coatings, whereas optimized conditions promote more uniform and stable layers. Consequently, these parameters determine pore size, surface roughness, phase composition, and overall coating performance, which directly influence corrosion resistance and bioactivity. The PEO coatings typically possess a porous outer layer and dense inner barrier layer, which improve corrosion resistance and surface bioactivity. In addition, the porous structure increases surface wettability, promoting cell attachment and fibroblast proliferation. Electrolyte

chemistry plays a critical role in coating characteristics. Phosphate-based electrolytes are widely used to improve corrosion protection on Ti alloys, while silicate-based electrolytes enhance coating stability on Nb-containing alloys (Wu et al., 2022). However, studies on the optimal electrolytes for PEO processing of Ti-40Nb alloys remain limited. Lokeshkumar et al. (2023) reported that a phosphate-to-silicate ratio of 50:50 produces dense and relatively thick coatings with improved corrosion resistance on cast Ti-40Nb substrates. Furthermore, the incorporation of bioactive hydroxyapatite (HAp) into PEO electrolytes has been reported to enhance osteointegration. This improvement promotes stronger bone-implant interaction and contributes to long-term implant functionality (Ni et al., 2008; Yadav et al., 2022). Consequently, PEO coatings exhibit enhanced passivation behaviour, corrosion resistance, and biological activity (Zhang et al., 2020).

Several studies have investigated the PEO behavior on β -Ti alloys fabricated through conventional processing routes, such as casting and powder metallurgy (Chen et al., 2018; Kaseem et al., 2019; Maciej et al., 2023). These materials exhibit equilibrium β or $\alpha+\beta$ microstructures with coarse grain sizes and low defect densities. Such microstructure features influence oxide growth kinetics and plasma discharge behavior during the PEO process (Wu et al., 2023). In contrast, β -Ti alloys produced via SLM exhibit highly non-equilibrium microstructures formed under rapid solidification and repeated thermal cycling (Maurya et al., 2022). These microstructures contain retained metastable phases, refined grains, high dislocation density, and significant chemical and crystallographic heterogeneity. Such features significantly alter the substrate's local electrical conductivity and electrochemical response. Consequently, they influence the plasma discharge initiation, intensity, and spatial distribution during the PEO process (Sagidugumar et al., 2024). (Ferdyn et al., 2025) investigated the influence of SLM-processed Ti-21Zr-19Nb microstructure on PEO coating properties by comparing them with conventionally processed substrate. The SLM substrate produced thicker and more uniform PEO coatings with larger discharge pores, indicating stronger plasma discharge activity during oxidation. The coatings also showed higher incorporation of O, Ca, and P species, forming bioactive oxide/phosphate phases. These results demonstrate that the refined and defect-rich SLM microstructure promotes coating growth, modifies coating morphology, and enhances biological response. The cell culture was cultured in Dulbecco's Modified Eagle Medium (DMEM) and stained after 7 days of incubation to evaluate the cellular response. Figure 1.10 displays the fluorescence image of (a) control, (b) Ti-21Zr-19Nb cast-PEO coated, and (c) Ti-21Zr-19Nb PEO-coated SLM samples after staining the cells cultured in DMEM for 7 days.

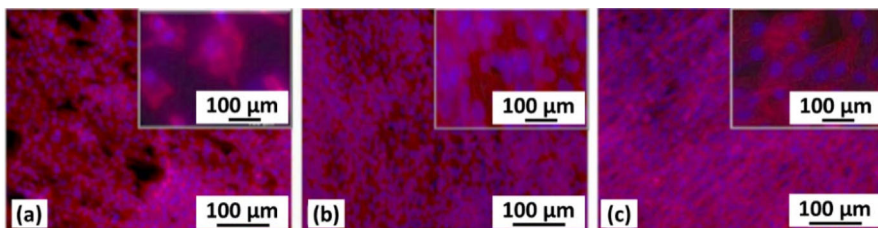


Figure 1.10. Fluorescent image of (a) control, (b) Ti-21Zr-19Nb cast-PEO coated, and (c) Ti-21Zr-19Nb PEO-coated SLM sample after 7 days of incubation in DMEM, reproduced with permission from (Ferdyn et al., 2025).

This study highlights that refined microstructures in SLM samples promote earlier dielectric breakdown of the oxide layer (Singh et al., 2021). It accelerates the rise in voltage and enhances micro-arc activity, resulting in thicker, denser coatings compared with conventionally processed materials. These effects are attributed to the increased number of charge transport pathways provided by grain boundaries, dislocations, and phase interfaces, which facilitate localized plasma formation and oxide growth (Pezzato et al., 2020). Despite these advances, systematic studies on PEO coating formation specifically on SLM-fabricated Ti-40Nb β -type alloys remain limited. The presence of a β -phase structure with high defect density in SLM-processed Ti-40Nb is expected to influence discharge behavior, coating morphology, and functional performance relative to conventionally processed alloys. Addressing this knowledge gap is essential to establishing structure-process-property relationships linking SLM-induced microstructures with PEO coating characteristics.

2 Materials and methods

2.1 SLM fabrication

Commercially pure titanium (CP-Ti, $\sim 25 \mu\text{m}$, $>99.9\%$, Nanoshell, UK), niobium (Nb, $\sim 27 \mu\text{m}$, $>99.9\%$, Pacific Particulate Materials Ltd., Canada) and iron powders (Fe, $\sim 25 \mu\text{m}$, $>99.9\%$, Materials Ltd., Canada) were used to prepare the elemental feedstock powder for SLM fabrication of bulk sample. Elemental powders were weighed and mixed to achieve a nominal composition of Ti-40Nb (60 wt.% Ti and 40 wt.% Nb) and Ti-35Nb-5Fe (60 wt.% Ti, 35 wt.% Nb, and 5 wt.% Fe). To ensure compositional homogeneity, the powders were blended in a sealed polymeric container using a low-energy mixer operated at 10 rpm for 24 h.

The bulk Ti-40Nb (TN) and Ti-35Nb-5Fe (TNF) samples were fabricated using an SLM system (SLM 280 2.0, SLM Solutions). The machine incorporates a 700 W IPG fiber laser with a wavelength of 1064 nm and a spot size of $\sim 110 \mu\text{m}$. Sample fabrication was carried out using the process parameters as mentioned in Table 2.1.

Table 2.1. Process parameters utilized for the SLM-fabrication of bulk samples.

| Sample designation | Power (W) | Scan speed (mm.s^{-1}) | Hatch spacing (mm) | Layer thickness (mm) | Hatch rotation ($^\circ$) | Energy density (J.mm^{-3}) |
|--------------------|-----------|-----------------------------------|--------------------|----------------------|-----------------------------|---------------------------------------|
| TN-S | | | | | | |
| TN-T | 650 | 650 | 0.035 | 0.03 | 67 | 952 |
| TNF-T | | | | | | |

A stripe scanning strategy was applied to ensure uniform melt-track overlap and controlled thermal input throughout the build. In the single melting (S) condition, each layer was melted once, whereas in the triple melting (T) condition, each layer was melted three times using identical process parameters and scan direction, without hatch rotation. A schematic representation of the melting strategies is shown in Figure 2.1.

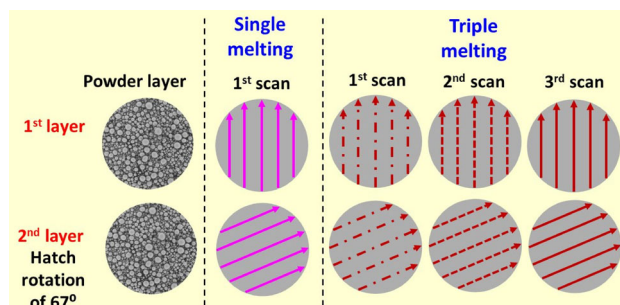


Figure 2.1. Schematic representation of remelting strategy utilized in the SLM-fabrication of bulk samples, adapted from paper II.

During fabrication, the build chamber was continuously purged with high-purity argon gas (99.9%) to minimize oxidation. The samples were fabricated on a 30 mm thick pure Ti substrate and subsequently detached using wire electrical discharge

machining (WEDM). Cubic samples measuring 5 × 5 × 5 mm were prepared for subsequent microstructural and mechanical evaluations. In addition, cylindrical discs of TN-T with a thickness of 2 mm were fabricated for surface modification studies.

2.2 Structural and microstructural characterization

Phase identification of the feedstock powder and the SLM-fabricated bulk samples was carried out using an X-ray diffractometer (XRD, Bruker AXS) with Cu-K α radiation ($\lambda = 1.54 \text{ \AA}$). Diffraction patterns were collected over a 2θ range of 30°-90° with a step increment of 0.02°. Quantitative phase analysis of the TN-S, TN-T and TNF-T was performed using the Rietveld refinement method in Xpert Highscore Plus software. Microstrain analysis was conducted on TN-S and TN-T samples using the Williamson-Hall (W-H) method. The relationship is given by following equation (Khorsand et al., 2011)

$$\beta \cos \theta = \frac{k\lambda}{D} + 4\epsilon \sin \theta \quad (3)$$

where D represents the crystallite size, k is the Scherrer constant (0.94), λ is the wavelength of the incident X-ray radiation, β corresponds to the full width at half maximum (FWHM) of the diffraction peaks, θ is the Bragg angle, and ϵ denotes the microstrain. A linear fit of $\beta \cos \theta$ versus $4 \sin \theta$ was used to extract the microstrain from the slope of the resulting plot.

The SLM-fabricated samples were prepared using standard metallographic techniques for microstructural characterization. Initially, the samples were sequentially polished with silicon carbide (SiC) abrasive papers ranging from P400 to P4000 grit. Final polishing was performed using a 0.05 μm colloidal silica suspension to achieve a mirror-quality surface. Porosity analysis on the unetched TN-S and TN-T samples was carried out using optical microscopy (OM, Zeiss, Germany). Quantitative OM image analysis was performed using ImageJ software to determine the porosity fraction. In addition, micro-computed tomography (μ -CT) analysis was carried out to analyze the bulk porosity percentage. Micro electropolishing was carried out using a Struers LectroPol 5 system with electrolyte A3, composed of 58.82% methanol, 35.29% 2-n-butoxyethanol, and 5.89% perchloric acid. The polishing was performed at an applied voltage of 32 V (corresponding to a current density of 0.2 A.cm⁻²) for 12 s at 25 °C. The polished samples were subsequently analyzed using scanning electron microscopy (SEM) and electron backscatter diffraction (EBSD) for detailed microstructural characterization. The grain size of the SLM-fabricated samples was determined from EBSD data using the area fraction method. An approximate scan area of 450 μm × 335 μm was selected for EBSD analysis.

2.3 Mechanical testing

The Vickers microhardness measurements of the SLM-fabricated bulk were carried out using a Buehler Micromet microhardness tester. Indentations were performed using an applied load of 1000 g, with a dwell time of 10 s. For each condition, ten indentations were made at different locations (0.5 mm distance from each other) on the sample surface, and the average hardness value was reported. In addition, a hardness profile mapping (5 × 5 matrix) was measured to evaluate the effect of remelting on hardness variation across the sample surface.

Uniaxial compression tests of SLM-fabricated TN-T and TNF-T samples were carried out at room temperature using an INSTRON 5967 universal testing machine fitted with a 30 kN load cell. A constant strain rate of $1 \times 10^{-3} \text{mm.s}^{-1}$ was applied. Cylindrical specimens (3 mm diameter, 6 mm height) were extracted from SLM-fabricated cuboidal samples by wire electrical discharge machining, following ASTM E9 standard (Affolter et al., 2015). For each processing condition, three samples were tested to ensure repeatable and reliable mechanical data.

2.4 Passivation studies

The passivation behavior of the SLM-fabricated TN-T and TNF-T samples was investigated using a standard three-electrode electrochemical cell coupled with a potentiostat. Phosphate-buffered saline (PBS) at pH 7 served as the electrolyte. The bulk samples acted as the working electrode, with a platinum sheet as the counter electrode and an Ag/AgCl as the reference. Potentiodynamic polarization (PDP) measurements were conducted on an exposed area of 0.5 cm^2 at a scan rate of 0.01 V.s^{-1} over a potential window of -0.5 to $+2 \text{ V}_{\text{Ag/AgCl}}$. Electrochemical impedance spectroscopy (EIS) was performed at open-circuit potential using a small sinusoidal perturbation ($\pm 10 \text{ mV}$) across a frequency range of 10^{-2} to 10^5 Hz . Mott–Schottky (M-S) analysis was carried out at 1 kHz to evaluate the semiconducting characteristics of the passive film. All tests were carried out in PBS at $37 \text{ }^\circ\text{C}$ and pH 7 to replicate physiological conditions, with each experiment repeated three times for reproducibility.

The passive film composition of TN-T and TNF-T samples exposed in PBS solution for 72 h was carried out by X-ray Photoelectron Spectroscopy (XPS, Thermo Scientific Nexsa).

2.5 Surface modification and its characterization

Plasma electrolytic oxidation (PEO) coatings were deposited on the TN-T sample using a direct current (DC) power source in an aqueous electrolyte. During the PEO process, the TN-T sample acted as the anode, while the stainless-steel electrolyte container served as the cathode. The process parameter used for the coating is mentioned in Table 2.2.

Table 2.2. Process parameters and electrolyte utilized for the development of PEO coating on the SLM-fabricated TN-T sample.

| Sample designation | Electrolyte | Current density (mA.cm^{-2}) | Duty cycle (%) | Pulse frequency (Hz) | Time (s) |
|---------------------------|-----------------------------------|---|-----------------------|-----------------------------|-----------------|
| TN-T-S | Phosphate-silicate | | | | |
| TN-T-H | Phosphate-silicate-hydroxyapatite | 200 | 90 | 1000 | 360 |

Two distinct electrolyte formulations were used to produce coatings with different chemical functionalities: phosphate-silicate (PS) and phosphate-silicate-hydroxyapatite (PSHA). The PS electrolyte consisted of an equimolar (50:50) combination of sodium metasilicate and trisodium orthophosphate, with a total

concentration of 5 g dissolved in 1 L of distilled water. For the PSHA system, 5 g of hydroxyapatite (HAp) powder was introduced into the PS electrolyte and uniformly dispersed in 1 L of distilled water. The HAp nanoparticles were synthesized using a microwave-assisted route, yielding particles with a width of ~15-20 nm and a length of ~60-80 nm. To enhance electrolyte stability and achieve uniform nanoparticle dispersion, 10 mL of triethanolamine and 5 mL of ethylene glycol were introduced as dispersing additives. The electrolyte was magnetically stirred until a stable and homogeneous suspension was achieved before PEO processing.

The wettability of the PEO-coated samples was evaluated through static contact angle measurements using a Kyowa interface science goniometer (Japan). The contact angle formed between 3 μ l of deionized water droplet and the sample surface was recorded, and the corresponding surface energy was calculated using the following relation (Nisar et al., 2024),

$$E_S = E_{vl} \cos\theta \quad (4)$$

where θ is the contact angle, and E_{vl} is the surface energy of deionized water (72.8 mJ \cdot m⁻²). For each sample, five measurements were taken at different surface locations to account for surface heterogeneity, and the average contact angle value was reported.

2.6 *In-vitro* cell viability studies

MC3T3 pre-osteoblast cells were used to assess *in-vitro* biocompatibility of SLM-fabricated TN-T and PEO-coated TN-T-S and TN-T-H samples. Cells were cultured in α -minimum essential medium (α -MEM) supplemented with 10% fetal bovine serum (FBS) and 1% penicillin-streptomycin and maintained at 37 °C in a humidified atmosphere containing 5% CO₂. Upon reaching ~85% confluence, cells were detached using 0.25% trypsin-EDTA and subcultured for subsequent experiments. To ensure consistency and retention of osteogenic activity, only cells between passages 2 and 6 were utilized. Metallic disc samples with dimensions of 15 mm in diameter and 2 mm in thickness, in both uncoated and coated conditions, were used as substrates for *in-vitro* cytocompatibility assessment. MC3T3 pre-osteoblast cells were directly seeded onto the sample surfaces and cultured for 24 h and 72 h. All tests were conducted in triplicate to ensure statistical reliability. Before cell seeding, the samples were sequentially cleaned with acetone and ethanol and subsequently sterilized by autoclaving. Cellular responses on the coated specimens were systematically evaluated relative to the uncoated controls. Cell viability was assessed using the Alamar Blue assay (Invitrogen, DAL1025), which relies on the metabolic reduction of resazurin to fluorescent resorufin by living cells. Experiments were performed in 24-well plates with a seeding density of 10,000 cells per well. Following incubation for 24 h and 72 h, Alamar Blue reagent (10% v.v⁻¹) was added and incubated for 4 h at 37 °C. 150 μ l of supernatant from each well was collected, and absorbance was measured at 570 nm and 600 nm to evaluate relative cell viability.

Fluorescence staining was performed on day 3 (72 h) to assess cell morphology and cytoskeletal arrangement. Following removal of the culture medium, samples were rinsed three times with phosphate-buffered saline and fixed with 3.7% formaldehyde (Sigma-Aldrich) for 15 min. Cell membranes were permeabilized

using 1% Triton X-100 for 3 min. The actin filaments were stained with Rhodamine Phalloidin (1:200 in PBS; Cytoskeleton, PHDR1), while nuclei were counterstained with DAPI (Life Technologies) during the final 5 min. After thorough PBS washing, samples were imaged at 10× magnification using a laser scanning confocal microscope (Olympus FLUOVIEW FV3000, Japan), following the manufacturer's staining protocols.

3 Results and discussion

3.1 Powder characterization

Figure 3.1 depicts the morphology, chemical composition, and XRD patterns of the mixed TN and TNF powders. XRD analysis of the mixed powder displays diffraction peaks corresponding to the hexagonal close-packed (hcp) crystal structure of Ti and body-centred cubic (bcc) crystal structure of Nb and Fe, indicating the coexistence of the constituent elemental phases before SLM. The EDS analysis confirms compositional homogeneity, yielding average compositions of 58.5 ± 0.3 wt.% Ti and 41.5 ± 0.2 wt.% Nb for TN and 59.7 ± 0.3 wt.% Ti, 36.7 ± 0.2 wt.% Nb, and 4.5 ± 0.1 wt.% Fe for TNF.

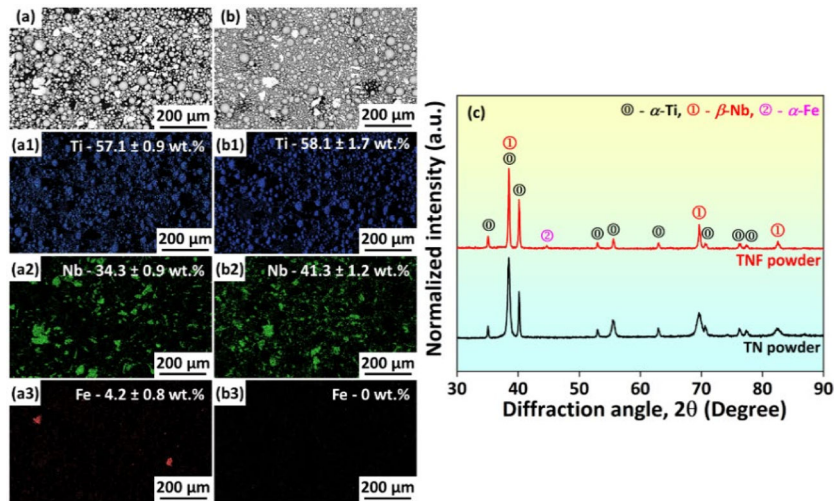


Figure 3.1. (a) SEM images and corresponding EDS area mapping of mixed (a-a3) TNF and (b-b3) TN powders, showing the powder morphology and elemental composition. (c) XRD patterns of TN and TNF powders.

3.2 Effect of remelting on SLM-fabricated Ti-Nb alloy

3.2.1 Phase analysis

Figure 3.2 presents the XRD patterns of the SLM-fabricated TN-S and TN-T samples in comparison with the TN elemental powder. Both TN-S and TN-T samples exhibit the presence of a dominant β -phase with a bcc crystal structure (Im-3m) in concordance with existing literature (Qiu, et al., 2022; Pilz et al., 2022). The β -phase in the TN-S is attributed to a combination of the β -TiNb and residual unmelted Nb particles. In contrast, the β -phase in TN-T corresponds to the β -TiNb, as remelting favored the complete melting of Nb. Although diffraction peaks associated with the α' -phase (P6₃/mmc) were not detectable in the TN-S within the detectable limits of XRD, the TN-T exhibited a noticeable increase in the intensity of peaks corresponding to the (002), (101), (110), and (112) planes. This implies enhanced α' -martensite formation in TN-T.

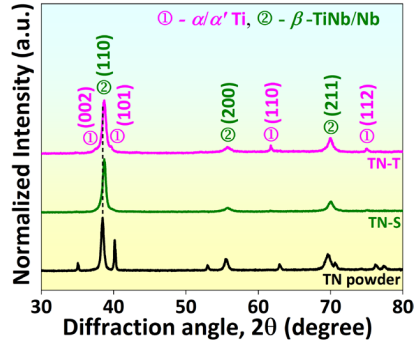


Figure 3.2. XRD patterns of TN powder compared with SLM-fabricated TN-S and TN-T samples, adapted from paper II.

During cooling from above the β -transus temperature (~ 882 °C), Ti-Nb alloys transform into stable (α , β) or metastable (α' , α'' , ω , β) phases depending on the cooling rate. The rapid solidification inherent to the SLM process promotes non-equilibrium phase transformations (Zhao et al., 2020). This results in the formation of metastable α' martensite along with retained β -phase in both TN-S and TN-T samples. The lattice parameters obtained from Rietveld refinement (Table 3.1) are consistent with reported values of Ti alloys exhibiting β and $\alpha'+\beta$ phase (Liu et al., 2019; Thoenmes et al., 2021).

Table 3.1. The table provides the Rietveld-refined lattice parameter values of the $\alpha'+\beta$ phase in TN powder, and SLM fabricated TN-S and TN-T samples, adapted from paper II.

| Sample | a_{β} (nm) | $a_{\alpha'}$ (nm) | $c_{\alpha'}$ (nm) |
|-----------|--------------------|--------------------|--------------------|
| TN powder | 0.3309 ± 0.002 | 0.2951 ± 0.003 | 0.4681 ± 0.002 |
| TN-S | 0.3294 ± 0.003 | 0.2999 ± 0.002 | 0.4761 ± 0.003 |
| TN-T | 0.3292 ± 0.002 | 0.2976 ± 0.001 | 0.4775 ± 0.002 |

In addition, the TN-S and TN-T samples show broadening and shift of the $\beta(110)$ diffraction peak toward higher 2θ angles, as compared to the mixed elemental powder. The peak shift corresponds to a reduction in the β -phase lattice parameter (a_{β} (nm)), indicating lattice contraction induced by substitutional Nb incorporation into the Ti matrix. Despite the nearly identical atomic radii of Ti (0.147 nm) and Nb (0.146 nm), substitutional incorporation of Nb into the Ti lattice induces lattice contraction, leading to localized straining of the unit cell (Borgman et al., 2021). The associated peak broadening indicates increased microstrain, quantified using the Williamson-Hall method. The microstrain increased from 0.3×10^{-3} in the TN powder to 4.2×10^{-3} for TN-S and 3.6×10^{-3} for TN-T samples, demonstrating the strong influence of SLM thermal cycling on strain accumulation and metastable phase stabilization.

3.2.2 Relative density analysis

OM images of the unetched TN-S and TN-T samples in Figure 3.3(a,b) reveal no distinct features apart from the presence of porosity. The TN-S sample exhibits pores in sizes ranging from 20 to 70 μm , with an average diameter of ~ 40 μm . In contrast,

no visible pores are observed in the TN-T sample within the resolution limits of OM, emphasizing a notable increase in densification due to remelting. Consistent with the OM observations, μ -CT analysis shown in Figure 3.3(c,d) confirms the reduction in porosity with remelting. The volume fraction of porosity decreases from 1.33% in the TN-S to 0.77% in the TN-T sample. The enhanced thermal input during remelting promotes melt pool reflow and improved interlayer bonding, leading to reduced porosity (S. Huang et al., 2021). Consequently, the relative density increases from \sim 96% for the TN-S sample to \sim 99.5% for the TN-T sample. These results are consistent with earlier studies (Lv et al., 2021), where remelting improved densification and reduced porosity in the SLM-fabricated alloys.

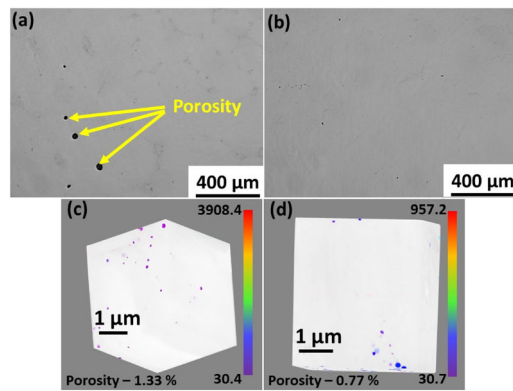


Figure 3.3. OM and μ -CT images of the SLM-fabricated (a&c) TN-S and (b&d) TN-T samples, respectively. The yellow arrow in the image indicates the presence of porosity, adapted from paper II.

3.2.3 Microstructural analysis

The SEM images in Back Scattered Electron (BSE) mode and EDS analysis of the SLM-fabricated TN-S and TN-T samples are shown in Figure 3.4. The TN-S sample exhibits a non-uniform microstructure with porosity, partially melted Nb particles, and areas rich and deficient in Nb. Grey regions correspond to the β -phase matrix, black regions correspond to α' -martensite, and bright regions indicate unmelted Nb particles. The presence of Nb-rich and Nb-depleted zones in the TN-S indicates incomplete melting and alloying of Nb under a single melting condition. The α' -martensite in TN-S is randomly distributed within the β matrix and exhibits a dot-like morphology characteristic of the high cooling rates associated with single-melting. In contrast, the TN-T sample exhibits a homogeneous microstructure, with complete melting and alloying Nb particles. The α' -martensite is uniformly distributed within the β matrix. It indicates that the remelting strategy effectively promotes Nb dissolution and alloying, resulting in improved homogeneity. In addition, the α' -martensite shows plate-like morphology, indicating a reduced cooling rate that facilitates martensite growth and grain coarsening. The microstructural evolution observed is associated with the thermal history and heat input during SLM processing (Subramanian et al., 2026). Work by (Song et al., 2022) reported that remelting with heat input (P/v) above $0.6 \text{ J}\cdot\text{mm}^{-1}$ will result in decreased cooling rate. Similarly, remelting with a heat input of $1 \text{ J}\cdot\text{mm}^{-1}$ in the TN-T sample resulted in a reduced cooling rate that increased thermal accumulation and melt pool lifetime, enabling complete Nb melting (Karimi

et al., 2022). ImageJ analysis of lower-magnification SEM images (Figure 3.4(a,d)) shows that the average grain size increased from $19 \pm 6 \mu\text{m}$ in TN-S to $26 \pm 7 \mu\text{m}$ in TN-T. A concurrent increase in α' martensite dimensions was observed, with the average length increasing from $0.4 \pm 0.1 \mu\text{m}$ to $3.0 \pm 0.6 \mu\text{m}$ and the width from $0.21 \pm 0.04 \mu\text{m}$ to $0.31 \pm 0.06 \mu\text{m}$.

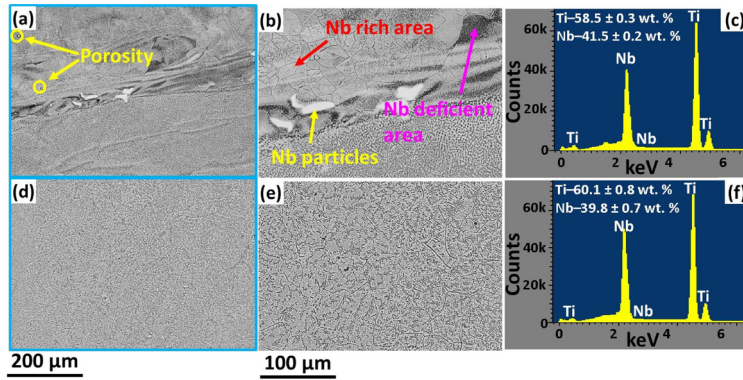


Figure 3.4. SEM images and corresponding EDS analysis of SLM-fabricated (a-c) TN-S and (d-e) TN-T samples. Porosity and unmelted Nb particles are indicated by yellow arrows, Nb-rich and Nb-deficient regions are indicated by red and pink arrows, respectively. Blue outlines highlight the area of elemental analysis, adapted from paper II.

3.2.4 Microhardness distribution

Figure 3.5 presents the variation in Vickers hardness of the SLM-fabricated TN-S and TN-T samples using hardness distribution maps.

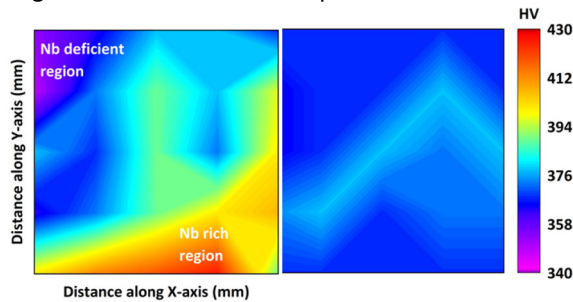


Figure 3.5. Plot presenting the variation in Vickers hardness of SLM-fabricated TN-S and TN-T samples as a function of remelting using hardness distribution maps, adapted from paper II.

The average hardness decreases from $384 \pm 13 \text{ HV}$ in the TN-S to $368 \pm 7 \text{ HV}$ in TN-T after remelting. This reduction is primarily attributed to grain coarsening induced by repeated thermal exposure during remelting. The TN-S sample exhibits pronounced variations in hardness across the transverse cross-section, reflecting microstructural and compositional heterogeneity. This behavior correlates with SEM observations of Nb-rich and Nb-deficient regions, where Nb-rich areas contribute to locally higher hardness due to the inherent higher hardness of Nb compared to Ti. In contrast, the TN-T sample shows a nearly uniform hardness distribution, indicating improved chemical homogeneity resulting from enhanced Nb melting and alloying during remelting. Despite the reduction in hardness upon remelting, both TN-S and

TN-T samples exhibit higher hardness than conventionally SLM-processed Ti-Nb alloys, due to the presence of α' -martensite (Afonso et al., 2007; Fikeni et al., 2021; Wang et al., 2017).

3.2.5 Influence of remelting

The SLM processing condition plays a crucial role in the cooling rate, melt pool characteristics, and solidification kinetics of the samples. The temperature distribution within the melt pool during laser scanning can be estimated using the Rosenthal moving heat source model, which describes the peak temperature at a distance r from the heat source as (Kou, 2002):

$$T_p = T_0 + \frac{Q}{2\pi kr} \exp\left(-\frac{vx}{2\alpha}\right) \quad (5)$$

where T_0 is the initial temperature (298 K), Q is the effective heat input from the laser, k is the thermal conductivity of the TN (powder - 6 W/m.K and bulk - 11.5 W/m.K) (Bychkov et al., 1981), v is the scan speed, and α is the thermal diffusivity. The thermal diffusivity is given by the following:

$$\alpha = \frac{k}{\rho C_p} \quad (6)$$

where ρ is the density of TN (5.570 g.m⁻³) and C_p is its heat capacity (525 J.kg⁻¹.K⁻¹).

The difference between TN-S and TN-T conditions lies in the dominant heat-transfer medium. During SM, heat is primarily conducted through the powder bed, which has a relatively low thermal conductivity (~6 W.m-1.K-1) due to inter-particle voids. In contrast, during TM, subsequent laser passes interact with a previously solidified layer, enabling heat conduction through bulk TN with a significantly higher thermal conductivity (~11.5 W.m-1.K-1). Consequently, the melt pool temperature and cooling rate differ substantially between the TN-S and TN-T samples. The cooling rate can be expressed as follows:

$$CR = 2\pi kv \frac{(T - T_0)}{Q} \quad (7)$$

where k is the thermal conductivity of the TN alloy in W.m⁻¹.K⁻¹, T is the melt pool temperature in K, T_0 is the initial temperature of the material in K (298 K), v is the scan speed in m.s⁻¹, and Q is heat transferred to the substrate from the laser source in W. Using the respective thermal conductivity values for powder (TN-S) and bulk (TN-T), the calculated peak melt pool temperature and cooling rate are ~5606 K and ~6.9 × 10⁵ K.s⁻¹ for TN-S, whereas TN-T shows a reduced peak temperature ~3067 K and a lower cooling rate ~3.2 × 10⁵ K.s⁻¹. According to Newton's law of cooling, the heat extraction rate is proportional to the temperature gradient. This explains the faster cooling experienced under the TN-S condition. The difference in cooling rate is further supported by thermal penetration depth, which represents the depth to which heat diffuses into the material and can be estimated by :

$$\delta_{th} = 2\sqrt{\alpha t} \quad (8)$$

where t is the laser exposure time. The calculated thermal penetration depth is approximately 32 μm for TN-S and 44 μm for TN-T. The increased penetration depth in TN-T indicates a deeper melt pool and enhanced heat accumulation, which

together reduce the thermal gradient across the solidified region. This reduction in temperature gradient slows down solidification and provides a longer time for atomic diffusion. In the *in-situ* alloyed TN fabricated from elemental powders, Nb diffusion is strongly affected by the large melting-temperature difference between Ti (1668 °C) and Nb (2468 °C). Under TN-S condition, the shallow melt pool, rapid cooling rate ($\sim 6.9 \times 10^5 \text{ K.s}^{-1}$), and limited melt pool lifetime restrict solute redistribution, resulting in incomplete Nb melting. In contrast, the TN-T condition significantly enhances Nb melting due to increased thermal penetration depth ($\sim 44 \text{ }\mu\text{m}$) and heat accumulation, which extends the melt pool lifetime. The deeper melt pool intensifies Marangoni convection, promoting repeated fluid circulation and effective transport of Nb throughout the molten region. The combined effects of enhanced Marangoni convection and reduced cooling rate ($\sim 3.2 \times 10^5 \text{ K.s}^{-1}$) enable complete Nb melting and alloying, yielding a homogeneous $\alpha'+\beta$ microstructure. The thermal history in the TN-T condition strongly influences microstructural evolution. Both TN-S and TN-T samples exhibit a dual-phase $\alpha'+\beta$ microstructure. However, the lower cooling rate in TN-T promotes grain growth and martensite coarsening. Quantitative analysis indicates an increase of $\sim 43\%$ in average grain size, accompanied by $\sim 13\%$ and $\sim 6\%$ increases in α' martensite length and width, respectively, compared to TN-S. Overall, remelting proved to be an effective strategy to reduce porosity and promote complete melting and alloying of Nb, resulting in enhanced microstructural homogeneity (Subramanian et al., 2025).

3.3 Effect of Fe addition on the SLM-fabricated Ti-Nb alloy

3.3.1 Phase analysis

Figure 3.6 presents the XRD patterns of the SLM-fabricated TN-T and TNF-T samples. The TN-T sample exhibits the presence of $\alpha'+\beta$ phase, consistent with previous work (Subramanian et al., 2025). This indicates incomplete β -phase stabilization, which resulted in martensitic transformation during solidification. In contrast, the TNF-T sample exhibits the presence of a single metastable β -phase, indicating suppression of the α' -martensitic phase due to Fe addition.

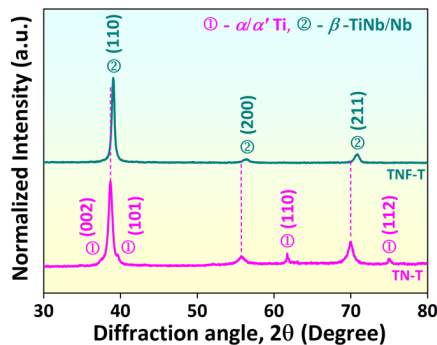


Figure 3.6. XRD patterns of SLM-fabricated TN-T and TNF-T samples, adapted from paper IV.

Quantitative Rietveld refinement confirms that Fe addition increases the β -phase fraction from $\sim 85.4\%$ in TN-T to $\sim 99.7\%$ in TNF-T sample. The stabilization of the β -phase in the TNF-T alloy upon Fe addition can be explained using the Mo_{eq} and the

(e/a) ratio. A Mo_{eq} value of above 10 wt.% and (e/a) ratio > 4.2 , results in the retention of metastable β -phase at room temperature (Alberta et al., 2023). Based on the calculation using equation (1) and (e/a) ratio, the TNF-T exhibits a higher Mo_{eq} (11.8) and e/a (4.43) values than the TN-T ($Mo_{eq} = 11.2$ and e/a = 4.26). This increase in both parameters with Fe addition promoted the β -phase stability at room temperature by inhibiting the $\beta \rightarrow \alpha'$ martensitic transformation.

3.3.2 Microstructural analysis

The microstructural analysis was carried out using EBSD to assess the grain morphology and crystallographic orientation. The inverse pole figure (IPF) maps, grayscale image quality (IQ) maps, and grain size distribution histograms for the TN-T and TNF-T samples are presented in Figure 3.7. The IPF maps indicate random grain orientation in both samples, confirming the absence of strong texture. It also suggests uniform solidification under rapid cooling conditions typical of an SLM-fabricated sample (Subramanian et al., 2026). The IQ maps reveal well-defined β grains and boundaries where TNF-T exhibits refined grains compared to the TN-T sample. The grain size as measured by the EBSD area fraction method shows that TN-T shows a broader distribution ($\sim 1 - 100 \mu\text{m}$) with an average grain size of $48 \pm 29 \mu\text{m}$. The higher standard deviation in TN-T indicates the coexistence of $\alpha' + \beta$ phase, leading to a bimodal grain distribution with fine and coarse grains. In contrast, the TNF-T shows a narrow distribution ($\sim 1 - 50 \mu\text{m}$) with an average grain size of $11 \pm 8 \mu\text{m}$.

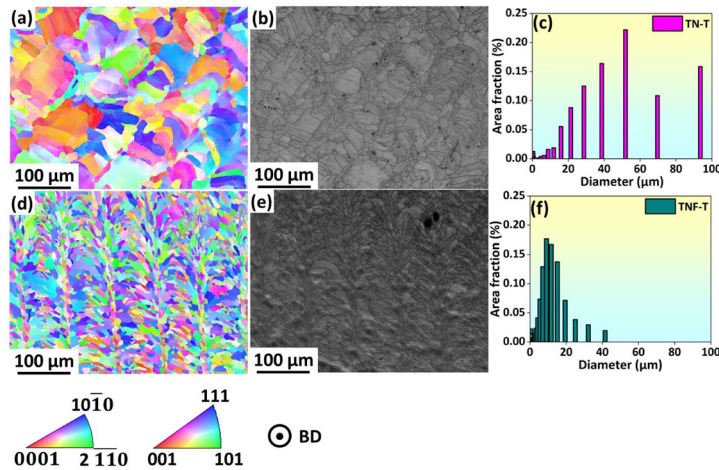


Figure 3.7. EBSD results showing the inverse pole figure maps, image quality maps, and the grain size distribution plots of the SLM-fabricated (a-c) TN-T, and (d-f) TNF-T samples. BD represents the build direction, adapted from paper IV.

The grain refinement in TNF-T is attributed to the combined effects of nucleation and restricted grain growth during solidification. The high diffusive β -stabilizing effect of Fe enhances heterogeneous nucleation and restricts grain growth by the grain boundary pinning effect (Huang et al., 2025). Parallely, Fe increases constitutional undercooling, which accelerates nucleation during rapid solidification. The effect of solute elements on growth restriction is quantified using the growth restriction factor (Q_f), defined as: (Fetzer et al., 2011)

$$Q_f = m_1 C_0 (k - 1) \quad (9)$$

where m_1 is the slope of the liquidus line, C_0 is the solute concentration, and k is the equilibrium partition coefficient. Higher Q_f values indicate stronger growth restriction and increased nucleation density. The m_1 values of the Nb and Fe are 10 and -18, respectively, while the k values of the Nb and Fe are 1.25 and 0.38, respectively (Birmingham et al., 2008). Using these parameters, the calculated Q_f is found to be lower for TN-T (100) than for TNF-T (143.3). This confirms that Fe addition effectively enhances growth restriction, suppresses grain coarsening, resulting in significantly refined β grains.

3.3.3 Mechanical properties

The effect of Fe addition on the mechanical behavior of SLM-fabricated samples was evaluated using Vickers microhardness and compression testing. The Vickers hardness plot shown in Figure 3.8(a) emphasizes that TN-T exhibits an average hardness of 374 ± 12 HV₁, whereas the TNF-T shows a higher average hardness of 494 ± 11 HV₁. This increase in hardness with the addition of Fe is attributed to grain refinement that reduces the dislocation mean free path and increases resistance to dislocation motion (Issariyapat et al., 2025). The compressive stress-strain curves shown in Figure 3.8(b) further highlight the effect of Fe addition on the mechanical properties. Table 3.2 provides the mechanical properties of SLM-fabricated TN-T and TNF-T samples.

Table 3.2. Vickers hardness and compressive strength values of the SLM-fabricated TN-T and TNF-T samples.

| Sample | Hardness (HV) | YS (MPa) | UCS (MPa) | E (GPa) | Strain (%) |
|--------|---------------|--------------|---------------|--------------|----------------|
| TN-T | 374 ± 12 | 845 ± 24 | 1490 ± 20 | 34 ± 0.3 | 33.4 ± 4.0 |
| TNF-T | 494 ± 11 | 908 ± 33 | 1945 ± 17 | 30 ± 0.7 | 47.1 ± 3.5 |

The TN-T exhibits a yield strength of 845 ± 24 MPa and an ultimate compressive strength of 1490 ± 20 MPa, with a plastic strain of ~33%. In comparison, TNF-T shows higher values, with a yield strength of 908 ± 33 MPa, an ultimate compressive strength of 1945 ± 17 MPa, and a plastic strain of ~48%. In addition, the elastic modulus decreased from 34 GPa in TN-T to 30 GPa in TNF-T owing to suppression of the α' -martensite and stabilization of the β -phase (Li et al., 2022). The strain hardening behavior displayed in Figure 3.8(c) exhibits three distinct regions for both samples. Region I exhibits a rapid decrease in hardening rate after yielding. Region II shows a relatively stable response, while region III shows a further decrease. Although both alloys show similar trends in Region I, TNF-T maintains a higher strain hardening behavior in Region II, indicating enhanced work hardening and improved compressive deformability. This difference in mechanical behavior is closely related to the phase constitution of the samples. TN-T consists of a bimodal $\alpha'+\beta$ phase structure. The hcp crystal structure of the α' phase provides limited slip systems for plastic deformation. In contrast, β -phase structure with a bcc crystal structure exhibited by the TNF-T offers multiple slip systems enabling more uniform plastic deformation (Kent et al., 2013). In particular, the strengthening mechanism involved in both samples is governed by solid solution and grain boundary effects. Solid

solution strengthening ($\Delta\sigma_{ss}$) results from the substitution of Nb and Fe atoms into the β -Ti lattice, generating lattice distortion and resistance to dislocation motion. Using the following equation, the contribution of solid solution strengthening can be calculated (Jawed et al., 2020).

$$\Delta\sigma_{ss} = (\sum_i B_i^{3/2} X_i)^{2/3} \quad (10)$$

where B_i is the strengthening coefficient (71 MPa.at.^{-2/3} for Nb and 1715 MPa.at.^{-2/3} for Fe) (Zhao et al., 2019) and X_i is the atomic fraction of the solute element. The calculated higher value of ~50 MPa for TNF-T than the ~36.7 MPa for TN-T indicates that Fe addition significantly enhanced properties through the solid solution strengthening. The contribution of grain boundary strengthening can be calculated using the Hall-Petch relation, (Guo et al., 2025)

$$\Delta\sigma_{ss} = (\sum_i B_i^{3/2} X_i)^{2/3} \quad (11)$$

Based on the calculated values, the contribution is ~65 MPa for TN-T and ~135 MPa for TNF-T. The finer grain structure in TNF-T increases grain boundary density, which effectively impedes dislocation motion. The overall β -phase stability, improvement in strength, ductility, and reduced elastic modulus are attributed to the solid solution strengthening and grain boundary strengthening caused by Fe addition (Subramanian et al., 2026).

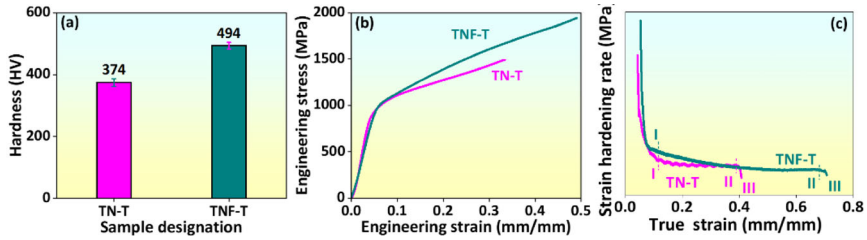


Figure 3.8. (a) Vickers hardness plot, (b) compressive stress-strain curve, and (c) strain hardening behavior plot of the SLM-fabricated TN-T and TNF-T samples, adapted from paper IV.

3.3.4 Passivation behavior

The passivation behavior of SLM-fabricated TN-T and TNF-T samples was investigated using PDP, EIS, and M-S analysis in PBS at 37 °C (simulated physiological condition). The Tafel plot displayed in Figure 3.9(a) shows an active-passive transition for both TN-T and TNF-T samples. The corrosion potential (E_{corr}), corrosion current density (I_{corr}), polarization potential (E_{pp}), and the passivation current density (I_p) obtained from the Tafel plot of both samples are summarized in Table 3.3.

Table 3.3. The table provides the PDP values of SLM-fabricated TN-S and TN-T samples obtained from the Tafel plot, adapted from paper IV.

| Sample | E_{corr} (V _{Ag/AgCl}) | I_{corr} (μ A.cm ⁻²) | E_{pp} (V _{Ag/AgCl}) | I_p (μ A.cm ⁻²) |
|--------|------------------------------------|---|----------------------------------|------------------------------------|
| TN-T | -0.29 ± 0.03 | 1.57 ± 0.03 | 0.13 ± 0.01 | 73.02 ± 0.02 |
| TNF-T | -0.24 ± 0.04 | 1.06 ± 0.09 | 0.25 ± 0.02 | 73.01 ± 0.01 |

The current density of both samples increases from E_{corr} to E_{pp} due to active dissolution, followed by a stable passive region up to 1.5 V_{Ag/AgCl}. The TNF-T exhibits a shift in E_{corr} towards a more noble value and a reduction in i_{corr} as compared to TN-T, indicating improved corrosion resistance. The passive current density remains similar for both samples, suggesting similar passive film stability.

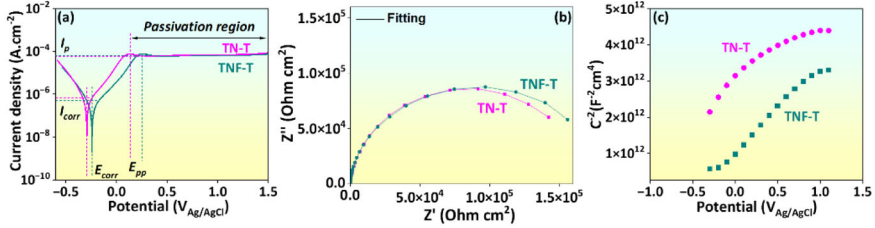


Figure 3.9. (a) Tafel plot, (b) Nyquist plot, and (c) M-S plot of the SLM-fabricated TN-T and TNF-T samples evaluated in PBS at 37 °C, adapted from paper IV.

To evaluate the passive film characteristics, EIS measurements were performed at OCP after 0.5 h immersion. The Nyquist plots shown in Figure 3.9(b) for both TN-T and TNF-T samples show a single incomplete semicircle arc, indicating a one dominant time constant associated with passive film behavior. The impedance spectra were fitted using a modified Randles circuit [$R_s(QR_p)$], to obtain the electrolyte resistance (R_s), polarization resistance (R_p), and constant phase element (Q) values. The circuit elements enclosed in parentheses are connected in parallel, whereas those within square brackets are connected in series. The fitted values shown in Table 3.4 show good agreement with experimental data ($\chi^2 \sim 10^{-3}$). For both TN-T and TNF-T samples, the constant phase exponent n value is ~ 0.95 . It indicates near-ideal capacitive behavior, suggesting the formation of a uniform passive layer. The R_s value is similar for both samples, indicating similar solution resistance. The slightly higher R_p value of TNF-T than that of TN-T indicates increased resistance and improved protection of the passive film (Bagoury et al., 2019). From the obtained fitting values, the capacitance of the passive film can be calculated using the following Brug's equation (Brug et al., 1984)

$$C = [Q(R_s^{-1} + R_p^{-1})^{n-1}]^{1/n} \quad (12)$$

where, R_s is the solution resistance, R_p is the polarization resistance, Q is a proportionality constant with units of $\Omega^{-1}.s^n$, n is the exponent of Q (constant phase element) with values ranging from -1 to 1 (-1 represents inductance, 0 represents resistance, and 1 represents capacitance). By incorporating the C value in the following equation, the thickness of the passive film can be estimated (Jayaraj et al., 2012).

$$C = \frac{\epsilon \epsilon_0 A}{d} \quad (13)$$

where ϵ_0 is the vacuum permittivity (8.854×10^{-14} F.cm⁻¹), d is the passive film thickness, and ϵ is the dielectric constant of the passive film. The dielectric constants of TiO₂, Nb₂O₅, and Fe₂O₃ are 80, 28, and 26, respectively (Lunt et al., 2013; Nanda et al., 2020). The passive films formed on TN-T and TNF-T are expected to consist of mixed oxides of Ti, Nb, and Fe. The dielectric constant data for mixed oxides in the Ti-

Nb-Fe system are not available in the literature. As the passive film composition in both samples is predominantly Ti-Nb-based oxides, an effective ϵ value of 51 was adopted based on reported literature on the TN alloy (Çaha et al., 2023b). Accordingly, the passive film thickness was estimated using this effective dielectric constant and is provided in Table 3.4. A slight increase in R_p of TN-T is accompanied by a slight decrease in C value. This reduction in C corresponds to a modest increase in passive film thickness, from 1.59 nm to 1.68 nm.

Table 3.4. The table summarizing the EIS data, along with capacitance and passive film thickness values of SLM-fabricated TN-S and TN-T samples, adapted from paper IV. S represents sample, and T represents immersion time.

| S | T (h) | R_s ($\Omega.cm^2$) | Y_o ($\mu\Omega^{-1}.s^n.cm^{-2}$) | n (no unit) | R_p ($M\Omega.cm^2$) | C ($\mu F.cm^{-2}$) | d (nm) |
|-------|----------|----------------------------|---|--------------------|-----------------------------|--------------------------|--------------------|
| TN-T | 0.5 | 14.47 ± 0.94 | 41.32 ± 0.76 | 0.95 ± 0.01 | 0.15 ± 0.19 | 28.11 ± 0.60 | 1.59 ± 0.01 |
| TNF-T | 0.5 | 14.52 ± 0.71 | 40.66 ± 0.56 | 0.95 ± 0.01 | 0.17 ± 0.24 | 27.79 ± 0.50 | 1.68 ± 0.02 |

To evaluate the semiconducting behavior of the passive film developed, M-S analysis was carried out in PBS at 37 °C (Figure 3.9(c)). The $1.C^{-2}$ vs potential plot of TN-T and TNF-T exhibits a linear region with a positive slope in the range of -1.1 to $0.3 V_{Ag/AgCl}$, and -0.2 to $0.8 V_{Ag/AgCl}$, respectively, confirming n-type semiconducting behavior. This indicates that oxygen vacancies and metal interstitials act as dominant donor defects governing charge transport through the passive film. The donor density (N_D) in the developed passive film can be calculated using the following equation (Jayaraj et al., 2012).

$$C^{-2} = \frac{2}{\epsilon\epsilon_0 e N_D} \left(E - E_{fb} - \frac{kT}{e} \right) \quad (14)$$

where ϵ is the dielectric constant of the passive film, and ϵ_0 is the dielectric constant of vacuum, e is the electronic charge, and E_{fb} is the flat band potential, obtained from the M-S plot as $-0.26 V_{Ag/AgCl}$ for TN-T and $-1.05 V_{Ag/AgCl}$ for TNF-T. The calculated N_D is higher for the TN-T ($4.7 \times 10^{21} cm^{-3}$) sample as compared to the TNF-T ($3.1 \times 10^{21} cm^{-3}$). This decrease in N_D with Fe addition correlates with the higher R_p obtained from EIS, confirming the formation of a more resistive and protective passive film in the TNF-T sample. The observed differences in N_D and semiconducting behavior can be explained using the point defect model (PDM). The growth of passive film on the sample is governed by the generation of oxygen vacancies at the film/sample interface that are consumed by the oxygen ion from the electrolyte/film interface. In TN-T, the formation of oxygen vacancies and cation defects increases electronic conductivity, leading to higher N_D values and comparatively lower film resistance. Although Nb^{5+} incorporation modifies the passive film structure, it does not effectively suppress defect formation. In contrast, the addition of Fe significantly alters the defect chemistry in TNF-T. Fe oxidizes to Fe^{3+} and substitutes for Ti^{4+} sites. This substitution promotes charge compensation by interacting with oxygen vacancies, thereby reducing donor defect concentration. As a result, the passive film becomes denser and more stable, with lower N_D . The combined effect of Nb^{5+}

strengthening the passive film and Fe³⁺ reducing defect density leads to a compact and protective passive film. This is evident from the lower N_D, higher R_p, and improved corrosion resistance observed for the TNF-T sample.

The surface chemistry of the passive films was analyzed using XPS for both TN-T and TNF-T samples. The high-resolution XPS spectra of Ti 2p, Nb 3d, and Fe 2p for both TN-T and TNF-T samples are presented in Figure 3.10. The passive film of both TN-T and TNF-T display the presence of the Ti 2p spectrum with Ti 2p_{3/2} (~459 eV) and Ti 2p_{1/2} (~465 eV) peaks, corresponding to TiO₂ and Nb 3d spectrum with Nb 3d_{5/2} (~207 eV) and Nb 3d_{3/2} (~210 eV) peaks corresponding to Nb₂O₅. An additional Fe 2p spectrum with Fe 2p (~710 eV) corresponding to Fe₂O₃ is evident in the TNF-T sample, confirming the presence of Fe in the passive film. No metallic Ti (~454.6 eV), Nb (~202 eV), or Fe (~706 eV) peaks are observed on the surface region of the passive film, indicating a fully oxidized surface. The passive film on TN-T is mainly composed of TiO₂ and Nb₂O₅, whereas the TNF-T passive film consists of TiO₂, Nb₂O₅, and Fe₂O₃ (Subramanian, Manivasagam, et al., 2026).

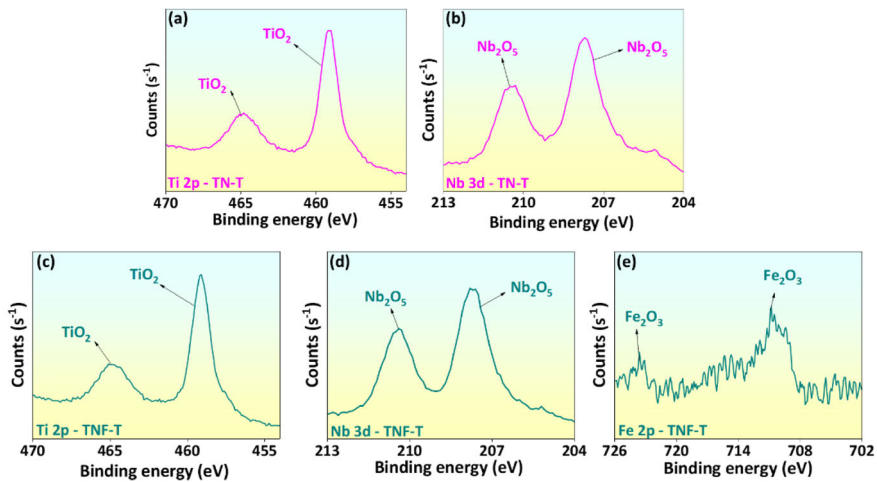


Figure 3.10. High-resolution XPS spectra of SLM-fabricated (a-b) TN-T, and (c-e) TNF-T samples showing the passive film chemistry on the surface after 72 h of immersion in PBS at 37 °C, adapted from paper IV.

3.4 Effect of surface modification on SLM-fabricated Ti-Nb alloy

3.4.1 Phase analysis of PEO coatings

The XRD pattern (Figure 3.11) of the PEO-coated TN-T-S and TN-T-H samples shows the presence of TiO₂ (anatase and rutile) and Nb₂O₅ oxide phases. The uncoated TN-T sample used as a reference shows the presence of a dual α'+β phase. The crystallization of anatase and rutile within the oxide coating is attributed to localized plasma discharges generated during PEO. Regardless of the addition of HAP in the TN-T-H sample, no distinct HAP peaks are detected, indicating its fraction is below the detection limit of XRD (Ferraz et al., 2017; Wu et al., 2023). The comparative phase analysis of the coated samples reveals a higher fraction of rutile in TN-T-H than in TN-T-S. During the initiation of TiO₂ oxide formation, the anatase phase forms first due to its lower surface free energy, as compared to other

polymorphs of TiO₂. However, metastable anatase transforms to the stable rutile phase between 400 °C and 1200 °C. The elevated discharge energy and higher processing voltage associated with the TN-T-H enhance the anatase-to-rutile transformation, resulting in a higher fraction of the rutile phase (Friedemann et al., 2017; Hanaor et al., 2011).

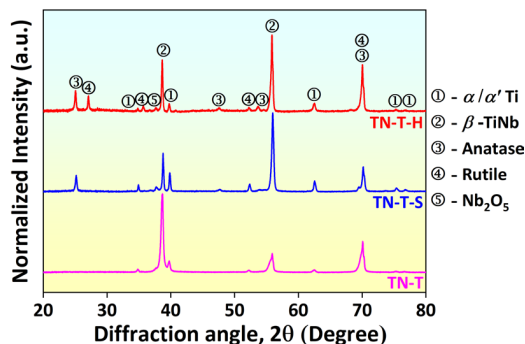


Figure 3.11. XRD patterns of the SLM-fabricated TN-T and PEO-coated TN-T-S and TN-T-H samples, adapted from paper III.

3.4.2 Surface morphology of PEO coatings

The SEM images showing the surface morphology of the coated TN-T-S and TN-T-H samples are presented in Figure 3.12. The TN-T-S coating in Figure 3.12(a) exhibits a uniform distribution of irregularly shaped micro- and nanopores. In contrast, the TN-T-H in Figure 3.12(d) exhibits uniformly distributed circular and elliptical pores with smoother pore edges resembling volcanic-like features. The incorporation of HAP nanoparticles into the electrolyte altered the discharge behavior by reducing electrolyte conductivity, thereby modifying pore geometry and distribution. During the PEO process, intense plasma discharges generate localized high temperatures, leading to melting and oxidation of the substrate. The ejection of molten oxides and gas evolution through discharge channels results in the formation of a porous oxide structure (Valizade et al., 2024). The pore morphology of the coating is governed by discharge behavior and applied voltage. Higher voltage increases molten oxide formation, which partially fills discharge pores and reduces overall porosity (Arun et al., 2023). Accordingly, the quantitative image analysis by ImageJ software shows that the TN-T-H with high process voltage exhibited lower porosity ($16 \pm 4 \%$) with an average pore size of $2.32 \pm 0.9 \mu\text{m}$, as compared to the TN-T-S ($26 \pm 3 \%$) with an average pore size of $3.04 \pm 1.4 \mu\text{m}$. The incorporation of HAp nanoparticles significantly increased the pore filling and smooth oxide formation, that lead to the formation of interconnected pores, reducing overall porosity.

The elemental distribution mapping of the TN-T-S and TN-T-H samples is presented in Figure 3.12(c&f). Both coatings contain Ti, Nb, O, P, and Si, indicating incorporation of substrate and electrolyte species. The TN-T-H coating additionally consists of Ca, confirming the successful incorporation of calcium- and phosphate-containing species from the HAP-enriched electrolyte. The higher oxygen and phosphate intensities observed in TN-T-H correlate with increased discharge energy and oxide growth rate under elevated voltage conditions.

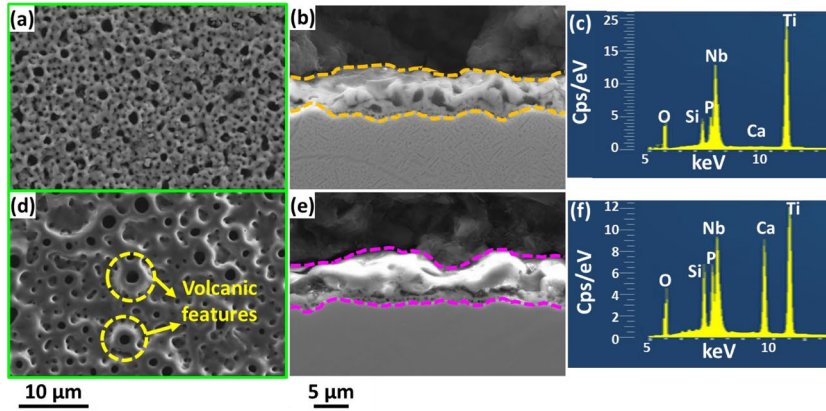


Figure 3.12. SEM images displaying the surface morphology, coating thickness, and elemental mapping of the PEO-coated (a-c) TN-T-S and (d-f) TN-T-H samples, adapted from paper III.

Figure 3.10(b&e) shows the SEM images of the cross-sectional morphology of the TN-T-S and TN-T-H coatings. Both coatings exhibit a dual-layer structure consisting of a dense inner barrier layer and a porous outer layer. The coating thickness measured using ImageJ indicated an increase from $6.9 \pm 1 \mu\text{m}$ for TN-T-S to $8.0 \pm 1.5 \mu\text{m}$ for TN-T-H. The relationship between coating thickness (t) and applied voltage is described by the following equation (Wu et al., 2010):

$$t = A \exp k(V_p - V_b) \quad (15)$$

where V_p is the processing voltage, V_b is the breakdown voltage, and A , k are material- and electrolyte-dependent constants. The relation shows that the coating thickness is directly proportional to the processing and breakdown voltage. In accordance with the relation, the TN-T-H coating with a higher voltage condition exhibited higher coating thickness. Additionally, the presence of HAp nanoparticles increases the electrolyte ionic concentration and dielectric breakdown frequency, which enhances discharge activity and oxide growth. The combined effect of higher voltage and nanoparticle-influenced discharge behavior results in a thicker coating with smaller and reduced porosity in TN-T-H compared to TN-T-S (Subramanian et al., 2026).

3.4.3 Surface wettability

Wettability reflects the surface characteristics of a material and is governed by the interaction between a liquid and a solid surface upon contact. It is commonly quantified by the contact angle formed at the liquid-solid interface and provides insight into the hydrophilic (contact angle $< 90^\circ$) or hydrophobic (contact angle $> 90^\circ$) nature of the surface (Kulkarni et al., 2015). Figure 3.13 shows the contact angle measurements for the TN-T, TN-T-S, and TN-T-H samples. All samples exhibit hydrophilic behavior, as indicated by contact angles below 90° (Figure 3.13). A progressive reduction in contact angle is observed from $70 \pm 1.9^\circ$ (TN-T) to $53 \pm 1^\circ$ (TN-T-S) and further to $39 \pm 1^\circ$ (TN-T-H), demonstrating a progressive enhancement in wettability following PEO treatment. In parallel, the calculated surface energy increases from $24.9 \pm 1.8 \text{ mJ.m}^{-2}$ for TN-T to $43.8 \pm 1.6 \text{ mJ.m}^{-2}$ for TN-T-S and $56.5 \pm 1.2 \text{ mJ.m}^{-2}$ for TN-T-H, respectively.

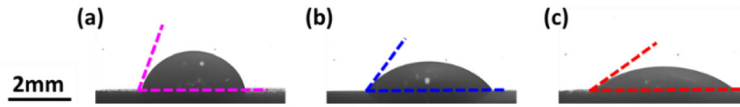


Figure 3.13. Contact angle measurement images of SLM-fabricated TN-T and PEO-coated TN-T-S and TN-T-H samples using deionized water, adapted from paper III.

Among the coated samples, TN-T-H exhibits the highest wettability, which arises from the combined effects of surface morphology and chemical composition. The incorporation of Ca^{2+} and PO_4^{3-} species alongside TiO_2 significantly enhances surface polarity and hydration capability, promoting water adsorption and spreading ability. This contribution of chemical composition and surface morphology accounts for the superior hydrophilic behavior observed for the TN-T-H sample (Fazel et al., 2019; Molaei et al., 2022).

3.4.4 Cell-viability evaluation

The biocompatibility of the TN-T, TN-T-S, and TN-T-H samples evaluated using the Alamar Blue assay after 24 h and 72 h of cell culture is shown in Figure 3.14. At the 24 h time point, both coated samples demonstrated a clear improvement in cell-viability compared to the uncoated TN-T. It indicates that surface modification significantly enhances early-stage cell attachment. This improvement can be attributed to the surface alterations introduced by PEO, including enhanced wettability and the formation of an oxide-based bioactive layer, all of which are known to positively influence cell-material interactions.

With prolonged incubation, TN-T-H consistently exhibited the highest level of cell proliferation among all samples. This enhanced biological response is closely linked to the combined effects of surface morphology and chemical composition. The porous morphology generated during PEO provides micro-scale features that support cell anchorage, while the presence of HAp within the coating introduces bioactive sites that favor cellular activity. In particular, the gradual release of Ca^{2+} and PO_4^{3-} ions from the HAp-containing surface contributes to improved cell proliferation and supports processes associated with bone tissue formation.

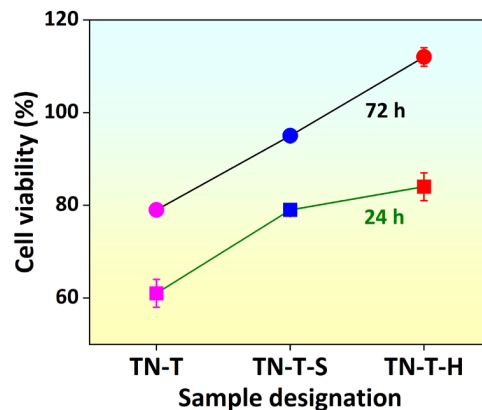


Figure 3.14. Plot shows the cell-viability assessment carried out on SLM-fabricated TN-T and PEO-coated TN-T-S and TN-T-H samples using the Alamar Blue assay at 24 h and 72 h time points, adapted from paper III.

Fluorescence microscopy images of MC3T3 pre-osteoblast cells cultured on the TN-T, TN-T-S, and TN-T-H (Figure 3.15) further corroborate the quantitative cell-viability results. Cells adhered and remained viable on all samples. In particular, the TN-T-H surface exhibited noticeably higher cell density and more extensive spreading. The well-developed cytoskeletal organization observed on TN-T-H suggests strong cell-surface interactions, facilitated by the porous architecture and chemically active coating. The presence of smooth pore edges and surface promotes filopodia extension, enabling efficient cell migration and intercellular connectivity (Subramanian et al., 2026).

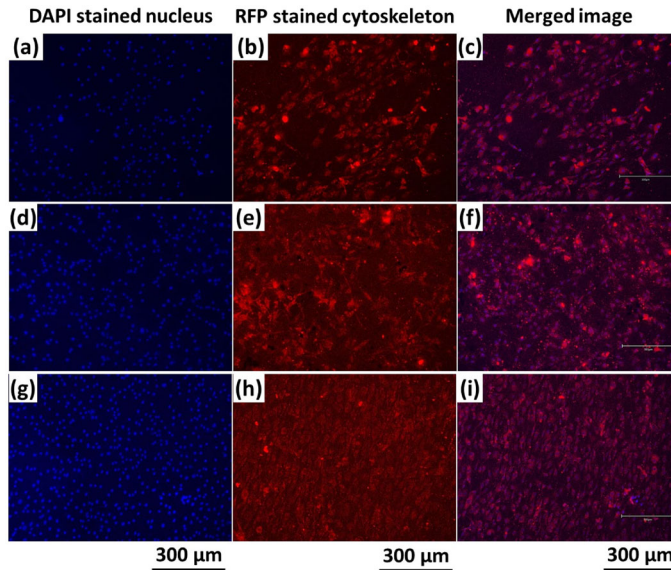


Figure 3.15. Fluorescence microscopy images of MC3T3 pre-osteoblast cells cultured on the (a-c) SLM-fabricated TN-T, and PEO-coated (d-f) TN-T-S, and (g-i) TN-T-H samples after a 72 h cell-viability study. The blue stains highlight the nucleus of the cell, while the red stains highlight the cytoskeleton of the cell, adapted from paper III.

Overall, the PEO process markedly enhances the surface functionality of SLM-fabricated TN alloy, leading to improved surface wettability and biological response. The HAp-enriched TN-T-H coating provides a dense oxide layer with enhanced wettability and Ca-P incorporation, which collectively promote superior cell attachment and proliferation. These findings demonstrate the potential of HAp-based PEO coatings for developing biofunctional surfaces tailored for orthopedic implant applications.

4 Conclusion

In this thesis, a systematic investigation has been conducted to address the research objectives associated with the *in-situ* alloying of Ti-Nb-based alloys by SLM using elemental powder for orthopedic applications.

1. The effect of remelting strategy, especially the triple melting conditions, confirmed that repeated laser exposure ensures complete melting and alloying of Nb in the Ti-40Nb and Ti-35Nb-5Fe alloys. SEM and XRD analysis confirm that the laser remelting approach is an effective method for microstructural homogenization.
2. The SLM-fabricated Ti-40Nb alloy exhibited $\alpha'+\beta$ microstructure. The addition of 5 wt.% Fe significantly improved β -phase stability upto 99.7% as confirmed by the XRD-Rietveld refinement method.
3. In comparison to the Ti-40Nb alloy, the Ti-35Nb-5Fe alloy exhibited improved properties such as high compressive strength, high ductility, and lower elastic modulus, which resulted from refined grain size and β -phase structure.
4. Electrochemical passivation studies in simulated physiological conditions revealed similar passivation behavior for both Ti-40Nb and Ti-35Nb-5Fe alloys. Mott-Schottky analysis confirmed an n-type semiconducting behavior of the passive film, with lower defect densities for the Ti-35Nb-5Fe alloy. XPS analysis confirmed that the passive film is composed of TiO_2 , Nb_2O_5 , and Fe_2O_3 oxides in Ti-35Nb-5Fe alloy.
5. Surface modification of SLM-fabricated Ti-40Nb using PEO produced a double oxide structure consisting of a dense inner barrier layer and a porous outer layer, predominantly of rutile phase. *In-vitro* cell study confirmed that HAp-containing PEO coatings significantly enhanced surface wettability and bioactivity. The presence of Ca-P species promoted cell adhesion and proliferation, indicating improved osteogenic potential.

Overall, this study establishes a process-microstructure-property relationship in the *in-situ* alloyed Ti-Nb-based alloys fabricated by SLM using elemental powder. Remelting strategy, Fe addition, and PEO-based surface modification were demonstrated to be effective approaches for achieving microstructural homogenization, enhancing β -phase stability, superior passivation, and achieving enhanced biological performance. These findings provide a strong foundation for the development of next-generation β -type Ti alloys for orthopedic applications.

5 Future work

Building upon the findings of this work, future studies can be directed toward extending alloy design, structural optimization, and multifunctional surface engineering.

1. The Ti-Nb-based alloys will be extended to lattice architectures, with emphasis on strut integrity, geometric complexity, and defect sensitivity.
2. PEO coatings on the Ti-Nb-based alloys can be further engineered to incorporate antibacterial agents and drug-delivery functionalities, enabling simultaneous corrosion protection, infection control, and enhanced osteointegration.
3. The synergistic interaction between mechanical wear and electrochemical degradation will be investigated under biologically relevant conditions, including the presence of proteins, body fluids, and bone or cartilage counterparts. These studies are essential to understand the stability of passive or coated surfaces under realistic physiological loading.
4. The fabricated and surface-modified Ti-Nb-based alloys will be evaluated under in-vivo conditions using appropriate animal models to assess biological response, osseointegration, degradation behavior, and long-term implant stability.

References

- Affolter, C., Müller, U., Leinenbach, C., & Weisse, B. (2015). Compressive Testing of Ductile High-Strength Alloys. *Journal of Testing and Evaluation*, 43(6), 1554–1562. doi: 10.1520/JTE20140301
- Afonso, C. R. M., Aleixo, G. T., Ramirez, A. J., & Caram, R. (2007). Influence of cooling rate on microstructure of Ti-Nb alloy for orthopedic implants. *Materials Science and Engineering C*, 27(4), 908–913. doi: 10.1016/j.msec.2006.11.001
- Ahmad, M., Javaid, M., & Haleem, A. (2024). Enhancing biocompatible metal alloy fabrication for bio implants through laser-based additive manufacturing (LBAM). *Biomedical Analysis*, 1(1), 73–85. doi: 10.1016/j.bioana.2024.02.001
- Akman, A., Douest, Y., Alberta, L. A., Perrin, K., Trunfio Sfarighiu, A.-M., Courtois, N., Ter-Ovanessian, B., Pilz, S., Zimmermann, M., Calin, M., & Gebert, A. (2024). Tribocorrosion behaviour of additively manufactured β -type Ti-Nb alloy for implant applications. *Journal of Materials Research and Technology*, 31, 1419–1429. doi: 10.1016/j.jmrt.2024.06.172
- Alberta, L. A., Fortouna, Y., Vishnu, J., Pilz, S., Gebert, A., Lekka, C., Nielsch, K., & Calin, M. (2023). Effects of Ga on the structural, mechanical and electronic properties of β -Ti-45Nb alloy by experiments and ab initio calculations. *Journal of the Mechanical Behavior of Biomedical Materials*, 140, 105728. doi: 10.1016/j.jmbbm.2023.105728
- Al-Shalawi, F. D., Mohamed Ariff, A. H., Jung, D.-W., Mohd Ariffin, M. K. A., Seng Kim, C. L., Brabazon, D., & Al-Osaimi, M. O. (2023). Biomaterials as Implants in the Orthopedic Field for Regenerative Medicine: Metal versus Synthetic Polymers. *Polymers*, 15(12), 2601. doi: 10.3390/polym15122601
- Arabnejad, S., Johnston, B., Tanzer, M., & Pasini, D. (2017). Fully porous 3D printed titanium femoral stem to reduce stress-shielding following total hip arthroplasty. *Journal of Orthopaedic Research*, 35(8), 1774–1783. doi: 10.1002/jor.23445
- Arun, S., Ahn, S.-G., & Choe, H.-C. (2023). Surface characteristics of HA-coated and PEO-treated Ti-6Al-4V alloy in solution containing Ag nanoparticles. *Surfaces and Interfaces*, 39, 102932. doi: 10.1016/j.surfin.2023.102932
- Balasubramani, T., Kumar, N. M., Aseer, J. R., & Sivaram, N. M. (2025). Additive Manufacturing of Ti-6 Al-4 V Alloys: Fabrication Techniques and Material Properties—Review. *Transactions of the Indian Institute of Metals*, 78(8), 200. doi: 10.1007/s12666-025-03625-8
- Bălțatu, M. S., Vizureanu, P., Tiorean, M. H., Minciună, M. G., & Achiței, D. (2015). Ti-Mo Alloys Used in Medical Applications. *Advanced Materials Research*, 1128, 105–111. doi: 10.4028/www.scientific.net/AMR.1128.105
- Banerjee, D., & Williams, J. C. (2013). Perspectives on Titanium Science and Technology. *Acta Materialia*, 61(3), 844–879. doi: 10.1016/j.actamat.2012.10.043
- Birmingham, M. J., McDonald, S. D., Dargusch, M. S., & St.John, D. H. (2008). Grain-refinement mechanisms in titanium alloys. *Journal of Materials Research*, 23(1), 97–104. doi: 10.1557/jmr.2008.0002
- Bignon, M., Bertrand, E., Rivera-Díaz-del-Castillo, P. E. J., & Tancret, F. (2021). Martensite formation in titanium alloys: Crystallographic and compositional effects. *Journal of Alloys and Compounds*, 872. doi: 10.1016/j.jallcom.2021.159636

- Borgman, J. M., Wang, J., Zani, L., Conway, P. P., & Torres-Sanchez, C. (2021). The Effect of Energy Density and Nb Content on the Microstructure and Mechanical Properties of Selective Laser Melted Ti-(10-30 wt.%) Nb. *Journal of Materials Engineering and Performance*, 30(12), 8771–8783. doi: 10.1007/s11665-021-06239-5
- Brodie, E. G., Medvedev, A. E., Frith, J. E., Dargusch, M. S., Fraser, H. L., & Molotnikov, A. (2020). Remelt processing and microstructure of selective laser melted Ti25Ta. *Journal of Alloys and Compounds*, 820, 153082. doi: 10.1016/j.jallcom.2019.153082
- Brug, G. J., van den Eeden, A. L. G., Sluyters-Rehbach, M., & Sluyters, J. H. (1984). The analysis of electrode impedances complicated by the presence of a constant phase element. *Journal of Electroanalytical Chemistry and Interfacial Electrochemistry*, 176(1–2), 275–295. doi: 10.1016/S0022-0728(84)80324-1
- Bychkov, Yu. F., Herzog, R., & Khukhareva, I. S. (1981). Thermal conductivity and electrical resistivity of Nb Ti alloys at low temperatures. *Cryogenics*, 21(12), 741–745. doi: 10.1016/0011-2275(81)90219-8
- Çaha, I., Alves, A. C., Chirico, C., Maria Pinto, A., Tsiapas, S., Gordo, E., Bondarchuk, O., Leonard Deepak, F., & Toptan, F. (2023). Atomic-scale investigations of passive film formation on Ti-Nb alloys. *Applied Surface Science*, 615, 156282. doi: 10.1016/j.apsusc.2022.156282
- Cardoso, G. C., Grandini, C. R., & Rau, J. V. (2024). Comprehensive review of PEO coatings on titanium alloys for biomedical implants. *Journal of Materials Research and Technology*, 31, 311–328. doi: 10.1016/j.jmrt.2024.06.068
- Chang, L. L., Wang, Y. D., & Ren, Y. (2016). In-situ investigation of stress-induced martensitic transformation in Ti–Nb binary alloys with low Young’s modulus. *Materials Science and Engineering: A*, 651, 442–448. doi: 10.1016/J.MSEA.2015.11.005
- Chen, L., Wei, K., Qu, Y., Li, T., Chang, B., Liao, B., & Xue, W. (2018). Characterization of plasma electrolytic oxidation film on biomedical high niobium-containing β -titanium alloy. *Surface and Coatings Technology*, 352, 295–301. doi: 10.1016/j.surfcoat.2018.08.025
- Chen, Q., & Thouas, G. A. (2015). Metallic implant biomaterials. *Materials Science and Engineering: R: Reports*, 87, 1–57. doi: 10.1016/j.mser.2014.10.001
- Choi, S., Kwon, J., Suk, K., Kim, H., Moon, S., Park, S., & Lee, B. H. (2023). The Clinical Use of Osteobiologic and Metallic Biomaterials in Orthopedic Surgery: The Present and the Future. *Materials*, 16(10), 3633. doi: 10.3390/ma16103633
- Dobromyslov, A. V., & Elkin, V. A. (2001). Martensitic transformation and metastable β -phase in binary titanium alloys with d-metals of 4–6 periods. *Scripta Materialia*, 44(6), 905–910. doi: 10.1016/S1359-6462(00)00694-1
- Duan, R., Li, S., Cai, B., Tao, Z., Zhu, W., Ren, F., & Attallah, M. M. (2021). In situ alloying based laser powder bed fusion processing of β Ti–Mo alloy to fabricate functionally graded composites. *Composites Part B: Engineering*, 222, 109059. doi: 10.1016/j.compositesb.2021.109059
- Ehtemam-Haghighi, S., Liu, Y., Cao, G., & Zhang, L.-C. (2016). Phase transition, microstructural evolution and mechanical properties of Ti-Nb-Fe alloys induced by Fe addition. *Materials & Design*, 97, 279–286. doi: 10.1016/j.matdes.2016.02.094

- El-Bagoury, N., Ahmed, S. I., Ahmed Abu Ali, O., El-Hadad, S., Fallatah, A. M., Mersal, G. A. M., Ibrahim, M. M., Wysocka, J., Ryl, J., Boukherroub, R., & A. Amin, M. (2019). The Influence of Microstructure on the Passive Layer Chemistry and Corrosion Resistance for Some Titanium-Based Alloys. *Materials*, *12*(8), 1233. doi: 10.3390/ma12081233
- Elias, C. N., Lima, J. H. C., Valiev, R., & Meyers, M. A. (2008). Biomedical applications of titanium and its alloys. *The Journal of The Minerals, Metals & Materials Society*, *60*(3), 46–49. doi: 10.1007/s11837-008-0031-1
- Fan, L., Chen, S., Yang, M., Liu, Y., & Liu, J. (2024). Metallic Materials for Bone Repair. *Advanced Healthcare Materials*, *13*(3). doi: 10.1002/adhm.202302132
- Fazel, M., Salimijazi, H. R., Shamanian, M., Apachitei, I., & Zadpoor, A. A. (2019). Influence of hydrothermal treatment on the surface characteristics and electrochemical behavior of Ti-6Al-4V bio-functionalized through plasma electrolytic oxidation. *Surface and Coatings Technology*, *374*, 222–231. doi: 10.1016/j.surfcoat.2019.05.088
- Feng, S., Jia, D., Fu, Y., Kong, X., Lv, Z., Zeng, E., & Gao, Q. (2024). Preparation of additive manufacturing powder by external field-enabled: a comparative assessment. *The International Journal of Advanced Manufacturing Technology*, *131*(5–6), 3239–3265. doi: 10.1007/s00170-023-12073-x
- Ferdyn, Z., Gołasz, P., Pisarek, M., Diedkova, K., Grine, L., Dulski, M., Gawecki, R., Wójcik, D., Boroduskis, M., Kosinov, O., Mishchenko, O., Pogorielov, M., & Simka, W. (2025). Modification of 3D printed TiZrNb titanium alloy surface via plasma electrolytic oxidation. *Surface and Coatings Technology*, *514*. doi: 10.1016/j.surfcoat.2025.132589
- Ferraz, N. P., Marcos, F. C. F., Nogueira, A. E., Martins, A. S., Lanza, M. R. V., Assaf, E. M., & Asencios, Y. J. O. (2017). Hexagonal-Nb₂O₅/Anatase-TiO₂ mixtures and their applications in the removal of Methylene Blue dye under various conditions. *Materials Chemistry and Physics*, *198*, 331–340. doi: 10.1016/j.matchemphys.2017.06.029
- Fikeni, L., Annan, K. A., Mutombo, K., & Machaka, R. (2021). Effect of Nb content on the microstructure and mechanical properties of binary Ti-Nb alloys. *Materials Today: Proceedings*, *38*, 913–917. doi: 10.1016/j.matpr.2020.05.315
- Fischer, M., Joguet, D., Robin, G., Peltier, L., & Laheurte, P. (2016). In situ elaboration of a binary Ti–26Nb alloy by selective laser melting of elemental titanium and niobium mixed powders. *Materials Science and Engineering: C*, *62*(12), 852–859. doi: 10.1016/j.msec.2016.02.033
- Friedemann, A. E. R., Gesing, Th. M., & Plagemann, P. (2017). Electrochemical rutile and anatase formation on PEO surfaces. *Surface and Coatings Technology*, *315*, 139–149. doi: 10.1016/j.surfcoat.2017.01.042
- Geetha, M., Singh, A. K., Asokamani, R., & Gogia, A. K. (2009). Ti based biomaterials, the ultimate choice for orthopaedic implants – A review. *Progress in Materials Science*, *54*(3), 397–425. doi: 10.1016/j.pmatsci.2008.06.004
- Guo, C., Yuan, B., Du, P., Chen, H., Zhou, Y., Zhang, H., Song, R., & Zhang, L. (2025). Laser beam powder bed fusion of NiTiFe shape memory alloys by in-situ alloying: microstructural evolution and generation of strain glass. *Virtual and Physical Prototyping*, *20*(1). doi: 10.1080/17452759.2024.2438896

- Hanaor, D. A. H., & Sorrell, C. C. (2011). Review of the anatase to rutile phase transformation. *Journal of Materials Science*, 46(4), 855–874. doi: 10.1007/s10853-010-5113-0
- Haq, M. A., Ali, I., Song, Y., & Kim, B. S. (2024). Insights into the development of Fe modified Ti-Nb alloy: A powder metallurgy perspective. *Materials Today Communications*, 38, 107743. doi: 10.1016/j.mtcomm.2023.107743
- Huang, S., Kumar, P., Yeong, W. Y., Narayan, R. L., & Ramamurty, U. (2022). Fracture behavior of laser powder bed fusion fabricated Ti41Nb via in-situ alloying. *Acta Materialia*, 225. doi: 10.1016/j.actamat.2021.117593
- Huang, S., Narayan, R. L., Tan, J. H. K., Sing, S. L., & Yeong, W. Y. (2021). Resolving the porosity-unmelted inclusion dilemma during in-situ alloying of Ti34Nb via laser powder bed fusion. *Acta Materialia*, 204, 116522. doi: 10.1016/j.actamat.2020.116522
- Huang, S., Sing, S. L., & Yeong, W. Y. (2019). Selective Laser Melting of Ti42Nb Composite Powder and the Effect of Laser Re-Melting. *Key Engineering Materials*, 801, 270–275. doi: 10.4028/www.scientific.net/KEM.801.270
- Huang, W., Chen, G., Huang, X., Zeng, Z., Du, Y., & Qin, S. (2025). Effect of Fe content on the microstructure and mechanical properties of Al-Cu-Ni-Ti-Fe alloy fabricated by selective laser melting. *Vacuum*, 242, 114746. doi: 10.1016/j.vacuum.2025.114746
- Ikonopisov, S. (1977). Theory of electrical breakdown during formation of barrier anodic films. *Electrochimica Acta*, 22(10), 1077–1082. doi: 10.1016/0013-4686(77)80042-X
- Issariyapat, A., Huang, J., Kariya, S., Chen, B., Li, S., Umeda, J., Yamanaka, K., Chiba, A., & Kondoh, K. (2025). Sustainable alloy design: Fe-enhanced Ti alloys for superior mechanical performance in additive manufacturing. *Journal of Alloys and Compounds*, 1010, 177767. doi: 10.1016/j.jallcom.2024.177767
- Jackson, M. J., Kopac, J., Balazic, M., Bombac, D., Brojan, M., & Kosel, F. (2016). Titanium and Titanium Alloy Applications in Medicine. In *Surgical Tools and Medical Devices* (pp. 475–517). Cham: Springer International Publishing. doi: 10.1007/978-3-319-33489-9_15
- Jakubowicz, J. (2020). Special Issue: Ti-Based Biomaterials: Synthesis, Properties and Applications. *Materials*, 13(7), 1696. doi: 10.3390/ma13071696
- Jawed, S. F., Rabadia, C. D., Liu, Y. J., Wang, L. Q., Qin, P., Li, Y. H., Zhang, X. H., & Zhang, L. C. (2020). Strengthening mechanism and corrosion resistance of beta-type Ti-Nb-Zr-Mn alloys. *Materials Science and Engineering: C*, 110, 110728. doi: 10.1016/j.msec.2020.110728
- Jayaraj, J., Ravi Shankar, A., & Kamachi Mudali, U. (2012). Electrochemical and passive characterization of a beta type Ti45Zr38Al17 cast rod in nitric acid medium. *Electrochimica Acta*, 85, 210–219. doi: 10.1016/j.electacta.2012.08.047
- Ji, P. F., Li, B., Chen, B. H., Wang, F., Ma, W., Zhang, X. Y., Ma, M. Z., & Liu, R. P. (2020). Effect of Nb addition on the stability and biological corrosion resistance of Ti-Zr alloy passivation films. *Corrosion Science*, 170, 108696. doi: 10.1016/J.CORSCI.2020.108696
- Jin, J., Yang, H., Liu, Y., Yang, J., Li, K., Yi, Y., Chen, D., Zhang, W., & Zhou, S. (2024). Microstructure and enhanced strength-ductility of TiNbCu alloys produced by laser powder bed fusion. *Materials Science and Engineering: A*, 890(4), 145889. doi: 10.1016/j.msea.2023.145889

- Karimi, J., Kollo, L., Rahmani, R., Ma, P., Jia, Y. D., & Prashanth, K. G. (2022). Selective laser melting of in-situ CoCrFeMnNi high entropy alloy: Effect of remelting. *Journal of Manufacturing Processes*, 84, 55–63. doi: 10.1016/j.jmapro.2022.09.056
- Kaseem, M., & Choe, H.-C. (2019). Electrochemical and bioactive characteristics of the porous surface formed on Ti-xNb alloys via plasma electrolytic oxidation. *Surface and Coatings Technology*, 378, 125027. doi: 10.1016/j.surfcoat.2019.125027
- Kent, D., Wang, G., & Dargusch, M. (2013). Effects of phase stability and processing on the mechanical properties of Ti–Nb based β Ti alloys. *Journal of the Mechanical Behavior of Biomedical Materials*, 28, 15–25. doi: 10.1016/j.jmbbm.2013.07.007
- Khorsand Zak, A., Abd. Majid, W. H., Abrishami, M. E., & Yousefi, R. (2011). X-ray analysis of ZnO nanoparticles by Williamson–Hall and size–strain plot methods. *Solid State Sciences*, 13(1), 251–256. doi: 10.1016/j.solidstatesciences.2010.11.024
- Kim, H. M., Lee, Y. J., Lee, J. G., & Lee, D. G. (2024). Effect of Fe content on microstructural evolution and mechanical properties of Ti-5Mo-xFe alloys. *Journal of Materials Research and Technology*, 33(6), 7406–7417. doi: 10.1016/j.jmrt.2024.11.140
- Kong, W., Cox, S. C., Lu, Y., Villapun, V., Xiao, X., Ma, W., Liu, M., & Attallah, M. M. (2021). The influence of zirconium content on the microstructure, mechanical properties, and biocompatibility of in-situ alloying Ti-Nb-Ta based β alloys processed by selective laser melting. *Materials Science and Engineering: C*, 131, 112486. doi: 10.1016/j.msec.2021.112486
- Kou, S. (2002). *Welding Metallurgy*. Wiley. doi: 10.1002/0471434027
- Kulkarni, M., Patil-Sen, Y., Junkar, I., Kulkarni, C. V., Lorenzetti, M., & Iglíč, A. (2015). Wettability studies of topologically distinct titanium surfaces. *Colloids and Surfaces B: Biointerfaces*, 129, 47–53. doi: 10.1016/j.colsurfb.2015.03.024
- Lele, M., Kapur, S., Hargett, S., Sureshbabu, N. M., & Gaharwar, A. K. (2024). Global trends in clinical trials involving engineered biomaterials. *Science Advances*, 10(29). doi: 10.1126/sciadv.abq0997
- Lewis, G. (2022). Aspects of the Powder in Metal Additive Manufacturing: A Review. *World Journal of Engineering and Technology*, 10(02), 363–409. doi: 10.4236/wjet.2022.102022
- Li, Q., Huang, Q., Li, J., He, Q., Nakai, M., Zhang, K., Niinomi, M., Yamana, K., Chiba, A., & Nakano, T. (2022). Microstructure and mechanical properties of Ti–Nb–Fe–Zr alloys with high strength and low elastic modulus. *Transactions of Nonferrous Metals Society of China*, 32(2), 503–512. doi: 10.1016/S1003-6326(22)65811-4
- Li, Z., Qiu, J., Xu, H., Dong, A., He, L., Zhu, G., Du, D., Xing, H., Liu, X., & Sun, B. (2022). Characteristics of β -type Ti-41Nb alloy produced by laser powder bed fusion: Microstructure, mechanical properties and in vitro biocompatibility. *Journal of Materials Science and Technology*, 124, 260–272. doi: 10.1016/j.jmst.2022.02.026
- Li, Z., Xu, H., Dong, A., Cai, X., He, L., Du, D., Xing, H., Zhu, G., & Sun, B. (2022). Mechanical anisotropy of laser powder bed fusion fabricated Ti-41Nb alloy using pre-alloyed powder: Roles played by grain morphology and crystallographic orientation. *Journal of Alloys and Compounds*, 925, 166572. doi: 10.1016/j.jallcom.2022.166572

- Liang, S. (2020). Review of the Design of Titanium Alloys with Low Elastic Modulus as Implant Materials. *Advanced Engineering Materials*, 22(11). doi: 10.1002/ADEM.202000555
- Liu, S., & Shin, Y. C. (2019). Additive manufacturing of Ti6Al4V alloy: A review. *Materials & Design*, 164, 107552. doi: 10.1016/j.matdes.2018.107552
- Lokeshkumar, E., Premchand, C., Manojkumar, P., Shishir, R., Krishna, L. R., Prashanth, K. G., & Rameshbabu, N. (2023). Effect of electrolyte composition on the surface characteristics of plasma electrolytic oxidation coatings over Ti-40Nb alloy. *Surface and Coatings Technology*, 465. doi: 10.1016/j.surfcoat.2023.129591
- Lopes, É. S. N., Salvador, C. A. F., Andrade, D. R., Cremasco, A., Campo, K. N., & Caram, R. (2016). Microstructure, Mechanical Properties, and Electrochemical Behavior of Ti-Nb-Fe Alloys Applied as Biomaterials. *Metallurgical and Materials Transactions A*, 47(6), 3213–3226. doi: 10.1007/s11661-016-3411-0
- Lunt, R. A., Jackson, A. J., & Walsh, A. (2013). Dielectric response of Fe₂O₃ crystals and thin films. *Chemical Physics Letters*, 586(40), 67–69. doi: 10.1016/j.cplett.2013.09.023
- Luo, X., Li, Y., Yang, C., Zhao, C., Ma, H., Song, T., Sun, M., Liu, X., Li, D., & Li, N. (2025). Insights into laser powder bed fused β -type titanium alloy: Investigating corrosion behavior and wear properties after post-heat treatment. *Journal of Materials Research and Technology*, 37, 1596–1605. doi: 10.1016/j.jmrt.2025.06.120
- Lv, F., Liang, H., Xie, D., Mao, Y., Wang, C., Shen, L., & Tian, Z. (2021). On the role of laser in situ re-melting into pore elimination of Ti-6Al-4V components fabricated by selective laser melting. *Journal of Alloys and Compounds*, 854, 156866. doi: 10.1016/j.jallcom.2020.156866
- Maciej, A., Marny, M., Sowa, M., Blacha-Grzechnik, A., Stolarczyk, A., Michalska, J., & Simka, W. (2023). Microstructure and corrosion resistance of Ti and Ti-40Nb alloy modified by plasma electrolytic oxidation in tricalcium phosphate suspension. *Electrochimica Acta*, 468, 143185. doi: 10.1016/j.electacta.2023.143185
- Marin, E., & Lanzutti, A. (2025). History of Metallic Orthopedic Materials. *Metals*, 15(4), 378. doi: 10.3390/met15040378
- Maurya, H. S., Kosiba, K., Juhani, K., Sergejev, F., & Prashanth, K. G. (2022). Effect of powder bed preheating on the crack formation and microstructure in ceramic matrix composites fabricated by laser powder-bed fusion process. *Additive Manufacturing*, 58(February), 103013. doi: 10.1016/j.addma.2022.103013
- Molaei, M., Fattah-alhosseini, A., Nouri, M., Mahmoodi, P., & Nourian, A. (2022). Incorporating TiO₂ nanoparticles to enhance corrosion resistance, cytocompatibility, and antibacterial properties of PEO ceramic coatings on titanium. *Ceramics International*, 48(14), 21005–21024. doi: 10.1016/j.ceramint.2022.04.096
- Mosallanejad, M. H., Niroumand, B., Aversa, A., & Saboori, A. (2021). In-situ alloying in laser-based additive manufacturing processes: A critical review. *Journal of Alloys and Compounds*, 872, 159567. doi: 10.1016/j.jallcom.2021.159567
- Nakano, T. (2010). Mechanical properties of metallic biomaterials. In *Metals for Biomedical Devices* (pp. 71–98). Elsevier. doi: 10.1533/9781845699246.2.71

- Nanda, G., Awin, E. W., Gasyak, T., Koroleva, E., Filimonov, A., Vakhrushev, S., Sujith, R., & Kumar, R. (2020). Temperature dependent conductivity and broadband dielectric response of precursor-derived Nb₂O₅. *Ceramics International*, *46*(7), 9512–9518. doi: 10.1016/j.ceramint.2019.12.213
- Ni, J.-H., Shi, Y.-L., Yan, F.-Y., Chen, J.-Z., & Wang, L. (2008). Preparation of hydroxyapatite-containing titania coating on titanium substrate by micro-arc oxidation. *Materials Research Bulletin*, *43*(1), 45–53. doi: 10.1016/j.materresbull.2007.02.019
- Niinomi, M., & Nakai, M. (2011). Titanium-Based Biomaterials for Preventing Stress Shielding between Implant Devices and Bone. *International Journal of Biomaterials*, *2011*. doi: 10.1155/2011/836587
- Nisar, S. S., & Choe, H.-C. (2024). Mechanical hydroxyapatite coatings on PEO-treated Ti–6Al–4V alloy for enhancing implant’s surface bioactivity. *Ceramics International*, *50*(10), 17703–17719. doi: 10.1016/j.ceramint.2024.02.259
- Palaniappan, S., Sharma, S., Radhakrishnan, M., Krishna, K. V. M., Joshi, S. S., Banerjee, R., & Dahotre, N. B. (2025). Process thermokinetics influenced microstructure and corrosion response in additively in-situ manufactured Ti-Nb-Sn and Ti-Nb alloys. *Journal of Manufacturing Processes*, *152*, 427–441. doi: 10.1016/j.jmapro.2025.08.010
- Pezzato, L., Dabalà, M., Gross, S., & Brunelli, K. (2020). Effect of microstructure and porosity of AlSi10Mg alloy produced by selective laser melting on the corrosion properties of plasma electrolytic oxidation coatings. *Surface and Coatings Technology*, *404*, 126477. doi: 10.1016/j.surfcoat.2020.126477
- Pilz, S., Bönisch, M., Datye, A., Zhang, S., Günther, F., Drescher, S., Kühn, U., Schwarz, U. D., Zimmermann, M., & Gebert, A. (2024). Tailoring microstructure and mechanical properties of an LPBF-processed beta Ti-Nb alloy through post-heat treatments. *Materials & Design*, *239*, 112799. doi: 10.1016/j.matdes.2024.112799
- Pilz, Stefan, Gustmann, T., Günther, F., Zimmermann, M., Kühn, U., & Gebert, A. (2022). Controlling the Young’s modulus of a β -type Ti-Nb alloy via strong texturing by LPBF. *Materials & Design*, *216*, 110516. doi: 10.1016/j.matdes.2022.110516
- Polozov, I., Sokolova, V., Gracheva, A., Zolotarev, A., Nefyodova, V., & Popovich, A. (2024). Ti-Ta-Cu Biocompatible Alloy System Development via Selective Laser Melting for Prosthetic Applications. *Metals* *2024*, Vol. *14*, 14(10). doi: 10.3390/met14101177
- Popovich, A., & Sufiiarov, V. (2016). Metal Powder Additive Manufacturing. In *New Trends in 3D Printing*. InTech. doi: 10.5772/63337
- Prashanth, K. G., Scudino, S., Maity, T., Das, J., & Eckert, J. (2017). Is the energy density a reliable parameter for materials synthesis by selective laser melting? *Materials Research Letters*, *5*(6), 386–390. doi: 10.1080/21663831.2017.1299808
- Qazi, J. I., & Rack, H. J. (2005). Metastable Beta Titanium Alloys for Orthopedic Applications. *Advanced Engineering Materials*, *7*(11), 993–998. doi: 10.1002/adem.200500060
- Qin, P., Chen, L. Y., Zhao, C. H., Liu, Y. J., Cao, C. D., Sun, H., & Zhang, L. C. (2021). Corrosion behavior and mechanism of selective laser melted Ti35Nb alloy produced using pre-alloyed and mixed powder in Hank’s solution. *Corrosion Science*, *189*, 109609. doi: 10.1016/j.corsci.2021.109609

- Sagidugumar, A., Dogadkin, D., Turlybekuly, A., & Kaliyev, D. (2024). Calcium Phosphate Coatings Deposited on 3D-Printed Ti–6Al–4V Alloy by Plasma Electrolytic Oxidation. *Coatings*, *14*(6), 696. doi: 10.3390/coatings14060696
- Schmid-Fetzer, R., & Kozlov, A. (2011). Thermodynamic aspects of grain growth restriction in multicomponent alloy solidification. *Acta Materialia*, *59*(15), 6133–6144. doi: 10.1016/j.actamat.2011.06.026
- Schwab, H., Prashanth, K., Löber, L., Kühn, U., & Eckert, J. (2015). Selective Laser Melting of Ti-45Nb Alloy. *Metals*, *5*(2), 686–694. doi: 10.3390/met5020686
- Sharkeev, Y. P., Eroshenko, A. Y., Kovalevskaya, Z. G., Saprykin, A. A., Ibragimov, E. A., Glukhov, I. A., Chimich, M. A., Uvarin, P. V., & Babakova, E. V. (2016). Phase Composition and Microstructure of Ti-Nb Alloy Produced by Selective Laser Melting. *IOP Conference Series: Materials Science and Engineering*, *140*(1). doi: 10.1088/1757-899X/140/1/012020
- Sharkeev, Yu. P., Dmitriev, A. I., Knyazeva, A. G., Eroshenko, A. Yu., Saprykin, A. A., Khimich, M. A., Ibragimov, E. A., Glukhov, I. A., Mairambekova, A. M., & Nikonov, A. Yu. (2017). Selective Laser Melting of the Ti–(40–50) wt.% Nb Alloy. *High Temperature Material Processes An International Quarterly of High-Technology Plasma Processes*, *21*(2), 161–183. doi: 10.1615/HighTempMatProc.2017024814
- Sidambe, A. (2014). Biocompatibility of Advanced Manufactured Titanium Implants—A Review. *Materials*, *7*(12), 8168–8188. doi: 10.3390/ma7128168
- Singh, N., Srikanth, K. P., Gopal, V., Rajput, M., Manivasagam, G., Prashanth, K. G., Chatterjee, K., & Suwas, S. (2024). *In situ* production of low-modulus Ti–Nb alloys by selective laser melting and their functional assessment toward orthopedic applications. *Journal of Materials Chemistry B*, *12*(24), 5982–5993. doi: 10.1039/D4TB00379A
- Singh, S., Jinoop, A. N., Palani, I. A., Paul, C. P., Tomar, K. P., & Prashanth, K. G. (2021). Microstructure and mechanical properties of NiTi-SS bimetallic structures built using Wire Arc Additive Manufacturing. *Materials Letters*, *303*, 130499. doi: 10.1016/j.matlet.2021.130499
- Song, J., Tang, Q., Feng, Q., Han, Q., Ma, S., Chen, H., Guo, F., & Setchi, R. (2022). Effect of remelting processes on the microstructure and mechanical behaviours of 18Ni-300 maraging steel manufactured by selective laser melting. *Materials Characterization*, *184*, 111648. doi: 10.1016/j.matchar.2021.111648
- Soong, S. Z., Lai, W. L., & Kay Lup, A. N. (2023). Atomization of metal and alloy powders: Processes, parameters, and properties. *American Institute of Chemical Engineers*, *69*(11). doi: 10.1002/aic.18217
- Subramanian, S., Manivasagam, G., Jayaraj, J., & Prashanth, K. G. (2026). Microstructural refinement, mechanical enhancement, and superior passivation of SLM Ti-Nb-Fe fabricated through insitu alloying. *Journal of Alloys and Compounds*, *1064*, 187930. doi: 10.1016/J.JALLCOM.2026.187930
- Subramanian, S., Mohanty, S., & Prashanth, K. (2023). Effect of process parameters on the properties of β -Ti-Nb-based alloys fabricated by selective laser melting: A review. *Materials Today: Proceedings*. doi: 10.1016/j.matpr.2023.03.461
- Subramanian, S., Praveenkumar, K., Rameshbabu, N., Lokeshraj, K., Raheem, A., Jayaraj, J., & Prashanth, K. G. (2026). Biofunctionalization of SLM Ti–40Nb alloy through hydroxyapatite-modified plasma electrolytic oxidation coating. *Applied Surface Science Advances*, *31*, 100917. doi: 10.1016/J.APSADV.2025.100917

- Subramanian, S., Yadav, M. K., Jayaraj, J., Yangyang, F., Xi, L., & Prashanth, K. G. (2025). Microstructural homogenization through laser remelting in an additively manufactured Ti–40Nb sample from elemental feedstock powders. *Journal of Materials Research and Technology*, *38*, 4305–4320. doi: 10.1016/j.jmrt.2025.08.203
- Tang, W., Li, J., Wu, B., Panwisawas, C., Li, M., Wang, J., Ren, N., Zeng, L., Xia, M., & Li, J. (2025). Elemental segregation and solute transport in the in-situ alloying of miscible Ti-Nb alloys using laser powder bed fusion. *Acta Materialia*, *299*, 121417. doi: 10.1016/J.ACTAMAT.2025.121417
- Thoemmes, A., Bataev, I. A., Lazurenko, D. V., Ruktuev, A. A., Ivanov, I. V., Afonso, C. R. M., Stark, A., & Jorge, A. M. (2021). Microstructure and lattice parameters of suction-cast Ti–Nb alloys in a wide range of Nb concentrations. *Materials Science and Engineering: A*, *818*. doi: 10.1016/j.msea.2021.141378
- Ummethala, R., Jayaraj, J., Karamched, P. S., Rathinavelu, S., Singh, N., Surreddi, K. B., & Prashanth, K. G. (2021). In Vitro Corrosion Behavior of Selective Laser Melted Ti-35Nb-7Zr-5Ta. *Journal of Materials Engineering and Performance*, *30*(11), 7967–7978. doi: 10.1007/s11665-021-05940-9
- Valizade, N., Sabour Rouh Aghdam, A., & Jarjoura, G. (2024). Corrosion and biological study on biofunctionalized porous coating on titanium produced by plasma electrolytic oxidation. *Colloids and Surfaces A: Physicochemical and Engineering Aspects*, *688*, 133567. doi: 10.1016/j.colsurfa.2024.133567
- Wang, J. C., Liu, Y. J., Liang, S. X., Zhang, Y. S., Wang, L. Q., Sercombe, T. B., & Zhang, L. C. (2022). Comparison of microstructure and mechanical behavior of Ti-35Nb manufactured by laser powder bed fusion from elemental powder mixture and prealloyed powder. *Journal of Materials Science and Technology*, *105*, 1–16. doi: 10.1016/j.jmst.2021.07.021
- Wang, J. C., Liu, Y. J., Qin, P., Liang, S. X., Sercombe, T. B., & Zhang, L. C. (2019). Selective laser melting of Ti–35Nb composite from elemental powder mixture: Microstructure, mechanical behavior and corrosion behavior. *Materials Science and Engineering: A*, *760*, 214–224. doi: 10.1016/j.msea.2019.06.001
- Wang, J., Liu, Y., Rabadia, C. D., Liang, S. X., Sercombe, T. B., & Zhang, L. C. (2021). Microstructural homogeneity and mechanical behavior of a selective laser melted Ti-35Nb alloy produced from an elemental powder mixture. *Journal of Materials Science and Technology*, *61*, 221–233. doi: 10.1016/j.jmst.2020.05.052
- Wang, Q., Han, C., Choma, T., Wei, Q., Yan, C., Song, B., & Shi, Y. (2017). Effect of Nb content on microstructure, property and in vitro apatite-forming capability of Ti-Nb alloys fabricated via selective laser melting. *Materials & Design*, *126*, 268–277. doi: 10.1016/j.matdes.2017.04.026
- Woldemedhin, M. T., Raabe, D., & Hassel, A. W. (2012). Characterization of thin anodic oxides of Ti–Nb alloys by electrochemical impedance spectroscopy. *Electrochimica Acta*, *82*, 324–332. doi: 10.1016/j.electacta.2012.06.029
- Wu, G., Li, L., Sun, M., Wang, Y., Luo, F., Zhang, Q., Liu, R., Chen, Z., & Yao, J. (2023). Microstructural evolution and biological properties of PEO coating on SLM-prepared NiTi alloy. *Surface and Coatings Technology*, *452*, 129065. doi: 10.1016/j.surfcoat.2022.129065

- Wu, T., Blawert, C., Serdechnova, M., Karlova, P., Dovzhenko, G., Florian Wieland, D. C., Stojadinovic, S., Vasilic, R., Wang, L., Wang, C., Mojsilovic, K., & Zheludkevich, M. L. (2022). Role of phosphate, silicate and aluminate in the electrolytes on PEO coating formation and properties of coated Ti6Al4V alloy. *Applied Surface Science*, 595, 153523. doi: 10.1016/j.apsusc.2022.153523
- Wu, X. Q., Xie, F. Q., Hu, Z. C., & Wang, L. (2010). Effects of additives on corrosion and wear resistance of micro-arc oxidation coatings on TiAl alloy. *Transactions of Nonferrous Metals Society of China*, 20(6), 1032–1036. doi: 10.1016/S1003-6326(09)60253-3
- Yadav, M. K., Pandey, V., Mohanta, K., & Singh, V. K. (2022). A low-cost approach to develop silica doped Tricalcium Phosphate (TCP) scaffold by valorizing animal bone waste and rice husk for tissue engineering applications. *Ceramics International*, 48(17), 25335–25345. doi: 10.1016/j.ceramint.2022.05.207
- Yao, J., Wang, Y., Wu, G., Sun, M., Wang, M., & Zhang, Q. (2019). Growth characteristics and properties of micro-arc oxidation coating on SLM-produced TC4 alloy for biomedical applications. *Applied Surface Science*, 479, 727–737. doi: 10.1016/j.apsusc.2019.02.142
- Yi, J., Chen, Z., Li, R., Xu, Z., Song, Y., Fan, Q., Wang, J., & Chai, W. (2025). Orthopedic Implant Infection Management: Prevention, Barrier Breakthrough, and Immunomodulation. *ACS Nano*, 19(30), 27009–27032. doi: 10.1021/acsnano.4c17509
- Yılmaz, E., Gökçe, A., Findik, F., & Gulsoy, Ho. O. (2018). Metallurgical properties and biomimetic HA deposition performance of Ti-Nb PIM alloys. *Journal of Alloys and Compounds*, 746, 301–313. doi: 10.1016/j.jallcom.2018.02.274
- Zerwas, A. A., da Silva, F. C., Guardani, R., Achelis, L., & Fritsching, U. (2024). Impact of the gas atomizer nozzle configuration on metal powder production for additive manufacturing. *Powder Technology*, 443, 119974. doi: 10.1016/j.powtec.2024.119974
- Zhang, X., Wu, Y., Lv, Y., Yu, Y., & Dong, Z. (2020). Formation mechanism, corrosion behaviour and biological property of hydroxyapatite/TiO₂ coatings fabricated by plasma electrolytic oxidation. *Surface and Coatings Technology*, 386, 125483. doi: 10.1016/J.SURFCOAT.2020.125483
- Zhao, D., Han, C., Li, J., Liu, J., & Wei, Q. (2020). In situ fabrication of a titanium-niobium alloy with tailored microstructures, enhanced mechanical properties and biocompatibility by using selective laser melting. *Materials Science and Engineering: C*, 111, 110784. doi: 10.1016/j.msec.2020.110784
- Zhao, G.-H., Liang, X. Z., Kim, B., & Rivera-Díaz-del-Castillo, P. E. J. (2019). Modelling strengthening mechanisms in beta-type Ti alloys. *Materials Science and Engineering: A*, 756, 156–160. doi: 10.1016/j.msea.2019.04.027
- Zhou, L., Yuan, T., Li, R., Tang, J., Wang, M., & Mei, F. (2018). Anisotropic mechanical behavior of biomedical Ti-13Nb-13Zr alloy manufactured by selective laser melting. *Journal of Alloys and Compounds*, 762, 289–300. doi: 10.1016/j.jallcom.2018.05.179
- Zhou, Y. H., Zhang, Z. H., Wang, Y. P., Liu, G., Zhou, S. Y., Li, Y. L., Shen, J., & Yan, M. (2019). Selective laser melting of typical metallic materials: An effective process prediction model developed by energy absorption and consumption analysis. *Additive Manufacturing*, 25, 204–217. doi: 10.1016/J.ADDMA.2018.10.046

Acknowledgement

The journey to completing this Ph.D. was not easy, but the support, encouragement, and kindness of many people helped me move forward and reach this stage. I would like to take this opportunity to express my sincere gratitude to all those who have been part of this journey.

Firstly, I would like to express my deepest gratitude to my supervisor, Prof. Prashanth Konda Gokuldoss, for giving me the opportunity to work on this research and for his continuous guidance and support throughout my Ph.D. His mentorship has greatly contributed to my development as a researcher. I extend my sincere thanks to my co-supervisor, Prof. Jayaraj Jayamani, for his constant support, for sharing his knowledge, and for his valuable suggestions and guidance, which significantly contributed to my learning. I express my sincere gratitude to their families, Mrs. Devarani and Mrs. Shanthini, for their kindness and warm hospitality.

I gratefully acknowledge the financial support received for my Ph.D. from the Estonian Research Council (Project No. ETAG21021), under the project titled Waste-to-resource: eggshells as a source for next-generation biomaterials for bone regeneration.

I would like to thank Kerli Roosimaa and Program Directors, Dr. Rocio Estefania Rojas Hernandez, and Prof. Jüri Majak for their support in securing Erasmus+ mobility funding, which enabled my participation in summer schools and short-term research stays.

I sincerely thank the administration and academic staff at Tallinn University of Technology (TalTech), Mrs. Ruth Kulbas, Dr. Marek Tarraste, Dr. Maksim Antonov, Dr. Rainer Traksmäa, Dr. Mart Viljus, Mrs. Laivi Väljaots, Dr. Le Liu, Dr. Märt Kolnes, and Dr. Mart Kolnes, Prof. Kristo Karjus and Prof. Fjodor Sergejev for their support, valuable guidance, knowledge sharing, and training in SLM, SPS, and various experimental characterization techniques such as XRD and SEM, which greatly supported this research.

I would like to extend my special thanks to the experimental technicians, Mr. Hans Vallner and Mr. Mykola Semeniuk, for their continuous assistance and support during my experimental work. Their willingness to help, along with their warm smiles and positive nature, made the research process much smoother and more enjoyable. My sincere appreciation goes to the Department of Mechanical Engineering at TalTech for providing excellent facilities, infrastructure, and a supportive research environment.

Most importantly, I would like to thank my dear friends - Dr. Shalini Mohanty, Dr. Himanshu Singh Maurya, Dr. Riddhi Shukla, Mr. Mayank Kumar Yadav, Dr. Praveenkumar Kesavan, Ms. Sibel Yöyler, Mr. Furqan Anwar, Mr. Tabeen Halawat Pampori, and Dr. Marmar Mehrparvar for their encouragement, understanding, and companionship during both the challenging and memorable moments of this journey.

Finally, I would like to express my heartfelt gratitude to my family - father Mr. Subramanian Periyasamy; mother Mrs. Pappathi Subramanian; sister Mrs. Maivizhi, husband Mr. Lokeshraj Kuppuswamy, and other family members Mr. Muruganandham, Mr. Rajarajan, Mrs. Amuthavalli, Mr. Kuppusamy, Mrs. Jayalakshmi, Ms. Rajaroja and Mr. Rajagoutham, Mr. Gokul Prasad and friends Mrs. Manju Priya, Mr. Hariharan, Mrs. Vaneeswari - for their unconditional love, endless support, and unwavering belief in me. They are the backbone of my strength and the foundation of who I am today. This thesis is lovingly dedicated to my parents, whose sacrifices, encouragement, and constant support have been a part of this journey. Every step of this achievement stands on their love, sacrifices, and unwavering belief in me.

Abstract

Fabrication of In-Situ Alloyed Ti-Nb via Selective Laser Melting for Orthopedic Applications

β -type titanium alloys are increasingly explored for orthopedic implant applications due to their low elastic modulus, high corrosion resistance, and excellent biocompatibility. Among these alloys, Ti-Nb-based systems are particularly attractive. However, their fabrication via selective laser melting using elemental powders presents significant challenges. It includes incomplete alloying, microstructural heterogeneity, and defect formation arising from large differences in melting temperature between Ti and Nb. In addition, long-term implant performance requires both optimized bulk properties and enhanced surface biofunctionality. This thesis addresses these challenges by establishing an integrated processing-microstructure-property-function framework for Ti-Nb-based alloys fabricated by SLM and biofunctionalized using the plasma electrolytic oxidation process.

In the first part of this work, the SLM process was utilized for the successful fabrication of dense bulk Ti-40Nb components through in-situ alloying of elemental powders. A remelting strategy was implemented to stabilize melt pool dynamics, enhance Nb dissolution, and reduce processing-induced defects such as porosity and unmelted Nb particles. Detailed microstructural investigations revealed the formation of a dual phase $\alpha'+\beta$ microstructure. Remelting significantly reduced Nb segregation, reduced cooling rate, and promoted microstructural homogenization. As a result, the Ti-40Nb alloy exhibited a favorable balance between mechanical strength and ductility, characterized by a low elastic modulus closer to that of bone and high compressive strength. This strength-ductility synergy is essential for load-bearing orthopedic implants, ensuring mechanical reliability while minimizing stress-shielding effects.

In the second part, alloy design was extended by introducing Fe to develop the Ti-403b-5Fe alloy. Phase analysis confirmed that Fe acted as a strong β -stabilizer and significantly increased the β -phase fraction. Microstructural analysis revealed pronounced grain refinement, leading to improved hardness and strength. The retention β -phase reduced the elastic modulus and enhanced strain hardening behavior. This ensures the strength-ductility trade-off that is essential for load-bearing orthopedic implants. Electrochemical studies in physiological environments confirmed the formation of a stable passive film composed of TiO₂, Nb₂O₅, and Fe₂O₃. The alloy exhibited higher polarization resistance and lower capacitance. Mott-Schottky analysis indicated reduced donor density, suggesting improved passive film stability and defect chemistry.

In the third part, SLM-fabricated Ti-40Nb substrates were surface-engineered via plasma electrolytic oxidation in phosphate-silicate and phosphate-silicate-hydroxyapatite electrolytes. The homogenized bulk microstructure was found to be critical for achieving uniform discharge behavior and reproducible coating morphology during PEO. The resulting coatings exhibited a characteristic duplex structure consisting of a dense inner barrier layer and a porous outer layer. Incorporation of HAp nanoparticles led to the formation of TiO₂-Nb₂O₅-Ca-P composite oxide coatings with reduced porosity, increased rutile content, and enhanced coating compactness. Biological assessment using MC3T3 pre-osteoblast

cells revealed enhanced cell adhesion, proliferation, and cytoskeletal organization on the HAp-containing coatings. The combined effects of increased surface roughness, improved wettability, and controlled release of bioactive Ca^{2+} and PO_4^{3-} ions promoted a biomimetic surface environment conducive to early-stage osseointegration.

Overall, this thesis demonstrates that the combination of in-situ alloying, microstructural control through remelting, alloy modification via Fe addition, and PEO-based biofunctionalization significantly enhances the properties of Ti-Nb-based alloys. The developed materials exhibit a homogenized microstructure, improved mechanical properties, stable passivation behavior, and enhanced biological response. This integrated approach provides a pathway for the design of next-generation β -Ti-Nb-based implants and highlights the potential of in-situ alloying by SLM for cost-effective and clinically applicable biomedical applications.

Lühikokkuvõte

In-situ legeritud Ti–Nb sulamite valmistamine selektiivse lasersulatamise abil ortopeedilisteks rakendusteks

β -tüüpi titaansulamid on ortopeediliste implantaatide rakendustes üha enam uurimise all tänu nende madalale elastsusmoodulile, kõrgele korrosioonikindlusele ja suurepärasele biosobivusele. Nende sulamite hulgas on Ti–Nb-põhised süsteemid eriti atraktiivsed. Kuid nende valmistamine selektiivse lasersulatamise (SLM) teel elementaarpulbriest kujutab endast märkimisväärseid väljakutseid. Nende hulka kuuluvad mittetäielik legeerumine, mikrostruktuurne heterogeensus ning defektide teke, mis tuleneb Ti ja Nb suurest sulamistemperatuuri erinevusest. Lisaks nõuab implantaatide pikaajaline toimivus nii optimeeritud mahulisi omadusi kui ka täiustatud pinna biofunktsionaalsust. Käesolev väitekiri käsitleb neid väljakutseid, luues integreeritud töötamise–mikrostruktuuri–omaduste–funktsiooni raamistiku SLM-i teel valmistatud ja plasmaelektrolüütilise oksüdatsiooni (PEO) protsessiga biofunktsionaliseeritud Ti–Nb-põhiste sulamite jaoks.

Töö esimeses osas kasutati SLM-protsessi tihedate mahuliste Ti-40Nb komponentide edukaks valmistamiseks elementaarpulbri in-situ legeerimise teel. Sulavanni dünaamika stabiliseerimiseks, Nb lahustumise parandamiseks ning töötlemisest tingitud defektide, nagu poorsuse ja sulamata Nb-osakeste, vähendamiseks rakendati ümbersulatamise strateegiat. Üksikasjalikud mikrostruktuuriuuringud näitasid kahefaasilise $\alpha'+\beta$ mikrostruktuuri teket. Ümbersulatamine vähendas oluliselt Nb segregatsiooni, alandas jahutuskiirust ja soodustas mikrostruktuuri homogeniseerumist. Selle tulemusena saavutati Ti-40Nb sulamis soodne tasakaal mehaanilise tugevuse ja plastilisuse vahel, mida iseloomustab luukoole lähedasem madal elastsusmoodul ja kõrge survetugevus. Selline tugevuse ja plastilisuse sünergia on oluline koormust kandvate ortopeediliste implantaatide puhul, tagades mehaanilise töökindluse ning vähendades stressi varjestumise efekti.

Teises osas laiendati sulami disaini Fe lisamisega, et arendada Ti-40Nb-5Fe sulamit. Faasianalüüs kinnitas, et Fe toimib tugeva β -faasi stabilisaatorina ja suurendab oluliselt β -faasi osakaalu. Mikrostruktuuri analüüs näitas märgatavat terade peenestumist, mis viis kõvaduse ja tugevuse paranemiseni. Säilinud β -faasi olemasolu vähendas elastsusmoodulit ja parandas deformatsioonikõvenemise käitumist, tagades vajaliku tugevuse–plastilisuse kompromissi koormust kandvate implantaatide jaoks. Elektrokeemilised uuringud füsioloogilistes keskkondades kinnitasid stabiilse passiivkihi teket, mis koosneb TiO_2 -st, Nb_2O_5 -st ja Fe_2O_3 -st. Sulam näitas kõrgemat polarisatsioonitakistust ja madalamat mahtuvust. Mott–Schottky analüüs näitas doonortiheduste vähenemist, viidates paranenud passiivkihi stabiilsusele ja defektikeemiale.

Kolmandas osas modifitseeriti SLM-teel valmistatud Ti-40Nb substraatide pindu plasmaelektrolüütilise oksüdatsiooni abil fosfaat-silikaat ja fosfaat-silikaat-hüdroksüapatiit elektrolüütides. Homogeniseeritud mahuline mikrostruktuur osutus kriitiliseks ühtlase tühjenemiskäitumise ja reprodutseeritava kattekihi morfoloogia saavutamisel PEO protsessi käigus. Saadud katted näitasid iseloomulikke kahekihilist struktuuri, mis koosneb tihedast sisemisest barjäärkihist ja poorsast väliskihist. HAp nanoosakeste lisamine viis TiO_2 – Nb_2O_5 –Ca–P komposiitoksiidkatete tekkeni, millel oli

väiksem poorsus, suurem rutiilfaasi sisaldus ja parem kompaktsus. Bioloogilised katsed MC3T3 preosteoblast-rakkudega näitasid paremat rakkude adhesiooni, proliferatsiooni ja tsütoskeleti organiseerumist HAp-d sisaldavatel katetel. Suurenenud pinnakaredus, paranenud märguvus ja bioaktiivsete Ca^{2+} ja PO_4^{3-} ionide kontrollitud vabanemine soodustasid biomimeetilise pinnakeskkonna teket, mis on soodne varajase osseointegratsiooni jaoks.

Kokkuvõttes näitab käesolev väitekiri, et in-situ legerimise, ümbersulatamise abil saavutatud mikrostruktuuri kontrolli, Fe lisamisega tehtud sulami modifitseerimise ning PEO-põhise biofunktsionaliseerimise kombinatsioon parandab märkimisväärselt Ti-Nb-põhiste sulamite omadusi. Arendatud materjalid näitavad homogeniseeritud mikrostruktuuri, paremaid mehaanilisi omadusi, stabiilset passiivkäitumist ja paremat bioloogilist vastust. See integreeritud lähenemine pakub võimaluse järgmise põlvkonna β -Ti-Nb-põhiste implantaatide kavandamiseks ning toob esile SLM-il põhineva in-situ legerimise potentsiaali kuluefektiivsete ja kliiniliselt rakendatavate biomaterjalide arendamisel.

Appendix

Publication I

Subramanian, S., Mohanty, S., & Prashanth, K. G. (2023). Effect of process parameters on the properties of β -Ti-Nb-based alloys fabricated by selective laser melting: A review. *Materials Today: Proceedings*. doi: 10.1016/j.matpr.2023.03.461



ELSEVIER

Contents lists available at ScienceDirect

Materials Today: Proceedings

journal homepage: www.elsevier.com/locate/matpr

Effect of process parameters on the properties of β -Ti-Nb-based alloys fabricated by selective laser melting: A review

Shangavi Subramanian^a, Shalini Mohanty^a, KG Prashanth^{a,b,c,*}

^a Department of Mechanical and Industrial Engineering, Tallinn University of Technology, 19086 Tallinn, Estonia

^b Erich Schmid Institute of Materials Science, Austrian Academy of Sciences, A-8700 Leoben, Austria

^c CBCMT, School of Mechanical Engineering, Vellore Institute of Technology, Vellore 632 014, Tamil Nadu, India

ARTICLE INFO

Article history:
Available online xxx

Keywords:
 β -Ti-alloys
Additive manufacturing
Selective laser melting
Process parameters

ABSTRACT

Metallic materials based on Ti and its alloys are regarded as vital subject matter in biomedical applications owing to their superior properties like excellent biocompatibility, and good mechanical, and corrosion resistance. To instigate the efficiency and positive outcomes of the Ti-based implants, designing and production of patient-specific geometries are the prerequisites. Materials processed by the additive manufacturing technique called selective laser melting (SLM) are capable of fabricating complex designs without any constraints. The work presents a brief review of the SLM of Ti-Nb-based alloys used for biomedical implants. The recent advances involved in the processing of these sophisticated materials through SLM are discussed in this review article. The influence of different process parameters on the microstructural and mechanical properties of Ti-Nb implants is discussed along with an overview of various research work conducted so far. The potential applications of such implants are also described in this work along with the prospects of these alloys in biomedical industries.

© 2023 Elsevier Ltd. All rights reserved. Selection and peer-review under responsibility of the scientific committee of the International Conference on Materials and Manufacturing for Sustainable Developments – 2022.

1. Introduction

The ever-increasing demand for the replacement and repair of human hard tissues, such as hip and knee joints, tooth caps, bones, etc. because of accidental damages, genetic abnormalities, and other diseases with stringent requirements has kindled the development of biomedical implant materials in recent decades [1,2]. On average, about 70–80% of hard tissue prostheses are made of metallic materials [3,4]. These metallic materials used in biomedical applications must fulfil unique properties to serve their purpose [5]. These critical properties include biocompatibility, minimal toxicity, high strength, low modulus, good wear, and corrosion resistance [6]. Among the commercially available metallic materials, Ti-based alloys are extensively utilized as candidates for hard tissue prostheses due to their biocompatibility, strength, corrosion resistance, and longevity [7–10]. Based on the crystal structures at the equilibrium state, Ti-based alloys are differentiated into α , $\alpha + \beta$, and β -type alloys [11–13]. α -type pure Ti (cp-Ti) was the first

commercial Ti-based implant material available for biomedical application [14,15]. However, their usage was constrained due to their strength and wear resistance [16]. Pure Ti was alloyed with V and Al to further enhance the properties, and several grades of Ti6Al4V (Ti64) were concocted. The cp-Ti and Ti64 alloys unveiled high corrosion resistance as they form an inert oxide layer when placed in an oxidizing medium [6,17].

According to the American Society for Testing and Materials (ASTM) the Ti grades were specified from Grade 1 to Grade 5 based on the alloy composition, where Grade 1 represents the unalloyed cp-Ti and Grade 5 is the maximum alloyed Ti64. The mechanical properties of the different Grades are mentioned in Table 1 [5]. Regardless of their high corrosion resistance and biocompatible nature when implanted inside the human body, Ti64 still posed cytotoxic effects by the presence of Al and V [18,19]. Additionally, the elastic modulus of cp-Ti and Ti64 is higher than that of the human bone. The discrepancy in young's modulus value amid bone and implant triggers a stress shielding effect, instigating resorption of bone around the implant, eventually leads to loosening of the implant and further surgeries [20–22]. This paved way for the development of new β -type alloys, with low modulus to diminish the stress shielding effect by selecting alloying elements with less

* Corresponding author at: Department of Mechanical and Industrial Engineering, Tallinn University of Technology, 19086 Tallinn, Estonia.
E-mail address: kgprashanth@gmail.com (KG Prashanth).

<https://doi.org/10.1016/j.matpr.2023.03.461>

2214-7853/© 2023 Elsevier Ltd. All rights reserved. Selection and peer-review under responsibility of the scientific committee of the International Conference on Materials and Manufacturing for Sustainable Developments – 2022.

Table 1
Mechanical Properties of the Ti-based materials and Human Bone [5,22].

| Material | Specification | Yield Strength (MPa) | Elongation (%) | Elastic Modulus (GPa) |
|-----------------|-------------------|----------------------|----------------|-----------------------|
| CP-Ti | ASTM F67 Grade 1 | 170 | 24 | 103–107 |
| – | ASTM F67 Grade 2 | 275 | 20 | 103–107 |
| – | ASTM F67 Grade 3 | 380 | 18 | 103–107 |
| – | ASTM F67 Grade 4 | 483 | 15 | 103–107 |
| Ti6Al4V | ASTM F136 Grade 5 | 795 | 10 | 114–120 |
| Cortical Bone | – | 120–160 | 0.55–0.94 | 7–30 |
| Cancellous Bone | – | 1.75 | 0.78 | 0.3–4 |

or non-cytotoxicity like Nb, Zr, Sn, Ta, Mo, etc [23–26]. The first generation β -Ti-based materials comprehended Ti–13Nb–13Zr, Ti–35Nb–5Ta–7Zr, Ti–29Nb–13Ta–4.6Zr, Ti–12Mo–6Zr–2Fe [17,27–29]. Among the β stabilizers, Nb showed promising results by reducing stiffness and increasing corrosion resistance [30].

Numerous Additive Manufacturing (AM) techniques are available for the development of Ti-Nb-based alloys [31]. A few of the powder bed fusion methods include selective laser melting (SLM) or laser powder-bed fusion process (LPBF), electron beam melting (EBM), etc. where a majority of the research is focused on the parameter-microstructure-property optimization [32–34]. Among these techniques, SLM/LPBF is attracting much significance in recent years due to its ability to process a wide spectrum of materials [35–59]. Optimizing the process parameters have a direct influence on the microstructural and mechanical property of the final product [52,60–62]. It also facilitates the generation of complex structures that are patient specific involving minimal cost and wastage at a faster rate [63–65]. The foremost motivation of this work is to review the SLM process parameters and mechanical properties of the TiNb-based β alloys fabricated by SLM.

2. Fundamentals of SLM process and its parameters

SLM is a laser-based powder bed fusion process developed to fabricate 3D metal parts from metallic powders. The parts are built by means of layer-by-layer melting and consolidation of powder, laid over the built platform inside a closed chamber under a pro-

TECTIVE atmosphere [66,67]. The process is controlled by computer-aided design (CAD) software, through which the parts with required geometries are designed as 3D models. The major components of the SLM constitute a high-energy laser source, sample platform, powder feeder, a chamber with an inert atmosphere, and a software-aided system for designing CAD models. Fig. 1 represents the schematic representation of the SLM process, and the components associated with it. Generally, a single crystal of Nd:YAG or Yb:YAG is used as the source of the laser beam, which is focused over the powder bed via an optical and scanner system. The fabrication process involves several steps from developing the model to the separation of the finished product from the sample platform. In the initial step, the CAD model is designed in software and uploaded to the SLM machine. CAD models comprise details of the support structure and sliced data that act as guidelines for the laser over each layer. First, a layer of powder is uniformly spread as a thin layer over the platform. Upon this layer, a high-energy laser beam is focused on the predefined area, that melts and solidifies the powder as specified by the CAD design. The end of the laser scan completes the melting step at that layer and the platform moves downwards for the deposition of powder in the subsequent. For each consecutive formation of layers, the platform is displaced downwards at a fixed height and a detachable recoater or feeder spreads a uniform layer of required powder over the melted areas. Until the desired output is achieved, the process is repeated. Once the printing is finished, the unmelted powder is removed, and the part is detached from the substrate [68–70].

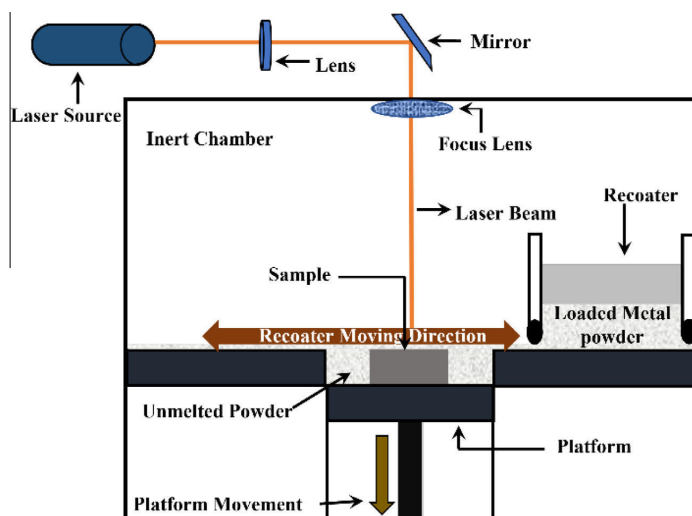


Fig. 1. Figures illustrating the basic components of the selective laser melting device [68].

The SLM process has many advantages over conventional manufacturing methods, including near-net-shape production, excellent material utilization rates, and the absence of geometrical restrictions, which enables the production of complex shapes without boundaries [71-73]. The key objective of the SLM process is to obtain maximum densification in bulk components/structures with improved functionalities. As no mechanical loading is applied during the process, only capillary force, gravity, and thermal effect act on the sample, which may lead to defects like porosity. Additionally, the mechanical property of the finished product depends on the microstructure and defects generated during the process, which is dictated by the process parameters [74,75]. To achieve a high degree of densification with minimal defects, it is mandatory to carefully optimize the process parameters. Currently, several parameters (Fig. 2) are available for optimization that are classified as pre-process, in-process, and post-process constraints [76,77]. Improper selection of parameters for a given alloy results either in defective samples or complete failure to print. The residual stresses generated during the solidification process act as the preferable sites for the initiation of cracks, which severely affects the properties of the product. The pre-process parameters include the powder properties including flowability, optical penetration, packing density, and thermal conductivity, which influence the properties of the final component. As the powder flow varies from machine to machine, the pre-process parameters are seldom conferred by the gap in information associated to pre-process parameters [77,78]. The in-process parameter is well demarcated (Fig. 3) with the aid of below mentioned volumetric energy density, E equation,

$$E = \frac{P}{(v \cdot t \cdot s)} \quad (1)$$

where P is the laser power in Watt, v is the scanning speed in mm/s, t is the layer thickness in mm and s is the hatch spacing in mm.

In general, to achieve a high-quality component, an optimum value of laser energy density is required [75]. This value varies from material to material and is based on their properties. With increasing energy density (by increasing the laser power and decreasing the scan speed) the product density and mechanical property of the parts may increase. Alternatively, when the laser power is decreased with increasing scan speed, the quality of the

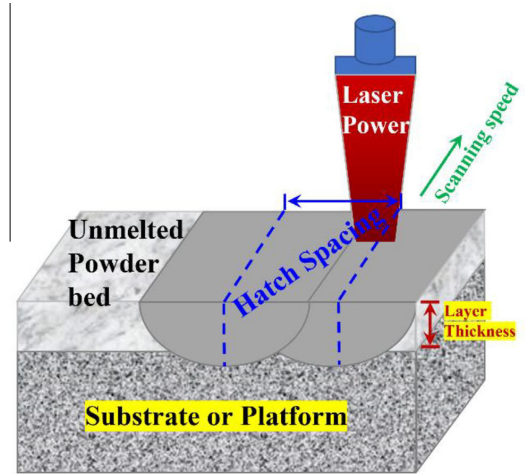


Fig. 3. Schematic representation illustrating the process parameters including scan speed, layer thickness, laser power and hatch spacing [77].

product is affected [75]. The most common defects formed during the process are keyhole porosity caused by the vaporization of particles due to overheating and balling effect (spheroidal beads formed because of insufficient wetting of preformed layers and surface tension). Irregularly shaped porosities will be formed if improper process parameter sets are used. The hatch spacing is explained as the distance between the centers of two subsequent laser scans having the least impact. The porosity and surface roughness of SLM-produced parts are greatly influenced by scan spacing, which controls the overlap of consecutive solidified tracks. To guarantee strong bonding between neighbouring tracks, the scan spacing should be carefully set. The layer thickness (t) indicates how much power is required and how long it will take to produce a layer of powder. Layer thickness is crucial because remelting previously processed layers is obligatory to achieve an adequate connection between layers [79-81]. Other significant fac-

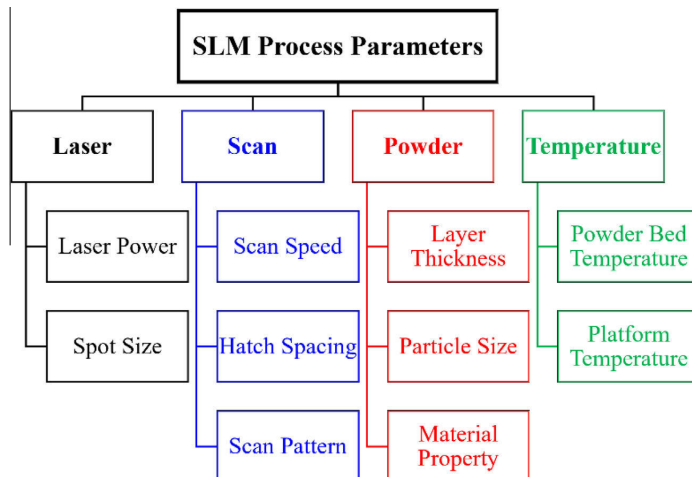


Fig. 2. Schematics illustrating the various process parameters involved during the production of parts using the selective laser melting process [77].

tors during the SLM process include the way in which the melting takes place (i.e.) the hatch style/scan style/hatch strategy. The pattern typically consists of parallel and straight lines with some possibility of circular and spiral coverage. The scan strategy/hatch strategy can be modified between single or consecutive layers based on the requirement. Generally, three different variations found are unidirectional, bidirectional, and zigzag. Furthermore, the scanning direction can be rotated to various angles between consecutive layers. These patterns impact the quality of processed parts [82,83].

3. Ti-based materials processed by SLM

Ti and its alloys are the second largely investigated material after Fe-based alloys due to their diverse applications in the biomedical (medical) and aerospace (structural) sectors. Due to its high reactivity and sensitivity to atmospheric elements like N, O, H, and C, processing Ti, and its alloys via a conventional method like casting is difficult and at the same time machining pure Ti is also a daunting task. In addition, the reduction and refining of Ti from its ores makes it an expensive metal. High production cost and criticality in producing complex structures made SLM an ideal route for fabricating Ti and its alloys [84]. Versatile properties of Ti like high strength, low modulus, and corrosion resistance enable their usage in numerous fields including aerospace, chemical industry, biomedical application, and so on. However, the low elastic modulus and high corrosion resistance of Ti alloys resulting in reduced cytotoxicity when implanted qualify for long-term usage in biomedical applications. Based on the alloying elements the properties of the material vary [6,82]. Cp-Ti and Ti64 are FDA-approved, and commercially available implant materials. Various studies influencing the mechanical and microstructural properties by varying the process parameters were investigated on cp-Ti and Ti64 materials. It is inferred that by varying the process parameters, the resulting microstructure is influenced, which directly affects the properties of the material. A study by H. Attar et al. on cp-Ti varied the laser power and laser scan speed in the range of 85 W to 165 W and 71 mm/s to 138 mm/s, respectively, to achieve parts with a relative density of $\sim 99.5\%$ [85]. The outcomes revealed that an optimal combination of process parameters can lead to parts with improved hardness, tensile and compressive strength with minimal porosity and detrimental effects as a result of the formation of α' martensitic grains [85]. Gu et al. worked on

the microstructural evolution of cp-Ti to achieve a fully dense parts with varying scanning speeds (200–300 mm/s [86]). Accordingly, the microstructure changes from initial coarse α grain to acicular α' martensite. Thijs et al. work on Ti64 showed improved hardness and strength for the SLM fabricated part as compared to the counterpart fabricated by conventional casting due to the formation of martensitic microstructure [72]. Other reports also show that the SLM fabricated Ti64 shows improved properties as compared to their cast counterparts [87–89]. Specific process parameters providing short interaction, high localization, and higher temperature gradient results in the formation of epitaxial martensitic phases. The toxic effect displayed by vanadium in Ti64 paved the way for the evolution of Ti-6Al-7Nb (Ti67) alloy with reduced toxicity [90,91]. Furthermore, to have a reduced stress shielding effect between bone and the implant, low Young's modulus is an additional prerequisite for an implant material. For this purpose, β -type Ti-Nb alloys possessing reduced Young's modulus values are studied intensively in the field of biomedical applications.

4. Microstructure and mechanical properties of β -type Ti-Nb alloys

Nb as an alloying element is an isomorphous β -phase stabilizer and aids in the prevention of the α phase formation by stabilizing the β -phase at room temperature. As α -phase is responsible for the higher modulus at room temperature, replacing it with β -phase will benefit in the drastic reduction of the modulus value [92,93]. Compared to other β -phase stabilizers Nb is found to have high strength and low modulus values, enabling them as a potential candidate for orthopaedic application [94,95]. The fraction of alloying elements influences the biomechanical properties of the final product by affecting their microstructure [96]. The biomechanical property of the implants plays a key role in its long-run in load-bearing applications. The elastic modulus between bone and implant should match to improve implant efficiency. By tuning the process parameters, the Young's modulus of desired value can be achieved (Fig. 4).

A set of Ti-45Nb was investigated by varying the process parameter to check the resulting changes in the nano hardness and Young's Modulus of the SLM fabricated parts. By varying laser power (60, 65, 70, 75, and 80 W) with 60 mm/s laser scan speed and by varying laser scan speed (40, 50, 60, and 70 mm/s) with a

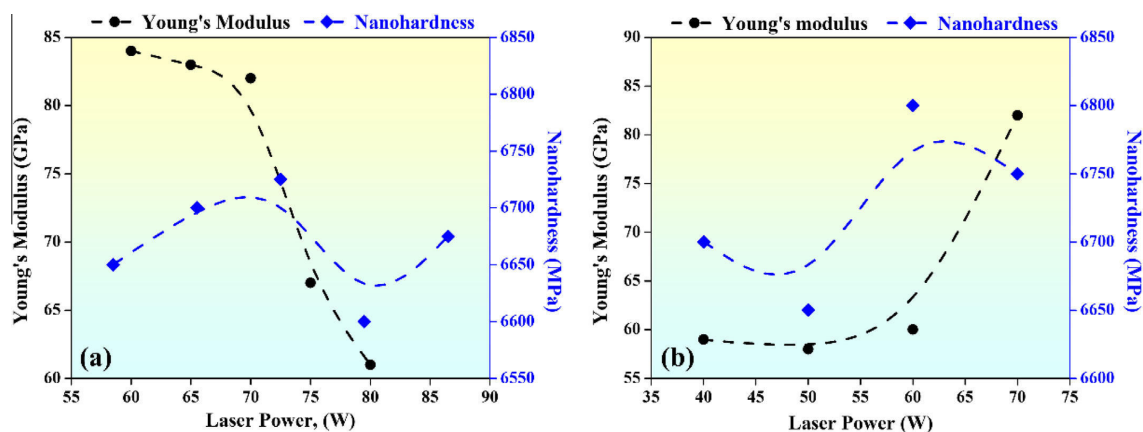


Fig. 4. Young's Modulus and nano hardness values of Ti-Nb specimens with the following process parameters: (a) 60 mm/s scan speed with varied power, and (b) 80 W with varied scan speed [97].

Table 2
Mechanical properties of several Ti-Nb alloys fabricated by selective laser melting.

| Alloy | Laser power (W) | Scan speed (mm/s) | Layer thickness (mm) | Hatch spacing (mm) | Device | Yield strength (MPa) | Young's Modulus (GPa) | Vickers Hardness (HV) | Elongation (%) | Post Processing (if any) |
|---------------------------------------|-----------------|-------------------|----------------------|--------------------|-------------------|---|--|-----------------------|------------------------------------|--|
| Ti-15Nb, Ti-25Nb, Ti-45Nb [96] | 330 | 1000 | 0.1 | 0.03 | EOS M280 SLM | 501 ± 30 516 ± 58 583 ± 67 | 24.3 ± 0.5 18.7 ± 1.4 24.5 ± 2.2 | - | - | - |
| Ti-20Nb [64] | 140 | 186 | 0.03 | 0.11 | TruPrint 1000 LMF | 769 ± 36 | 65.2 ± 1.8 | - | - | - |
| Ti-25Nb [104] | 210-330 | 1000 | 0.03 | 0.01 | Huake-250 SLM | 640 ± 15-645 ± 23 | 83.5 ± 0.8-88.7 ± 0.9 | 245 ± 2-264 ± 6 | 17.3 ± 2.8-20.7 ± 1.4 | - |
| Ti-26Nb [100] | 120-360 | 2500 | 0.03 | 0.01-0.1 | Realizer SLM 250 | - | 76.0-77.7 ± 0.2 | 268 | - | - |
| Ti-30Nb [105] | 200 | 450-500 | 0.05 | 0.11 | SLM 280 HL | Before HT - 894 After HT - 971 | - | 318 ± 13 326 ± 7 | - | Annealed at 1000 °C for 24 h under vacuum |
| Ti-35Nb [106] | 200 | 500 | 0.05 | 0.1 | Realizer SLM-100 | Before (HT) 648 ± 13 | 84 ± 2 | 274 ± 7 | 3.9 ± 1.1 | Post heat treatment (HT) (24 h, 1000 °C) |
| Ti-40Nb (meshes) [107] | 320 | 800 | 0.03 | 0.01 | - | After (HT) 602 ± 14 | 86 ± 2 | 311 ± 16 | 5.6 ± 1.9 | - |
| Ti-42Nb [108] | 300 | 300 | 0.03 | 0.06 | LPBF 280 | 567.5 ± 3.5 | 65.5 ± 0.2 | 310 ± 7 | 9.2 ± 0.5 | - |
| Ti-45Nb [109] | 150-250 | 35 | 0.01 | - | - | 1180 ± 40 | 56.7 ± 2 | ~192-~211 | - | - |
| Ti-13Nb-13Zr [27] | 325 | 1000 | 0.03 | 0.12 | SLM 250HL | 794 ± 15 | 65 | 211 | 5.0 ± 0.3 | - |
| Ti-24Zr-4Nb-8Sn [73] | 200 | 50-900 | 0.01 | - | SLM 250HL | 563 ± 38 | 53 ± 1 | - | 13.8 ± 4.1 | - |
| Ti-25Nb-3Zr-3Mo-2Sn [110] | 300 | 1000 | 0.05 | - | BLI-S300 SLM | 592 ± 21 | - | 202-230 | 37.0 ± 5.0 | - |
| Ti-30Nb-5Ti-8Zr (Lattices) [111] | 280 | 800 | - | - | EOS M290 | 12.5-67 | 0.7 to 4.4 | - | 5.7 | Stress-relieving annealing |
| Ti-33Nb-4Sn (Porous) [112] | 225 | 1200 | 0.03 | 0.05 | Farsoon 271 M | - | 1.8-2.3 | - | - | - |
| Ti-35Nb-7Zr-5Ti [113] | 100 | 167-250 | 0.05 | 0.08 | Realizer SLM 50 | ~630 | ~81 | - | ~15 | - |
| Ti-34.52Nb-6.91Zr-4.94Ta-1.26Si [114] | 250 | 1400 | 0.03 | 0.06 | SLM EOS M290 | Before HT - 1116 ± 25 | 71.3 ± 3.3 | - | 2.6 ± 0.8 | Heat treatment at different temperature (1150, 1200, 1250, 1300 and 1350 °C) for 30 min followed by quenching in ice water |
| Ti-37Nb-6Sn [101] | 225-350 | 800-1200 | 0.03 | 0.05-0.12 | Farsoon 271 M | 1150 °C - 959 ± 6 1200 °C - 978 ± 7 1250 °C - 1031 ± 4 1300 °C - 951 ± 14 1350 °C | 66.5 ± 5 64.2 ± 5.1 59.2 ± 2.2 | - | 5.7 ± 1.6 10.4 ± 2.0 7 ± 1.8 | - |
| Ti-2Re, Ti-4Re [115] | 400 | 1000 | 0.05 | 0.1 | Realizer II 250 | 956 ± 9 965 ± 85 | 70.8 ± 2 66 | - | 0.8 ± 0.1 27.5 | - |

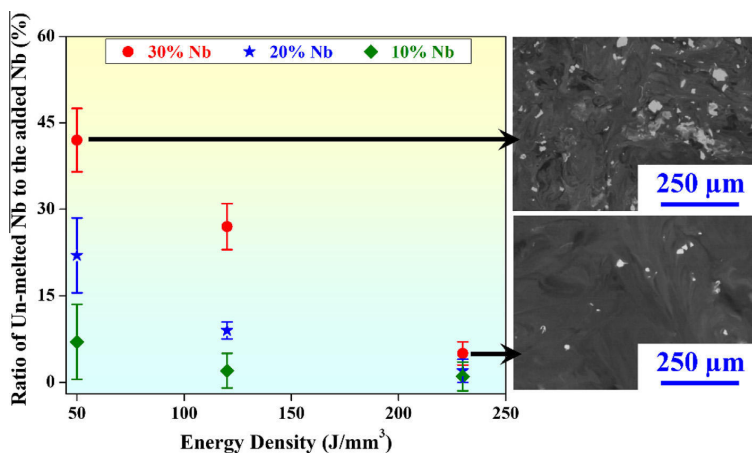


Fig. 5. Plot showing the relation between the energy density considered and the ration of the unmelted Nb particle retained to the added Nb (%).

constant laser power of 80 W was used with straight line strategy and a layer thickness of 0.05 mm. The obtained results depicted that the selected power and laser scan speed influence Young's modulus greatly. An average Young's modulus of 84 GPa was observed for the sample fabricated with power ranging between 60 and 70 W and further increase of laser power to 80 W, the value of Young's modulus decreases to 58 GPa. A similar average value of 58 GPa was obtained for the samples fabricated between the scanning speeds of 40–60 mm/s. Further increasing the scanning speed to 70 mm/s, Young's modulus surges to 82 GPa. This in turn demonstrated that a surge in Nb content decreases the Young's Modulus [97]. Mechanical properties of different TiNb alloys with respect to their process parameter is stated in Table 2. Microstructure study on Ti-Nb alloys exhibited primarily β -phase along with several martensitic phases like α' -(Nb < 13 wt%), α' -(Nb > 25 wt%) and ω - (hexagonal) along the grain boundaries, with varying wt.% of Nb and energy density. For samples processed with low energy density, residual Nb particles are observed, which is responsible for the presence of martensitic phases. Since Nb has a higher melting point than Ti, lower values of energy density may possibly leave unmelted Nb particles. With increasing energy density, a more homogeneous β -microstructure may be formed. The rapid cooling rate of SLM gives rise to dendritic structures formed along the build directions [98,99]. Several works inferred that increasing the Nb content increases the volume of the β phase, and the energy density value influences the resulting microstructure [85,96,100-103] (Fig. 5).

5. Conclusions

The present study is a brief review of the SLM processing of Ti-Nb β -based alloys intended for biomedical applications. It is evident that the process parameters play a key role in the resulting microstructural properties of the Ti-Nb alloy. The difference in the melting point between Ti and Nb gives rise to unmelted Nb particles distributed in the β grains. To achieve a more homogeneous microstructure, an optimum energy density value coupled with a slow scan rate should be utilized, so that sufficient time will be provided for the complete melting of Nb particle. Among the studied alloys, Titanium with 35–40% Nb is found to have the lowest Young's modulus value of ~50 MPa. The future scope of the work is to study the mechanical properties of the Ti-40 Nb alloy

post-heat treatment. It is expected to depict a much lower young's modulus value, that can be utilized in the hard tissue application.

Funding statement

The present work is funded by project ETAG21021.

CRediT authorship contribution statement

Shangavi Subramanian: Conceptualization, Writing – original draft, Data curation. **Shalini Mohanty:** Supervision, Writing – review & editing. **KG Prashanth:** Writing – review & editing, Validation, Project administration.

Declaration of Competing Interest

The authors declare that they have no known competing financial interests or personal relationships that could have appeared to influence the work reported in this paper.

References

- [1] M. Geetha, A.K. Singh, R. Asokamani, A.K. Gogia, Ti based biomaterials, the ultimate choice for orthopaedic implants – A review, *Prog. Mater. Sci.* 54 (2009) 397–425, <https://doi.org/10.1016/j.pmatsci.2008.06.004>.
- [2] A. Sumayli, Recent trends on bioimplant materials: A review, *Mater. Today: Proc.* 46 (2021) 2726–2731, <https://doi.org/10.1016/j.MATPR.2021.02.395>.
- [3] L. Kunčická, R. Kocich, T.C. Lowe, Advances in metals and alloys for joint replacement, *Prog. Mater. Sci.* 88 (2017) 232–280, <https://doi.org/10.1016/j.pmatsci.2017.04.002>.
- [4] A.T. Sidambe, Biocompatibility of advanced manufactured titanium implants-A review, *Materials* 7 (2014) 8168–8188, <https://doi.org/10.3390/ma7128168>.
- [5] C.N. Elias, J.H.C. Lima, R. Valiev, M.A. Meyers, *Biomedical applications of titanium and its alloys*, *Biol. Mater. Sci.* 46–49 (2008) 1–4.
- [6] D. Bombac, M. Brojan, P. Fajfar, F. Kosel, R. Turk, Review of materials in medical applications, *RMZ – Mater. Geoenviron.* 54 (2007) 471–499.
- [7] R.E. McMahon, J. Ma, S.V. Verkhoturov, D. Munoz-Pinto, I. Karaman, F. Rubitschek, H.J. Maier, M.S. Hahn, A comparative study of the cytotoxicity and corrosion resistance of nickel–titanium and titanium–niobium shape memory alloys, *Acta Biomater.* 8 (2012) 2863–2870, <https://doi.org/10.1016/j.actbio.2012.03.034>.
- [8] H. Matsuno, A. Yokoyama, F. Watari, M. Uo, T. Kawasaki, Biocompatibility and osteogenesis of refractory metal implants, titanium, hafnium, niobium, tantalum and rhenium, *Biomaterials* 22 (2001) 1253–1262, [https://doi.org/10.1016/S0142-9612\(00\)00275-1](https://doi.org/10.1016/S0142-9612(00)00275-1).
- [9] K. Prashanth, K. Zhuravleva, I. Okulov, M. Calin, J. Eckert, A. Gebert, Mechanical and Corrosion Behavior of New Generation Ti-45Nb Porous

- Alloys Implant Devices, Technologies (Basel) 4 (2016) 33, <https://doi.org/10.3390/technologies4040033>.
- [10] K. Zhuravleva, M. Bönisch, K.G. Prashanth, U. Hempel, A. Helth, T. Gemming, M. Calin, S. Scudino, L. Schultz, J. Eckert, A. Gebert, Production of Porous β -Type Ti-40Nb Alloy for Biomedical Applications: Comparison of Selective Laser Melting and Hot Pressing, *Materials* 6 (2013) 5700–5712, <https://doi.org/10.3390/ma6125700>.
- [11] M. Niinomi, Recent Research and Development in Metallic Materials for Biomedical, Dental and Healthcare Products Applications, *Mater. Sci. Forum* 539–543 (2007) 193–200, <https://doi.org/10.4028/www.scientific.net/MSF.539-543.193>.
- [12] J. Jakubowicz, Special Issue: Ti-Based Biomaterials: Synthesis, Properties and Applications, *Materials* 13 (2020) 1696, <https://doi.org/10.3390/MA13071696>.
- [13] M. Kaczmarek, K. Jurczyk, D. Purwin, J.K. Koper, A. Romaniuk, N. Lipinska, J. Jakubowicz, M.U. Jurczyk, Molecular analysis of biocompatibility of anodized titanium with deposited silver nanodendrites, *Mater. Sci. Eng. C* 93 (2018) 437–444, <https://doi.org/10.1016/j.msec.2018.08.001>.
- [14] H. Attar, K.G. Prashanth, L.C. Zhang, M. Calin, I.V. Okulov, S. Scudino, C. Yang, J. Eckert, Effect of powder particle shape on the properties of in situ Ti-TiB composite materials produced by selective laser melting, *J. Mater. Sci. Technol.* 31 (2015) 1001–1005, <https://doi.org/10.1016/j.jmst.2015.08.007>.
- [15] H. Attar, L. Löber, A. Funk, M. Calin, L.C. Zhang, K.G. Prashanth, S. Scudino, Y.S. Zhang, J. Eckert, Mechanical behavior of porous commercially pure Ti and Ti-TiB composite materials manufactured by selective laser melting, *Mater. Sci. Eng. A* 625 (2015) 350–356, <https://doi.org/10.1016/j.msea.2014.12.036>.
- [16] H. Attar, K.G. Prashanth, A.K. Chaubey, M. Calin, L.C. Zhang, S. Scudino, J. Eckert, Comparison of wear properties of commercially pure titanium prepared by selective laser melting and casting processes, *Mater. Lett.* 142 (2015) 38–41, <https://doi.org/10.1016/j.matlet.2014.11.156>.
- [17] M. Niinomi, T. Akahori, S. Katsura, K. Yamauchi, M. Ogawa, Mechanical characteristics and microstructure of drawn wire of Ti-29Nb-13Ta-4.6Zr for biomedical applications, *Mater. Sci. Eng. C* 27 (2007) 154–161, <https://doi.org/10.1016/j.msec.2006.04.008>.
- [18] F. Technique, R. Metals, T.T. Alloys, Q.C. Program, T.T. Alloys, X.F. Spectrometry, F. Technique, R. Metals, Q.C. Program, T.T. Alloys, F. Spectrometry, F. Technique, R. Metals, T.T. Alloys, A. Bar, ASTM F136 – Standard Specification for Wrought Titanium-6Aluminum-4Vanadium ELI (Extra Low Interstitial) Alloy for Surgical Implant Applications (UNS), (2012) 1–5, <https://doi.org/10.1520/F0136-12.2>.
- [19] E. Mueller, R. Kammula, D. Marlowe, Regulation of “Biomaterials” and Medical Devices, *MRS Bull.* 16 (1991) 39–41, <https://doi.org/10.1557/S0883769400056037>.
- [20] S. Arabnejad, B. Johnston, M. Tanzer, D. Pasini, Fully porous 3D printed titanium femoral stem to reduce stress-shielding following total hip arthroplasty, *J. Orthop. Res.* 35 (2017) 1774–1783, <https://doi.org/10.1002/jor.23445>.
- [21] I.D. Engler, P.-A. Hart, D.P. Swanson, J.M. Kirsch, J.P. Murphy, M.A. Wright, A. Murthi, A. Jawa, High prevalence of early stress shielding in stemless shoulder arthroplasty, *Semin. Arthroplasty: JSES* (2022) 6–11, <https://doi.org/10.1053/j.sart.2022.07.001>.
- [22] M. Niinomi, M. Nakai, Titanium-based biomaterials for preventing stress shielding between implant devices and bone, *Int. J. Biomater.* (2011), <https://doi.org/10.1155/2011/836587>.
- [23] M. Calin, L.C. Zhang, J. Eckert, Tailoring of microstructure and mechanical properties of a Ti-based bulk metallic glass-forming alloy, *Scr. Mater.* 57 (2007) 1101–1104, <https://doi.org/10.1016/j.scriptamat.2007.08.018>.
- [24] X. Chen, C. Qiu, Development of a novel metastable beta titanium alloy with ultrahigh yield strength and good ductility based on laser powder bed fusion, *Addit. Manuf.* 49 (2022), <https://doi.org/10.1016/j.addma.2021.102501>.
- [25] L. Chen, Y. Cui, L. Zhang, Recent Development in Beta Titanium Alloys for, (2020).
- [26] D. Eylon, A. Vassel, Y. Combres, R.R. Boyer, P.J. Bania, R.W. Schutz, Issues in the development of beta titanium alloys, *JOM* 46 (1994) 14–15, <https://doi.org/10.1007/BF03220741>.
- [27] L. Zhou, T. Yuan, R. Li, J. Tang, M. Wang, F. Mei, Anisotropic mechanical behavior of biomedical Ti-13Nb-13Zr alloy manufactured by selective laser melting, *J. Alloys Compd.* 762 (2018) 289–300, <https://doi.org/10.1016/j.jallcom.2018.05.179>.
- [28] S. Nag, R. Banerjee, H.L. Fraser, Microstructural evolution and strengthening mechanisms in Ti-Nb-Zr-Ta, Ti-Mo-Zr-Fe and Ti-15Mo biocompatible alloys, *Mater. Sci. Eng. C* 25 (2005) 357–362, <https://doi.org/10.1016/j.msec.2004.12.013>.
- [29] D. Kuroda, H. Kawasaki, A. Yamamoto, S. Hiromoto, T. Hanawa, Mechanical properties and microstructures of new Ti-Fe-Ta and Ti-Fe-Ta-Zr system alloys, *Mater. Sci. Eng. C* 25 (2005) 312–320, <https://doi.org/10.1016/j.msec.2005.04.004>.
- [30] B. Yuan, B. Yang, Y. Gao, M. Lai, X.H. Chen, M. Zhu, Achieving ultra-high superelasticity and cyclic stability of biomedical Ti-11Nb-40 (at.%) alloys by controlling Nb and oxygen content, *Mater. Des.* 92 (2016) 978–982, <https://doi.org/10.1016/j.matdes.2015.12.148>.
- [31] P.K. Gokuldoss, S. Kolla, J. Eckert, Additive Manufacturing Processes: Selective Laser Melting, Electron Beam Melting and Binder Jetting—Selection Guidelines, *Materials* 10 (2017) 672, <https://doi.org/10.3390/ma10060672>.
- [32] K.G. Prashanth, S. Scudino, J. Eckert, Defining the tensile properties of Al-12Si parts produced by selective laser melting, *Acta Mater.* 126 (2017) 25–35, <https://doi.org/10.1016/j.actamat.2016.12.044>.
- [33] D. Herzog, V. Seyda, E. Wycisk, C. Emmelmann, Additive manufacturing of metals, *Acta Mater.* 117 (2016) 371–392, <https://doi.org/10.1016/j.actamat.2016.07.019>.
- [34] G. Pyka, G. Kerckhofs, I. Papantoniou, M. Speirs, J. Schrooten, M. Wevers, Surface roughness and morphology customization of additive manufactured open porous Ti6Al4V structures, *Materials* 6 (2013) 4737–4757, <https://doi.org/10.3390/ma6104737>.
- [35] D. Kumar, G. Shankar, K.G. Prashanth, S. Suwas, Texture dependent strain hardening in additively manufactured stainless steel 316L, *Mater. Sci. Eng. A* 820 (2021), <https://doi.org/10.1016/j.msea.2021.141483>.
- [36] D. Kumar, S. Jhavar, A. Arya, K.G. Prashanth, S. Suwas, Mechanisms controlling fracture toughness of additively manufactured stainless steel 316L, *Int. J. Fract.* 235 (2022) 61–78, <https://doi.org/10.1007/s10704-021-00574-3>.
- [37] H. Chen, T. Lu, Y. Wang, Y. Liu, T. Shi, K.G. Prashanth, K. Kosiba, Laser additive manufacturing of nano-TiC particles reinforced CoCrFeMnNi high-entropy alloy matrix composites with high strength and ductility, *Mater. Sci. Eng. A* 833 (2022), <https://doi.org/10.1016/j.msea.2021.142512>.
- [38] J. Karimi, P. Ma, Y.D. Jia, K.G. Prashanth, Linear patterning of high entropy alloy by additive manufacturing, *Manuf. Lett.* 24 (2020) 9–13, <https://doi.org/10.1016/j.mfglet.2020.03.003>.
- [39] R. Rahmani, N. Kamboj, M. Brojan, M. Antonov, K.G. Prashanth, Hybrid metal-ceramic biomaterials fabricated through powder bed fusion and powder metallurgy for improved impact resistance of craniofacial implants, *Materialia (Oxf)* 24 (2022), <https://doi.org/10.1016/j.mtla.2022.101465>.
- [40] S. Tang, R. Ummethala, C. Suryanarayana, J. Eckert, K.G. Prashanth, Z. Wang, Additive Manufacturing of Aluminum-Based Metal Matrix Composites—A Review, *Adv. Eng. Mater.* 23 (2021) 2100053, <https://doi.org/10.1002/adem.202100053>.
- [41] Y.D. Jia, L.B. Zhang, P. Ma, S. Scudino, G. Wang, J. Yi, J. Eckert, K.G. Prashanth, Thermal expansion behavior of Al-XSi alloys fabricated using selective laser melting, *Progress Addit. Manuf.* 5 (2020) 247–257, <https://doi.org/10.1007/s40964-020-00130-w>.
- [42] K.G. Prashanth, S. Scudino, Quasicrystalline Composites by Additive Manufacturing, *Key Eng. Mater.* 818 (2019) 72–76, <https://doi.org/10.4028/www.scientific.net/KEM.818.72>.
- [43] K.G. Prashanth, Processing of Al-based composite material by selective laser melting: A perspective, *Mater. Today: Proc.* 57 (2022) 498–504, <https://doi.org/10.1016/j.matpr.2022.01.391>.
- [44] K. Prashanth, S. Scudino, R. Chatterjee, O. Salman, J. Eckert, Additive Manufacturing: Reproducibility of Metallic Parts, *Technologies (Basel)* 5 (2017) 8, <https://doi.org/10.3390/technologies5010008>.
- [45] K.G. Prashanth, Z. Wang, Additive Manufacturing: Alloy Design and Process Innovations, *Materials* 13 (2020) 542, <https://doi.org/10.3390/ma13030542>.
- [46] C. Zhao, Z. Wang, D. Li, M. Xie, L. Kollo, Z. Luo, W. Zhang, K.G. Prashanth, Comparison of additively manufacturing samples fabricated from pre-alloyed and mechanically mixed powders, *J. Alloys Compd.* 830 (2020), <https://doi.org/10.1016/j.jallcom.2020.154603>.
- [47] P. Konda Gokuldoss, Design of next-generation alloys for additive manufacturing, *Mater. Design Process. Commun.* 1 (2019) 19–22, <https://doi.org/10.1002/mdp2.50>.
- [48] S. Scudino, C. Unterdörfer, K.G. Prashanth, H. Attar, N. Ellendt, V. Uhlenwinkel, J. Eckert, Additive manufacturing of Cu–10Sn bronze, *Mater. Lett.* 156 (2015) 202–204, <https://doi.org/10.1016/j.matlet.2015.05.076>.
- [49] S. Singh, A.N. Jinoop, G.T.A.V.T. Kumar, A. Shukla, I.A. Palani, N. Resnina, C.P. Paul, K.G. Prashanth, Laser Hybrid Wire Arc Additive Manufacturing for Fabricating Thin Sections, *Trans. Indian Natl. Acad. Eng.* 7 (2022) 175–183, <https://doi.org/10.1007/s41403-021-00258-3>.
- [50] Z. Wang, S.Y. Tang, S. Scudino, Y.P. Ivanov, R.T. Qu, D. Wang, C. Yang, W.W. Zhang, A.L. Greer, J. Eckert, K.G. Prashanth, Additive manufacturing of a martensitic Co–Cr–Mo alloy: Towards circumventing the strength–ductility trade-off, *Addit. Manuf.* 37 (2021), <https://doi.org/10.1016/j.addma.2020.101725>.
- [51] N. Kamboj, M.A. Rodriguez, R. Rahmani, K.G. Prashanth, I. Hussainova, Bioceramic scaffolds by additive manufacturing for controlled delivery of the antibiotic vancomycin, *Proc. Est. Acad. Sci.* 68 (2019) 185, <https://doi.org/10.3176/proc.2019.2.10>.
- [52] H.S. Maurya, K.A. Juhani, F. Sergejev, K.G. Prashanth, Additive manufacturing of TiC-based cermet with stainless steel as a binder material, *Mater. Today: Proc.* 57 (2022) 824–828, <https://doi.org/10.1016/j.matpr.2022.02.428>.
- [53] S. Singh, A.N. Jinoop, I.A. Palani, C.P. Paul, K.P. Tomar, K.G. Prashanth, Microstructure and mechanical properties of NiTiSS bimetallic structures built using Wire Arc Additive Manufacturing, *Mater. Lett.* 303 (2021), <https://doi.org/10.1016/j.matlet.2021.130499>.
- [54] R. Rahmani, M. Brojan, M. Antonov, K.G. Prashanth, Perspectives of metal-diamond composites additive manufacturing using SLM-SPS and other techniques for increased wear-impact resistance, *Int. J. Refract. Metals Hard Mater.* 88 (2020), <https://doi.org/10.1016/j.jrmhm.2020.105192>.
- [55] H.S. Maurya, K. Kosiba, K. Juhani, F. Sergejev, K.G. Prashanth, Effect of powder bed preheating on the crack formation and microstructure in ceramic matrix composites fabricated by laser powder-bed fusion process, *Addit. Manuf.* 58 (2022), <https://doi.org/10.1016/j.addma.2022.103013>.
- [56] K.G. Prashanth, H. Shakur Shahabi, H. Attar, V.C. Srivastava, N. Ellendt, V. Uhlenwinkel, J. Eckert, S. Scudino, Production of high strength

- A185Nd8Ni5Co2 alloy by selective laser melting, *Addit. Manuf.* 6 (2015) 1–5, <https://doi.org/10.1016/j.addma.2015.01.001>.
- [57] P. Hameed, C.-F. Liu, R. Ummethala, N. Singh, H.-H. Huang, G. Manivasagam, K.G. Prashanth, Biomorphic porous Ti6Al4V gyroid scaffolds for bone implant applications fabricated by selective laser melting, *Progr. Addit. Manuf.* 6 (2021) 455–469, <https://doi.org/10.1007/s40964-021-00210-5>.
- [58] R. Sokkalingam, K. Sivaprasad, N. Singh, V. Muthupandi, P. Ma, Y.D. Jia, K.G. Prashanth, Subtle change in the work hardening behavior of fcc materials processed by selective laser melting, *Progr. Addit. Manuf.* 7 (2022) 453–461, <https://doi.org/10.1007/s40964-022-00301-x>.
- [59] R.J. Vikram, L. Kollo, K.G. Prashanth, S. Suwas, Investigating the Structure, Microstructure, and Texture in Selective Laser-Melted Sterling Silver 925, *Metall. Mater. Trans. A* 52 (2021) 5329–5341, <https://doi.org/10.1007/S11661-021-06471-7/FIGURES/11>.
- [60] H.S. Maurya, L. Kollo, K. Juhani, F. Sergejev, K.G. Prashanth, Effect of preheating and cooling of the powder bed by laser pulse shaping on the microstructure of the TiC based ceramets, *Ceram. Int.* (2022), <https://doi.org/10.1016/j.ceramint.2022.04.029>.
- [61] H.S. Maurya, L. Kollo, M. Tarraste, K. Juhani, F. Sergejev, K. Gokuldoss Prashanth, Effect of the Laser Processing Parameters on the Selective Laser Melting of TiC-Fe-Based Ceramets, *J. Manuf. Mater. Process.* 6 (2022) 35, <https://doi.org/10.3390/JMMP6020035>.
- [62] H.S. Maurya, L. Kollo, M. Tarraste, K. Juhani, F. Sergejev, K.G. Prashanth, Selective Laser Melting of TiC-Fe via Laser Pulse Shaping: Microstructure and Mechanical Properties, (2021), <https://www.liebertpub.com/doi/abs/10.1089/3dp.2021.0221> (accessed January 7, 2022).
- [63] A.A. Saprykin, Y.P. Sharkeev, E.A. Ibragimov, E.V. Babakova, D.V. Dudikhin, Forming a single layer of a composite powder based on the Ti-Nb system via selective laser melting (SLM), *IOP Conf. Ser. Mater. Sci. Eng.* 140 (2016), <https://doi.org/10.1088/1757-899X/140/1/012001>.
- [64] J.M. Borgman, J. Wang, L. Zani, P.P. Conway, C. Torres-Sanchez, The Effect of Energy Density and Nb Content on the Microstructure and Mechanical Properties of Selective Laser Melted Ti-(10–30 wt.%) Nb, *J. Mater. Eng. Perform.* 30 (2021) 8771–8783, <https://doi.org/10.1007/s11665-021-06239-5>.
- [65] K. Prashanth, L. Löber, H.-J. Klaus, U. Kühn, J. Eckert, Characterization of 316L Steel Cellular Dodecahedron Structures Produced by Selective Laser Melting, *Technologies (Base)* 4 (2016) 34, <https://doi.org/10.3390/technologies4040034>.
- [66] D.D. Gu, W. Meiners, K. Wissenbach, R. Poprawe, Laser additive manufacturing of metallic components: materials, processes and mechanisms, *Int. Mater. Rev.* 57 (2012) 133–164, <https://doi.org/10.1179/1743280411Y.0000000014>.
- [67] C.Y. Yap, C.K. Chua, Z.L. Dong, Z.H. Liu, D.Q. Zhang, L.E. Loh, S.L. Sing, Review of selective laser melting: Materials and applications, *Appl. Phys. Rev.* 2 (2015), <https://doi.org/10.1063/1.4935926>.
- [68] N. Singh, P. Hameed, R. Ummethala, G. Manivasagam, K.G. Prashanth, J. Eckert, Selective laser manufacturing of Ti-based alloys and composites: impact of process parameters, application trends, and future prospects, *Mater. Today Adv.* 8 (2020), <https://doi.org/10.1016/j.mtadv.2020.100097>.
- [69] J.P. Kruth, P. Mercelis, J. van Vaerenbergh, L. Froyen, M. Rombouts, Binding mechanisms in selective laser sintering and selective laser melting, *Rapid Prototyp. J.* 11 (2005) 26–36, <https://doi.org/10.1108/13552540510573365>.
- [70] K.G. Prashanth, Selective laser melting: Materials and applications, *J. Manuf. Mater. Process.* 4 (2020) 15–17, <https://doi.org/10.3390/jmmp4010013>.
- [71] K.G. Prashanth, S. Scudino, H.J. Klaus, K.B. Surreddi, L. Löber, Z. Wang, A.K. Chaubey, U. Kühn, J. Eckert, Microstructure and mechanical properties of Al-12Si produced by selective laser melting: Effect of heat treatment, *Mater. Sci. Eng. A* 590 (2014) 153–160, <https://doi.org/10.1016/j.msea.2013.10.023>.
- [72] L. Thijs, F. Verhaeghe, T. Craeghs, J. Van Humbeeck, J.-P. Kruth, A study of the microstructural evolution during selective laser melting of Ti-6Al-4V, *Acta Mater.* 58 (2010) 3303–3312, <https://doi.org/10.1016/j.actamat.2010.02.004>.
- [73] L.C. Zhang, D. Klemm, J. Eckert, Y.L. Hao, T.B. Sercombe, Manufacture by selective laser melting and mechanical behavior of a biomedical Ti-24Nb-4Zr-8Sn alloy, *Scr. Mater.* 65 (2011) 21–24, <https://doi.org/10.1016/j.scriptamat.2011.03.024>.
- [74] J.P. Kruth, M. Badrossamay, E. Yasa, J. Deckers, L. Thijs, J. Van Humbeeck, Part and material properties in selective laser melting of metals, 16th International Symposium on Electromachining, ISEM 2010, (2010) 3–14, <https://doi.org/978-7-313-05630-6>.
- [75] K.G. Prashanth, S. Scudino, T. Maity, J. Das, J. Eckert, Is the energy density a reliable parameter for materials synthesis by selective laser melting?, *Mater. Res. Lett.* 5 (2017) 386–390, <https://doi.org/10.1080/21663831.2017.1299808>.
- [76] H. Shipley, D. McDonnell, M. Culleton, R. Coull, R. Lupoi, G. O'Donnell, D. Trimble, Optimisation of process parameters to address fundamental challenges during selective laser melting of Ti-6Al-4V: A review, *Int. J. Mach. Tool Manuf.* 128 (2018) 1–20, <https://doi.org/10.1016/j.jmactools.2018.01.003>.
- [77] L.C. Zhang, H. Attar, M. Calin, J. Eckert, Review on manufacture by selective laser melting and properties of titanium based materials for biomedical applications, *Maney Publishing* (2016), <https://doi.org/10.1179/175355715Y.0000000076>.
- [78] A.T. Sutton, C.S. Kriewall, M.C. Leu, J.W. Newkirk, Powder characterisation techniques and effects of powder characteristics on part properties in powder-bed fusion processes, <http://dx.doi.org/10.1080/17452759.2016.1250605> 12 (2016) 3–29, <https://doi.org/10.1080/17452759.2016.1250605>.
- [79] J. Karimi, C. Suryanarayana, I. Okulov, K.G. Prashanth, Selective laser melting of Ti6Al4V: Effect of laser re-melting, *Mater. Sci. Eng. A* 805 (2020), <https://doi.org/10.1016/j.msea.2020.140558>.
- [80] J. Karimi, M. Antonov, L. Kollo, K.G. Prashanth, Role of laser remelting and heat treatment in mechanical and tribological properties of selective laser melted Ti6Al4V alloy, *J. Alloys Compd.* 897 (2022), <https://doi.org/10.1016/j.jallcom.2021.163207>.
- [81] J. Karimi, M.S. Xie, Z. Wang, K.G. Prashanth, Influence of substructures on the selective laser melted Ti-6Al-4V alloy as a function of laser re-melting, *J. Manuf. Process.* 68 (2021) 1387–1394, <https://doi.org/10.1016/j.jmapro.2021.06.059>.
- [82] L.-C. Zhang, H. Attar, Selective Laser Melting of Titanium Alloys and Titanium Matrix Composites for Biomedical Applications: A Review, *Adv. Eng. Mater.* 18 (2016) 463–475, <https://doi.org/10.1002/adem.201500419>.
- [83] P.A. Kulkarni, R.J. Berry, M.S.A. Bradley, Review of the flowability measuring techniques for powder metallurgy industry, <http://dx.doi.org/10.1243/09544089JPM2E99>, 224 (2010) 159–168, <https://doi.org/10.1243/09544089JPM2E99>.
- [84] T.B. Sercombe, L.-C. Zhang, S. Li, Y. Hao, Additive manufacturing of cp-Ti, Ti-6Al-4V and Ti2448, in: *Titanium in Medical and Dental Applications*, Elsevier, 2018, pp. 303–324, <https://doi.org/10.1016/B978-0-12-812456-7.00014-7>.
- [85] H. Attar, M. Calin, L.C. Zhang, S. Scudino, J. Eckert, Manufacture by selective laser melting and mechanical behavior of commercially pure titanium, *Mater. Sci. Eng. A* 593 (2014) 170–177, <https://doi.org/10.1016/j.msea.2013.11.038>.
- [86] A.V. Polyakov, L. Dluhoš, G.S. Dyakonov, G.I. Raab, R.Z. Valiev, Recent Advances in Processing and Application of Nanostructured Titanium for Dental Implants, *Adv. Eng. Mater.* 17 (2015) 1869–1875, <https://doi.org/10.1002/adem.201500212>.
- [87] K.G. Prashanth, R. Damodaram, T. Maity, P. Wang, J. Eckert, Friction welding of selective laser melted Ti6Al4V parts, *Mater. Sci. Eng. A* 704 (2017) 66–71, <https://doi.org/10.1016/j.msea.2017.08.004>.
- [88] N. Singh, R. Ummethala, P.S.P.S. Karamched, R. Sokkalingam, V. Gopal, G. Manivasagam, K.G.K.G. Prashanth, Spark plasma sintering of Ti6Al4V metal matrix composites: Microstructure, mechanical and corrosion properties, *J. Alloys Compd.* 865 (2021), <https://doi.org/10.1016/j.jallcom.2021.158875>.
- [89] P.T. Qin, R. Damodaram, T. Maity, W.W. Zhang, C. Yang, Z. Wang, K.G. Prashanth, Friction welding of electron beam melted Ti-6Al-4V, *Mater. Sci. Eng. A* 761 (2019), <https://doi.org/10.1016/j.msea.2019.138045>.
- [90] T. Marcu, M. Todea, I. Gligor, P. Berce, C. Popa, Effect of surface conditioning on the flowability of Ti6Al7Nb powder for selective laser melting applications, *Appl. Surf. Sci.* 258 (2012) 3276–3282, <https://doi.org/10.1016/j.apsusc.2011.11.081>.
- [91] E. Chlebus, B. Kuźnicka, T. Kurzynowski, B. Dybala, Microstructure and mechanical behaviour of Ti-6Al-7Nb alloy produced by selective laser melting, *Mater. Charact.* 62 (2011) 488–495, <https://doi.org/10.1016/j.matchar.2011.03.006>.
- [92] Y.-H. Hon, J.-Y. Wang, Y.-N. Pan, Composition/Phase Structure and Properties of Titanium-Niobium Alloys, *Mater. Trans.* 44 (2003) 2384–2390, <https://doi.org/10.2320/matertrans.44.2384>.
- [93] A. Biesiekierski, J. Wang, M. Abdel-Hady Gepreel, C. Wen, A new look at biomedical Ti-based shape memory alloys, *Acta Biomater.* 8 (2012) 1661–1669, <https://doi.org/10.1016/j.actbio.2012.01.018>.
- [94] D.C. Zhang, Y.F. Mao, Y.L. Li, J.J. Li, M. Yuan, J.G. Lin, Effect of ternary alloying elements on microstructure and superelasticity of Ti-Nb alloys, *Mater. Sci. Eng. A* 559 (2013) 706–710, <https://doi.org/10.1016/j.msea.2012.09.012>.
- [95] S. Luo, Y. Su, Z. Wang, Tailored microstructures and strengthening mechanisms in an additively manufactured dual-phase high-entropy alloy via selective laser melting, *Sci. China Mater.* 63 (2020) 1279–1290, <https://doi.org/10.1007/s40843-020-1291-9>.
- [96] Q. Wang, C. Han, T. Choma, Q. Wei, C. Yan, B. Song, Y. Shi, Effect of Nb content on microstructure, property and in vitro apatite-forming capability of Ti-Nb alloys fabricated via selective laser melting, *Mater. Des.* 126 (2017) 268–277, <https://doi.org/10.1016/j.matdes.2017.04.026>.
- [97] Z.G. Kovalevskaia, M.A. Khimich, A.V. Belyakov, Evaluation of Physicomechanical Properties of Ti-45Nb Specimens Obtained by Selective Laser Melting, *Key Eng. Mater.* 743 (2017) 9–12, <https://doi.org/10.4028/www.scientific.net/KEM.743.9>.
- [98] H.Y. Jung, S.J. Choi, K.G. Prashanth, M. Stoica, S. Scudino, S. Yi, U. Kühn, D.H. Kim, K.B. Kim, J. Eckert, Fabrication of Fe-based bulk metallic glass by selective laser melting: A parameter study, *Mater. Des.* 86 (2015) 703–708, <https://doi.org/10.1016/j.matdes.2015.07.145>.
- [99] C. Zhao, Z. Wang, D. Li, L. Kollo, Z. Luo, W. Zhang, K.G. Prashanth, Cu-Ni-Sn alloy fabricated by melt spinning and selective laser melting: a comparative study on the microstructure and formation kinetics, *J. Mater. Res. Technol.* 9 (2020) 13097–13105, <https://doi.org/10.1016/j.jmrt.2020.09.047>.
- [100] M. Fischer, D. Jougat, G. Robin, L. Peltier, P. Laheurte, In situ elaboration of a binary Ti-26Nb alloy by selective laser melting of elemental titanium and niobium mixed powders, *Mater. Sci. Eng. C* 62 (2016) 852–859, <https://doi.org/10.1016/j.msec.2016.02.033>.
- [101] W. Chen, C. Chen, X. Zi, X. Cheng, X. Zhang, Y.C. Lin, K. Zhou, Controlling the microstructure and mechanical properties of a metastable β titanium alloy by selective laser melting, *Mater. Sci. Eng. A* 726 (2018) 240–250, <https://doi.org/10.1016/j.msea.2018.04.087>.



- [102] C. Schulze, M. Weinmann, C. Schweigel, O. Keßler, R. Bader, Mechanical Properties of a Newly Additive Manufactured Implant Material Based on Ti-42Nb, *Materials* 11 (2018) 124, <https://doi.org/10.3390/ma11010124>.
- [103] Z. Kovalevskaya, Y. Sharkeev, M. Khimich, E. Parilov, I. Glukhov, E. Komarova, The investigation of the influence of formation conditions on the structure of Ti-40Nb alloy, in: *AIP Conf Proc*, 2016; p. 030010. <https://doi.org/10.1063/1.4964548>.
- [104] D. Zhao, C. Han, J. Li, J. Liu, Q. Wei, In situ fabrication of a titanium-niobium alloy with tailored microstructures, enhanced mechanical properties and biocompatibility by using selective laser melting, *Mater. Sci. Eng. C* 111 (2020), <https://doi.org/10.1016/j.msec.2020.110784>.
- [105] I. Vonavkova, D. Vojtech, D. Palousek, Characterization of β -Ti alloy prepared by SLM method, *Manuf. Technol.* 20 (2020) 690–696, <https://doi.org/10.21062/mft.2020.091>.
- [106] J. Wang, Y. Liu, C.D. Rabadia, S.-X. Liang, T.B. Sercombe, L.-C. Zhang, Microstructural homogeneity and mechanical behavior of a selective laser melted Ti-35Nb alloy produced from an elemental powder mixture, *J. Mater. Sci. Technol.* 61 (2021) 221–233, <https://doi.org/10.1016/j.jmst.2020.05.052>.
- [107] D. Zhao, H. Dong, Y. Niu, W. Fan, M. Jiang, K. Li, Q. Wei, W.M. Palin, Z. Zhang, Electrophoretic deposition of novel semi-permeable coatings on 3D-printed Ti-Nb alloy meshes for guided alveolar bone regeneration, *Dent. Mater.* 38 (2022) 431–443, <https://doi.org/10.1016/j.dental.2021.12.026>.
- [108] H. Ben Boubaker, P. Laheurte, G. Le Coz, S.-S. Biraie, P. Didier, P. Lohmuller, A. Moufki, Impact of the Loading Conditions and the Building Directions on the Mechanical Behavior of Biomedical β -Titanium Alloy Produced In Situ by Laser-Based Powder Bed Fusion, *Materials* 15 (2022) 509, <https://doi.org/10.3390/ma15020509>.
- [109] H. Schwab, K. Prashanth, L. Löber, U. Kühn, J. Eckert, Selective Laser Melting of Ti-45Nb Alloy, *Metals (Basel)* 5 (2015) 686–694, <https://doi.org/10.3390/met5020686>.
- [110] Y.J. Liu, Y.S. Zhang, L.C. Zhang, Transformation-induced plasticity and high strength in beta titanium alloy manufactured by selective laser melting, *Materialia (Oxf)* 6 (2019), <https://doi.org/10.1016/j.mtla.2019.100299>.
- [111] J.P. Luo, Y.J. Huang, J.Y. Xu, J.F. Sun, M.S. Dargusch, C.H. Hou, L. Ren, R.Z. Wang, T. Ebel, M. Yan, Additively manufactured biomedical Ti-Nb-Ta-Zr lattices with tunable Young's modulus: Mechanical property, biocompatibility, and proteomics analysis, *Mater. Sci. Eng. C* 114 (2020), <https://doi.org/10.1016/j.MSEC.2020.110903>.
- [112] X. Cheng, S. Liu, C. Chen, W. Chen, M. Liu, R. Li, X. Zhang, K. Zhou, Microstructure and mechanical properties of additive manufactured porous Ti-33Nb-4Sn scaffolds for orthopaedic applications, *J. Mater. Sci. – Mater. Med.* 30 (2019) 91, <https://doi.org/10.1007/s10856-019-6292-0>.
- [113] R. Ummethala, P.S. Karamched, S. Rathinavelu, N. Singh, A. Aggarwal, K. Sun, E. Ivanov, L. Kollo, I. Okulov, J. Eckert, K.G. Prashanth, Selective laser melting of high-strength, low-modulus Ti-35Nb-7Zr-5Ta alloy, *Materialia (Oxf)* 14 (2020), <https://doi.org/10.1016/j.mtla.2020.100941>.
- [114] X. Luo, L.H. Liu, C. Yang, H.Z. Lu, H.W. Ma, Z. Wang, D.D. Li, L.C. Zhang, Y.Y. Li, Overcoming the strength–ductility trade-off by tailoring grain-boundary metastable Si-containing phase in β -type titanium alloy, *J. Mater. Sci. Technol.* 68 (2021) 112–123, <https://doi.org/10.1016/j.jmst.2020.06.053>.
- [115] K. Majchrowicz, Z. Pakieła, T. Brynk, B. Romelczyk-Baishya, M. Płocińska, T. Kurzynowski, E. Chlebus, Microstructure and mechanical properties of Ti–Re alloys manufactured by selective laser melting, *Mater. Sci. Eng. A* 765 (2019), <https://doi.org/10.1016/j.msea.2019.138290>.

Publication II

Subramanian, S., Yadav, M. K., Jayaraj, J., Yangyang, F., Xi, L., & Prashanth, K. G. (2025). Microstructural homogenization through laser remelting in an additively manufactured Ti–40Nb sample from elemental feedstock powders. *Journal of Materials Research and Technology*, 38, 4305–4320. doi: 10.1016/J.JMRT.2025.08.203



Microstructural homogenization through laser remelting in an additively manufactured Ti–40Nb sample from elemental feedstock powders

Shangavi Subramanian^a, Mayank Kumar Yadav^a, J. Jayaraj^{b,c,*} , Fan Yangyang^d, Lixia Xi^e, K.G. Prashanth^{a,f,g,**} 

^a Department of Mechanical and Industrial Engineering, Tallinn University of Technology, Ehitajate Tee 5, Tallinn, 19086, Estonia

^b Materials Technology, Dalarna University, Falun, SE-79188, Sweden

^c Department of Mechanical and Materials Engineering, Karlstad University, SE-65188, Karlstad, Sweden

^d Zhengzhou Research Institute, Harbin Institute of Technology, Zhengdong New District, Zhengzhou City, Henan Province, China

^e Jiangsu Provincial Engineering Laboratory for Laser Additive Manufacturing of High-Performance Metallic Components, College of Materials Science and Technology, Nanjing University of Aeronautics and Astronautics, Yudao Street 29, Nanjing, 210016, China

^f Department of Biosciences, Saveetha School of Engineering, Saveetha Institute of Medical and Technical Sciences, Chennai, 602117, India

^g National Engineering Research Center of Near-Net-Shape Forming for Metallic Materials, South China University of Technology, Guangzhou, 510640, China

ARTICLE INFO

Handling editor: M Meyers

Keywords:

Additive manufacturing
Ti–Nb alloy
Remelting
In-situ alloying

ABSTRACT

Ti–Nb alloy fabricated via selective laser melting (SLM) serves as a promising candidate for orthopedic implants due to its exceptional biocompatibility and ability to mitigate stress-shielding effects. However, processing of in-situ alloyed Ti–Nb powder results in non-homogeneous microstructures and incomplete melting and diffusion of Nb hindering material homogeneity. In this study a laser remelting strategy was employed to enhance microstructural homogenization, Nb diffusion, and defect reduction. The effect of the cooling rate on the microstructure and mechanical properties of the resultant samples was explored. X-ray diffraction confirmed the presence of $\alpha' + \beta$ phase in single and triple melted samples. Remelted samples exhibited superior microstructural uniformity, reduced porosity, larger grain size, and increased α' martensite morphology as confirmed by scanning electron microscopy (SEM) and transmission electron microscopy (TEM). TEM analysis shows reduced dislocation density and twins upon remelting. The mechanical properties of the remelted sample maintained a desirable combination of low modulus and high strength with a hardness of 368 ± 7 HV, yield strength of 820 ± 35 MPa, compressive strength of 1480 ± 50 MPa, and an elastic modulus of 33 ± 3 GPa. This work proves laser remelting is an effective strategy for fabricating Ti–40Nb alloy from elemental powder contributing to the development of orthopedic implants.

1. Introduction

Implants are synthetic materials that replace or support damaged biological components, enhancing their functions [1]. The application of these implants varies widely from simple dental applications to complex systems such as pacemakers, orthopedic parts, etc. [2]. With the growing elderly population suffering from arthritis and other joint injuries, the need to replace damaged bones with orthopedic implants has recently increased [2]. Implants must exhibit adequate strength and biocompatibility to effectively support the damaged bones and integrate them with physiological conditions [3]. Based on these requirements, 70–80 % of orthopedic implants are made of metallic materials such as

stainless steel (SS), cobalt-chromium (Co–Cr), and titanium (Ti) based alloys [4,5]. However, Ti-based alloys are preferred over other materials owing to their superior corrosion resistance, high strength-to-weight ratio, and biocompatibility [6]. Among the different Ti-based alloys, Ti–6Al–4V gained much attention due to its high strength and corrosion resistance [7]. Regardless of its advantages, Ti–6Al–4V exhibits a higher elastic modulus (100–120 GPa) than the cortical bone (<30 GPa) [8]. This difference in elastic modulus leads to osteopenia, which causes the developing bone to attain insufficient density because of the stress-shielding effect [9]. In the long term, due to insufficient stiffness and thickness of regrown bone tissues, the loosening of implants occurs triggering implant failure [2]. In addition, Ti–6Al–4V exhibits poor wear

* Corresponding author. Department of Mechanical and Materials Engineering, Karlstad University, SE-65188, Karlstad, Sweden

** Corresponding author. Department of Mechanical and Industrial Engineering, Tallinn University of Technology, Ehitajate tee 5, 19086 Tallinn, Estonia
E-mail addresses: jayaraj.jayamani@kau.se (J. Jayaraj), kgprashanth@gmail.com (K.G. Prashanth).

<https://doi.org/10.1016/j.jmrt.2025.08.203>

Received 15 July 2025; Received in revised form 18 August 2025; Accepted 23 August 2025

Available online 25 August 2025

2238-7854/© 2025 The Authors. Published by Elsevier B.V. This is an open access article under the CC BY license (<http://creativecommons.org/licenses/by/4.0/>).

resistance and the release of toxic metal ions like V can provoke adverse tissue reactions [10]. Consequently, the recent demands increased the emphasis on developing novel implant material that addresses the stress-shielding effect with non-toxic metals [11].

For the long-term usage of implants, they should include low elastic modulus, high strength, non-toxicity, biocompatibility, corrosion, and wear resistance [12]. In response to these requirements, the β -type Ti alloys have emerged as a promising alternative to Ti-6Al-4V ($\alpha+\beta$) alloy due to their favorable combination of low elastic modulus, corrosion resistance, biocompatibility, and non-toxicity [13,14]. Some of the commonly used non-toxic β -stabilizing elements include niobium (Nb), tantalum (Ta), zirconium (Zr), and molybdenum (Mo) [15–17]. The advancements in the β -type Ti alloys have led to the development of Ti-Nb [18], Ti-Nb-Ta [19], Ti-Mo [20], TNZT, and other alloys [13,21]. In particular, the Ti-Nb alloy has been explored extensively for its superior cell adhesion, non-toxicity, bioinertness, and lower elastic modulus ranging from 30 to 90 GPa [22]. This alloy exhibits superior toughness, a critical property for enhancing the long-term mechanical durability and fatigue resistance of orthopedic implants [13]. Furthermore, Ti-Nb alloy forms an oxide layer (Nb_2O_5) on the surface and promotes the growth and proliferation of osteoblasts more effectively than other β -type alloys [23]. Based on the implant requirement, the properties of Ti-Nb alloy can be tailored by varying the alloy composition and processing conditions. In the allotropic Ti-Nb system, the composition (wt.%) of Nb significantly influences the alloy properties. An increase in Nb content leads to a decrease in elastic modulus due to the formation of a body-centered cubic (bcc) structured β -phase at room temperature [24]. However, an excessive amount of Nb addition to Ti results in an increase in the elastic modulus of the Ti-Nb alloy [25,26]. The influence of β -stabilizing elements on the stabilization of the low modulus β -phase can be evaluated using the molybdenum equivalence ($M_{o_{eq}}$) parameter, which is defined as follows:

$$M_{o_{eq}} = 1.0 (\text{wt. \% Mo}) + 0.28 (\text{wt. \% Nb}) + 0.67 (\text{wt. \% V}) + 0.44 (\text{wt. \% W}) + 0.22 (\text{wt. \% Ta}) + 2.9 (\text{wt. \% Fe}) + 1.6 (\text{wt. \% Cr}) - 1.0 (\text{wt. \% Al}) \quad (1)$$

It has been reported that the volume fraction of the β -phase increases with higher $M_{o_{eq}}$ values, and the β -phase is fully stabilized when the $M_{o_{eq}}$ value exceeds 10% [27]. Based on the published reports and the $M_{o_{eq}}$, the critical wt.% of Nb required to stabilize the β -phase at room temperature ranges between 40 and 50 wt% [28]. Henceforth, in the present study, Ti with 40 wt% Nb, was taken as the alloy for consideration.

Due to a higher melting temperature of Nb (~2750 K) than Ti (~1940 K), the development of suitable fabrication techniques to achieve a homogeneous microstructure with complete melting and mixing of the elements has become a critical issue. Traditionally, techniques such as casting and sintering were employed for the manufacturing of the Ti-Nb alloy. Studies by Lee et al. [29], Rafael et al. [30], etc. demonstrated the structure-property relationship of Ti-Nb alloy fabricated by casting methods. Studies by Hao et al. [31], Karre et al. [32], etc. investigated the fabrication of Ti-Nb alloy via spark plasma sintering (SPS) process. Regardless of the advantages offered by these methods, they encounter challenges such as high material wastage, long processing time, and post-processing requirements. In this regard, additive manufacturing (AM) has emerged as a promising alternative for the fabrication of Ti-Nb alloy with distinct advantages like design flexibility, rapid prototyping, and rapid manufacturing. The AM includes processing methods such as powder bed fusion (PBF), direct energy deposition (DED), binder jetting (BJ), material jetting (MJ), VAT polymerization, metal extrusion and sheet lamination [33,34]. For metallic materials the powder bed fusion (PBF) method such as selective laser melting (SLM) and electron beam melting (EBM) is the widely utilized owing to its layer-by-layer part construction and producing

near-net-shaped components with the ability to print customizable patient-specific implants [35–37]. However, owing to smaller laser spot size enabling fabrication of finer parts, better surface finish due to the use of smaller powder size (15–45 μm) and ease of maintaining inert atmosphere during processing, SLM is widely explored as compared to electron based PBF process [38]. During the SLM fabrication of Ti-Nb alloy, pre-alloyed feedstock powder produced by gas-atomization has been widely adopted [15]. Similarly, Zhongjie et al. fabricated highly dense Ti-41Nb samples with uniform microstructure by utilizing pre-alloyed Ti-41Nb powder [39]. Stefan et al. controlled Young's modulus of the Ti-42Nb implant fabricated using the pre-alloyed powder by using a texturing approach [40]. Similarly, Qin et al. fabricated Ti-35Nb samples from pre-alloyed powder and evaluated its corrosion behavior in Hank's solution [41].

Despite the proven reliability of pre-alloyed powders, their application is constrained by several factors: (1) The substantial cost of pre-alloyed powder arising from multiple factors, including the atomizer design, expensive inert gas, energy consumption, and feedstock expenses. These combined elements significantly contribute to the overall price of pre-alloyed powder [42], (2) processing alloys or metals with high melting points using gas atomization presents several challenges, including low mass flow rate, heat extraction rate, viscosity of molten metal, and nozzle clogging creating complexities in their fabrication [43], (3) the gas entrapment during the atomization process may result in the formation of hollow and satellite powder particles, which affects the powder bulk density and the properties of the fabricated parts [44], (4) the small energy of high-pressure gas created during the atomization process has a notable impact on the fragmentation ratio of the molten melt, leading to decreased powder yield [42], and (5) finally, achieving the desired powder size range, precise control, and expertise over a complex process is necessary for its utilization in AM-based processes.

To address these constraints, researchers have transitioned to in-situ alloying of elemental powders that offer a more cost-effective, compositionally adaptable, sustainable, and readily available alternative [45]. Though reports have demonstrated the successful fabrication of Ti-Nb alloy using elemental powder, issues such as non-homogeneous microstructure, incomplete melting, and phase segregation of Nb particles persisted [46]. The disparities in the melting temperature of Ti (1668 °C) and Nb (2468 °C) induce incomplete melting (avoiding congruent melting), while the difference in the density (Ti - 4.5 g/cm³ and Nb - 8.6 g/cm³) and limited solubility of Nb in Ti (20–30 wt% in equilibrium condition) triggers phase segregation, and non-homogeneous microstructure formation [47]. Unlike the equilibrium condition, the non-equilibrium solidification process in the SLM, characterized by rapid cooling, improves the Nb solubility in Ti via the solute trapping effect, thereby facilitating the stabilization of the β -phase [48]. For instance, Ye et al. [49] investigated solute redistribution in binary Ti alloy systems during rapid solidification and found that high concentrations of solute could be retained within the solid phase, while the typical segregation behavior was suppressed due to the insufficient time available for atomic diffusion. Supporting this, the multi-physics modelling by Yongfu et al. [50] simulated the non-equilibrium solidification microstructure of Ti-41Nb alloy fabricated using SLM. The results revealed that the rapid solidification involved in the SLM process mitigated the micro segregation of Nb by the solute trapping effect. Hence, to harness the benefits of elemental powders effectively, it is essential to employ optimized process strategies. In this context, remelting has emerged as a promising approach. Upon working with β -type Ti-Ta alloy, Zhang et al. suggested that a remelting strategy could effectively address issues such as unmelted particles, phase segregation, and non-homogeneous microstructure [51]. In addition, several studies involving the remelting approach to fabricating Ti-based alloys have highlighted the advantages of using such a remelting strategy [52].

Karimi et al. carried out a comprehensive study on the influence of single, double, and triple melting sequences on the microstructure and mechanical properties of SLM-processed Ti6Al4V alloy [53]. It has been

reported that the different melting sequences employed significantly affected the microstructure of the Ti6Al4V alloy [53]. The size and distribution of martensitic phases were altered by the thermal cycles induced by each melting strategy. In particular, the triple melting resulted in a more refined and homogenous microstructure compared to single and double melting indicating that laser remelting can effectively enhance the microstructural characteristics of fabricated samples. A study revealed that remelting offered the formation of both α and β phases (increased concentration) due to the decomposition of metastable α' phase, while also influences in reducing the external defects (porosity) and hardness, especially at lower scanning speeds [54]. In the case of the remelting strategy, there are reports that state increased cooling rate with remelting and some reports also portray otherwise, where the cooling rate decreases with remelting [55]. It was suggested that the effect of cooling rate variation during remelting is alloy-dependent, even though microstructural homogenization and reduction in defect concentration are observed as the general trend.

Multiple reports involving surface remelting have been reported and it has been observed that with remelting surface defects such as cracks, surface roughness, and porosity were reduced drastically or eliminated [56,57]. In addition, remelting enhanced the mechanical and tribological properties of the processed materials by refining their microstructure and reducing the defects concentration [58,59]. Song et al. worked on the fabrication of 18Ni-300 maraging steel where they reported that remelting improved the relative density of the sample from 98 % to ~99.9 %. Similarly, Brodie et al. and Karimi et al. have reported that remelting is a promising strategy for the fabrication of in-situ alloyed elemental powder via the SLM process with homogenized composition [51]. In addition, numerous studies have highlighted the benefits of employing a remelting strategy for the processing of Ti-based alloys; however, the information available on the effect of remelting on the properties of the Ti–Nb alloy is limited. Sheng et al. employed a remelting technique to fabricate in-situ alloyed Ti42Nb composite powder [60]. The laser remelting process, which incorporated single and double melting steps, demonstrated a reduction in the presence of unmelted Nb particles and defects such as porosity. Despite these improvements, the complete removal of unmelted Nb particles and porosity remained unattained even after double melting. In addition, an in-depth analysis of the phase composition, microstructural characteristics, or mechanical properties of the remelted samples is still unavailable.

Based on a detailed literature survey, and the gaps that exist w.r.t. the use of pre-alloyed powder, laser remelting strategy, and microstructural homogenization, this study aims to examine the impact of laser remelting on the properties of in-situ alloyed Ti–40Nb powder produced through the SLM process. To evaluate the effectiveness of the remelting strategy, two melting conditions such as single melting (SM) and triple melting (TM) were utilized for the fabrication of Ti–40Nb from elemental powders. A detailed structural and microstructural characterization has been carried out to evaluate the influence of the remelting strategy on the fabrication of Ti–40Nb alloy. In addition, the mechanical properties (hardness and compressive strength) of the SLM-processed Ti–40Nb are evaluated and the structure-property correlation has been elucidated. This study stands as a testimony to the fabrication of SLM-processed Ti–40Nb with uniform microstructure using a laser remelting strategy from the elemental powders.

2. Materials and methods

2.1. Feedstock material

The present study fabricates Ti–40Nb samples using elemental powders of commercially pure Ti (CP-Ti, 25 μm , Nanoshell, UK) and Niobium (Nb, 27 μm , Pacific Particulate Materials Ltd., Canada). To ensure a uniform distribution of the powder particles, 60 wt% of CP-Ti was mixed with 40 wt% of Nb in a plastic vial using a mechanical

mixer for 24 h at a rotating speed of 10 rpm.

2.2. Fabrication by selective laser melting

The bulk samples of Ti–40Nb(wt.%) alloy were fabricated using the SLM 280 2.0 machine (Manufacturer: SLM Solutions), equipped with an IPG 1064 nm fiber laser with a maximum power of 700 W and a spot size of ~110 μm . The process parameters utilized for the fabrication of the elemental Ti–40Nb samples include a laser power of 650 W, scan speed of 650 mm/s, hatch spacing of 0.035 mm, layer thickness of 0.03 mm, and hatch rotation of 67°. The volumetric energy density is calculated using equation (2).

$$E_d = \frac{P}{vht} \quad (2)$$

where P is the laser power (650 W), v is the scan speed (650 mm/s), h is the hatch spacing (0.035 mm), and t is the layer thickness (0.03 mm). The resulting volumetric energy density is approximately 900 J/mm³. A straight-line hatch strategy was employed to fabricate the bulk samples [61]. During fabrication, each layer is melted either once or thrice to study the effect of remelting. The schematic representation of the melting condition involved during the fabrication of Ti–40Nb samples is illustrated in Fig. 1. During the single melt (SM) process, each layer was melted once and during the triple melt (TM) process each layer was melted thrice with the same parameter in the same direction without any hatch rotation [62–64]. A continuous flow of Argon gas (99.9 % purity) maintained an inert atmosphere during the fabrication process to avoid oxygen contamination. The Ti–40Nb samples were printed over a Ti substrate of 30 mm thickness and the fabricated samples were removed from the substrate using wire electrical discharge machining (WEDM). Cuboid samples of dimensions of 5 mm \times 5 mm \times 5 mm were printed in the SM and TM conditions.

2.3. Material characterization

2.3.1. Structural characterization

The structural characterization of the powder and the bulk Ti–40Nb samples was carried out using the Brucker-AXS X-ray diffractometer (XRD) fitted with Cu-K α radiation (where $\lambda = 1.54 \text{ \AA}$). The diffraction

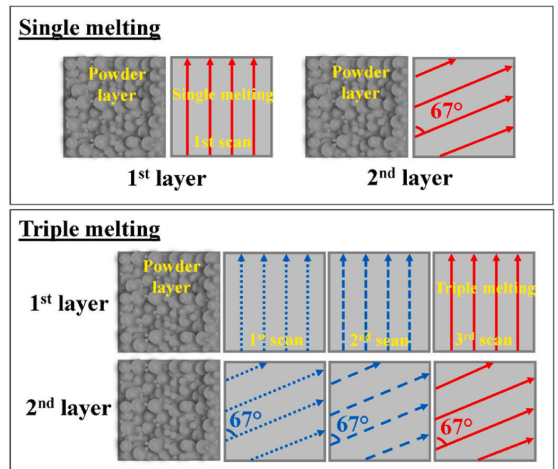


Fig. 1. Schematics illustrate the single and triple melting conditions employed during the selective laser melting of Ti–40Nb samples. During the single melting process, the powder bed was melted once and during the triple melting process, the same layer was melted three times without any hatch rotation.

experiments were carried out between the diffraction angle ‘ 2θ ’ from 30° to 90° with a step size of 0.02° . The phase analysis and unit cell parameters were analyzed by the Rietveld refinement using Highscore Expert Plus software. To evaluate micro strain, the Williamson-Hall (W–H) method was applied using the following relation [65].

$$\beta \cos \theta = \varepsilon 4 \sin \theta + \frac{k\lambda}{D} \quad (3)$$

where D is the crystallite size, k is the Scherer constant (0.94), λ is the wavelength of the Cu- $K\alpha$ radiation (1.54 \AA), β is the full width half maximum (FWHM) of the peaks, and θ is the peak position. A plot of $\beta \cos \theta$ vs $4 \sin \theta$ was constructed, from which the slope of the linear curve yielded the micro strain. The chemical composition of the Ti–40Nb alloy powder as evaluated by inductively coupled plasma optical emission spectroscopy (ICPOES) was found to be Nb $\sim 40.3 \text{ wt\%}$, O $< 0.07 \text{ wt\%}$, Ti – balance. The density of the bulk SM and TM samples was measured using Archimedes’ principle (Mettler Toledo ME204, Germany).

2.3.2. Microstructural characterization

The SLM-fabricated samples for microstructural analysis were mechanically ground using SiC paper with grits ranging from P400 to P4000 as per standard metallographic procedures. The final polishing to a mirror finish was performed using colloidal silica ($0.05 \mu\text{m}$ suspension). The porosity of the samples was analyzed using Zeiss optical microscopy (OM) and the image analysis of the optical micrographs was done using the ImageJ software to estimate the porosity level in the SM and TM samples. The microstructural details were analyzed using scanning electron microscopy (Zeiss FEG, Germany) in backscattered electron (BSE) imaging mode. In addition, image analysis of the SEM micrographs using Image J software was performed to measure the morphology of α' martensite and grain size of the SM and TM samples. A total of 100 measurements were taken to measure the length and width of the α' martensite as well as for grain size, and their average values were reported. The presence of twins and dislocation density were

characterized using a transmission electron microscope (TEM, Tecnai G2 F20, FEI, Germany) equipped with a 200 keV energy dispersive spectrometer (EDS), and a high-angle annular dark-field (HAADF) using an FEI 80–300, and nano diffraction.

2.3.3. Mechanical testing

The Vickers microhardness of the as-fabricated SM and TM samples was tested using the Buehler Micromet machine, with a 1000 g load and dwell time of 10 s. Ten values were taken for each sample and their average value was reported. A room temperature compression test was carried out on the INSTRON-5967 machine with a strain rate of 10^{-3} mm/s and load cell of 30 kN. The compression samples of 6 mm width x 3 mm diameter (according to the ASTM E8 standard) were cut from cuboid samples using WEDM. Three samples were tested in each condition to ascertain the reproducibility of the results.

3. Results

3.1. Powder characterization

The SEM images of the CP-Ti, Nb, and Ti–40Nb powders are displayed in Fig. 2. The gas-atomized CP-Ti powder, as depicted in Fig. 2(a and b) displays a spherical morphology with satellites attached to the surfaces of larger particles. These satellites were formed by the collision between semi-liquid particles and solid particles during the gas-atomization process [66]. The presence of satellites may hamper the flowability of the powder particles. The average particle size (diameter) of the CP-Ti particles is found to be $25 \pm 4 \mu\text{m}$ (Fig. 2(c)). The Nb powder, as shown in Fig. 2(d and e), exhibits irregularly shaped particles resulting from the milling process. During the solid-state mechanical milling, repeated cold welding (due to plastic deformation and agglomeration of particles leading increase in the size and change of shape of the samples), fracturing (reduction of size and change in morphology of the samples), and rewelding of the particles take place

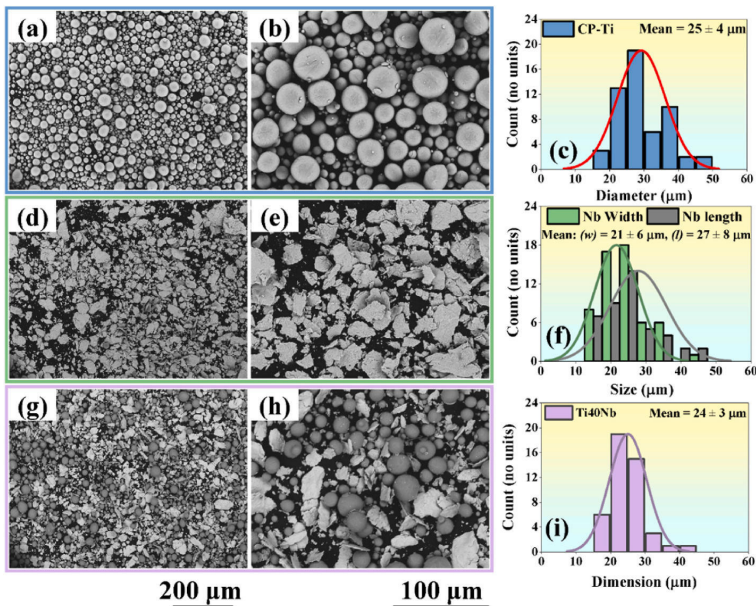


Fig. 2. Scanning electron microscopy images of the powders: (a,b) commercially pure titanium, (d,e) niobium, and (g,h) Ti–40Nb (wt.%) powder mixture. Plots showing the particle size distribution of the powders: (c) commercially pure titanium (average diameter - $25 \pm 4 \mu\text{m}$), (f) niobium (average width and length, $21 \pm 6 \mu\text{m}$ and $27 \pm 8 \mu\text{m}$, respectively), and (i) Ti–40Nb (wt.%) powder mixture (average size - $24 \pm 3 \mu\text{m}$).

(increase in the size of the sample and change in shape) [67]. During this process, samples with irregular morphology will be attained as shown in Fig. 2(d and e). The irregular morphology of the samples may hinder the flowability of the powder particles. The average particle size of the Nb powder is found to be $21 \pm 6 \mu\text{m}$ in width and $27 \pm 8 \mu\text{m}$ in length (Fig. 2(f)). The powder mixture (Ti–40Nb) shows the combination of Ti (spherical) and Nb (irregularly shaped) powder particles (Fig. 2(g and h)). It may be observed that the solute Nb is uniformly distributed around the Ti solvent particles. The average size of the powder mixture is observed to be $24 \pm 3 \mu\text{m}$ (Fig. 2(i)). Concerning the average particle size ($24 \pm 3 \mu\text{m}$) of the composite, it is within the usual range employed for the SLM fabrication process (20–60 μm). However, w.r.t. the powder shape, the mixture of spherical particles with satellites, and the irregularly shaped Nb particles may hamper their flowability and in turn the effective powder bed density (spreading of the powder particles).

3.2. Structural and microstructural analysis

The phase analysis of the powders and the bulk SM and TM Ti–40Nb samples is illustrated in Fig. 3. The CP-Ti powder exhibits the presence of a hexagonally closed-packed (*hcp*) α -phase with the space group of $P6_3/mmc$, and the Nb powder exhibits the presence of a body-centered cubic (*bcc*) β -phase with the space group of $Im-3m$ [68]. Accordingly, the Ti–40Nb powder exhibited the presence of both phases: α -CP-Ti (*hcp*) and β -Nb (*bcc*). Additionally, Table 1 furnishes the crystal lattice parameters for the powders and the SLM-fabricated bulk Ti–40Nb samples. Notably, the lattice parameters of CP-Ti (a_β and c_α) and Nb (a_β) align closely with values reported in the literature [68,69]. When the lattice parameters of CP-Ti and Nb are compared with the lattice parameters of the Ti–40Nb alloy mixture, no significant variations are observed, suggesting the absence of strain during the mixing of Ti–40Nb alloy powder [70,71].

The diffraction patterns of the bulk SLM-fabricated SM and TM Ti–40Nb samples in Fig. 3(a) demonstrated the presence of the metastable β -phase with a space group of $Im-3m$ [40]. This *bcc* crystal structure observed for the SM condition may be attributed to the presence of both the TiNb phase and the unmelted Nb (however, characterized here as β -phase – see microstructural analysis for more details). On the other hand, the *bcc* phase observed in the TM sample may be attributed solely to the TiNb phase - β -phase (since the unmelted Nb is absent). While the peaks corresponding to the metastable α' -phase (with a space group of $P6_3/mmc$) were not evident in the SM sample (within the XRD detectable limits), a noticeable increase in peak intensity for the

Table 1

The table furnishes the Rietveld-refined crystal lattice parameters for Ti–40Nb samples in powder and bulk forms.

| Sample description | a_β (nm) | a_α (nm) | c_α (nm) |
|-----------------------|----------------|-----------------|-----------------|
| CP-Ti powder | – | 0.29507 | 0.4684 |
| Nb powder | 0.3305 | – | – |
| Ti–40Nb powder | 0.3309 | 0.2951 | 0.4681 |
| SM Ti–40Nb bulk alloy | 0.3294 | 0.2999 | 0.4761 |
| TM Ti–40Nb bulk alloy | 0.3292 | 0.2976 | 0.4775 |

(002), (101), (110), and (112) planes were observed in the TM condition. Upon cooling from temperatures above the β -transit temperature (882 °C) (depending on the cooling rates), the metastable β -phase transforms completely into α phase or stable $\alpha+\beta$ phases [25,26]. However, the rapid heating and cooling involved during the SLM process hinder the growth of the stable $\alpha+\beta$ phases, subsequently leading to the formation of metastable phases like α' with *hcp* crystal structure or α' with orthorhombic crystal structure along with the β -phase at room temperature [9,12]. Consequently, the solidification mechanism observed during the cooling of the SM and TM Ti–40Nb samples involves a non-equilibrium phase transformation from the stable β -phase to the metastable α' and β phases. Furthermore, as shown in Table 1, the lattice parameters of α' martensite (a_α and c_α) in the TM sample align with the literature, confirming the presence of metastable α' and β phases [53].

Fig. 3(b) illustrates the shift and broadening in the β -phase (110) diffraction peaks for the SLM-fabricated SM and TM samples when compared to the elemental powder mixture. The peak shift toward higher 2θ values indicates a reduction in lattice parameter, attributed to the substitutional incorporation of Nb atoms into the Ti lattice, while the broadening effect is due to the strain created during the lattice contraction [72]. Although the atomic radii of Ti (0.147 nm) and Nb (0.146 nm) are nearly identical, the incorporation of Nb atoms into the Ti lattice results in contraction of the lattice, giving rise to localized strain in the unit cell. The Rietveld refinement confirms that the lattice parameter decreased from $a_\beta = 0.3305 \text{ nm}$ in the powder state to $a_\beta = 0.3291 \text{ nm}$ in the SLM-fabricated SM and TM samples. The micro strain values calculated by the W–H method were $0.3 \pm 0.02 \times 10^{-3}$ for the Ti–Nb powder, $4.2 \pm 0.1 \times 10^{-3}$ for the SM sample, and $3.6 \pm 0.1 \times 10^{-3}$ for the TM sample. These results confirm the effects of Nb solute incorporation in the peak shift and micro strain associated with peak broadening. The OM images in Fig. 4(a and b) illustrate the variation in porosity observed between the SM and TM Ti–40Nb samples. The unetched samples do not show any distinct features other than the

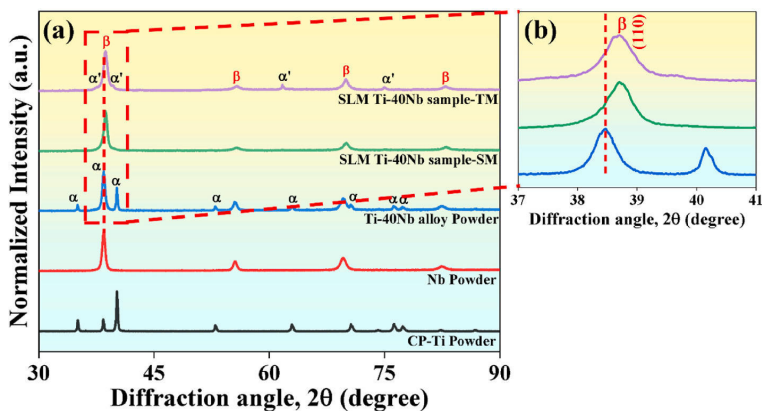


Fig. 3. (a) X-ray diffraction (XRD) patterns of the CP-Ti, Nb, and Ti–40Nb powders compared with the selective laser-melted Ti–40Nb samples in both single (SM) and triple (TM) melted conditions. (b) Magnified image of the XRD patterns of the Ti–40Nb powder and bulk samples in both SM and TM conditions showing the peak shift in the (110) plane (between the diffraction angle 2θ - 37° and 41°) along the higher diffraction angles.

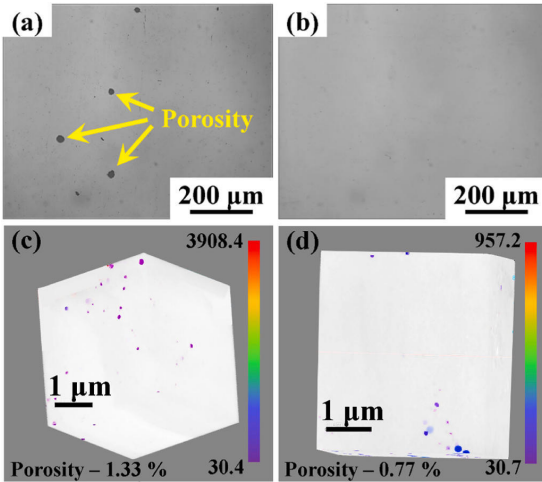


Fig. 4. Optical microscopy and micro-CT images of the selective laser melted (a,c) single melt and (b,d) triple melted Ti-40Nb samples. The yellow arrow in the image highlights the presence of porosity.

defects (porosity). Image analysis on the OM images revealed that the porosity size in the SM sample ranged from 20 μm to 70 μm with an average of ~ 40 μm . In contrast, no visible porosity was observed in the TM sample. In agreement with the OM image analysis, the micro-CT images in Fig. 4(c and d) show a reduced porosity from the SM (1.33 %) to the TM (0.77 %) sample because of remelting. This indicates that the remelting approach effectively reduced porosity, thereby enhancing the density of the remelted sample. The relative density of the sample increased from ~ 96 % in the SM condition to ~ 99.5 % in the TM condition. These findings align with the work of Fei et al., demonstrating that the remelting process promotes improved densification and a significant reduction in porosity [73].

The SEM images in Fig. 5 illustrate the microstructural features of SM and TM samples along with the elemental mapping. The SM sample (Fig. 5(a–c)) exhibits a non-homogeneous microstructure characterized by porosity, unmelted Nb particles, and regions with Nb-rich and deficient areas. The microstructure consists of three distinct regions: the grey regions correspond to the presence of β -phase, the dark region corresponds to the α' martensitic phase, and the bright regions

correspond to the unmelted Nb particles. The non-homogeneous microstructure, with areas rich and poor in Nb, indicates the insufficient melting and diffusion of Nb particles during the SLM process. This incomplete diffusion of Nb could arise from the differences in the melting temperature of Ti (1668 $^{\circ}\text{C}$) and Nb (2468 $^{\circ}\text{C}$). Further, the randomly oriented α' martensite was observed over the β matrix. The higher cooling rate observed during the SM processing restrained the growth of α' martensite, resulting in a finer α' resembling a dot-shaped morphology. In contrast, the TM sample (Fig. 5(d–f)) exhibits a homogeneous distribution of α' martensite over the β matrix. The relatively slower cooling rate observed during TM facilitated the growth in the morphology of the α' martensite leading to a plate-shaped morphology. Additionally, the remelting strategy employed effectively reduced the porosity volume and enhanced the melting and diffusion of Nb particles.

The cooling rates observed during the SLM process are significantly influenced by the heat input/energy input employed during the fabrication process. The heat input (in 2D) is calculated as the ratio of laser power (P) to scan speed (v) in W/mm. Previous studies on remelting indicated that a heat input below 0.6 W/mm resulted in an increased cooling rate, whereas a heat input above 0.6 W/mm led to a decreased cooling rate [54,59,63,64,74]. In the present work, the calculated heat input was observed to be ~ 1 W/mm. Consequently, the higher heat input employed in this study caused a reduction in the cooling rate during remelting. The larger grains observed in the TM samples are attributed to the presence of reduced cooling rates in the TM condition. Specifically, the average grain size increased from 19 ± 6 μm for SM to 26 ± 7 μm for the TM sample, representing a 20 % increase in grain size due to a reduced cooling rate. Furthermore, the SEM images (Fig. 5(d–f)) revealed an increase in the size of the α' martensite in the TM sample. With remelting, both the length and width of the α' martensite increased. The length increased from 0.41 ± 0.1 μm to 2.96 ± 0.6 μm , and the width increased from 0.21 ± 0.04 μm to 0.31 ± 0.06 μm , respectively and the results are plotted in Fig. 6.

The transmission electron microscopy (TEM) images along with their selected area diffraction (SAED) patterns are shown in Fig. 7. The microstructure of the SLM Ti-40Nb sample in the bright field (BF) mode shows the presence of the two-phased microstructure (Fig. 7(a–f)) for both the SM and TM conditions corroborating with the SEM images. The morphology of the dark phase present between the two conditions (SM and TM) differs, where a finer morphology is observed for the SM condition and a coarse/elongated morphology for the TM condition. The dark field (DF) images of the SM and TM samples are shown in Fig. 7 (b–g), respectively. The SAED patterns are recorded at three different locations: (a) matrix bright phase – (1) and (4) (b) dark phase (2) and (5) and (c) interface between the bright and dark phases (3) and (6) (as seen

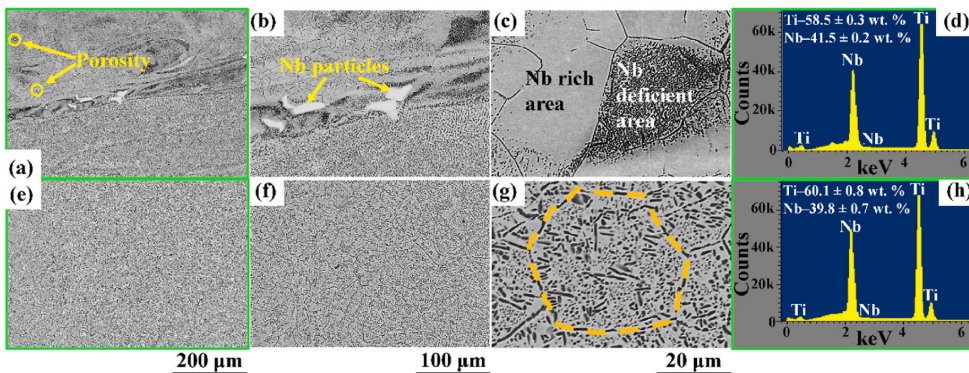


Fig. 5. Scanning electron microscopy images along with the EDX elemental mapping of the selective laser melted Ti-40Nb samples after (a–d) single melting and (e–h) triple melting. The porosity and unmelted Nb particles are indicated by yellow arrows, and the grain boundary is highlighted with orange dashed line respectively. The green outlined images highlight the region of elemental mapping.

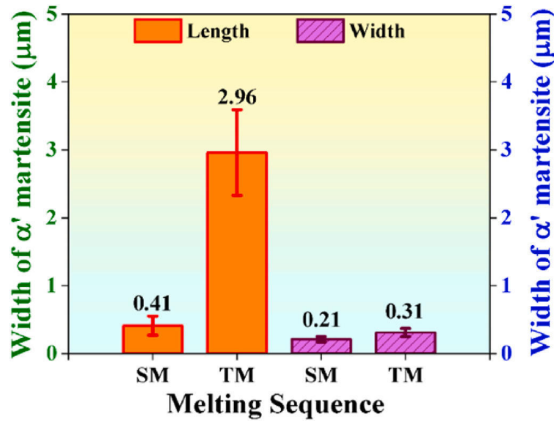


Fig. 6. Plot showing the increased size (both length and width) of the α' martensite in the Ti–40Nb samples fabricated by selective laser melting in two different conditions (single and triple melting).

in Fig. 7(b–g) to characterize and analyze the phases present in the microstructure. The SAED patterns (Fig. 7(c–h)) corresponding to the dark phase (observed in Fig. 7(b–g)) show a typical pattern for the cubic crystal structure (here in this case – body-centered cubic structure – *bcc*) along the zone axis $[\bar{1}11]$. Similarly, the SAED patterns (Fig. 7(d–i)) of the bright phases observed in Fig. 7(b–g) correspond to the *hcp* structure (in the presence case – α' microstructure). Even though the α' peaks are not observed in the XRD pattern (Fig. 3), they are present in the SM sample which can be confirmed using the SEM and TEM images. The concentration of α' may be small (below the deductible limits of the X-ray), hence they may be difficult to observe from the XRD pattern. The SAED patterns taken at the interface (Fig. 7(e–j)) from the TEM image (Fig. 7(b–g)) show the coexistence of both the *bcc* (β) and *hcp* (α') phases.

The high-angle annular dark-field image (HAADF) images along the energy-dispersive X-ray (EDX) maps are shown in Fig. 8. It may be evident from the HAADF images that both the SM and TM samples show a two-phased microstructure corroborating the SEM data. In addition, the difference in the morphology of the phases observed in the SM and TM samples also corroborates with the SEM data, where the SM samples show the presence of fine needle-shaped and the TM samples show

elongated/coarse needle-shaped phase (Fig. 8(a–d)). The EDX maps show the elemental distribution of both Ti and Nb, where the needle-like phase (plate-shaped morphology) is rich in Ti and the matrix consists of both Ti and Nb. This suggests that the needle-shaped phase corresponds to the α' martensite phase with *hcp* crystal structure and the matrix corresponds to the β phase with *bcc* crystal structure.

To further corroborate the elemental distribution and to quantify the same, point analysis has been carried out on the TEM image for the TM sample as shown in Fig. 9. It can be noted from the point scan analysis (Fig. 9(b)) that the bright phase (denoted as point 1) predominantly show the presence of Ti (>95 wt%) with some traces of supersaturated Nb (<5 wt%) – weak intense peaks in the EDX point scan, hence can be attributed as α' martensite with *hcp* crystal structure. On the other hand, the matrix (denoted as 2) – the dark phase shows the elemental distribution of both Ti and Nb. In this case, the Nb peaks show significant intensity as compared to the Ti peaks, and the concentration is observed as ~55 wt% Ti and ~45 wt% Nb.

The BF-TEM images show the presence of line defects (dislocations) and twins for both SM and TM samples (Fig. 10(a–c, f–h)). The dislocations are continuous and are observed in the form of lines, sometimes extending between grains/phases. A forest of dislocations is observed especially at the interface between the phases (β – *bcc* and α' – *hcp*) while the twins were seen inside the lamellar α' martensite. The presence of such a high volume of defects like dislocations and twins may be corroborated by the extreme solidification conditions existing during the SLM process [75]. In the SM sample, the dislocations are observed in the *bcc* β matrix and at the interface (Fig. 10(a–c)). The forest of dislocations piles up at the β – *bcc* and α' – *hcp* interface. In addition, the α' – *hcp* martensite exhibits the presence of twins running throughout the needles. On the other hand, in the TM sample, the forest of dislocations is restricted only at the β – *bcc* and α' – *hcp* interface without any dislocation significant dislocation network in the matrix β – *bcc* phase. However, some dislocations observed at the interface extend in the form of dislocation lines to their neighboring interface (Fig. 10(f–h)). Similar to the SM sample, the α' – *hcp* martensite shows the presence of twins, however, their concentration is significantly reduced (Fig. 10(f–h)). Although the number of twins and dislocations are not quantified, a larger volume of twins and dislocations were observed in the SM sample compared to TM. Due to the annihilation effect caused by the remelting approach, the twins and the dislocation density drastically reduced with remelted in the TM samples.

Fig. 10(d,e,i,j) furnishes the inverse fast Fourier transform (IFFT) images showing the presence of line defects, especially edge

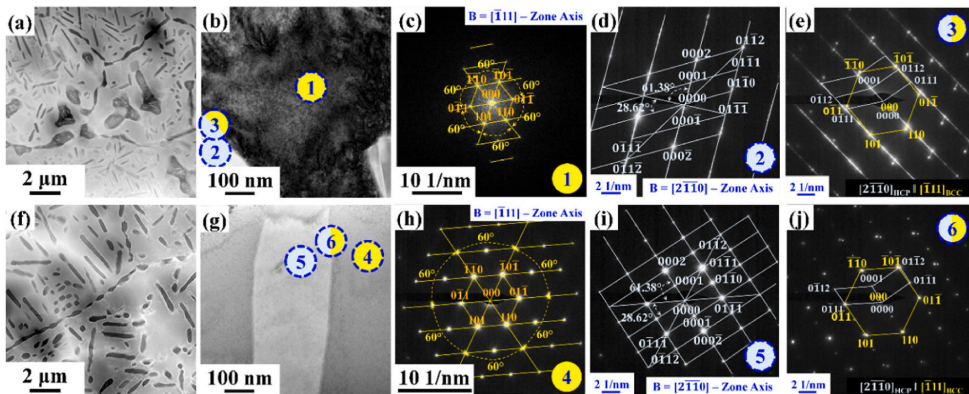


Fig. 7. Transmission electron microscopy bright field images of the selectively laser melted (SLM) Ti–40Nb samples in the (a,b) single (SM) and (f,g) triple melted (TM) conditions. Selected area diffraction (SAED) patterns of the SLM Ti–40Nb samples were taken along three different regions in images (b) and (g) for the (c–e) SM and (h–j) TM samples, respectively. The SAED patterns (c,h) correspond to the body-centered cubic structure (*bcc*), (d,i) correspond to the hexagonally closed packed structure (*hcp*), and (e,j) correspond to the combination of both *hcp* and *bcc* crystal structures.

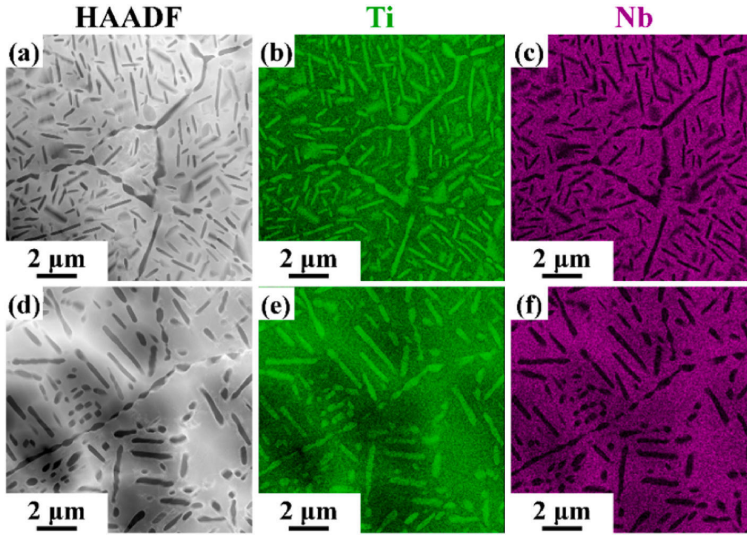


Fig. 8. High-angle annular dark-field image (HAADF) images of the selectively laser melted Ti-40Nb samples in the (a) single melted (SM) and (d) triple melted (TM) conditions. Energy dispersive X-ray maps of the selectively laser melted Ti-40Nb samples in the (b,c) SM and (e,f) TM conditions.

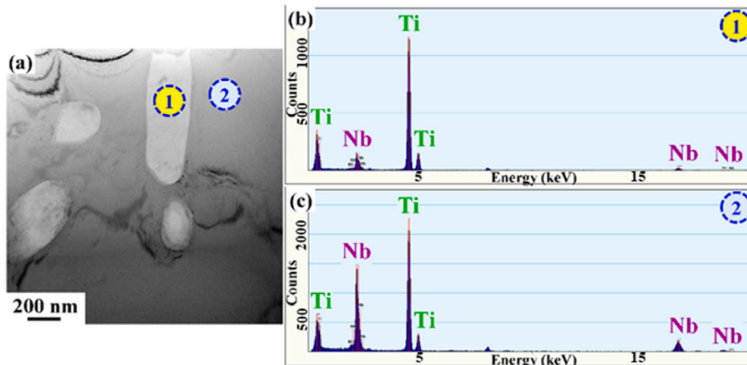


Fig. 9. Transmission electron microscopy (a) bright field image of the selectively laser melted Ti-40Nb samples in the triple melted condition (TM) and their corresponding point analysis take at two different positions: marked as position (b) 1 on the bright phase and (c) 2 on the dark phase.

dislocations. Both types of edge dislocations (positive and negative) are observed in the SLM-processed TiNb samples. Unlike most of the mechanically worked materials, these dislocations originate during the solidification of the melt. The rapid cooling rates observed during the SLM process induce significant strain over the solidifying surface (especially at the solidifying front) leading to both formation and multiplication of dislocations. The creation of positive edge dislocation will induce compressive strain in the material and on the other hand, the negative edge dislocation will induce tensile stress. Two striking differences are observed between the SLM-processed SM and TM samples: (1) It can be observed from Fig. 10(d and e) that almost equal numbers of positive and negative edge dislocations in the SLM-processed SM samples. On the other hand, it may be observed from Fig. 10(i) that more positive edge dislocations than negative edge dislocations are observed in the SLM processed TM samples. (2) In addition, more concentration of edge dislocations is observed in the SM sample compared to the TM sample. The interplanar spacing observed for the SM and TM samples from Fig. 10(d,e,i,j) is found to be 1.45 \AA and 1.63 \AA , respectively. Such

an increase in the interplanar distance for the TM samples may be attributed to the increase in strain in the lattices due to the complete diffusion of Nb to Ti.

3.3. Mechanical properties

Fig. 11(a) presents the Vickers hardness plot as a function of remelting and Fig. 11(b and c) shows the hardness distribution map of the Ti-40Nb samples in SM and TM conditions. The average Vickers hardness of the samples shown in Fig. 11(a) indicates a marginal reduction in the hardness from $384 \pm 13 \text{ HV}$ to $368 \pm 7 \text{ HV}$ for the SM and TM conditions, respectively. The decrease in hardness can be attributed to the grain coarsening effect caused by remelting. Furthermore, the hardness distribution plot of SM in Fig. 11(b) highlights a non-uniform hardness distribution across the transverse cross-section of the sample. This non-uniformity may be corroborated with the SEM results of the SM sample (Fig. 5(a–c)) which displayed a heterogeneous microstructure, leading to anisotropic hardness characteristics. Wysocki

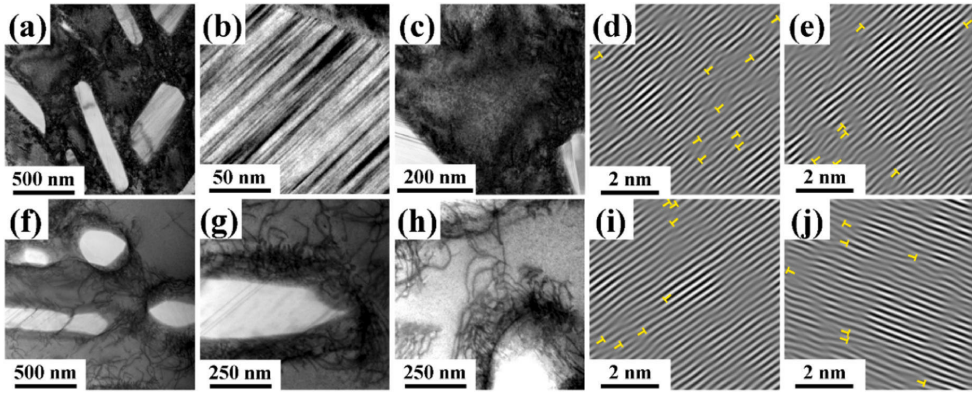


Fig. 10. The bright-field transmission electron microscopy images of the selectively laser melted Ti-40Nb samples in the (a–c) single melted (SM) and (f–h) triple melted (TM) conditions showing the presence of imperfections twins, and dislocations. Inverse Fourier-filtered image of the (d,e) SM and (i,j) TM samples showing the presence of edge dislocations.

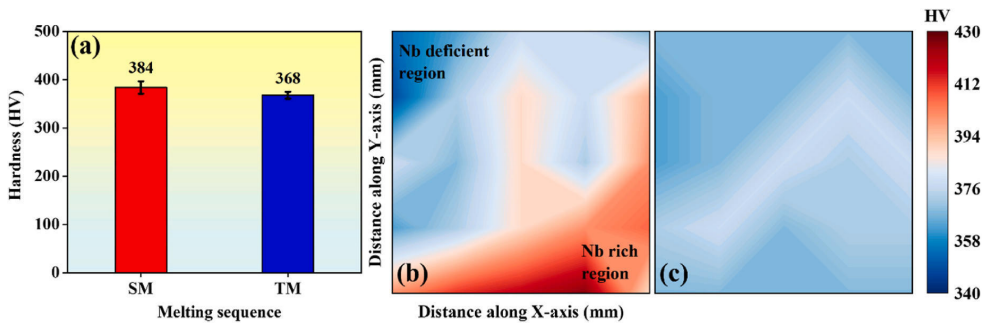


Fig. 11. (a) Vickers hardness plot of the selective laser melted Ti-40Nb samples observed for single and triple melt conditions. Hardness distribution map of the selective laser melted Ti-40Nb samples under (b) single and (c) triple melting conditions.

et al. [68] on SLM-processed CP-Ti and Liu et al. [76] on SLM-fabricated Nb have suggested that Nb possesses a higher average hardness than Ti. Consequently, regions with higher Nb content exhibited increased hardness, while regions with lower Nb content exhibited reduced hardness. In contrast, as corroborated by the SEM images (Fig. 5(d–f)), the TM sample exhibited a near-homogenous hardness distribution across the transverse cross-sectional surface suggesting that the multiple

remelting strategy has promoted microstructure and hardness homogenization. Despite the decrease in hardness due to remelting, the obtained hardness values observed in the present study (both SM and TM samples) are higher than the reported hardness values observed for the SLM-processed Ti-40Nb alloy [40]. The increased hardness observed in the present study may be attributed to the presence of α' martensite in both the SM and TM samples.

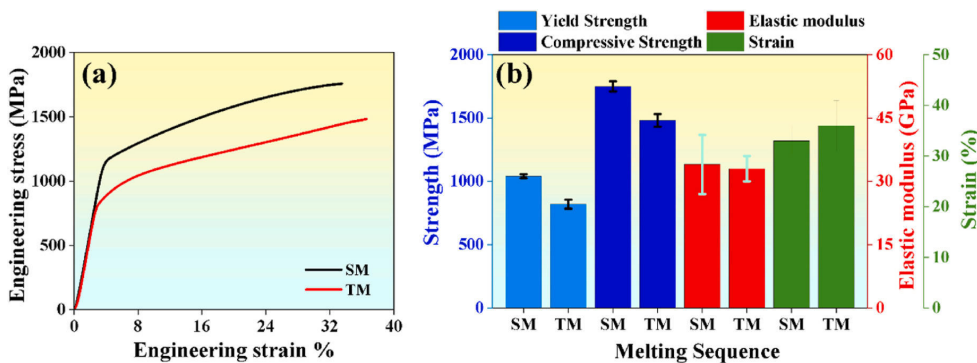


Fig. 12. (a) Compressive stress-strain curve of selective laser melted Ti-40Nb samples at single and triple melt conditions and (b) their corresponding data.

The compressive stress-strain curve of SLM-fabricated Ti–40Nb samples in both SM and TM conditions is depicted in Fig. 12(a). The corresponding values for elastic modulus (E), yield strength (YS), ultimate compressive strength (UCS), and strain (%) are presented in Fig. 12 (b). The SM sample exhibited an E of 34 ± 7 GPa, a YS of 1040 ± 15 MPa, and a UCS of 1752 ± 40 MPa. In contrast, the TM sample demonstrated an E of 33 ± 3 GPa, a YS of 820 ± 35 MPa, and a UCS of 1480 ± 50 MPa. It can be observed that remelting had a pronounced effect on the compressive strength of the TM sample. As illustrated in the grain size plot (Fig. 5(g)), remelting induced a slower cooling rate, which in turn promoted grain growth. According to the Hall-Petch relation, a material with a larger grain size exhibits lower strength; hence, the TM sample, with its larger grain size, demonstrated reduced strength compared to the SM sample. Despite the decrease in strength due to remelting, both SM and TM samples exhibited similar stiffness behavior. Furthermore, the plasticity of the TM sample improved by $\sim 2\%$.

4. Discussion

4.1. Cooling rate influence on microstructure

The phase analysis of the SM and TM samples revealed the presence of a dual-phase microstructure comprising α' and β phases. The formation of α' was confirmed through microstructural analysis carried out using SEM and TEM. The morphology of the α' in the SM and TM samples shows a characteristic martensitic structure, resembling the α' martensite formed during the selective laser melting of near- β and $\alpha+\beta$ Ti-based alloys [53,77–80]. Additionally, the crystal structure of the martensite as characterized by the TEM evaluation was found to be *hcp* affirming the presence of *hcp* – α' martensite (Fig. 7(d–i)). On comparing the microstructures of the SM and TM samples, it can be observed that the *hcp* – α' martensite morphology increased by $\sim 13\%$ in length and $\sim 6\%$ in width, while the average grain size increased by about $\sim 43\%$ in the TM sample as compared to the SM sample. This significant increase in the *hcp* – α' martensitic morphology and grain size in the TM sample can be attributed to the reduced cooling rate associated with the remelting process, which promotes grain growth and coarsening of the *hcp* – α' martensitic structure.

During the SLM process, the cooling rates observed are directly influenced by the temperature and size of the melt pool. The peak temperature (T_p) at the surface ($z = 0$) of the sample and at a distance Y from the center of the melt pool can be calculated using the Rosenthal equation [81]:

$$T_p = T_0 + \frac{Q}{2\pi kr} \exp\left(-\frac{\nu x}{2\alpha}\right) \quad (4)$$

where T_0 is the initial temperature in K (298 K), Q is the heat transferred to the substrate from the laser source in W [82], k is the thermal conductivity of powder in W/m.K (6 W/m.K), and bulk Ti–40Nb alloy (11.5 W/m.K) [83], r is the distance from the heat source to the point considered in m, given as $r = \sqrt{x^2 + y^2 + z^2}$, ν is the scan speed in m/s, T_m is the melting temperature of Ti–40Nb alloy in K (~ 2300 K) [84,85], and α is the thermal diffusivity in m^2/s , calculated as follows:

$$\alpha = \frac{k}{\rho C_p} \quad (5)$$

where ρ is the density of Ti–40Nb alloy in kg/m^3 (5570 kg/m^3), C_p is the heat capacity of Ti–40Nb alloy in $J/kg.K$ (525 $J/kg.K$). In addition, the cooling rate of the Ti–40Nb samples can be determined using the following equation [81]:

$$CR = 2\pi k\nu \frac{(T - T_0)}{Q} \quad (6)$$

where CR is the cooling rate, k is the thermal conductivity of the Ti–40Nb alloy in W/m.K, T is the melt pool temperature in K, T_0 is the initial temperature of the material in K (298 K), ν is the scan speed in m/s, P is the laser power in W, and Q is heat transferred to the substrate from the laser source in W.

To accurately determine the melt pool temperature and cooling rates of the SM and TM samples, it is essential to consider the thermal conductivity of both the powder and bulk Ti–40Nb alloy. During the initial melting (single melting), heat is primarily transferred through the powder layer. In contrast, during the remelting process (triple melting), heat transfer takes place through the powder layer initially during the first melting, and subsequently the heat transfer occurs through the bulk sample (during the second and third melting). Therefore, the melt pool temperature and cooling rate of the SM sample are calculated using the thermal conductivity of powder (~ 6 W/m.K), whereas the melt pool temperature and cooling rate of the TM sample are calculated using the thermal conductivity of the bulk sample (~ 11.5 W/m.K). Using equations (7) and (8), the calculated melt pool temperatures and cooling rates are summarized in Table 2. The result reveals that the SM sample exhibited a higher melt pool temperature (~ 5606 K) compared to the TM sample (~ 3067 K). Similarly, the cooling rate for the TM sample (3.2×10^5 K/s) was found to be lower than that of the SM sample (6.9×10^5 K/s). According to Newton's law of cooling, the rate of heat transfer is directionally proportional to the temperature gradient [86,87]. In accordance, the SM sample, which exhibited a higher temperature gradient in the melt pool, experienced a faster cooling rate, and the TM sample with a lower temperature gradient, displayed a slower cooling rate.

The observed decrease in cooling rate during remelting results from the combined effects of increased thermal penetration (melt pool depth) and heat accumulation. Thermal penetration denotes the depth to which laser-generated heat penetrates the material. It can be calculated as [53],

$$\delta_{th} = 2\sqrt{\alpha t} \quad (7)$$

where δ_{th} is thermal penetration depth in m, α is thermal diffusivity in m^2/s and t is exposure time in s. The thermal penetration depth of the SM sample was found to be ~ 32 μm and that of the TM sample was ~ 44 μm . This higher penetration depth in the TM sample results in a deeper melt pool compared to the SM sample. These factors combined reduce the temperature gradient across the sample, resulting in a slower cooling rate.

Fig. 13 illustrates a schematic representation of grain size variations taking place in the SLM-processed Ti–40Nb SM and TM samples. As the molten layer solidifies due to heat extraction, nucleation grains take place in the melt pool. Subsequently, the grains grow with further heat extraction. In general, the melt pool is surrounded by an inert gas atmosphere over the top, a powder layer on one side, and a solid substrate or preceding layer at the bottom [75]. Thus, heat extraction takes place through radiation at the top. Along the sides, convection dominates on one side, and on the other side it may be either convection or radiation depending on the presence of powder or solid surface. The heat transfer along the bottom will be via conduction mode [88]. The melt pool in the SM sample is surrounded by powder, argon atmosphere and preceding layer. Hence the cooling rate near the top, side and bottom is higher than the core of the melt pool [75]. Thus, the nucleation of smaller grains will be higher near the substrate and preceding layer of the sample, while the core of the melt pool results in coarser grains. During remelting, the melt

Table 2

Peak temperature and cooling rate of SM and TM Ti–40Nb samples.

| Sample designation | Peak temperature (T_p) (K) | Cooling rate (K/s) |
|--------------------|--------------------------------|--------------------|
| SM | 5606 | 6.9×10^5 |
| TM | 3067 | 3.2×10^5 |

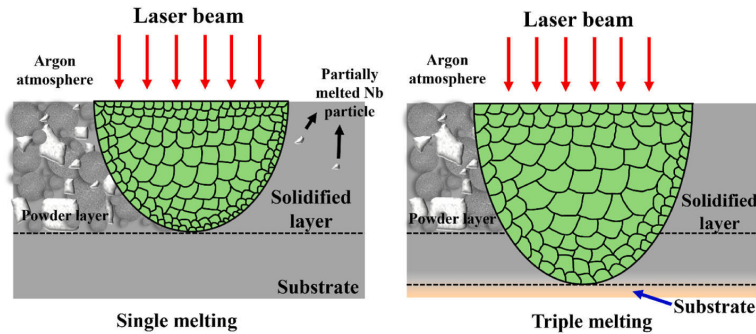


Fig. 13. Schematics illustrating the formation of grains and its variations in the selective laser melted Ti-40Nb samples after both single and triple melting.

pool in the TM sample is surrounded by preceding layers and argon atmosphere. In the first melting and solidification of the powder layer, the heat is extracted through the underlying solid substrate. Therefore, the solid surface underneath the solidified layer gets heated above room temperature. When the same layer is subjected to remelting and solidification, the underlying solid surface that is already maintained above room temperature cannot transfer the heat at the initial rates. This results in a reduced heat transfer and hence reduced temperature gradient across the sample promoting grain growth. Consequently, the grains on the bottom and side of the melt pool in the TM sample are larger than the SM sample. Furthermore, the deeper melt pool in TM provides additional space for the growth of coarser grains. Thus, the grain size in the TM sample is significantly coarser than that of the SM sample. In addition, since the cooling rate is reduced in the TM sample as compared to the SM condition, less internal strain will be generated during the solidification process and as a result, the TM samples show a reduced amount of internal crystal defects like the dislocation and twins.

4.2. Niobium diffusion

In the selective laser melted Ti-40Nb alloy (especially fabricated from the elemental powder mixtures), incomplete melting and diffusion of Nb are the major issues that affect the homogeneity of the material. One of the reasons will be the difference in the melting points of the elements (Ti and Nb). The difference in the melting points of Ti and Nb is ~800 K making congruent melting difficult during melting. Since rapid solidification is observed during the SLM process, there is not much time available for the Nb solute to diffuse with the Ti solvent. Hence, as shown in Fig. 5(a–c) the SLM-processed SM sample exhibited a non-homogeneous structure with incomplete Nb diffusion. However, the remelting approach employed effectively addresses this issue by achieving homogeneous melting and enhanced Nb diffusion. This enhancement can be ascribed to the Bernard-Marangoni convection [89]. The Marangoni convection plays a crucial role in mass transfer within the melt pool, driven by the temperature gradient that creates regions of low and high surface tension. The fluid flow transports the material from one part of the melt pool to the other, where the unmelted Nb particles are transported within the melt pool. This dynamic process ensures homogeneity through the continuous circulation of material within the melt pool.

During single melting, the interaction between the laser beam and the powder forms a smaller melt pool due to reduced thermal penetration, resulting from the low thermal conductivity of the powder caused by the presence of voids [53]. The smaller melt pool limits fluid flow, leading to non-homogeneity and incomplete melting of Nb particles. The incomplete melting occurs due to the larger size and higher melting point of Nb particles, which require more energy for complete melting and diffusion. The size of the powder particles significantly influences

the solidification process: smaller particles with a higher surface area-to-volume ratio and surface energy, melt and diffuse completely upon solidification, while larger particles, with a lower surface area-to-volume ratio and surface energy, melt and diffuse partially, leaving behind incompletely melted Nb particles. In addition, due to rapid solidification, the time required for the diffusion of Nb into Ti is insufficient, leading to partial diffusion. During the remelting process, the increased thermal conductivity of the bulk material enhances heat absorption into the metal, leading to higher thermal penetration. In addition, the heat accumulation associated with remelting minimizes the temperature gradient across the sample promoting the formation of a deeper melt pool [90]. This deeper melt pool generates a more severe vortex, enhancing fluid flow within the melt pool. As the size of previously incompletely melted Nb particles is smaller, their surface area decreases requiring less energy for complete melting. The remelting thus provides the necessary energy to facilitate the complete melting and diffusion of Nb particles, leading to a homogeneous mixture within the melt pool. In addition, the slower solidification rates allow sufficient time for the Nb to have a complete diffusion into Ti. Hence, upon solidification, this results in the formation of a homogeneous microstructure.

Fig. 14 shows the schematic representation of the Marangoni effect observed in the SM and TM samples, highlighting the differences in melt pool shape and fluid flow. In both SM and TM samples, the particles flow in an outward direction from the core of the melt pool, near the surface (peak temperature and low surface tension), to the edge and bottom of the melt pool (lower temperature and higher surface tension). When the powder layer is irradiated, the surface and central region of the melt pool melt first and flow toward the bottom, while particles from the bottom flow toward the surface. The smaller melt pool in the SM sample restricts fluid flow, limiting the ability to achieve homogeneous melting. In contrast, the deeper melt pool in the TM sample generates a more intense vortex, allowing the fluid to circulate multiple times within the melt pool, thereby promoting uniform melting. In the SM sample, insufficient melting leads to the presence of partially melted Nb particles in the preceding layer. However, when this preceding layer is remelted in the TM process, the enhanced Marangoni flow facilitates complete mixing and homogenization within the solidified layer. The effectiveness of the remelting was confirmed by the hardness distribution plot of the SM and TM shown in Fig. 11, where the increased remelting conditions resulted in uniform hardness distribution in the TM sample.

4.3. Mechanical property variation

Furthermore, the remelting strategy has a notable effect on the mechanical behaviour of the SM and TM samples. The mechanical properties of the fabricated sample are governed by a combination of factors, including β -phase stability, the presence of residual unmelted Nb

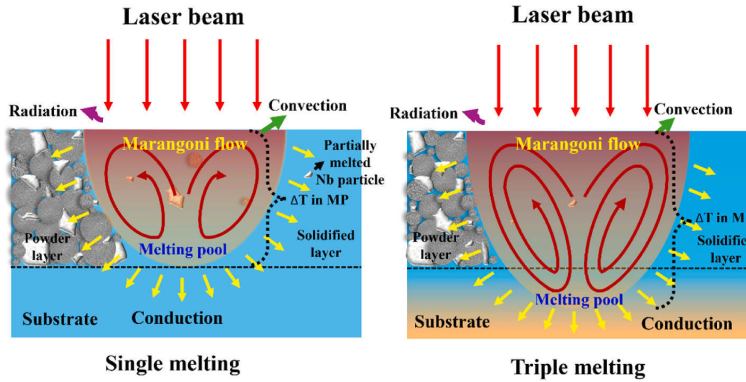


Fig. 14. Schematic representation of the Marangoni-convection observed in melt pool during the selective laser melting of Ti-40Nb samples both during single and trip melting.

particles, grain size, alloying - solid solution strengthening, martensitic transformation, and internal defects such as dislocations. In the SM, rapid solidification favors the formation of a metastable β -phase matrix, where Nb dissolution is incomplete, leaving residual Nb particles embedded in the matrix. Although β -phase exhibits lower strength compared to α' martensite, the overall strength of SM samples is improved through two primary mechanisms: (i) the formation of α' martensite, which enhances strength due to its hexagonal close-packed (hcp) structure with limited slip systems, and (ii) the presence of residual Nb particles that act as impenetrable barriers to dislocation glide, promoting dislocation bowing and entanglement in accordance with the Orowan strengthening mechanism. These obstacles increase the local dislocation density and inhibit slip, thereby improving yield strength despite the softer β matrix. In contrast, the TM condition promotes complete Nb dissolution and results in a uniform $\alpha' + \beta$ microstructure without discrete Nb inclusions. While this homogeneous structure is beneficial for microstructural stability, it presents fewer barriers to dislocation motion, reducing the potential for dislocation accumulation and interaction, and hence lowering the overall strength compared to SM. Additionally, the observed variation in hardness, yield strength, and ultimate compressive strength of the SM and TM samples can also be attributed to contributions from grain refinement strengthening and dislocation strengthening. Grain refinement strengthening refers to an increase in the strength of the material as the grain size decreases. Smaller grains result in a higher grain boundary density, which serves as barriers to dislocation motion [13]. These grain boundaries hinder the movement of dislocations, necessitating higher energy for dislocations to propagate through them. This increased resistance to dislocation motion leads to enhanced material strength. The grain boundary strengthening can be quantified by the Hall-pitch relationship, which is provided in equation (8) [91]:

$$\Delta\sigma_{HP} = k(D)^{-1/2} \quad (8)$$

where, k is the Hall-Petch constant and D is the grain size in μm . Based on the grain size observed from the SEM images, the $\Delta\sigma_{HP}$ for the SM sample is calculated to be ~ 114 MPa, which is higher than that of the TM sample (~ 96 MPa). The dislocation strengthening effect directly depends on the dislocation density of the fabricated Ti-40Nb samples [92]. The TEM analysis reveals a high dislocation density in SM as compared to TM. As dislocation density increases, the yield strength of the material also increases, making it more resistant to plastic deformation under applied stress. This increase in yield strength caused by dislocation can be expressed using equation (9) [93],

$$\Delta\sigma_{dislocation} = \beta M G b \sqrt{\rho_d} \quad (9)$$

where β is Taylor constant = 0.5 [94], M is Taylor factor = 3.06, G is the shear modulus of Ti-Nb alloy = 30 GPa [95], b is burger vector = $0.254 \times 10 \text{ nm}$ [96], and ρ_d - dislocation density as calculated from the XRD patterns. The dislocation density observed for the SM and TM samples are $0.99 \times 10^{15} \text{ m}^{-2}$ and $0.91 \times 10^{15} \text{ m}^{-2}$, respectively. Hence, the $\Delta\sigma_{dislocation}$ value for the SM is calculated to be ~ 367 MPa, and for the TM sample $\Delta\sigma_{dislocation}$ is observed to be ~ 348 MPa. The combined effects of grain refinement and dislocation strengthening contribute to the mechanical properties of the TM sample. However, the experimental strength of the material is observed to be lower than theoretical strength, which may be attributed to the processing defects and other experimental factors. Owing to the coarser grain size and reduced density of internal defects (twins and dislocations), the TM sample exhibits lower strength compared to the SM sample. However, the TM sample demonstrates improved plasticity, which can be attributed to the reduction in internal and external defects resulting from the remelting process. Despite the decrease in strength caused by the remelting approach, the presence of a dual microstructure ($\alpha' + \beta$ phase) in the TM sample significantly enhances the overall mechanical properties of the TM sample compared to the existing Ti-40Nb alloy [70,97,98]. Table 3 furnishes the comparison of the mechanical properties of existing Ti-Nb alloy fabricated via SLM with the Ti-40Nb alloy fabricated in the present work.

The overall schematic representation of the effect of remelting on the melt pool dimension and microstructure is illustrated in Fig. 15. During the SM process, the interaction between the laser beam and the powder layer results in the formation of a smaller melt pool with a higher temperature gradient. This leads to limited fluid flow within the melt pool and faster cooling rates are experienced, which in turn produces a heterogeneous microstructure with finer grains and smaller α' martensite. Additionally, an increase in internal defects such as twins and dislocation density are observed along with unmelted Nb particles. On the other hand, in the TM condition, a deeper melt pool with enhanced fluid flow resulted in a homogeneous microstructure with coarser grains and larger α' martensite. Additionally, a reduction in internal defects was observed. The current study on selective laser melting (SLM) of Ti-40Nb alloy demonstrates that the remelting strategy can be effectively applied in the SLM fabrication of elemental powders with in-situ alloying. This approach successfully reduces internal defects, including porosity, twins, and dislocations, thereby enhancing the density of the TM samples. It also addresses the incomplete diffusion of Nb, resulting in a homogenized microstructure. Although the remelted sample exhibits reduced strength, it maintains a combination of low modulus and high strength, which is desirable for orthopedic implants. Hence, using the remelting approach, powders with significant

Table 3

The table furnishes the mechanical properties of Ti–Nb alloy fabricated via SLM using pre-alloyed and elemental powder, where Comp. corresponds to the composition, H – hardness, EM – elastic modulus, CYS – compressive yield strength, UCS – ultimate yield strength, Ref. – reference, TWSM – this work and single melting, and TWTM – this work and triple melting condition.

| Comp. (wt.%) | Method | Powder condition | H, HV | EM, GPa | CYS, MPa | UCS, MPa | Ref. |
|--------------|--------|------------------|-------|---------|----------|----------|-------|
| Ti–45Nb | SLM | Pre-alloyed | 257 | 50 | 380 | 723 | [99] |
| Ti–42Nb | SLM | Pre-alloyed | – | 65 | 701 | 800 | [100] |
| Ti–35Nb | SLM | Pre-alloyed | 174 | 72 | – | – | [101] |
| Ti–41Nb | SLM | Pre-alloyed | – | – | 504 | 1100 | [102] |
| Ti–45Nb | SLM | Pre-alloyed | 155 | – | – | – | [103] |
| Ti–35Nb | SLM | Elemental | 274 | – | – | – | [104] |
| Ti–41Nb | SLM | Elemental | 268 | 77 | – | – | [105] |
| Ti–45Nb | SLM | Elemental | 356 | – | – | – | [106] |
| Ti–25Nb | SLM | Elemental | 264 | – | – | – | [107] |
| Ti–40Nb | SLM | Elemental | 278 | – | – | – | [108] |
| Ti–30Nb | SLM | Elemental | – | 82 | 650 | – | [109] |
| Ti–30Nb | SLM | Elemental | 318 | – | 894 | 1650 | [110] |
| Ti–45Nb | SLM | Elemental | – | 83 | – | – | [111] |
| Ti–35Nb | SLM | Elemental | 240 | 84 | 660 | – | [112] |
| Ti40Nb | SLM | Elemental | 384 | 34 | 1040 | 1752 | TWSM |
| Ti40Nb | SLM | Elemental | 368 | 33 | 820 | 1480 | TWTM |

disparities in melting temperature can be printed in the desired combination. Processing in-situ alloyed powder using a remelting strategy can serve as a promising alternative to costly pre-alloyed powder. However, further research on comparing the properties of remelted Ti–40Nb samples with other fabrication techniques is essential to gain a deeper understanding of the material’s properties and behavior.

5. Conclusion

The present study demonstrates the fabrication of Ti–40Nb alloy by selective laser melting via in-situ alloying of elemental powders using a laser remelting strategy, aiming for orthopedic applications. The effects of remelting on material homogenization, defect reduction (including porosity, twins, and dislocations), Nb diffusion, microstructural evolution, and mechanical properties were investigated. The key findings are as follows.

- (1) The phase composition of both the Ti–40Nb samples processed under single and triple melting conditions reveal the presence of *hcp* – α' martensite and *bcc* – β phases.
- (2) The heat input significantly affected the cooling rate of the remelted sample. Remelting with a laser power of 650 W and a scan speed of 650 mm/s resulted in a larger and deeper melt pool, reducing the cooling rate and allowing sufficient time for Nb diffusion.
- (3) Triple melting increased the length and width of lamellar *hcp* – α' martensite and grain size due to the decreased cooling rate. Importantly, triple melting also reduced internal defects such as porosity, dislocation density, and twins.
- (4) While remelting led to homogenization and a uniform hardness distribution across the triple-melted sample, grain growth due to the reduced cooling rate caused a decrease in hardness and ultimate strength compared to the single-melted sample. However, the combination of high strength and low modulus was maintained in the triple melt sample fulfilling the criteria for orthopedic application. In addition, the reduction of internal defects and enhanced homogeneity are advantageous for the long-term stability and performance of the implant.

The obtained results suggest that the remelting strategy allows for the fabrication of high-quality Ti–40Nb orthopedic implants directly from elemental powders replacing costly pre-alloyed powders. Additionally, the flexibility in controlling material properties through

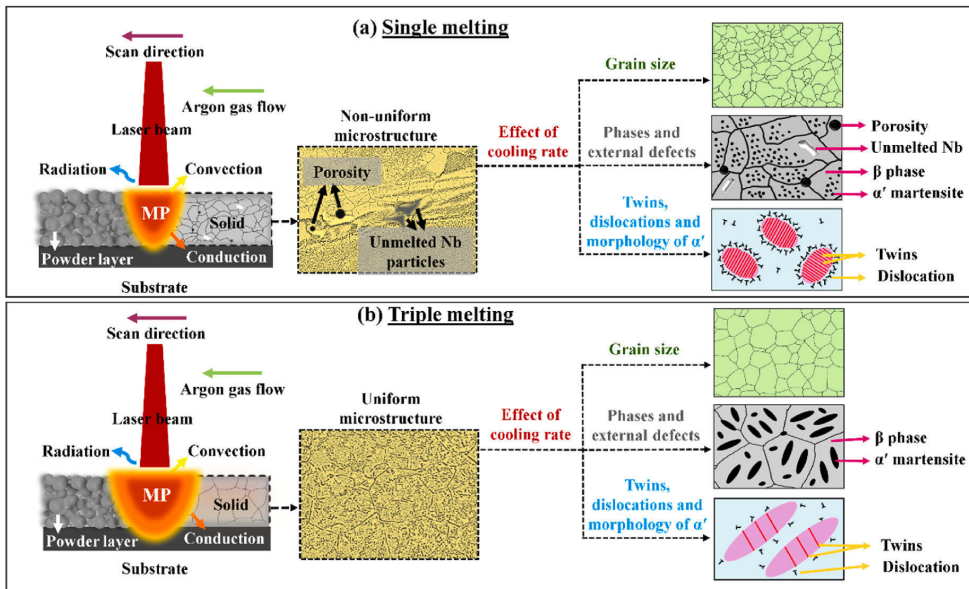


Fig. 15. Schematic representation of the effect of remelting on the microstructure and mechanical properties of the selective laser melted Ti–40Nb samples during (a) single and (b) triple melting.

remelting opens new possibilities for developing novel Ti–40Nb orthopedic implants tailored to specific patient needs.

Author contributions

Shangavi Subramanian – Conceptualization, methodology, data curation, investigation, formal analysis, writing – original draft; Mayank Kumar Yadav – methodology, data curation, investigation, formal analysis, writing – original draft; J. Jayaraj – conceptualization, investigation, data curation, validation, supervision, writing – review and editing; Fan Yangyang – data curation, investigation, formal analysis, writing – original draft; Lixia Xi – data curation, investigation, formal analysis, funding acquisition, writing – original draft; K.G. Prashanth – conceptualization, validation, resources, supervision, project administration, funding acquisition, writing – review and editing.

Data availability

Data may be made available at reasonable request to the authors.

Declaration of competing interest

The authors declare that they have no known competing financial interests or personal relationships that could have appeared to influence the work reported in this paper.

Acknowledgments

The present research was partially supported by the National Natural Science Foundation of China (52205382) and special fund of Jiangsu Province Science and Technology Plan (BZ2024019).

References

- [1] Sidambe AT. Biocompatibility of advanced manufactured titanium implants-A review. *Materials* 2014;7:8168–88. <https://doi.org/10.3390/ma7128168>.
- [2] Geetha M, Singh AK, Asokamani R, Gogia AK. Ti based biomaterials, the ultimate choice for orthopaedic implants - a review. *Prog Mater Sci* 2009;54:397–425. <https://doi.org/10.1016/j.pmatsci.2008.06.004>.
- [3] Al-Shalawi FD, Mohamed Ariff AH, Jung DW, Mohd Ariffin MKA, Seng Kim CL, Brabazon D, et al. Biomaterials as implants in the orthopedic field for regenerative medicine: metal versus synthetic polymers. *Polymers* 2023;15:2601. <https://doi.org/10.3390/POLYM15122601>. 2023;15:2601.
- [4] Nicholson J W. Titanium alloys for dental implants: a review. *Prosthesis* 2020;2: 100–116. <https://doi.org/10.3390/prosthesis2020011>.
- [5] Rabeeh VPM, Hanas T. Progress in manufacturing and processing of degradable Fe-based implants: a review. *Prog Biomater* 2022 11:2 2022;11:163–91. <https://doi.org/10.1007/s40204-022-00189-4>.
- [6] Sumayli A. Recent trends on biomaterial materials: a review. *Mater Today Proc* 2021;46:2726–31. <https://doi.org/10.1016/j.matpr.2021.02.395>.
- [7] Liu S, Shin YC. Additive manufacturing of Ti6Al4V alloy: a review. *Mater Des* 2019;164:107552. <https://doi.org/10.1016/j.matdes.2018.107552>.
- [8] Zhuravleva K, Müller R, Schultz L, Eckert J, Gebert A, Bobeth M, et al. Determination of the Young's modulus of porous β -type Ti–40Nb by finite element analysis. *Mater Des* 2014;64:1–8. <https://doi.org/10.1016/j.matdes.2014.07.027>.
- [9] Niinomi M, Nakai M. Titanium-based biomaterials for preventing stress shielding between implant devices and bone. *Int J Biomater* 2011;2011:836587. <https://doi.org/10.1155/2011/836587>.
- [10] Attar H, Prashanth KG, Chaubey AK, Calin M, Zhang LC, Scudino S, et al. Comparison of wear properties of commercially pure titanium prepared by selective laser melting and casting processes. *Mater Lett* 2015;142:38–41. <https://doi.org/10.1016/j.matlet.2014.11.156>.
- [11] Xiong S, Hao T, Sun Y, Yang J, Ma R, Wang J, et al. Defect passivation by nontoxic biomaterial yields 21% efficiency perovskite solar cells. *J Energy Chem* 2021;55: 265–71. <https://doi.org/10.1016/j.jechem.2020.06.061>.
- [12] Abd-Elaziem W, Darwish MA, Hamada A, Daoush WM. Titanium-Based alloys and composites for orthopedic implants Applications: a comprehensive review. *Mater Des* 2024;241:112850. <https://doi.org/10.1016/j.matdes.2024.112850>.
- [13] Ummethala R, Karamched PS, Rathinavelu S, Singh N, Aggarwal A, Sun K, et al. Selective laser melting of high-strength, low-modulus Ti–35Nb–7Zr–5Ta alloy. *Materialia* 2020;14:100941. <https://doi.org/10.1016/j.matla.2020.100941>.
- [14] Guillemot F. Recent advances in the design of titanium alloys for orthopedic applications. *Exp Rev Med Dev* 2005;2:741–8. <https://doi.org/10.1586/17434440.2.6.741>.
- [15] Caprio L, Göhkan Demir A, Previtali B, Wu C, Wen J, Zhang J, et al. Forming a single layer of a composite powder based on the Ti-Nb system via selective laser melting (SLM). *IOP Conf Ser Mater Sci Eng* 2016;140:012001. <https://doi.org/10.1088/1757-899X/140/1/012001>.
- [16] Brodie EG, Medvedev AE, Frith JE, Dargusch MS, Fraser HL, Molotnikov A. Remelt processing and microstructure of selective laser melted Ti25Ta. *J Alloys Compd* 2020;820:153082. <https://doi.org/10.1016/j.jallcom.2019.153082>.
- [17] Zhou L, Yuan T, Li R, Tang J, Wang M, Mei F. Anisotropic mechanical behavior of biomedical Ti–13Nb–13Zr alloy manufactured by selective laser melting. *J Alloys Compd* 2018;762:289–300. <https://doi.org/10.1016/j.jallcom.2018.05.179>.
- [18] Zhuravleva K, Bönisch M, Prashanth KG, Hempel U, Helth A, Gemming T, et al. Production of porous β -type Ti–40Nb alloy for biomedical applications: comparison of selective laser melting and hot pressing. *Materials* 2013;6: 5700–12. <https://doi.org/10.3390/ma6125700>.
- [19] Liu J, Ruan J, Chang L, Yang H, Ruan W. Porous Nb-Ti-Ta alloy scaffolds for bone tissue engineering: fabrication, mechanical properties and in vitro/vivo biocompatibility. *Mater Sci Eng C* 2017;78:503–12. <https://doi.org/10.1016/j.msec.2017.04.088>.
- [20] Bălăţu MS, Vizureanu P, Tierean MH, Minciună MG, Achiței DC. Ti-Mo alloys used in medical applications. *Adv Mater Res* 2015;1128:105–11. <https://doi.org/10.4028/www.scientific.net/AMR.1128.105>.
- [21] Maity T, Balci Gmitter C, Ivanov E, Eckert J, Prashanth KG. High pressure torsion induced lowering of Young's modulus in high strength TNZT alloy for bio-implant applications. *J Mech Behav Biomed Mater* 2020;108:103839. <https://doi.org/10.1016/j.jmbmm.2020.103839>.
- [22] Guo S, Zhang J, Cheng X, Zhao X. A metastable β -type Ti–Nb binary alloy with low modulus and high strength. *J Alloys Compd* 2015;644:411–5. <https://doi.org/10.1016/j.jallcom.2015.05.071>.
- [23] Prashanth K, Zhuravleva K, Okulov I, Calin M, Eckert J, Gebert A. Mechanical and corrosion behavior of new generation Ti–45Nb porous alloys implant devices. *Technologies* 2016;4:33. <https://doi.org/10.3390/technologies4040033>.
- [24] Hao YL, Li SJ, Sun SY, Yang R. Effect of Zr and Sn on Young's modulus and superelasticity of Ti-Nb-based alloys. *Mater Sci Eng* 2006;44:112–8. <https://doi.org/10.1016/j.msea.2006.09.051>.
- [25] Bönisch M, Panigrahi A, Calin M, Waitz T, Zehetbauer M, Skrotzki W, et al. Thermal stability and latent heat of Nb-rich martensitic Ti–Nb alloys. *J Alloys Compd* 2017;697:300–9. <https://doi.org/10.1016/j.jallcom.2016.12.108>.
- [26] Bönisch M, Calin M, Waitz T, Panigrahi A, Zehetbauer M, Gebert A, et al. Thermal stability and phase transformations of martensitic Ti–Nb alloys. *Sci Technol Adv Mater* 2013;14:55004–13. <https://doi.org/10.1088/1468-6996/14/5/055004>.
- [27] Qiang M, Yang X rong, jie Wang G, yan Liu X, Luo L, Ren Q, et al. Enhanced strength and reduced elastic modulus of biomedical metastable β Ti–Nb alloy via intermediate phase transformation. *Mater Des* 2025;251:113662. <https://doi.org/10.1016/j.matdes.2025.113662>.
- [28] Han MK, Kim JY, Hwang MJ, Song HJ, Park YJ. Effect of Nb on the microstructure, mechanical properties, corrosion behavior, and cytotoxicity of Ti–Nb alloys. *Materials* 2015;8:5986–6003. <https://doi.org/10.3390/MA8095287>. 2015;8:5986–6003.
- [29] Lee CM, Ju CP, Chern Lin JH. Structure-property relationship of cast Ti–Nb alloys. *J Oral Rehabil* 2002;29:314–22. <https://doi.org/10.1046/j.1365-2842.2002.00825.x>.
- [30] Dos Santos RF, Rossi MC, Vidilli AL, Amigó Borrás V, Afonso CRM. Assessment of β stabilizers additions on microstructure and properties of as-cast β Ti–Nb based alloys. *J Mater Res Technol* 2023;22:3511–24. <https://doi.org/10.1016/j.jmrt.2022.12.144>.
- [31] Hao D, Lei Z, Yuqin Z, Zongyu Z, Fei H. The microstructure, mechanical properties and in-vitro biological compatibility of porous Ti–40Nb alloy fabricated by spark plasma sintering. *Mater Res Express* 2019;6:1065f3. <https://doi.org/10.1088/2053-1591/ab40f5>.
- [32] Karre R, Kodli BK, Rajendran A, J N, Pattanayak DK, Ameyama K, et al. Comparative study on Ti–Nb binary alloys fabricated through spark plasma sintering and conventional P/M routes for biomedical application. *Mater Sci Eng C* 2019;94:619–27. <https://doi.org/10.1016/j.msec.2018.10.006>.
- [33] Ahmad M, Javaid M, Haleem A. Enhancing biocompatible metal alloy fabrication for bio implants through laser-based additive manufacturing (LBAM). *Biomed Anal* 2024;1:73–85. <https://doi.org/10.1016/j.bioana.2024.02.001>.
- [34] Balasubramani T, Kumar NM, Aseer JR, Sivaram NM. Additive manufacturing of Ti–6 Al–4 V alloys: fabrication techniques and material properties—review. *Trans Indian Inst Met* 2025;78:1–15. <https://doi.org/10.1007/s12666-025-03625-8/FIGURES/12>.
- [35] Sharkeev YP, Eroshenko AY, Kovalevskaya ZG, Saprykin AA, Ibragimov EA, Glukhov IA, et al. Phase composition and microstructure of Ti–Nb alloy produced by selective laser melting. In: *IOP conf ser mater sci eng*, vol. 140. Institute of Physics Publishing; 2016. <https://doi.org/10.1088/1757-899X/140/1/012020>.
- [36] Subramanian S, Mohanty S, Prashanth KG. Effect of process parameters on the properties of β -Ti–Nb-based alloys fabricated by selective laser melting: a review. *Mater Today Proc* 2023. <https://doi.org/10.1016/j.matpr.2023.03.461>.
- [37] Prashanth KG. Selective laser melting: materials and applications. *J Manuf Mater Proc* 2020;4:13. <https://doi.org/10.3390/jmmp4010013>.
- [38] Zhao X, Li S, Zhang M, Liu Y, Sercombe TB, Wang S, et al. Comparison of the microstructures and mechanical properties of Ti–6Al–4V fabricated by selective laser melting and electron beam melting. *Mater Des* 2016;95:21–31. <https://doi.org/10.1016/j.matdes.2015.12.135>.
- [39] Li Z, Qiu J, Xu H, Dong A, He L, Zhu G, et al. Characteristics of β -type Ti–41Nb alloy produced by laser powder bed fusion: microstructure, mechanical properties

- and in vitro biocompatibility. *J Mater Sci Technol* 2022;124:260–72. <https://doi.org/10.1016/J.JMST.2022.02.026>.
- [40] Pilz S, Gustmann T, Günther F, Zimmermann M, Kühn U, Gebert A. Controlling the Young's modulus of a β -type Ti-Nb alloy via strong texturing by LPBF. *Mater Des* 2022;216:110516. <https://doi.org/10.1016/J.MATDES.2022.110516>.
- [41] Qin P, Chen LY, Zhao CH, Liu YJ, Cao CD, Sun H, et al. Corrosion behavior and mechanism of selective laser melted Ti35Nb alloy produced using pre-alloyed and mixed powder in Hank's solution. *Corros Sci* 2021;189:109609. <https://doi.org/10.1016/J.CORSCI.2021.109609>.
- [42] Feng S, Jia D, Fu Y, Kong X, Lv Z, Zeng E, et al. Preparation of additive manufacturing powder by external field-enabled: a comparative assessment. *Int J Adv Des Manuf Technol* 2023;131(5):3239–65. <https://doi.org/10.1007/S00170-023-12073-X>. 2023;131.
- [43] Zerwas AA, da Silva FC, Guardani R, Achelis L, Frisching U. Impact of the gas atomizer nozzle configuration on metal powder production for additive manufacturing. *Powder Technol* 2024;443:119974. <https://doi.org/10.1016/J.POWTEC.2024.119974>.
- [44] Soong SZ, Lai WL, Kay Lup AN. Atomization of metal and alloy powders: processes, parameters, and properties. *AIChE J* 2023;69:e18217. <https://doi.org/10.1002/AIC.18217>.
- [45] Huang S, Narayan RL, Tan JHK, Sing SL, Yeong WY. Resolving the porosity-unmelted inclusion dilemma during in-situ alloying of Ti34Nb via laser powder bed fusion. *Acta Mater* 2021;204:116522. <https://doi.org/10.1016/J.ACTAMAT.2020.116522>.
- [46] Wei J, Sun H, Zhang D, Gong L, Lin J, Wen C. Influence of heat treatments on microstructure and mechanical properties of Ti–26Nb alloy elaborated in situ by laser additive manufacturing with Ti and Nb mixed powder. *Materials* 2019;12:61. <https://doi.org/10.3390/MA12010061>. 2018;12:61.
- [47] Schulze C, Weinmann M, Schweigel C, Keßler O, Bader R. Mechanical properties of a newly additive manufactured implant material based on Ti-42Nb. *Materials* 2018;11:124. <https://doi.org/10.3390/MA11010124>. 2018;11:124.
- [48] Ren N, Li J, Zhang R, Panwisawas C, Xia M, Dong H, et al. Solute trapping and non-equilibrium microstructure during rapid solidification of additive manufacturing. *Nat Commun* 2023;14. <https://doi.org/10.1038/s41467-023-43563-x>.
- [49] Ye Z, Zhao K, Yu Z, Prashanth KG, Zhang F, He Y, et al. Understanding the solute segregation and redistribution behavior in rapidly solidified binary Ti-X alloys fabricated through non-equilibrium laser processing. *Addit Manuf* 2024;96: 104561. <https://doi.org/10.1016/J.ADDMA.2024.104561>.
- [50] Cheng Y, Wang G, Qiu Z, Zheng Z, Zeng D, Tang X, et al. Multi-physics simulation of non-equilibrium solidification in Ti-Nb alloy during selective laser melting. *Acta Mater* 2024;272:119923. <https://doi.org/10.1016/J.ACTAMAT.2024.119923>.
- [51] Zhang K, Zhong N, Zhang X, Wen C, Zhou Y, Lu S. Effect of heat treatment on the microstructure and mechanical properties of biocompatible Ti-Ta-Nb-Zr alloys prepared by selective laser melting. *Int J Mater Res* 2024;115:349–58. <https://doi.org/10.1515/IJMR-2022-0467/MACHINEREADABLECITATION/RIS>.
- [52] Yu Z, Zheng Y, Chen J, Wu C, Xu J, Lu H, et al. Effect of laser remelting processing on microstructure and mechanical properties of 17-4 PH stainless steel during laser direct metal deposition. *J Mater Process Technol* 2020;284:116738. <https://doi.org/10.1016/J.JMATPROTEC.2020.116738>.
- [53] Karimi J, Suryanarayana C, Okulov I, Prashanth KG. Selective laser melting of Ti6Al4V: effect of laser re-melting. *Mater Sci Eng* 2020;805:140558. <https://doi.org/10.1016/j.msea.2020.140558>.
- [54] Bedmar J, de la Pezuela J, Riquelme A, Torres B, Rams J. Impact of remelting in the microstructure and corrosion properties of the Ti6Al4V fabricated by selective laser melting. *Coatings* 2022;12:284. <https://doi.org/10.3390/COATINGS12020284>. 2022;12:284.
- [55] Gustmann T, Schwab H, Kühn U, Pauly S. Selective laser remelting of an additively manufactured Cu-Al-Ni-Mn shape-memory alloy. *Mater Des* 2018;153: 129–38. <https://doi.org/10.1016/j.matdes.2018.05.010>.
- [56] Simoni F, Huxol A, Villmer FJ. Improving surface quality in selective laser melting based tool making. *J Intell Manuf* 2021;32:1927–38. <https://doi.org/10.1007/S10845-021-01744-9/FIGURES/14>.
- [57] dos Santos Paes LE, Pereira M, Xavier FA, Weingaertner WL, D'Oliveira ASCM, Costa EC, et al. Understanding the behavior of laser surface remelting after directed energy deposition additive manufacturing through comparing the use of iron and Inconel powders. *J Manuf Process* 2021;70:494–507. <https://doi.org/10.1016/J.JMAPRO.2021.08.061>.
- [58] Masood Arif Bukhari S, Husnain N, Arsalan Siddiqui F, Tuoqeer Anwar M, Abbas Khosa A, Imran M, et al. Effect of laser surface remelting on Microstructure, mechanical properties and tribological properties of metals and alloys: a review. *Opt Laser Technol* 2023;165:109588. <https://doi.org/10.1016/J.OPTLASTEC.2023.109588>.
- [59] Kuali Z, Li Z, Liu B, Liu W, Yang S. Effects of remelting on the surface morphology, microstructure and mechanical properties of AlSi10Mg alloy fabricated by selective laser melting. *Mater Chem Phys* 2022;285:125901. <https://doi.org/10.1016/J.MATCHEMPHYS.2022.125901>.
- [60] Huang S, Sing SL, Yeong WY. Selective laser melting of Ti42Nb composite powder and the effect of laser re-melting. *Key Eng Mater* 2019;801:270–5. <https://doi.org/10.4028/WWW.SCIENRFIC.NET/KEM.801.270>.
- [61] Prashanth KG, Scudino S, Eckert J. Defining the tensile properties of Al-12Si parts produced by selective laser melting. *Acta Mater* 2017;126:25–35. <https://doi.org/10.1016/j.actamat.2016.12.044>.
- [62] Karimi J, Antonov M, Kollo L, Prashanth KG. Role of laser remelting and heat treatment in mechanical and tribological properties of selective laser melted Ti6Al4V alloy. *J Alloys Compd* 2022;897:163207. <https://doi.org/10.1016/J.JALLCOM.2021.163207>.
- [63] Song J, Tang Q, Feng Q, Han Q, Ma S, Chen H, et al. Effect of remelting processes on the microstructure and mechanical behaviours of 18Ni-300 maraging steel manufactured by selective laser melting. *Mater Char* 2022;184:111648. <https://doi.org/10.1016/J.MATCHAR.2021.111648>.
- [64] Karimi J, Kollo L, Rahmani R, Ma P, Jia YD, Prashanth KG. Selective laser melting of in-situ CoCrFeMnNi high entropy alloy: effect of remelting. *J Manuf Process* 2022;84:55–63. <https://doi.org/10.1016/J.JMAPRO.2022.09.056>.
- [65] Eiumtadana S, Mahathanabodee S, Tongssri R, Vetayanugul B, Wiman P. Deformation and corrosion resistance of sintered AISI 303 austenitic stainless steel after hot forging. *J Mater Eng Perform* 2025;1–14. <https://doi.org/10.1007/S11665-025-11276-5/FIGURES/9>.
- [66] Zhang LC, Xu WY, Li Z, Zheng L, Liu YF, Zhang GQ. Mechanism of rapidly solidified satellites formation in gas atomized powders: simulation and characterization. *Powder Technol* 2023;418:118162. <https://doi.org/10.1016/J.POWTEC.2022.118162>.
- [67] Suryanarayana C. Mechanical alloying and milling, vol. 46; 2001. [https://doi.org/10.1016/S0079-6425\(99\)00010-9](https://doi.org/10.1016/S0079-6425(99)00010-9).
- [68] Wysocki B, Maj P, Krawczyńska A, Roźniatowski K, Zdunek J, Kurzydowski KJ, et al. Microstructure and mechanical properties investigation of CP titanium processed by selective laser melting (SLM). *J Mater Process Technol* 2017;241: 13–23. <https://doi.org/10.1016/J.JMATPROTEC.2016.10.022>.
- [69] Barns RL. Niobium: lattice parameter and density. *J Appl Phys* 1968;39:4044–5. <https://doi.org/10.1063/1.1656912>.
- [70] Kalita D, Rogal L, Czeppe T, Wójcik A, Kolano-Burian A, Zackiewicz P, et al. Microstructure and mechanical properties of Ti-Nb alloys prepared by mechanical alloying and spark plasma sintering. *J Mater Eng Perform* 2020;29:1445–52. <https://doi.org/10.1007/S11665-019-04417-0/FIGURES/11>.
- [71] Marczewski M, Wiecekzak K, Maeder X, Lapeyre L, Hain C, Jurczyk M, et al. Microstructure and mechanical properties of Ti-Nb alloys: comparing conventional powder metallurgy, mechanical alloying, and high power impulse magnetron sputtering processes for supporting materials screening. *J Mater Sci* 2024;59:9107–25. <https://doi.org/10.1007/S10853-024-09715-0/FIGURES/2>.
- [72] Tirfe DA, Batu T, Ewnetu M, Beyene E, Woldeyohannes AD. Powder bed fusion of β -Ti-Nb-based ternary and quaternary titanium alloys for orthopedic implants: a review. *J Adv Manuf Process* 2025;7. <https://doi.org/10.1002/amp.270002>.
- [73] Lv F, Liang H, Xie D, Mao Y, Wang C, Shen L, et al. On the role of laser in situ remelting into pore elimination of Ti-6Al-4V components fabricated by selective laser melting. *J Alloys Compd* 2021;854:156866. <https://doi.org/10.1016/J.JALLCOM.2020.156866>.
- [74] Xiao Z, Chen C, Hu Z, Zhu H, Zeng X. Effect of rescanning cycles on the characteristics of selective laser melting of Ti6Al4V. *Opt Laser Technol* 2020;122: 105890. <https://doi.org/10.1016/J.OPTLASTEC.2019.105890>.
- [75] Zhao C, Wang Z, Li D, Kollo L, Luo Z, Zhang W, et al. Cu-Ni-Sn alloy fabricated by melt spinning and selective laser melting: a comparative study on the microstructure and formation kinetics. *J Mater Res Technol* 2020;9:13097–105. <https://doi.org/10.1016/j.jmrt.2020.09.047>.
- [76] Liu M, Zhang J, Chen C, Geng Z, Wu Y, Li D, et al. Additive manufacturing of pure niobium by laser powder bed fusion: microstructure, mechanical behavior and oxygen assisted embrittlement. *Mater Sci Eng, A* 2023;866:144691. <https://doi.org/10.1016/J.MSEA.2023.144691>.
- [77] Suwas S, Deepak Kumar. Microstructure–texture–mechanical property relationship in alloys produced by additive manufacturing following selective laser melting (SLM) technique. *Trans Indian Nat Acad Eng* 2020;5(1):1–10. <https://doi.org/10.1007/S41403-019-00081-X>. 2020;5.
- [78] Chlebus E, Kuźnicka B, Kurzynowski T, Dybala B. Microstructure and mechanical behaviour of Ti–6Al–7Nb alloy produced by selective laser melting. *Mater Char* 2011;62:488–95. <https://doi.org/10.1016/J.MATCHAR.2011.03.006>.
- [79] Attar H, Ehtemam-Haghighi S, Kent D, Dargusch MS. Laser additive manufacturing of low-cost Ti–Mo alloys: microstructural evolution, phase analysis, and mechanical properties. *Adv Eng Mater* 2023;25:2201265. <https://doi.org/10.1002/ADEM.202201265>.
- [80] Yang J, Yu H, Yin J, Gao M, Wang Z, Zeng X. Formation and control of martensite in Ti-6Al-4V alloy produced by selective laser melting. *Mater Des* 2016;108: 308–18. <https://doi.org/10.1016/J.MATDES.2016.06.117>.
- [81] Kou S. *Welding metallurgy*. third ed. Hoboken, New Jersey: Wiley; 2020.
- [82] Panda BK, Sahoo S, Siva Kumar C, Kumar Nath A. Multiscale modelling of microstructure evolution, and local solidification behaviours of the AlSi10Mg build component in laser powder bed fusion process. *Opt Laser Technol* 2025; 180:111446. <https://doi.org/10.1016/J.OPTLASTEC.2024.111446>.
- [83] Bychkov YF, Herzog R, Khukhareva IS. Thermal conductivity and electrical resistivity of NbTi alloys at low temperatures. *Cryogenics* 1981;21:741–5. [https://doi.org/10.1016/0011-2275\(81\)90219-8](https://doi.org/10.1016/0011-2275(81)90219-8).
- [84] Moffat DL, Kattner UR. Stable and metastable Ti-Nb phase diagrams. *Metall Trans A* 1988;19 A:2389–97. <https://doi.org/10.1007/BF02645466/METRICS>.
- [85] Li C, Guo H, Zheng L, Yang J, Ye L, Liu L, et al. Phase equilibria of the Ti-Nb-Mn ternary system at 1173K, 1273K and 1373K. *Processes* 2023;11:424. <https://doi.org/10.3390/PR11020424>. 2023;11:424.
- [86] Vollmer M. Newton's law of cooling revisited. *Eur J Phys* 2009;30:1063. <https://doi.org/10.1088/0143-0807/30/5/014>.
- [87] Davidson ML. Newton's law of cooling and its interpretation. *Int J Heat Mass Tran* 2012;55:5397–402. <https://doi.org/10.1016/J.IJHEATMASSTRANSFER.2012.03.035>.
- [88] Alkhariri MR, Furumoto T, Ueda T, Hosokawa A, Tanaka R, Abdul Aziz MS. Thermal conductivity of metal powder and consolidated material fabricated via

- selective laser melting. *Key Eng Mater* 2012;523–524:244–9. <https://doi.org/10.4028/WWW.SCIENTIFIC.NET/KEM.523-524.244>.
- [89] Ma P, Fang Y, Wei S, Zhang Z, Yang H, Wan S, et al. Microstructure and mechanical properties of AlCoCrFeMnNi HEAs fabricated by selective laser melting. *J Mater Res Technol* 2023;25:7090–100. <https://doi.org/10.1016/J.JMRT.2023.07.124>.
- [90] Karimi J, Xie MS, Wang Z, Prashanth KG. Influence of substructures on the selective laser melted Ti-6Al-4V alloy as a function of laser re-melting. *J Manuf Process* 2021;68:1387–94. <https://doi.org/10.1016/j.jmappro.2021.06.059>.
- [91] Zhang JW, Dong YP, Tang JC, Wang DW, Lu WJ, Li YL, et al. Additive manufacturing of the high-strength and low modulus biomedical Ti-10 Nb alloy under reactive atmosphere. *Mater Today Commun* 2022;33:104837. <https://doi.org/10.1016/J.MTCOMM.2022.104837>.
- [92] Li W, Meng L, Wang S, Zhang H, Niu X, Lu H. Plastic deformation behavior and strengthening mechanism of SLM 316L reinforced by micro-TiC particles. *Mater Sci Eng, A* 2023;884:145557. <https://doi.org/10.1016/J.MSEA.2023.145557>.
- [93] Luo X, Yang C, Fu ZQ, Liu LH, Lu HZ, Ma HW, et al. Achieving ultrahigh-strength in beta-type titanium alloy by controlling the melt pool mode in selective laser melting. *Mater Sci Eng, A* 2021;823:141731. <https://doi.org/10.1016/J.MSEA.2021.141731>.
- [94] Karre R, Niranjana MK, Dey SR. First principles theoretical investigations of low Young's modulus beta Ti-Nb and Ti-Nb-Zr alloys compositions for biomedical applications. *Mater Sci Eng C* 2015;50:52–8. <https://doi.org/10.1016/J.MSEC.2015.01.061>.
- [95] Sun J, Yao Q, Xing H, Guo WY. Elastic properties of β , α' and ω metastable phases in Ti-Nb alloy from first-principles. *J Phys Condens Matter* 2007;19:486215. <https://doi.org/10.1088/0953-8984/19/48/486215>.
- [96] Zhan H, Wang G, Kent D, Dargusch M. The dynamic response of a metastable β Ti-Nb alloy to high strain rates at room and elevated temperatures. *Acta Mater* 2016;105:104–13. <https://doi.org/10.1016/J.ACTAMAT.2015.11.056>.
- [97] He Y, Zhang Y, Jiang Y, Zhou R. Fabrication and characterization of superelastic Ti-Nb alloy enhanced with antimicrobial Cu via spark plasma sintering for biomedical applications. *J Mater Res* 2017;32:2510–20. <https://doi.org/10.1557/JMR.2017.191/TABLES/3>.
- [98] Kim HY, Satoru H, Kim J II, Hosoda H, Miyazaki S. Mechanical properties and shape memory behavior of Ti-Nb alloys. *Mater Trans* 2004;45:2443–8. <https://doi.org/10.2320/MATERTRANS.45.2443>.
- [99] Schwab H, Prashanth K, Löber L, Kühn U, Eckert J. Selective laser melting of Ti-45Nb alloy. *Metals* 2015;5:686–94. <https://doi.org/10.3390/met5020686>.
- [100] Pilz S, Bönisch M, Datye A, Zhang S, Günther F, Drescher S, et al. Tailoring microstructure and mechanical properties of an LPBF-processed beta Ti-Nb alloy through post-heat treatments. *Mater Des* 2024;239:112799. <https://doi.org/10.1016/j.matdes.2024.112799>.
- [101] Wang JC, Liu YJ, Liang SX, Zhang YS, Wang LQ, Sercombe TB, et al. Comparison of microstructure and mechanical behavior of Ti-35Nb manufactured by laser powder bed fusion from elemental powder mixture and prealloyed powder. *J Mater Sci Technol* 2022;105:1–16. <https://doi.org/10.1016/j.jmst.2021.07.021>.
- [102] Li Z, Xu H, Dong A, Cai X, He L, Du D, et al. Mechanical anisotropy of laser powder bed fusion fabricated Ti-41Nb alloy using pre-alloyed powder: roles played by grain morphology and crystallographic orientation. *J Alloys Compd* 2022;925:166572. <https://doi.org/10.1016/J.JALLCOM.2022.166572>.
- [103] Akman A, Douest Y, Alberta LA, Perrin K, Trunfio Sfarighiu AM, Courtois N, et al. Tribocorrosion behaviour of additively manufactured β -type Ti-Nb alloy for implant applications. *J Mater Res Technol* 2024;31:1419–29. <https://doi.org/10.1016/J.JMRT.2024.06.172>.
- [104] Wang J, Liu Y, Rabadia CD, Liang SX, Sercombe TB, Zhang LC. Microstructural homogeneity and mechanical behavior of a selective laser melted Ti-35Nb alloy produced from an elemental powder mixture. *J Mater Sci Technol* 2021;61:221–33. <https://doi.org/10.1016/j.jmst.2020.05.052>.
- [105] Fischer M, Joguet D, Robin G, Peltier L, Laheurte P. In situ elaboration of a binary Ti-26Nb alloy by selective laser melting of elemental titanium and niobium mixed powders. *Mater Sci Eng C* 2016;62:852–9. <https://doi.org/10.1016/j.msec.2016.02.033>.
- [106] Wang Q, Han C, Choma T, Wei Q, Yan C, Song B, et al. Effect of Nb content on microstructure, property and in vitro apatite-forming capability of Ti-Nb alloys fabricated via selective laser melting. *Mater Des* 2017;126:268–77. <https://doi.org/10.1016/j.matdes.2017.04.026>.
- [107] Zhao D, Han C, Li J, Liu J, Wei Q. In situ fabrication of a titanium-niobium alloy with tailored microstructures, enhanced mechanical properties and biocompatibility by using selective laser melting. *Mater Sci Eng C* 2020;111:110784. <https://doi.org/10.1016/J.MSEC.2020.110784>.
- [108] Singh N, Srikanth KP, Gopal V, Rajput M, Manivasagam G, Prashanth KG, et al. In situ production of low-modulus Ti-Nb alloys by selective laser melting and their functional assessment toward orthopedic applications. *J Mater Chem B* 2024;12:5982–93. <https://doi.org/10.1039/D4TB00379A>.
- [109] Borgman JM, Wang J, Zani L, Conway PP, Torres-Sanchez C. The effect of energy density and Nb content on the microstructure and mechanical properties of selective laser melted Ti-(10-30 wt%) Nb. *J Mater Eng Perform* 2021;30:8771–83. <https://doi.org/10.1007/s11665-021-06239-5>.
- [110] Vonavkova I, Vojtech D, Palousek D. Characterization of β -Ti alloy prepared by SLM method. *Manuf Technol* 2020;20:690–6. <https://doi.org/10.21062/mft.2020.091>.
- [111] YuP Sharkeev, Dmitriev AI, Knyazeva AG, Ayu Eroshenko, Saprykin AA, Khimich MA, et al. SELECTIVE LASER MELTING OF THE Ti-(40-50) wt.% Nb ALLOY. *High Temp Quart High Technol Plasms Proc* 2017;21:161–83. <https://doi.org/10.1615/HighTempMatProc.2017024814>.
- [112] Wang JC, Liu YJ, Qin P, Liang SX, Sercombe TB, Zhang LC. Selective laser melting of Ti-35Nb composite from elemental powder mixture: microstructure, mechanical behavior and corrosion behavior. *Mater Sci Eng, A* 2019;760:214–24. <https://doi.org/10.1016/j.msea.2019.06.001>.

Publication III

Subramanian, S., Praveenkumar, K., Rameshbabu, N., Lokeshraj, K., Raheem, A., Jayaraj, J., & Prashanth, K. G. (2026). Biofunctionalization of SLM Ti-40Nb alloy through hydroxyapatite-modified plasma electrolytic oxidation coating. *Applied Surface Science Advances*, 31, 100917. <https://doi.org/10.1016/J.APSADV.2025.100917>



Contents lists available at ScienceDirect

Applied Surface Science Advances

journal homepage: www.sciencedirect.com/journal/applied-surface-science-advances

Full Length Article

Biofunctionalization of SLM Ti–40Nb alloy through hydroxyapatite-modified plasma electrolytic oxidation coating

Shangavi Subramanian^a, Kesavan Praveenkumar^b, Nagumothu Rameshbabu^c,
Kuppusamy Lokeshraj^d, Ansheed Raheem^e, Jayamani Jayaraj^{f,g},
Konda Gokuldoss Prashanth^{a,e,h,*}

^a Department of Mechanical and Industrial Engineering, Tallinn University of Technology, Ehitajate tee 5, 19086 Tallinn, Estonia

^b Faculty of Materials Science and Technology, VSB-Technical University of Ostrava, 17, listopadu 2172/15, 70800 Ostrava, Czech Republic

^c Department of Metallurgical and Materials Engineering, National Institute of Technology, Tiruchirappalli 620015, India

^d Department of Automotive Engineering, School of Mechanical Engineering (SMEC), Vellore Institute of Technology, School of Mechanical Engineering, Tamil Nadu 632014, India

^e Centre for Biomaterials, Cellular and Molecular Therapeutics (CBCMT), Vellore Institute of Technology, School of Mechanical Engineering, Tamil Nadu 632014, India

^f Materials Technology, Dalarna University, SE-79188 Falun, Sweden

^g Department of Mechanical and Materials Engineering, Karlstad University, SE-65188 Karlstad, Sweden

^h National Engineering Research Center of Near-Net-Shape Forming for Metallic Materials, South China University of Technology, Guangzhou 510640, China

ARTICLE INFO

Keywords:

Ti40Nb alloy
Selective laser melting
Surface modification
PEO coating
Biocompatibility

ABSTRACT

This study reports the successful development of bioactive coatings on in-situ alloyed Ti-40Nb substrates fabricated via selective laser melting (SLM) using plasma electrolytic oxidation (PEO). Two electrolytes were employed for PEO processing: phosphate–silicate (PS) and phosphate–silicate–hydroxyapatite (PSHA). A comparative evaluation was performed to investigate the influence of electrolyte composition on surface morphology, corrosion resistance, and biological performance. The incorporation of hydroxyapatite (HAp) in the PSHA electrolyte significantly modified the coating structure, resulting in reduced porosity, increased surface roughness, and enhanced wettability. X-ray diffraction analysis confirmed the formation of TiO₂ (anatase and rutile) and Nb₂O₅ phases, with a higher rutile fraction observed in the HAp-incorporated coatings due to intensified plasma discharges. Electrochemical testing in simulated body fluid (SBF) demonstrated improved corrosion resistance for the HAp-containing samples, as evidenced by lower corrosion current density and passivation current values. In vitro assays with MC3T3 pre-osteoblast cells further revealed superior cell viability and proliferation on the HAp-incorporated coatings, attributed to the synergistic effects of roughened topography and the sustained release of bioactive ions. Overall, the PEO-modified Ti40Nb samples exhibited enhanced corrosion protection and cytocompatibility, underscoring their strong potential as next-generation Ti-based orthopedic implant materials.

1. Introduction

Titanium (Ti) and its alloys are extensively utilized in biomedical applications, owing to their unique combination of high specific strength, exceptional corrosion resistance, and outstanding biocompatibility [1–6]. Among contemporary manufacturing techniques, laser powder bed fusion (LPBF) enables the fabrication of Ti-based alloys with complex, patient-specific geometries, facilitating improved structure–property relationships and seamless functional integration [7–10]. Ti

alloys fabricated via laser powder bed fusion (LPBF), also known as selective laser melting (SLM), have attracted considerable interest in clinical applications ranging from dental implants and orthopedic prostheses to cardiovascular devices, highlighting their adaptability and efficacy across diverse biomedical environments [11]. Despite these advantages, conventional α + β -Ti alloys –most notably Ti-6Al-4 V –exhibit significant limitations, primarily due to biocompatibility concerns associated with the incorporation of aluminum (Al) and vanadium (V) [12]. Al has been implicated in neurological disorders, including

* Corresponding author at: DNational Engineering Research Center of Near-Net-Shape Forming for Metallic Materials, South China University of Technology, Guangzhou 510640, China.

E-mail address: kgprashanth@gmail.com (K.G. Prashanth).

<https://doi.org/10.1016/j.apsadv.2025.100917>

Received 12 October 2025; Received in revised form 20 November 2025; Accepted 6 December 2025

Available online 11 December 2025

2666-5239/© 2025 The Author(s). Published by Elsevier B.V. This is an open access article under the CC BY-NC-ND license (<http://creativecommons.org/licenses/by-nc-nd/4.0/>).

Alzheimer's disease, while vanadium V has exhibited cytotoxic and mutagenic properties, contributing to hematological and biochemical disturbances [13]. Additionally, these conventional alloys exhibit a relatively high elastic modulus (~110 GPa), exceeding that of human cortical bone (10–30 GPa). This mismatch induces a stress-shielding effect, which can compromise load transfer and ultimately lead to implant loosening and long-term failure [14–16].

To address the limitations of $\alpha+\beta$ -Ti alloys, research has increasingly focused on developing novel β -Ti alloys. These compositions incorporate non-toxic β -stabilizing elements such as niobium (Nb), tantalum (Ta), zirconium (Zr), and molybdenum (Mo), which markedly mitigate the adverse biological effects linked to conventional alloying constituents [17–19]. Among these, Ti-40Nb has emerged as a highly promising candidate, distinguished by its reduced elastic modulus (~60–65 GPa), excellent biocompatibility, and superior corrosion resistance [20]. Nb plays a critical role in stabilizing the β -phase, effectively lowering the elastic modulus and enhancing biocompatibility with native bone tissue [21]. Studies indicate that increasing Nb content enhances both corrosion resistance and biological performance, reinforcing the suitability of Ti-40Nb as an alloy for orthopedic applications [22].

Although Ti-40Nb exhibits favorable mechanical and biological properties, its intrinsic bioinertness limits direct interaction with surrounding tissues, presenting challenges for sustained clinical integration and long-term performance [23]. This inherent bioinertness necessitates the implementation of surface modification strategies to enhance bioactivity and further augment corrosion resistance [24,25]. A wide range of surface modification techniques, such as anodization, sol-gel processing, dip coating, chemical vapor deposition (CVD), physical vapor deposition (PVD), and thermal spraying, have been extensively investigated [26]. Among these techniques, conventional anodization has been widely utilized to form protective oxide layers on Ti-based alloys [27]. However, this technique is often constrained by slow coating growth rates and yields relatively thin oxide layers, limiting long-term functionality and durability [28]. While CVD offers uniform coating distribution, its application is constrained by prolonged processing times and the formation of relatively thin films [26]. PVD techniques necessitate costly equipment and pose scalability challenges for large-scale applications. In contrast, thermal spray methods are often incompatible with substrates of complex geometry and may lead to non-uniform coating coverage [29]. Sol-gel and dip-coating techniques often suffer from poor adhesion and typically necessitate post-deposition heat treatments to attain adequate performance [30].

These cumulative limitations underscore the need for more versatile and efficient surface modification technologies suited to complex biomedical and engineering applications. In this context, plasma electrolytic oxidation (PEO) has gained prominence for its capacity to produce thick, dense, and strongly adherent oxide coatings on metallic substrates [31–33]. The plasma electrolytic oxidation (PEO) process produces a ceramic-like oxide layer that incorporates elements from both the substrate and the electrolyte. These coatings significantly enhance corrosion resistance and bioactivity by modifying surface chemistry and topography, thereby promoting favorable cellular responses and rendering PEO-treated surfaces well-suited for biomedical applications [34,35]. In addition, recent studies on PEO have reported that the usage of ultrasonic vibration during coating formation can improve the stability of nanoparticle-containing electrolyte by reducing agglomeration, enhancing dispersion, and maintaining a more stable suspension throughout the process [36–39].

The morphology of PEO coatings is strongly governed by electrolyte chemistry, phase composition, and the microstructural attributes of the underlying substrate [25]. Phosphate-based electrolytes have demonstrated excellent corrosion resistance on Ti substrates, while silicate-based electrolytes have proven highly effective for niobium Nb surfaces [40]. Until recently, the optimal electrolyte formulation for Ti-40Nb substrates, particularly with respect to phosphate and silicate compositions, remained relatively unexplored. Lokeshkumar et al.

demonstrated that a balanced 50:50 phosphate-to-silicate electrolyte yields coatings with exceptional compactness, enhanced corrosion resistance, and increased thickness [23]. Moreover, the incorporation of bioactive elements such as hydroxyapatite (HAp) into electrolyte systems markedly improves biological integration and osteoconductivity, both of which are essential for successful bone-implant interfacing [41–44].

Beyond investigations focused on electrolyte composition, PEO coatings on Ti-Nb alloys fabricated via conventional processing routes have been extensively studied [45]. Ti-based alloys produced through conventional routes such as casting, forging, or sintering typically develop equilibrium α , β , or $\alpha+\beta$ microstructures with relatively coarse grains and low defect density [46,47]. In contrast, SLM introduces extremely rapid solidification and repeated thermal cycling, giving rise to a refined and highly nonequilibrium microstructure that is notably different from traditionally processed Ti-Nb alloy [48–50]. It is important to recognize that the microstructure of samples produced via SLM often results in pronounced variations in coating morphology [51,52]. SLM Ti-Nb samples often contain metastable α' martensite, retained β regions, high dislocation densities, and fine cellular or dendritic substructures [53,54]. These features create heterogeneity in electrical conductivity, which can significantly influence plasma initiation, discharge behaviour, and oxide growth during PEO [55]. Pezzato et al. [56] compared the coating morphology on TC4 samples fabricated by conventional casting and SLM, revealing that SLM-derived coatings exhibited smoother surfaces with fewer and smaller pores, while cast samples showed higher porosity accompanied by visible cracking. Thus, the coating evolution on SLM substrates cannot be directly inferred from studies on conventionally processed Ti alloys, highlighting the need to evaluate the PEO-coating behavior on SLM fabricated Ti-Nb samples.

Wu et al. [55] investigated the influence of SLM-induced metastable microstructures in TC4 alloys on coating characteristics. Their findings revealed that SLM-fabricated samples exhibited lower porosity and greater coating thickness compared to commercially produced counterparts. Haibo et al. [57] investigated the influence of the microstructure of Ti6Al4V substrates fabricated via selective laser melting (SLM) on PEO coating behavior. The SLM-processed substrate exhibited a dense microstructure comprising fine acicular martensitic α' phase and coarser α grains, interspersed with structural defects such as dislocations, twins, and grain boundaries [58–60]. These features facilitated multiple pathways for electron and anion transport, thereby reducing the breakdown voltage of the anodic oxide film. This reduction accelerated the voltage ramp rate during the PEO process, enhancing microarc initiation and resulting in a significantly thicker oxide layer compared to that formed on the forged counterpart [57].

While PEO coatings on Ti-40Nb alloys fabricated via conventional sintering methods have been previously reported [33,45], studies addressing coatings on Ti-40Nb substrates produced by selective laser melting remain limited. The rapid solidification inherent to SLM results in a metastable $\alpha'+\beta$ microstructure with a high density of crystallographic defects, conditions that can markedly influence plasma discharge behaviour and oxide growth compared with traditionally processed Ti-Nb alloys. The present study offers new insights in three major areas. First, it evaluates the response of an in-situ alloyed SLM Ti-40Nb substrate to PEO processing, providing insight on microstructure effect on the initiation and evolution of micro-arc discharges. Second, it compares the detailed evaluation of the electrochemical behavior of the oxide layers in two electrolyte systems, phosphate-silicate and a HAp-modified phosphate-silicate. Third, the work establishes direct correlations between the substrate's microstructural characteristics and key coating features, including discharge intensity, oxide phase constitution, porosity development, corrosion behaviour, and cellular response. Thus, this work aims to provide comprehensive insights into the efficacy of these surface modifications in enhancing the durability and biocompatibility of SLM-fabricated Ti-40Nb alloys, thereby contributing to the development of next-generation biomedical implant

technologies.

2. Experimental methods and materials

2.1. Sample preparation

The Ti-40Nb alloy sample, comprising 60 wt. % Ti and 40 wt. % Nb, was fabricated via selective laser melting (SLM) using in-situ alloyed elemental powders (SLM 2802.0, SLM Solutions, Germany). Cylindrical specimens with dimensions of 15 mm in diameter and 2 mm in height were produced using optimized process parameters: laser power of 650 W, scanning speed of 650 mm/s, hatch spacing of 35 μm , and layer thickness of 30 μm . Following fabrication, the samples were separated from the Ti substrate using wire electrical discharge machining (EDM). The surfaces were then polished to a #1200 grit finish and subjected to ultrasonic cleaning in ethanol to ensure surface cleanliness before the PEO coating process.

2.2. PEO coating

The PEO coatings were synthesized using a direct current (DC) power supply within an aqueous electrolytic system. During the process, the Ti-40Nb sample served as the anode, while a stainless-steel bowl containing the sample and electrolyte functioned as the cathode. The PEO treatment was conducted under the following operational parameters: duty cycle of 90 %, current density of 200 mA/cm², frequency of 1000 Hz, and a processing duration of 6 min. Two distinct electrolyte systems were employed: phosphate-silicate (PS) and phosphate-silicate-hydroxyapatite (PSHA). The PS electrolyte comprised a 50:50 mixture of sodium metasilicate and trisodium orthophosphate, with a total concentration of 5 g dissolved in 1 L of distilled water. The PSHA electrolyte was prepared by incorporating 5 g of hydroxyapatite (HAp) powder into the PS mixture, also dissolved in 1 L of distilled water. The HAp nanoparticles were synthesized through the microwave-assisted synthesis method as reported in our earlier work [23,61]. The resulting HAp nanoparticles measured approximately 15–20 nm in width and 60–80 nm in length. To stabilize the nanoparticle suspension and impart surface charge, 10 mL of triethanolamine and 5 mL of ethylene glycol were added. The solution was magnetically stirred to ensure homogeneous dispersion of nanoparticles throughout the electrolyte. Following the PEO process, the coated samples were thoroughly rinsed with deionized water and air-dried before characterization. The samples were designated as S1 (uncoated Ti-40Nb alloy), S2 (PS-coated), and S3 (PSHA-coated).

2.3. Materials characterization and mechanical testing

Phase analysis of the S1, S2, and S3 samples was conducted using an X-ray diffractometer (Bruker-AXS) equipped with a Cu-K α radiation source ($\lambda = 1.54 \text{ \AA}$). Diffraction peaks were recorded over a 2 θ range of 30°–90° with a step size of 0.02°. Surface morphology, elemental composition, and coating thickness were characterized using an optical microscope (Motic Panthera, China) and a scanning electron microscope (SEM) (Zeiss Ultra 55, Germany). The pore size and porosity percentage are quantified using ImageJ software. Surface roughness measurements were performed using an atomic force microscope (Nanosurf, Switzerland) with a scanning area of 60 $\mu\text{m} \times 60 \mu\text{m}$. Wettability was assessed using a goniometer (Kyowa Interface Science, Japan) by measuring the contact angle between the sample surface and a droplet of deionized water. The corresponding surface energy (E_s) was calculated using Eq. (1),

$$E_s = E_{vl} \cos \theta \quad (1)$$

where the E_{vl} denotes the surface energy of distilled water (72.8 mJ/m²) [62], and θ represents the contact angle. Wettability measurements were

averaged over five readings, each using a 3 μL droplet of deionized water. Coating adhesion strength was assessed using a CSM Revetest system (Switzerland) equipped with a Rockwell C indenter (tip radius: 200 μm ; cone angle: 120°). A progressive load ranging from 0 to 20 N was applied over a scratch length of 5 mm at a loading rate of 19.5 N/min. Microhardness measurements were performed using a Buehler Micromet tester (Japan) under a load of 10 gf with a dwell time of 10 s. The reported values represent the average of ten measurements, with standard deviation included as error bars.

2.4. Corrosion study

Corrosion resistance of the samples was evaluated using a three-electrode cell system connected to a potentiostat (ACM Gillac, UK). Simulated body fluid (SBF) with a pH of 7, prepared according to Kokubo's protocol [63], served as the electrolyte. The Ti-40Nb sample functioned as the working electrode, a thin platinum (Pt) foil as the counter electrode, and a saturated calomel electrode (SCE) as the reference. Potentiodynamic polarization (PDP) analysis was performed over a 1 cm² sample surface area at a scan rate of 10 mV/s, spanning a potential range from -0.5 V to +3 V. The electrochemical impedance spectroscopy (EIS) was carried out at OCP with ± 10 mV amplitude in the frequency range of 10⁻² Hz to 10⁵ Hz in SBF with a pH of 7 at 37 °C. To ensure reliability and reproducibility, each test was conducted in triplicate. The chemistry of the passive/oxide layer before and after PDP studies for the S2 and S3 samples were evaluated using the X-ray photoelectron spectroscopy (XPS) ULVAC-PHI.

2.5. Cell studies

2.5.1. Cell culture

Cell culture was performed using MC3T3 pre-osteoblast cells. The growth medium comprised α -MEM supplemented with 10 % fetal bovine serum (FBS; Gibco-26,140,079, US) and 1 % penicillin-streptomycin (Gibco-15,140,122, US). Cultures were maintained at 37 °C in a humidified atmosphere containing 5 % CO₂. Subculturing was carried out upon reaching ~85 % confluence using 0.25 % trypsin-EDTA (Gibco-25,200,056, US) for cell detachment. All experiments utilized cells between passages 2 and 6 to preserve their phenotypic characteristics and differentiation potential.

2.5.2. Cell viability evaluation

Polished metal discs (15 mm diameter \times 2 mm height) served as substrates for cell culture. MC3T3 cells were seeded onto the sample surfaces and cultured for 24 h and 72 h to assess cytocompatibility. Each test was performed in triplicate and repeated three times to ensure statistical robustness. Prior to cell seeding, all samples were sequentially cleaned with acetone and ethanol, followed by sterilization via thermal autoclaving. Biological performance of coated samples was compared against uncoated controls. Cytocompatibility was evaluated using the Alamar Blue assay (Invitrogen, DAL1025), which quantifies the metabolic reduction of resazurin to fluorescent resorufin. Experiments were conducted in 24-well plates with a seeding density of 10,000 cells per well. At the end of each incubation period (24 h and 72 h), 10 % Alamar Blue reagent was added to each well and incubated for 4 h at 37 °C. Subsequently, 150 μL of medium was collected from each well, and absorbance was measured at 570 nm and 600 nm to determine cell viability.

2.5.3. Fluorescent imaging

Immunofluorescence staining was performed on day 3 to visualize cellular architecture. Following removal of the culture medium, samples were rinsed three times with phosphate-buffered saline (PBS). Cells were fixed with 3.7 % formaldehyde (Sigma-Aldrich) for 15 min and subsequently permeabilized using 1 % Triton X-100 for 3 min. Actin filaments were stained with Rhodamine Phalloidin (1:200 in PBS; Cytoskeleton,

PHDR1), and nuclei were counterstained with DAPI (Life Technologies) during the final 5 min of incubation. After staining, samples were rinsed with PBS and imaged at 10X magnification using laser scanning microscope (Olympus FLUOVUEV FV3000, Japan). All reagents were prepared and used in accordance with the manufacturers' protocols.

3. Results and discussion

3.1. PEO process

Plasma Electrolytic Oxidation (PEO) is an advanced surface modification technique that involves the electrochemical oxidation of a metallic substrate to produce a dense, adherent oxide coating enriched with elements from the electrolyte [25,64]. The voltage–time profile corresponding to different electrolyte systems is depicted in Fig. 1, with associated values summarized in Table 1. The profile reveals three distinct stages of the PEO process. Stage I corresponds to the initial anodization phase, characterized by a rapid voltage increase over time. During this stage, a passive oxide layer forms on the substrate surface and progressively thickens, while the influence of the electrolyte remains minimal. Stage II marks the dynamic PEO/spark discharge phase, during which the voltage continues to rise, indicating the onset of sparking phenomena. Upon reaching the breakdown potential, the passive layer ruptures, initiating plasma discharges that propagate randomly across the surface [65]. These discharges, visible as minute white sparks, induce localized melting of the substrate. The molten regions rapidly solidify upon quenching by the surrounding electrolyte, promoting the formation and densification of the oxide layer [66].

The breakdown potential is governed by both the composition and thermal conductivity of the electrolyte. The correlation between breakdown potential (V_b) and electrolyte thermal conductivity (k) is described by Eq. (2) [35],

$$V_b = a_B + b_B \log \frac{1}{k} \quad (2)$$

where a_B and b_B are constants. The equation illustrates an inverse relationship between breakdown potential and electrolyte conductivity—specifically, the breakdown potential increases as the conductivity of the electrolyte decreases. This trend is reflected in the voltage–time profile of the S3 sample, which exhibits a slightly higher breakdown potential than the S2 sample, attributed to the reduced conductivity of the HAp-containing electrolyte (15.2 mS/cm). Similar behavior has been reported in Ti alloys; for instance, Hanane et al. [67] demonstrated that the incorporation of HAp nanoparticles into the electrolyte lowered its electrical conductivity during PEO of Ti-6Al-4 V. This reduction in conductivity elevated the breakdown potential and intensified plasma discharge activity across the sample surface.

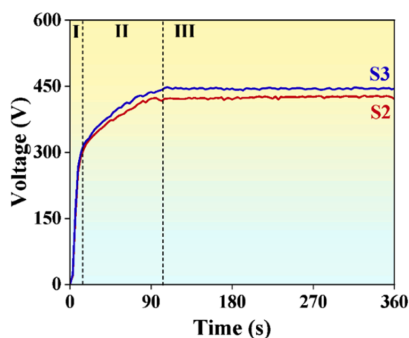


Fig. 1. The voltage–time evolution recorded during the plasma electrolytic oxidation of S2 and S3 samples was monitored over a 360 s processing duration.

Table 1

Table presenting the breakdown, peak voltages and thermal conductivity recorded for samples S2 and S3 during the plasma electrolytic oxidation process.

| Sample | Breakdown voltage (V_b), V | Peak voltage (V_p), V | Thermal conductivity (k) (mS/cm) |
|--------|--------------------------------|---------------------------|--------------------------------------|
| S2 | 317 | 448 | 16.3 |
| S3 | 324 | 455 | 15.2 |

Consistent with these findings, the present study confirms that the addition of HAp to the electrolyte decreases its conductivity, thereby increasing the breakdown potential observed in the S3 sample.

Stage III of the PEO process, commonly referred to as the critical voltage or micro-arc stage, is marked by the voltage approaching a near-steady state as the coating continues to develop. During this phase, the increasing thickness and density of the oxide layer elevate its electrical resistance, which in turn contributes to a further rise in voltage [26]. Analysis of the voltage–time profiles reveals that the final voltage attained by the S3 sample exceeds that of the S2 sample. This difference is attributed to the successful incorporation of hydroxyapatite (HAp) into the oxide layer, which increases the coating's resistance and intensifies the arcing phenomena [68]. The enhanced micro-arc activity promotes deeper oxidation of the underlying metal substrate, potentially influencing the surface morphology and structural characteristics of the S3 coating.

3.2. Phase analysis

Fig. 2 presents the XRD patterns of the SLM-fabricated Ti-40Nb substrate (S1) and the PEO-coated samples (S2 and S3). The diffraction peak at $2\theta \sim 38.4^\circ$ observed for S1 indicates the presence of the β phase, while peaks at $2\theta \sim 34.6^\circ$ and $\sim 39.7^\circ$ correspond to the α/α' martensitic phase. Given that both α and α' phases share a hexagonal close-packed (hcp) crystal structure, they are difficult to distinguish via XRD; however, based on complementary microstructural analysis, the phase is characterized here as α' martensite. These findings align with the typical $\alpha+\beta$ phase composition reported for Ti-based alloys in the literature [30, 69]. The formation of metastable $\alpha'+\beta$ phases is attributed to the rapid cooling and non-equilibrium solidification inherent to the SLM process [70–72]. These metastable regions, enriched with defects such as high dislocation density, represent energetically favorable sites for discharge channel formation and micro-arc activity during PEO [57]. In addition to the substrate-related α' and β peaks, the XRD patterns of S2 and S3 confirm the presence of oxide phases formed during PEO. The localized thermal effects induced by repeated plasma discharges promote the crystallization of TiO_2 and Nb_2O_5 within the coating layer [53]. Among the TiO_2 polymorphs, anatase and rutile phases were predominantly observed. Both S2 and S3 samples exhibited Nb_2O_5 along with anatase

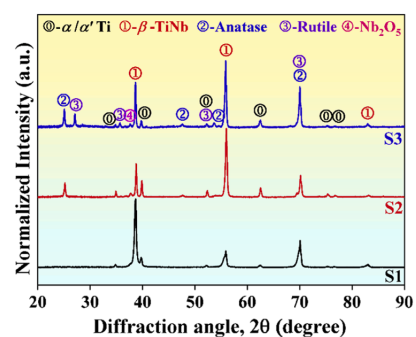


Fig. 2. X-ray diffraction (XRD) patterns of the selective laser melted Ti40Nb S1 sample, and plasma electrolytic oxidation-treated S2 and S3 samples.

and rutile TiO_2 phases, in addition to the underlying $\alpha'+\beta$ substrate peaks, consistent with previous reports [23,73]. Notably, no distinct diffraction peaks corresponding to hydroxyapatite (HAp) nanoparticles were detected in the S3 sample, likely due to the HAp concentration being below the detection threshold of XRD.

Comparative phase analysis indicates that the rutile phase is more prominent in the S3 sample than in S2. During TiO_2 layer formation, anatase typically forms first due to its lower surface free energy relative to rutile. However, anatase is thermodynamically metastable, possessing higher Gibbs free energy than rutile [74]. The anatase-to-rutile transformation is strongly temperature-dependent, generally occurring within the range of 400 °C to 1200 °C [75]. Consequently, this phase transition is influenced by thermal variations induced by discharge behavior during the PEO process. Based on the voltage–time profiles, the higher voltage observed in the S3 sample relative to S2 facilitated a more pronounced anatase-to-rutile transformation. This resulted in a progressive increase in rutile phase content in the S3 coating.

3.3. Surface morphology

Fig. 3(a–i) presents optical and SEM images illustrating the microstructure of the S1 sample and the coating morphologies of the S2 and S3 samples. The optical and SEM micrographs of the S1 sample (Fig. 3(a–c)) reveal a characteristic lath-shaped morphology indicative of the α' martensitic phase, confirming the coexistence of α' and β phases in the SLM-fabricated Ti-40Nb alloy. These observations are consistent with previously reported phase compositions for Ti-40Nb alloys [76]. The formation of metastable $\alpha'+\beta$ phases arises from the rapid cooling and non-equilibrium solidification inherent to the SLM process [77–79]. These metastable regions, enriched with structural defects such as high dislocation density, represent energetically favorable sites for discharge channel initiation and micro-arc activity during PEO treatment [62]. The S2 sample (Fig. 3(d–f)) exhibits a homogeneous distribution of irregularly shaped micro- and nanopores, whereas the S3 sample (Fig. 3(g–i)) displays uniformly distributed circular and elliptical micro- and nanopores. The incorporation of hydroxyapatite (HAp) nanoparticles into the electrolyte contributes to pore filling and surface modification,

resulting in the formation of interconnected porosity. Such porous architectures are characteristic of coatings produced via plasma electrolytic oxidation [25].

Intense arcing within discharge channels during the PEO process elevates localized temperatures, facilitating the melting and subsequent oxidation of the metal substrate [80]. The ejection of molten oxides and gas bubbles through these channels contributes to pore formation within the coating structure. As a result, the surface morphology of the coated samples exhibits a porous oxide layer with variations in pore size, shape, and distribution—features governed by discharge dynamics influenced by the applied voltage [65]. Haibo et al. [57] reported that higher process voltages during PEO promote the incorporation of greater amounts of molten oxide into the coating, which partially fills and covers discharge pores, thereby reducing overall porosity. Consistent with this observation, the S3 sample—processed at higher voltages—exhibited lower porosity compared to the S2 sample. High-magnification SEM images of S3 further revealed the presence of volcanic-like features within the coating morphology. Arun et al. [81] attributed such features to elevated voltage conditions during PEO, where intense plasma discharges generate localized regions of high temperature and pressure. These extreme conditions enhance the ejection of molten material through discharge channels, which subsequently solidifies to form crater-like structures with smooth rims, closely resembling volcanic morphology [81].

Quantitative analysis of pore size and porosity was performed using ImageJ software. The S2 sample exhibited an average pore size of $3.04 \pm 1.4 \mu\text{m}$, while the S3 sample showed a reduced average pore size of $2.32 \pm 0.9 \mu\text{m}$. Correspondingly, the porosity percentage was measured at $26 \pm 3 \%$ for S2 and $16 \pm 4 \%$ for S3. Ni et al. [41] demonstrated that increased electrolyte concentration leads to a reduction in pore size within PEO coatings. Arun et al. [81] further reported that the incorporation of hydroxyapatite (HAp) nanoparticles into the electrolyte promotes the formation of a smooth oxide layer uniformly decorated with HAp, contributing to partial pore filling and the development of interconnected porosity, thereby significantly lowering overall porosity. Additionally, Wang et al. [53] observed that elevated process voltages increase the volume of molten oxide, which can infiltrate and seal

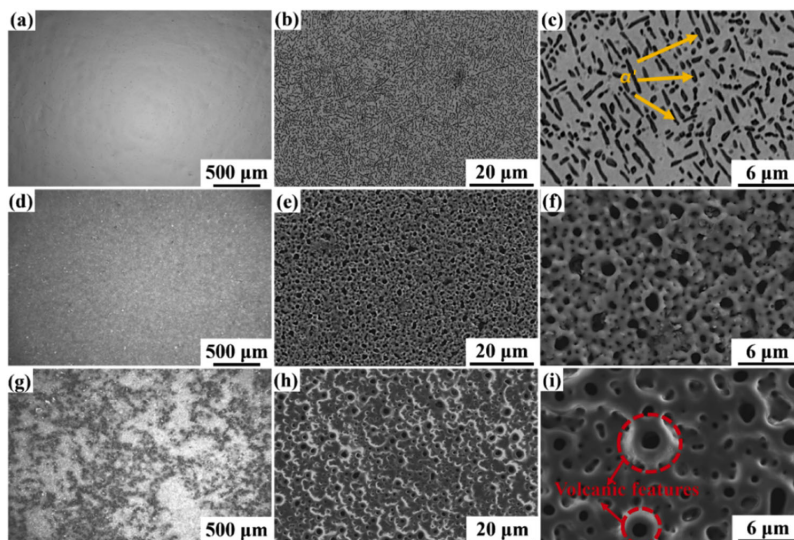


Fig. 3. Optical and scanning electron microscopy images illustrating the surface morphology of (a–c) uncoated Ti-40Nb (S1), (d–f) plasma electrolytic oxidation-coated S2, and (g–i) S3 samples. Orange arrows indicate the presence of lath-shaped α' martensite within the β -TiNb matrix, while red dotted rings highlight volcanic-like features characteristic of the coating morphology observed in the S3 sample.

discharge pores, further reducing porosity. In alignment with these findings, the S3 sample—processed with higher voltage and HAp-enriched electrolyte—exhibited interconnected pores and a notably lower porosity compared to the S2 sample.

Fig. 4(a-c7) presents the elemental maps and spectra of the Ti-40Nb substrate (S1) and the PEO-coated samples (S2 and S3). The uncoated S1 sample displays elemental signals corresponding to the base alloy constituents, Ti and Nb. In contrast, the oxide layers formed on S2 and S3 incorporate elements from both the substrate and the electrolyte [20]. Specifically, S2 exhibits the presence of Ti, Nb, O, P, and Si, while S3 additionally contains Ca, indicating successful incorporation of calcium and phosphate species from the HAp-enriched electrolyte. In both coated samples, oxygen corresponds to the formation of TiO₂ and Nb₂O₅, whereas P, Si, and Ca originate from the electrolyte, confirming their integration into the oxide matrix. Consistent with the voltage–time profiles, the more intense oxidation observed in the S3 sample led to a notable increase in oxygen content, along with enhanced incorporation of phosphate, silicate, and calcium species. The elevated phosphate content in S3 is particularly attributed to the dual contribution from phosphate ions in the electrolyte and HAp nanoparticles, resulting in a higher phosphate wt. % within the coating.

Fig. 5(a-d) presents the cross-sectional SEM images of the PEO-coated S2 and S3 samples. The coating morphology reveals a characteristic dual-layer structure comprising an inner dense layer and an outer porous layer. Quantitative analysis of the cross-sectional images using ImageJ software determined the coating thicknesses to be $6.9 \pm 1 \mu\text{m}$ for S2 and $8 \pm 1.5 \mu\text{m}$ for S3. The increased thickness observed in S3 is attributed to the higher process voltage applied during PEO. The relationship between coating thickness (t) and applied voltage is described by Eq. (3) [82]

$$t = A \exp k(V_p - V_b) \quad (3)$$

where V_p and V_b denote the process and breakdown voltages, respectively, and A and k are constants, the equation suggests that coating thickness is directly proportional to the applied voltage V . Accordingly, higher voltages yield thicker coatings. For instance, the S3 sample (Fig. 5 (c,d)), processed at a higher voltage, exhibits a thicker coating than the S2 sample (Fig. 5(a,b)) sample. Furthermore, the incorporation of hydroxyapatite (HAp) nanoparticles into the electrolyte elevates the ionic concentration, thereby facilitating the formation of a thicker and smoother oxide layer [80]. Nur et al. [83] demonstrated that increased ionic concentration enhances coating thickness and contributes to improved mechanical properties. In alignment with these findings, the

S3 sample exhibited a thicker coating with finer pore structures compared to the S2 counterpart.

3.3. Surface roughness and wettability

Fig. 6(a-c) presents atomic force microscopy (AFM) images illustrating the surface-roughness of the S1, S2, and S3 samples, respectively. Quantitative values are summarized in Table 2. Surface roughness was evaluated by comparing the surface conditions before and after the PEO treatment. Key factors influencing the oxide layer's roughness include pore density, pore size and shape, and the presence of volcanic-like features [65]. During the PEO process, micro-arc discharges and gas evolution contribute to the development of a porous coating structure, typified by hills and valleys, which significantly increases surface roughness. The average surface roughness (R_a) values for the S1, S2, and S3 samples were $0.21 \pm 0.01 \mu\text{m}$, $0.47 \pm 0.08 \mu\text{m}$, and $0.71 \pm 0.08 \mu\text{m}$, respectively indicating a substantial increase in roughness following coating. The SEM image (Fig. 3) reveals that the S2 sample exhibits pores with a rough surface texture, whereas the S3 sample appears smoother. However, despite the smoother pore morphology, the S3 sample demonstrates a higher overall surface roughness due to the random distribution and greater prevalence of volcanic features.

Wettability reflects the surface characteristics of a material, governed by the interaction between a liquid and the solid surface upon contact. It describes the liquid's tendency to spread over or adhere to the surface and is quantitatively assessed by the contact angle formed at the liquid-solid interface [84]. This parameter provides critical insight into the surface's hydrophilic (contact angle $< 90^\circ$) or hydrophobic (contact angle $> 90^\circ$) nature. Fig. 6(d-f) presents the contact angle measurements for the S1, S2, and S3 samples, with corresponding values summarized in Table 2. All samples exhibited hydrophilic behavior, as evidenced by contact angles below 90° . The degree of hydrophilicity increased progressively from S1 ($70 \pm 1.9^\circ$) to S2 ($53 \pm 1.3^\circ$), and further to S3 ($39 \pm 1.4^\circ$). Corresponding surface energy values were calculated as $24.9 \pm 1.8 \text{ mJ/m}^2$, $43.8 \pm 1.6 \text{ mJ/m}^2$, and $56.5 \pm 1.2 \text{ mJ/m}^2$ for S1, S2, and S3, respectively.

According to Wenzel's model, wettability is influenced by both surface roughness and chemical composition and is described by Eq. (4) [85,86],

$$\cos \theta_r = r \cos \theta_s \quad (4)$$

where θ_r and θ_s denote the actual contact angles on rough and smooth surfaces, respectively, and r represents the roughness ratio defined as the

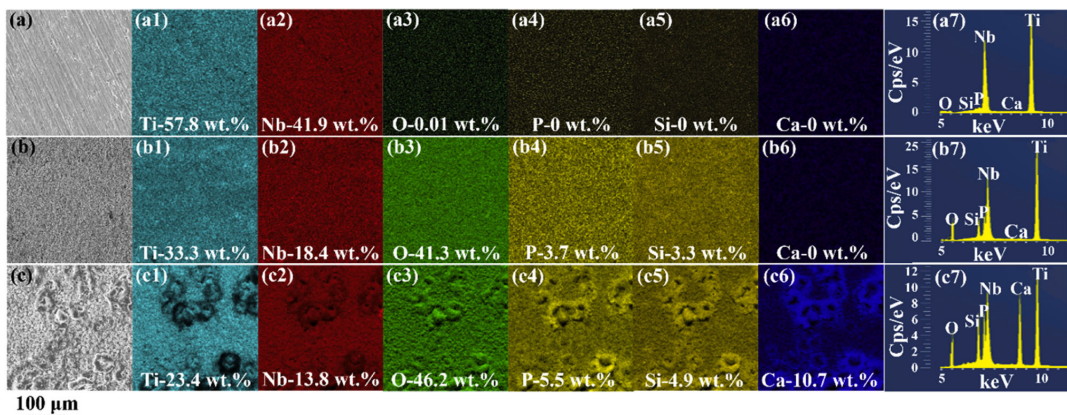


Fig. 4. Scanning electron microscopy images accompanied by energy-dispersive X-ray (EDX) elemental maps and spectra illustrating the surface composition of the uncoated Ti-40Nb substrate (a–a7) S1, and the plasma electrolytic oxidation-treated samples (b–b7) S2, and (c–c7) S3.

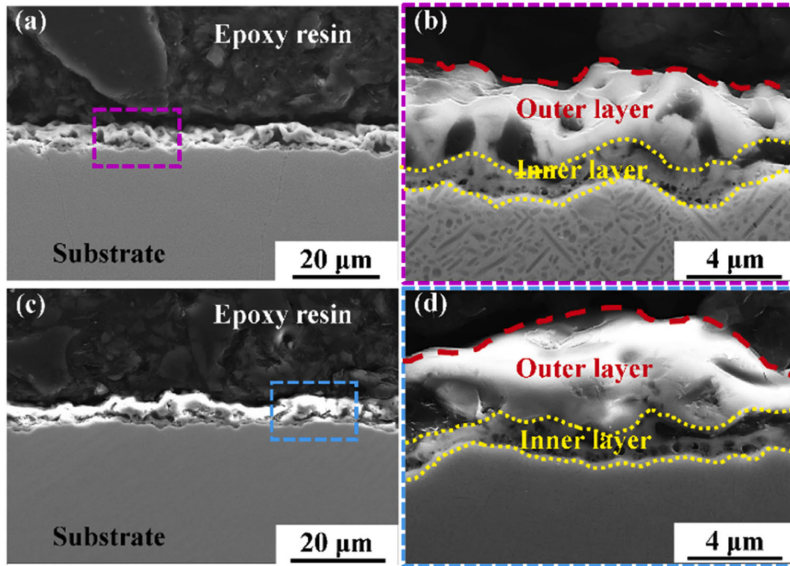


Fig. 5. Scanning electron microscopy images highlight the coating thickness of plasma electrolytic oxidation coated (a,b) S2 and (c,d) S3 samples. The yellow dotted line highlights the inner dense layer, and the red dotted line highlights the outer porous layer of the coating.

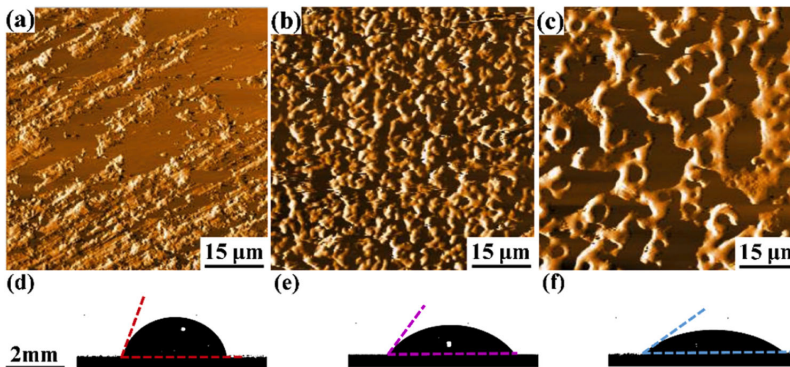


Fig. 6. Atomic force microscopy (AFM) images illustrating the surface roughness profiles (a-c) and corresponding contact angle measurements (d-f) for the uncoated S1 sample (a,d) and plasma electrolytic oxidation-treated samples S2 (b,e) and S3 (c,f).

Table 2

Surface roughness, contact angle, and surface energy values for samples S1, S2, and S3, highlighting the influence of surface modification on wettability and interfacial properties.

| Sample | R_{sa} , μm | Contact angle θ , degree | Surface energy, mJ/m^2 |
|--------|--------------------------|---------------------------------|--|
| S1 | 0.21 ± 0.01 | 70 ± 1.9 | 24.9 ± 1.8 |
| S2 | 0.47 ± 0.08 | 53 ± 1.3 | 43.8 ± 1.6 |
| S3 | 0.76 ± 0.08 | 39 ± 1.4 | 56.5 ± 1.2 |

ratio of the actual surface area to the projected surface area. According to Wenzel's model, increasing surface roughness amplifies the intrinsic wettability: rough hydrophobic surfaces become more hydrophobic, while rough hydrophilic surfaces become more hydrophilic [84]. The TiO_2 component within the oxide layer exhibits pronounced hydrophilic behavior due to its high surface polarity, which facilitates strong interactions with water molecules [87,88]. Accordingly, the S2 and S3

samples are characterized by hydrophilic surfaces and greater surface roughness than the uncoated reference demonstrated enhanced wettability. Among the coated samples, S3 exhibited the most pronounced wettability, attributable to its specific chemical composition. The incorporation of Ca^{2+} and PO_4^{3-} ions alongside TiO_2 further augments the hydrophilicity of the S3 surface, enhancing both hydration capacity and water affinity. These ions significantly increase surface polarity and promote water adsorption, as substantiated by previous studies [89,90].

3.4. Hardness and adhesion strength

Fig. 7(a) presents the variation in Vickers microhardness across samples S1, S2, and S3, with measured values of $337 \pm 27 \text{ HV}_{0.1}$, $506 \pm 73 \text{ HV}_{0.1}$, and $622 \pm 44 \text{ HV}_{0.1}$, respectively. The enhanced hardness observed in the coated samples S2 and S3 is attributed to the formation of the rutile phase, as confirmed by XRD analysis. This phase contributes to the improved surface hardness relative to the uncoated, SLM-

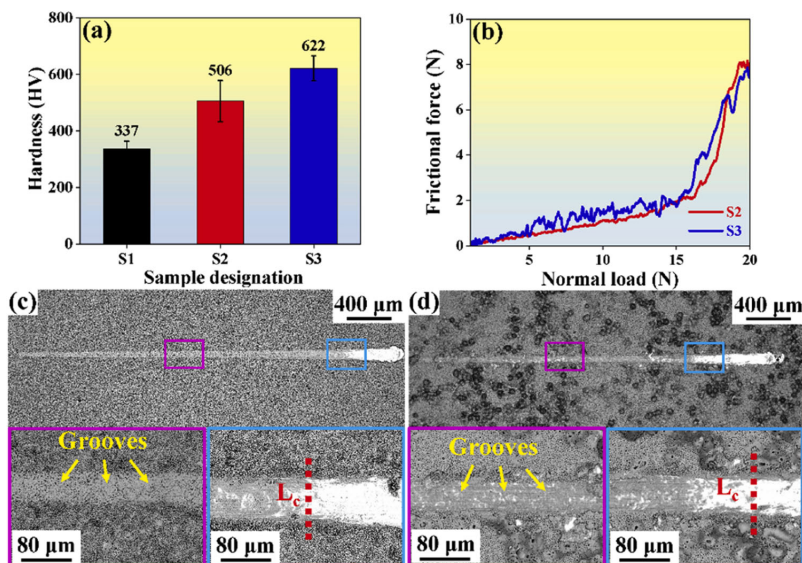


Fig. 7. (a) Vickers microhardness plot illustrating the hardness variation across samples S1, S2, and S3. (b) Frictional force versus normal load curves for S2 and S3 coatings, accompanied by corresponding scanning electron microscopy images of the scratch tracks: (c) S2 and (d) S3. The yellow arrows indicate grooves formed during the initial phase of testing, consistent with cohesive failure, while the red dotted lines mark the critical load (L_c) corresponding to the onset of adhesive failure and coating delamination.

fabricated S1 sample. Notably, the S3 sample exhibits the highest hardness, which is consistent with its greater rutile phase fraction. Previous studies have demonstrated that the presence of crystalline rutile significantly enhances coating hardness [91,92], corroborating the superior mechanical performance of the S3 surface.

Adhesion strength is a critical parameter in biomedical implant applications, as insufficient interfacial bonding between the coating and substrate can compromise mechanical stability during functional use. In this study, the adhesive performance of the S2 and S3 samples was assessed via instrumented scratch testing, with the frictional force versus normal load profiles shown in Fig. 7(b). Adhesion strength reflects the mechanical integrity of the coating–substrate interface and is commonly evaluated by identifying the critical load (L_c) at which complete coating delamination occurs [93,94]. The scratch test involved applying a linearly increasing normal load across the coated surface, inducing progressive mechanical deformation. Coating failure may manifest either adhesive failure at the interface or cohesive failure within the coating layer [82]. The onset of coating failure (L_c) is typically marked by a sudden rise in frictional force relative to the applied load and scratch length. Factors influencing L_c include surface morphology, coating thickness, roughness, and chemical composition [95]. In both S2 and S3 samples, a gradual increase in frictional force was observed with increasing scratch length. The L_c values were determined to be approximately 16 N for the S2 and 15.5 N for the S3 sample, indicating comparable adhesion performance.

In addition, SEM analysis was conducted to investigate the L_c and morphology of scratch tracks on the S2 (Fig. 7(c)) and S3 (Fig. 7(d)) samples. During the initial phase of the scratch test, well-defined grooves aligned with the scratch direction were observed, indicative of cohesive failure within the coating. This stage corresponded to a relatively stable frictional force profile, suggesting internal damage without interfacial separation. As the applied load approached the critical threshold, adhesive failure became dominant, marked by a sharp rise in frictional force and the onset of coating delamination. SEM imaging in backscattered electron (BSE) mode provided enhanced compositional contrast, clearly delineating the delaminated regions and

the underlying metallic substrate. Both coatings exhibited comparable adhesion strength, supporting their potential suitability for long-term biomedical implant applications.

3.5. Corrosion studies

In this study, the corrosion behavior of samples S1, S2, and S3 was assessed using electrochemical and impedance spectroscopy (EIS) and potentiodynamic polarization (PDP) testing. Simulated body fluid (SBF) with a pH of 7 served as the electrolyte, maintained at a physiological temperature of 37 °C to replicate in vivo conditions.

3.5.1. Electrochemical study

In addition to the potentiodynamic polarization results, the electrochemical behaviour of the samples was evaluated using electrochemical impedance spectroscopy. Fig. 8 represents the Nyquist plot of S1, S2, and S3 samples, along with the equivalent circuit used to fit the EIS data of the S1, S2, and S3 samples. The EIS spectra were fitted using an equivalent-circuit approach, with χ^2 values in the 10^{-3} range confirming good agreement between the model and experimental data. The uncoated sample (S1) was represented by a single time constant Fig. 8(b), while the coated samples (S2 and S3) were represented by a two-time constant Fig. 8(c), consistent with the porous outer layer and compact inner barrier typical of PEO coatings. The circuit contained resistive elements (R_s –solution resistance, R_{out} –outer porous layer resistance/ R_p –Polarization resistance (for bare sample), R_{in} –inner dense layer resistance) and constant-phase elements (Q). To address the surface roughness and non-uniform film morphology of the oxide layer, Q was used instead of ideal capacitors.

The Nyquist plot in Fig. 8(a) shows a significant difference between the uncoated substrate (S1) and the PEO-coated samples (S2 and S3). S1 displays a semicircle with lower resistance, while the S2 and S3 coatings exhibit semicircles with higher resistance, owing to the porous outer layer and the dense inner layer that are characteristic of PEO-derived oxide systems [38,86]. The fitted parameters in Table 3 show that S1 exhibits the lowest resistance values, consistent with the weak

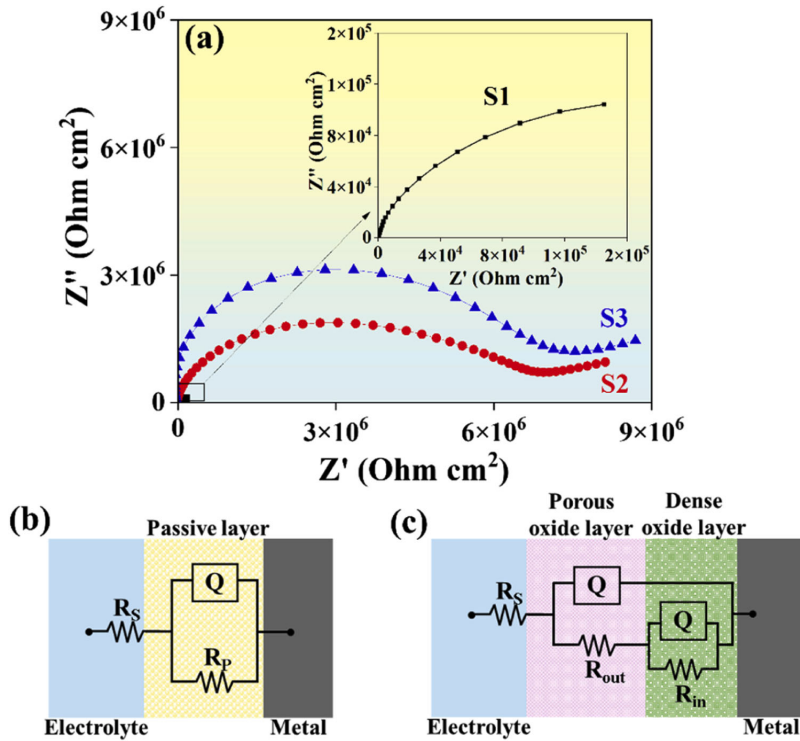


Fig. 8. (a-f). X-ray photoelectron spectroscopy (XPS) spectra of Ti2p, Nb3d, O1s, Ca2p, P2p, and Si2p of the S2 and S3 samples after potentiodynamic polarization (PDP) curve in simulated body fluid (SBF) at pH 7 and 37 °C. The dotted line denotes the spectra before PDP studies, and the solid line denotes the spectra after PDP studies.

Table 3
Electrochemical impedance parameters of S1, S2 and S3 samples obtained from the equivalent circuits.

| Sample | R_s , $\Omega \text{ cm}^2$ | $Q\text{-}Y_o$, $\Omega^{-1} \text{ cm}^{-2} \text{ s}^n$ | $Q\text{-}n$ | R_{out} , $\Omega \text{ cm}^2$ | $Q\text{-}Y_o$, $\Omega^{-1} \text{ cm}^{-2} \text{ s}^n$ | $Q\text{-}n$ | R_{in} , $\Omega \text{ cm}^2$ | $\chi^2 \cdot 10^{-3}$ |
|--------|-------------------------------|--|--------------|-----------------------------------|--|--------------|----------------------------------|------------------------|
| S1 | 11.2 | 4.3×10^{-6} | 0.85 | 2.4×10^5 | - | - | - | 0.3 |
| S2 | 3.54 | 1.99×10^{-10} | 0.74 | 6.1×10^5 | 1.4×10^{-8} | 0.79 | 5.9×10^6 | 0.5 |
| S3 | 4.62 | 6.02×10^{-11} | 0.72 | 9.2×10^5 | 9.1×10^{-8} | 0.87 | 1.3×10^9 | 0.5 |

protective nature of the native oxide on Ti-Nb alloys [33]. S2 showed improved resistance than S1, with $R_{out} = 6.1 \times 10^5 \Omega \cdot \text{cm}^2$ and $R_{in} = 6.9 \times 10^6 \Omega \cdot \text{cm}^2$, indicating the formation of a protective compact oxide. S3 exhibited the highest impedance values, with $R_{out} = 9.2 \times 10^5 \Omega \cdot \text{cm}^2$ and $R_{in} = 1.3 \times 10^9 \Omega \cdot \text{cm}^2$, demonstrating the superior performance of the HAp-modified oxide coating. The lower Q ($Q \sim 6.02 \times 10^{-11}$ and $9.1 \times 10^{-8} \Omega^{-1} \cdot \text{cm}^{-2} \cdot \text{s}^n$) and higher n ($n = 0.87$) for S3 further indicate a more uniform dielectric behaviour and reduced porosity [96]. These improvements are attributed to the incorporation of HAp, which partially fills surface pores and promotes the development of stable $\text{TiO}_2/\text{Nb}_2\text{O}_5/\text{HAp}$ composite oxide in accord with the XPS results. Similar strengthening of barrier performance through nanoparticle incorporation has been reported in earlier studies [23,41]. Overall, the EIS result shows that the S3 sample provides the highest corrosion resistance, attributed to its compact oxide layer. These findings correlate well with PDP and XPS results, confirming that the HAp-modified electrolyte produces a more stable oxide film.

3.5.2. Potentiodynamic polarization curve

The potentiodynamic polarization curves for samples S1, S2, and S3

are presented in Fig. 9, with the corresponding corrosion potential

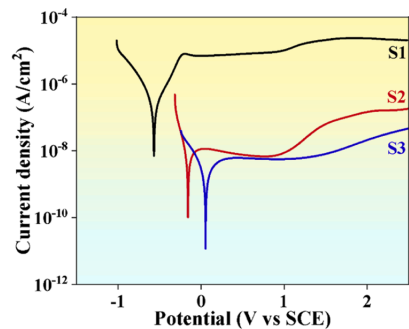


Fig. 9. Potentiodynamic polarization curves of the uncoated S1 sample and plasma electrolytic oxidation-treated S2 and S3 samples, recorded in simulated body fluid (SBF) at pH 7 and 37 °C to simulate physiological conditions.

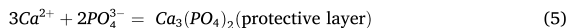
(E_{corr}), corrosion current density (I_{corr}), passivation current (I_p), and passivation potential (E_p) summarized in Table 4. Among the samples, S3 exhibited a higher E_{corr} and a lower I_{corr} compared to S2 and S1, indicating superior corrosion resistance and enhanced electrochemical stability.

Analysis of the potentiodynamic polarization (PDP) curve reveals that the anodic region comprises three distinct zones: active, passivation, and transpassive. The active region corresponds to the dissolution of the passive layer, marked by a rising corrosion current density due to increased charge transfer at the metal–electrolyte interface. As the applied potential reaches a critical threshold, the rate of oxidation surpasses that of dissolution, initiating passivation [97]. During the passivation phase, a stable and protective oxide layer forms, effectively suppressing charge transfer and thereby reducing the corrosion current density. Notably, the S3 sample exhibited a lower passivation current density ($0.006 \mu\text{A}/\text{cm}^2$) compared to S2 ($0.01 \mu\text{A}/\text{cm}^2$), indicating enhanced corrosion resistance. This improvement reflects the synergistic effect of the plasma electrolytic oxidation (PEO)-induced oxide coating and the passivated surface layer. Beyond the breakdown potential, the passive layer undergoes rupture, resulting in a sharp increase in corrosion current density and transition into the transpassive region.

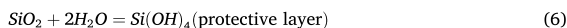
The S3 sample exhibited a higher breakdown potential (1.04 V) compared to the S2 sample (0.90 V), indicating enhanced resistance to corrosion under aggressive electrochemical conditions. Both the potentiodynamic polarization (PDP) curves and the corresponding electrochemical parameters confirm that S3 possesses superior corrosion resistance relative to S2 and the uncoated S1 sample. This improvement is primarily attributed to the structural integrity and morphology of the oxide layer formed during plasma electrolytic oxidation (PEO). The incorporation of hydroxyapatite (HAp) nanoparticles facilitated the formation of a dense and compact oxide layer, effectively minimizing direct exposure of the substrate to corrosive ions [62]. This barrier delayed the onset of corrosion and impeded ion transport across the metal–electrolyte interface, thereby enhancing overall corrosion performance [35]. A comparative summary of the corrosion results from this study and previous investigations involving PEO processing with different electrolytes is presented in Table 5.

The corrosion resistance of plasma electrolytic oxidation (PEO) coatings is governed by several factors, including coating thickness, chemical composition, porosity, and pore size. Coatings with greater thickness and reduced porosity have been shown to offer superior corrosion protection [67]. The S3 sample, distinguished by its increased coating thickness and low porosity, exhibited a higher corrosion potential (E_{corr}) and lower corrosion current density (I_{corr}) compared to S2, indicating enhanced electrochemical stability. The incorporation of hydroxyapatite (HAp) nanoparticles contributed to the formation of an HAp-enriched layer both over and within the pores of the phosphate–silicate matrix. The resulting oxide layer displayed smooth pores with sufficient surface roughness, acting as an effective barrier against the penetration and leaching of aggressive electrolyte species. The influence of coating composition on corrosion resistance can be further understood through the nature of the oxide layer formed during passivation, as represented by reactions (5–8). In the case of S2, the anodic process

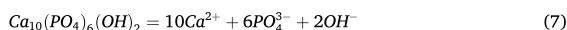
involves the interaction of PO_4^{3-} ions from the coating with Ca^{2+} ions from the electrolyte, leading to the formation of a protective calcium phosphate (CaP) layer,



Silicate components enhance the stability of the passive layer through the formation of silica-rich complexes, which reinforce the structural integrity of the oxide barrier and inhibit electrolyte penetration,



In the S3 sample, dissolution of hydroxyapatite (HAp) nanoparticles leads to the release of Ca^{2+} , PO_4^{3-} , and OH^- ions into the surrounding medium.



The release of OH^- ions elevate the local pH, generating an alkaline microenvironment conducive to passive layer formation. These hydroxide ions interact with the simulated body fluid (SBF), promoting the reprecipitation of a protective hydroxyapatite layer on the surface:

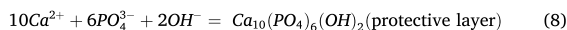


Fig. 10(a–c) presents SEM images and EDS elemental mapping of samples S1, S2, and S3 following potentiodynamic polarization testing, highlighting surface morphology and compositional features. Consistent with the PDP results, the SEM analysis revealed no significant damage or severe coating delamination, confirming the structural stability of the coatings. The S1 sample exhibited a relatively intact surface, while S2 and S3 displayed porous morphologies with localized regions of dissolution. EDS analysis of S1 confirmed the presence of Ti, Nb, and O, indicative of TiO_2 and Nb_2O_5 oxide layers. However, the lower corrosion resistance of S1 is attributed to its reduced oxide content compared to the coated samples. As described in reactions (5) and (6), interaction between the S2 coating and the electrolyte facilitated the formation of a protective layer composed of silicate and calcium phosphate (CaP) phases, in addition to TiO_2 and Nb_2O_5 . This composite oxide structure contributed to the enhanced corrosion resistance observed in the coated samples.

The presence of O, Si, Ca, and P in the EDS mapping (Fig. 10(b–b8)) confirms the formation of a composite protective layer on the S2 sample. As described in reaction (8), the interaction between the S3 coating and the electrolyte led to the development of a Ca–P-rich oxide layer, in addition to TiO_2 and Nb_2O_5 phases. This is further supported by the higher weight percentage of Ca and P detected in the EDS mapping of the S3 sample (Fig. 10(c–c8)). Beyond the ceramic oxide coating and the reprecipitated protective layer, the increased fraction of the rutile phase in S3 significantly contributed to its enhanced corrosion resistance. Moreover, the superior performance of hydroxyapatite (HAp) in S3 compared to S2 is attributed to its intrinsic chemical stability and elevated Ca content. The presence of hydroxyl groups in HAp imparts stability across a wide pH range, reducing dissolution and thereby improving corrosion resistance [67].

In addition to the EDX analysis, XPS analysis was performed to investigate the composition of the oxide layer following potentiodynamic polarization study. Fig. 11(a–f) highlights the chemistry of the oxide layer of the S2 and S3 samples before and after the PDP studies. In the Ti2p region, both coatings display the doublet peaks with Ti2p_{3/2} near ~455–459 eV, confirming TiO_2 as the dominant species. After PDP, S3 exhibits a stronger Ti2p signal and slight peak broadening, indicating the growth of a more hydrated TiO_2 layer [103]. The Nb3d spectra show peaks near ~205–205 eV and ~206–209.8 eV, corresponding to Nb_2O_5 , and their increased intensity in S3 after PDP suggests enhanced stabilization of Nb-oxide species, contributing to improved passivity [104].

The O1s peaks reveal lattice oxygen near ~528–530 eV and hydroxyl species at ~531.5–532.5 eV. S3 shows a more pronounced increase in

Table 4

Potentiodynamic polarization data for the uncoated S1 sample and plasma electrolytic oxidation-treated S2 and S3 samples, obtained in simulated body fluid (SBF) at pH 7 and 37 °C. Parameters include passivation current (I_p), passivation potential (E_p), and breakdown potential (E_b).

| Sample | E_{corr} (V vs SCE) | I_{corr} ($\mu\text{A}/\text{cm}^2$) | I_p ($\mu\text{A}/\text{cm}^2$) | E_p (V vs SCE) | E_b (V vs SCE) |
|--------|-----------------------|--|-------------------------------------|------------------|------------------|
| S1 | -0.6 ± 0.01 | 0.52 ± 0.04 | 8 | -0.05 | 0.87 |
| S2 | -0.2 ± 0.04 | 0.014 ± 0.001 | 0.010 | 0.14 | 0.9 |
| S3 | 0.1 ± 0.09 | 0.002 ± 0.001 | 0.006 | 0.5 | 1.04 |

Table 5

Comparison of potentiodynamic polarization results from the present study with existing literature on plasma electrolytic oxidation (PEO) coatings using various electrolyte systems. Parameters include coating composition (Comp.), processing time (T) in min, coating thickness (D) in μm , corrosion potential (E_{corr}) in V, corrosion current density (I_{corr}) in $\mu\text{A}/\text{cm}^2$, electrolyte type (E), and reference (Ref.).

| Material | Process | Comp. | T | D | E_{corr} | I_{corr} | E | Ref. |
|------------|------------|--|-------|----------------|--------------------------------|----------------------|-------------------|-----------|
| Ti40Nb | SLM | Phosphate and Silicate | 6 | 6.9 ± 1 | (-0.2 ± 0.04) V vs SHE | 0.014 ± 0.001 | SBF | This work |
| | | Phosphate, Silicate, and HA | | 8 ± 1.5 | (0.1 ± 0.09) V vs SHE | 0.002 ± 0.001 | | |
| Ti40Nb | Wrought | Phosphate, calcium,0.3 Ag | 5–10 | 41.6 ± 4.2 | 0.64 V vs SCE | 0.00148 | Ringer's solution | [33] |
| | | Phosphate, calcium,1.0Ag | | 54.6 ± 2.8 | 0.62 V vs SCE | 0.002 | | |
| Ti40Nb | Wrought | Phosphate and Silicate | 6 | 11.5 ± 1 | -0.28 V vs SCE | 0.57 | SBF | [23] |
| | | Phosphate, Silicate, and HA | | 6 | 16 ± 1 | -0.13 V vs SCE | | |
| Ti15Nb | Cast | Calcium, phosphate | 1 | 6.7 | -0.384 V vs Ag/AgCl | 0.41 | SBF | [98] |
| Ti40Nb | | Magnesium | | 1.3 | -0.147 V vs Ag/AgCl | 0.03 | | |
| TiNbTaZr | Hot-forged | TiO ₂ , (HA) and (TCP) | 5 | 50–90 | -0.069 – 0.12 V vs Ag/AgCl | 0.14–1.4 | SBF | [99] |
| Ti10Nb | Cast | calcium acetate and calcium glycerophosphate | 3 | 1.82 | -0.645 V vs SCE | 6.95 | SBF | [100] |
| Ti30Nb | | | | 1.85 | -0.353 V vs SCE | 0.006 | | |
| Ti50Nb | Wrought | KOH solution | 1 | 1.86 | -0.406 V vs SCE | 0.253 | PBS | [101] |
| Ti39Nb6Zr | | | | 9 | -0.061 V vs SCE | 0.159 | | |
| Ti18Zr15Nb | Cast | Phosphate | 2.5–5 | 17–21 | 0.2 – 0.26 V vs SCE | 0.002–0.003 | Ringer's solution | [102] |

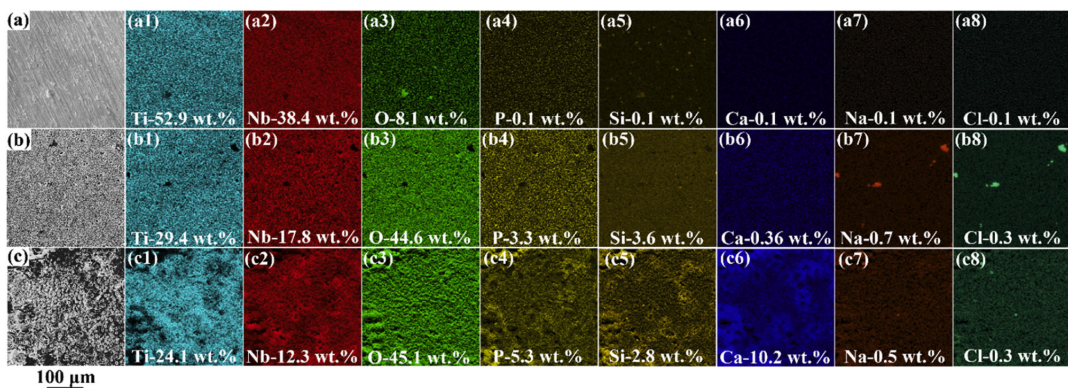


Fig. 10. Scanning electron microscopy (SEM) images of samples S1, S2, and S3 following potentiodynamic polarization testing, accompanied by energy-dispersive spectroscopy (EDS) elemental mapping illustrating surface morphology and compositional distribution.

the hydroxyl component after corrosion, which is known to promote Ca–P nucleation [51]. The increased peak intensity of Ca2p (Ca2p_{3/2} at ~ 346 eV) and P2p (~ 130 – 134 eV) in S3, indicates deposition of calcium–phosphate species from the SBF [105]. In contrast, S2 presents weaker Ca–P accumulation. The Si2p peak near ~ 99 – 103 eV also shows an increase in S3, suggesting better retention of silicate species within the oxide. Overall, the XPS spectra confirm S3 coating provides a more stable oxide layer during exposure to SBF, characterised by enhanced oxide growth, higher hydroxylation, and stronger Ca–P enrichment trends consistent with previously reported PEO systems exhibiting superior corrosion resistance [51].

3.6. Cell study

The biocompatibility of samples S1, S2, and S3 was evaluated using the Alamar Blue assay following 24 h and 72 h incubation periods. Fig. 12(a) presents the cell viability profiles for all samples at both points of time. Notably, S2 and S3 exhibited higher cell viability after 24 h compared to S1, indicating improved initial cell attachment on the coated surfaces. Key surface characteristics such as roughness,

wettability, and coating composition—play a critical role in modulating cell adhesion and cytoskeletal development. Increased surface roughness enhances the available area for cellular anchorage, while hydrophilic surfaces promote cell spreading and proliferation [53,62]. These synergistic effects foster a favorable microenvironment for cellular interactions, enabling robust adhesion and integration through both mechanical interlocking and chemical bonding mechanisms [98]. Such surface attributes are particularly important in biomedical applications, including tissue engineering and implantology, where rapid and stable cellular integration is essential for achieving successful clinical outcomes [106,107].

Among the coatings, the S3 sample exhibited the highest rate of cell proliferation, attributed to the synergistic effects of increased surface roughness and the presence of bioactive ions that enhance hydrophilicity. The incorporation of hydroxyapatite (HAp) nanoparticles significantly increased the effective surface area and surface energy, thereby enhancing surface reactivity and enabling the sustained release of Ca²⁺ and PO₄³⁻ ions—key factors in promoting cell proliferation and tissue integration [42,108]. Furthermore, the presence of HAp nanoparticles supports osteogenic differentiation and enhances bone cell activity,

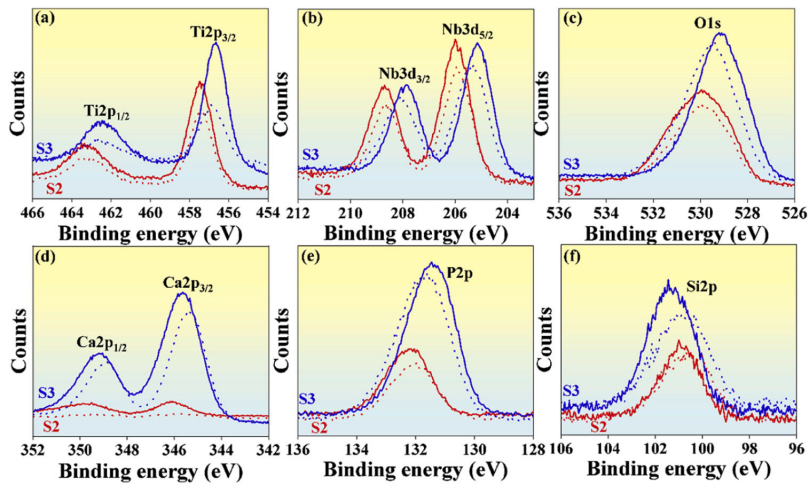


Fig. 11. (a-f). X-ray photoelectron spectroscopy (XPS) spectra of Ti2p, Nb3d, O1s, Ca2p, P2p, and Si2p of the S2 and S3 samples after potentiodynamic polarization (PDP) curve in simulated body fluid (SBF) at pH 7 and 37 °C. The dotted line denotes the period before PDP studies, and the solid line denotes the period after PDP studies.

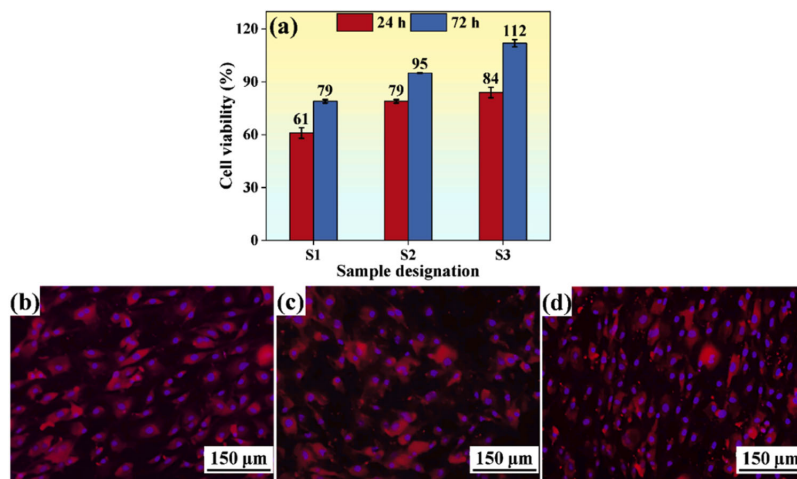


Fig. 12. (a) Cell viability of S1, S2, and S3 samples assessed using the Alamar Blue assay with MC3T3 pre-osteoblast cells after 24 h and 72 h of incubation. (b-d) Fluorescence images of MC3T3 pre-osteoblast cells cultured on the surfaces of S1, S2, and S3 samples, respectively, after 72 h of incubation.

contributing to improved biological performance of the coating [109].

Fig. 12(b-d) presents fluorescent imaging of MC3T3 pre-osteoblast cells cultured on the surfaces of samples S1, S2, and S3. Dual staining was performed using DAPI (blue-fluorescent DNA stain) and RFP (Red Fluorescent Protein) to visualize cellular components. DAPI selectively stains nuclear DNA, while RFP highlights the cytoskeletal architecture, enabling clear differentiation of cell morphology on the sample surfaces. All samples exhibited healthy cell morphology; however, the fluorescence image of S3 (Fig. 12(d)) revealed markedly enhanced cellular attachment and spreading. This behavior is attributed to the favorable microenvironment provided by the porous, HAp-rich coating, which offers anchoring features such as pore walls and surface edges that facilitate initial cell adhesion. The rough and porous surface texture promotes the extension of filopodia and lamellipodia, enhancing cell mobility, an essential factor in the early stages of osseointegration.

Additionally, HAP nanoparticles act as active nucleation sites for apatite formation, closely mimicking the mineral phase of natural bone [110]. In agreement with the Alamar Blue assay results, the fluorescence imaging confirms a higher density of viable cells with well-defined morphology on the S3 surface. The combined presence of surface roughness, bioactive ions from HAp, and the $\text{TiO}_2\text{-Nb}_2\text{O}_5$ oxide matrix contributes to the coating's suitability for implant applications. These findings validate that surface functionalization of the Ti40Nb alloy via plasma electrolytic oxidation in a phosphate-silicate-hydroxyapatite-based electrolyte yields a bioactive surface with significantly improved corrosion resistance and biocompatibility.

4. Conclusion

In summary, this study demonstrates the potential of plasma

electrolytic oxidation as an effective surface modification strategy to enhance the biomedical performance of in-situ alloyed Ti40Nb fabricated via SLM:

1. Structural characterization confirmed the formation of key oxide phases, including TiO₂ (anatase and rutile) and Nb₂O₅, in the S2 and S3 coatings. The incorporation of hydroxyapatite (HAp) nanoparticles in S3 promoted a higher fraction of rutile, attributed to localized thermal effects during PEO processing.
2. Surface morphology was significantly improved by HAp incorporation, resulting in reduced porosity, increased coating thickness, and refined pore structure. The distinct volcanic-like features observed in S3 contributed to greater surface roughness and effective surface area, while the release of bioactive Ca²⁺ and PO₄³⁻ ions enhanced hydrophilicity through hydroxyl group adsorption.
3. Electrochemical testing revealed superior corrosion resistance in coated samples (S2 and S3) compared to the uncoated S1. Among them, S3 exhibited the highest polarization resistance and lowest corrosion current density, attributed to the formation of a more compact and stable oxide layer.
4. In vitro biocompatibility analysis demonstrated that the HAp-enriched S3 coating significantly enhanced cell adhesion, viability, and proliferation, confirming its improved osseointegration potential.

Considering, the combination of a rough, bioactive surface with controlled porosity and tailored chemical functionality supports osteogenic activity, making the material highly suitable for orthopedic applications. Overall, these findings suggest that PEO-treated, SLM-processed Ti40Nb alloys with HAp incorporation represent a promising class of advanced materials for next-generation orthopedic implants.

CRedit authorship contribution statement

Shangavi Subramanian: Writing – original draft, Methodology, Investigation, Formal analysis, Data curation, Conceptualization. **Kesavan Praveenkumar:** Writing – review & editing, Validation, Methodology, Data curation. **Nagumothu Rameshbabu:** Validation, Resources, Methodology, Conceptualization. **Kuppusamy Lokeshraj:** Writing – original draft, Investigation, Formal analysis, Data curation. **Ansheed Raheem:** Writing – original draft, Investigation, Formal analysis, Data curation. **Jayamani Jayaraj:** Writing – review & editing, Validation, Supervision, Investigation, Data curation, Conceptualization. **Konda Gokuldoss Prashanth:** Writing – review & editing, Validation, Supervision, Resources, Project administration, Investigation, Funding acquisition, Conceptualization.

Declaration of competing interest

The authors declare that they have no known competing financial interests or personal relationships that could have appeared to influence the work reported in this paper.

Data availability

Data will be made available on request.

References

- [1] L.C. Zhang, H. Attar, Selective laser melting of titanium alloys and titanium matrix composites for biomedical applications: a review, *Adv. Eng. Mater.* 18 (2016) 463–475, <https://doi.org/10.1002/adem.201500419>.
- [2] C.N. Elias, J.H.C. Lima, R. Valiev, M.A. Meyers, Biomedical applications of titanium and its alloys *Biological Materials Science* 46–49, *Biol. Mater. Sci.* (2008) 1–4. www.tms.org/jom.html.
- [3] T. Maity, C.Gammer Balci, E. Ivanov, J. Eckert, K.G. Prashanth, High pressure torsion induced lowering of Young's modulus in high strength TNZT alloy for bio-implant applications, *J. Mech. Behav. Biomed. Mater.* 108 (2020) 103839, <https://doi.org/10.1016/j.jmbmm.2020.103839>.
- [4] M.K. Yadav, V. Pandey, A.Kumar Jyoti, K. Mohanta, V.K. Singh, Mechanical and biological behaviour of porous Ti–SiO₂ scaffold for tissue engineering application, *Ceram. Int.* 47 (2021) 22191–22200, <https://doi.org/10.1016/J.CERAMINT.2021.04.242>.
- [5] R. Shukla, M.K. Yadav, L.Y.C. Madruga, J. Jayaraj, K. Popat, Z. Wang, L. Xi, K. G. Prashanth, A novel Ti-eggshell-based composite fabricated by combined additive manufacturing-powder metallurgical routes as bioimplants, *Ceram. Int.* 51 (2025) 6281–6291, <https://doi.org/10.1016/J.CERAMINT.2024.12.073>.
- [6] M.K. Yadav, R. Shukla, L. Xi, Z. Wang, K.G. Prashanth, Metallic multimaterials fabricated by combining additive manufacturing and powder metallurgy, *J. Compos. Sci.* 2025 9 (2025) 809, <https://doi.org/10.3390/JCS9020080>, Page80.
- [7] Q. Yan, B. Chen, N. Kang, X. Lin, S. Lv, K. Kondoh, S. Li, J.S. Li, Comparison study on microstructure and mechanical properties of Ti-6Al-4V alloys fabricated by powder-based selective-laser-melting and sintering methods, *Mater. Charact.* 164 (2020) 110358, <https://doi.org/10.1016/j.matchar.2020.110358>.
- [8] H. Schwab, K. Prashanth, L. Löber, U. Kühn, J. Eckert, Selective laser melting of Ti-45Nb alloy, *Metals* 5 (2015) 686–694, <https://doi.org/10.3390/met5020686>.
- [9] N. Singh, P. Hameed, R. Ummethala, G. Manivasagam, K.G. Prashanth, J. Eckert, Selective laser manufacturing of Ti-based alloys and composites: impact of process parameters, application trends, and future prospects, *Mater. Today Adv.* 8 (2020) 100097, <https://doi.org/10.1016/j.mtadv.2020.100097>.
- [10] R. Ummethala, J. Jayaraj, P.S. Karamched, S. Rathinavelu, N. Singh, K. B. Surreddi, K.G. Prashanth, Vitro corrosion behavior of selective laser melted Ti-35Nb-7Zr-5Ta, *J. Mater. Eng. Perform.* (2021) 1–12, <https://doi.org/10.1007/s11665-021-05940-9>.
- [11] M. Niinomi, Recent research and development in metallic materials for biomedical, dental and Healthcare products applications, *Mater. Sci. Forum* 539–543 (2007) 193–200, <https://doi.org/10.4028/www.scientific.net/MSF.539-543.193>.
- [12] H. Shipley, D. McDonnell, M. Culleter, R. Coull, R. Lupoi, G. O'Donnell, D. Trimble, Optimisation of process parameters to address fundamental challenges during selective laser melting of Ti-6Al-4V: a review, *Int. J. Mach. Tools. Manuf.* 128 (2018) 1–20, <https://doi.org/10.1016/j.ijmactools.2018.01.003>.
- [13] T. Ozaki, H. Matsumoto, S. Watanabe, S. Hanada, Beta Ti alloys with Low Young's modulus, *Mater. Trans.* 45 (2004) 2776–2779, <https://doi.org/10.2320/matertrans.45.2776>.
- [14] Yu.P. Sharkeev, A.I. Dmitriev, A.G. Knyazeva, A.Yu. Eroshenko, A.A. Saprykin, M. A. Khimich, E.A. Ibragimov, I.A. Glukhov, A.M. Mairambekova, A.Yu. Nikonov, SELECTIVE LASER MELTING OF THE Ti-(40-50) wt.% Nb ALLOY, high temperature material processes an international quarterly of high-technology plasma processes 21 (2017) 161–183. <https://doi.org/10.1615/HighTempMatProc.2017024814>.
- [15] M. Marczewski, K. Wieczerek, X. Maeder, L. Lapeyre, C. Hain, M. Jurczyk, T. Nelis, Microstructure and mechanical properties of Ti-Nb alloys: comparing conventional powder metallurgy, mechanical alloying, and high power impulse magnetron sputtering processes for supporting materials screening, *J. Mater. Sci.* 59 (2024) 9107–9125, <https://doi.org/10.1007/s10853-024-09715-0>.
- [16] P. Hameed, C.F. Liu, R. Ummethala, N. Singh, H.H. Huang, G. Manivasagam, K. G. Prashanth, Biomorphic porous Ti6Al4V gyroid scaffolds for bone implant applications fabricated by selective laser melting, *Prog. Addit. Manuf.* 6 (2021) 455–469, <https://doi.org/10.1007/s40964-021-00210-5>.
- [17] R. Karre, M.K. Niranjan, S.R. Dey, First principles theoretical investigations of low Young's modulus beta Ti-Nb and Ti-Nb-Zr alloys compositions for biomedical applications, *Mater. Sci. Eng. C* 50 (2015) 52–58, <https://doi.org/10.1016/j.msec.2015.01.061>.
- [18] J. Liu, J. Ruan, L. Chang, H. Yang, W. Ruan, Porous Nb-Ti-Ta alloy scaffolds for bone tissue engineering: fabrication, mechanical properties and in vitro/vivo biocompatibility, *Mater. Sci. Eng.: C* 78 (2017) 503–512, <https://doi.org/10.1016/j.msec.2017.04.088>.
- [19] X. Wang, S. Zuo, G. Wang, J. Cao, Y. Zhang, M. Jin, Influence of Nb content on mechanical behavior and microstructure of Ti-Nb alloys, *Int. J. Mater. Res.* 113 (2022) 205–213, <https://doi.org/10.1515/ijmr-2020-8050>.
- [20] L. Fikeni, K.A. Annan, K. Mutombo, R. Machaka, Effect of Nb content on the microstructure and mechanical properties of binary Ti-Nb alloys, *Mater Today Proc.* Elsevier Ltd., 2021, pp. 913–917, <https://doi.org/10.1016/j.matpr.2020.05.315>.
- [21] Q. Wang, C. Han, T. Choma, Q. Wei, C. Yan, B. Song, Y. Shi, Effect of Nb content on microstructure, property and in vitro apatite-forming capability of Ti-Nb alloys fabricated via selective laser melting, *Mater. Des.* 126 (2017) 268–277, <https://doi.org/10.1016/j.matdes.2017.04.026>.
- [22] M.K. Han, J.Y. Kim, M.J. Hwang, H.J. Song, Y.J. Park, Effect of Nb on the microstructure, mechanical properties, corrosion behavior, and cytotoxicity of Ti-Nb alloys, *Materials* 8 (2015) 5986–6003, <https://doi.org/10.3390/ma8095287>.
- [23] E. Lokeshkumar, C. Premchand, P. Manojkumar, R. Shishir, L.R. Krishna, K. G. Prashanth, N. Rameshbabu, Effect of electrolyte composition on the surface characteristics of plasma electrolytic oxidation coatings over Ti-40Nb alloy, *Surf. Coat. Technol.* 465 (2023), <https://doi.org/10.1016/j.surfcoat.2023.129591>.
- [24] M. Tian, Y. Guan, F. Zhao, Y. Xiong, J. Bai, W. Zhao, X. Jia, H. Guo, H. San, Review of the processing parameters of the plasma electrolytic oxidation on titanium alloys for biological application, *Innov. Sci. Technol.* 4 (2025) 1–20, <https://doi.org/10.56397/IST.2025.01.01>.

- [25] G.C. Cardoso, C.R. Grandini, J.V. Rau, Comprehensive review of PEO coatings on titanium alloys for biomedical implants, *J. Mater. Res. Technol.* 31 (2024) 311–328, <https://doi.org/10.1016/j.jmrt.2024.06.068>.
- [26] F. Barrino, Hybrid organic–inorganic materials prepared by sol–Gel and sol–Gel-coating method for biomedical use: study and synthetic review of synthesis and properties, *Coatings* 2024 14 (2024) 42514, <https://doi.org/10.3390/COATINGS14040425>, Page425.
- [27] V.P. Ricci, R.F.M. dos Santos, G.H. Asato, V. Roche, A.M. Jorge, C.R.M. Afonso, Assessment of anodization conditions and annealing temperature on the microstructure, elastic modulus, and wettability of β -Ti40Nb alloy, *Thin Solid Films* 737 (2021) 138949, <https://doi.org/10.1016/j.tsf.2021.138949>.
- [28] L.-C. Zhang, L.-Y. Chen, L. Wang, Surface modification of titanium and titanium alloys: technologies, developments, and future interests, *Adv. Eng. Mater.* 22 (2020), <https://doi.org/10.1002/adem.201901258>.
- [29] S. Kowalski, W. Gonciarz, R. Belka, A. Góral, M. Chmiela, E. Lechowicz, W. Kaca, W. Żorawski, Plasma-sprayed hydroxyapatite coatings and their biological properties, *coatings* 2022, Vol. 12, Page 131712 (2022) 1317, <https://doi.org/10.3390/COATINGS12091317>.
- [30] J.R.F. Neto, R.P. Ribeiro, N.C. da Cruz, E.C. Rangel, B. de O. Pinto, J.E. M. Torrente, C.R. Grandini, U.F. Kaneko, D.R.N. Correa, Effect of bulk phase composition on the growth of PEO coatings on the biomedical Ti-6Al-4V alloy, *Materials* 18 (2025) 955, <https://doi.org/10.3390/MA18050955>.
- [31] P.A.B. Kuroda, C.R. Grandini, C.R.M. Afonso, Surface characterization of new β Ti-25Ta-Zr-Nb alloys modified by micro-arc oxidation, *Materials* 2023 16 (2023) 235216, <https://doi.org/10.3390/MA16062352>, Page2352.
- [32] Z.Y. Zhang, T.Y. Huang, D.J. Zhai, H.B. Wang, K.Q. Feng, L. Xiang, Study on strontium doped bioactive coatings on titanium alloys surfaces by micro-arc oxidation, *Surf. Coat. Technol.* 451 (2022) 129045, <https://doi.org/10.1016/j.surfcoat.2022.129045>.
- [33] A. Maciej, M. Marny, M. Sowa, A. Blacha-Grzechnik, A. Stolarczyk, J. Michalska, W. Simka, Microstructure and corrosion resistance of Ti and Ti-40Nb alloy modified by plasma electrolytic oxidation in tricalcium phosphate suspension, *Electrochim. Acta* 468 (2023) 143185, <https://doi.org/10.1016/j.electacta.2023.143185>.
- [34] S. Sarbishei, M.A. Faghghi Sani, M.R. Mohammadi, Effects of alumina nanoparticles concentration on microstructure and corrosion behavior of coatings formed on titanium substrate via PEO process, *Ceram. Int.* 42 (2016) 8789–8797, <https://doi.org/10.1016/j.ceramint.2016.02.120>.
- [35] M. Roknian, A. Fattah-alhosseini, S.O. Gashti, M.K. Keshavarz, Study of the effect of ZnO nanoparticles addition to PEO coatings on pure titanium substrate: microstructural analysis, antibacterial effect and corrosion behavior of coatings in Ringer’s physiological solution, *J. Alloys Compd.* 740 (2018) 330–345, <https://doi.org/10.1016/j.jallcom.2017.12.366>.
- [36] K.P. Surwondo, D.A. Fitriani, S.A. Azahra, A. Nugroho, P.S. Ashfiya, M. Kozin, P. Puranto, M.P. Kamil, Hybrid organic-inorganic coatings of plasma electrolytic oxidation and polyaniline for improving corrosion protection of Al alloys in diverse pH environments, *Surf. Coat. Technol.* 504 (2025) 132045, <https://doi.org/10.1016/j.surfcoat.2025.132045>.
- [37] S. Fatimah, F. Hazmatulhaq, Y. Sheng, T. Suhartono, J.M. Oh, N. Nashrah, J. H. Kang, Y.G. Ko, Effect of ultrasonic frequency on structure and corrosion properties of coating formed on magnesium alloy via plasma electrolytic oxidation, *Materials* 16 (2023) 5424, <https://doi.org/10.3390/MA16155424>.
- [38] L. Pezzato, M. Dabala, K. Brunelli, Microstructure and corrosion properties of PEO coatings produced on am–aluminum alloys. *Key Eng Mater.* Trans Tech Publications Ltd, 2019, pp. 298–303, <https://doi.org/10.4028/www.scientific.net/KEM.813.298>.
- [39] B. Makurat-Kasprolewicz, M. Wekwejt, L. Pezzato, A. Ronowska, J. Krupa, S. Zimowski, S. Dzionk, A. Ossowska, Effect of ultrasound on the physicochemical, mechanical and adhesive properties of micro-arc oxidized coatings on Ti13Nb13Zr bio-alloy, *Sci. Rep.* 202414:114 (2024) 25421, <https://doi.org/10.1038/s41598-024-75626-4>.
- [40] T. Wu, C. Blawert, M. Serdechnova, P. Karlova, G. Dovzhenko, D.C. Florian Wieland, S. Stojadinovic, R. Vasilic, L. Wang, C. Wang, K. Mojsilovic, M. L. Zheludkevich, Role of phosphate, silicate and aluminate in the electrolytes on PEO coating formation and properties of coated Ti6Al4V alloy, *Appl. Surf. Sci.* 595 (2022) 153523, <https://doi.org/10.1016/j.apsusc.2022.153523>.
- [41] J.H. Ni, Y.L. Shi, F.Y. Yan, J.Z. Chen, L. Wang, Preparation of hydroxyapatite-containing titania coating on titanium substrate by micro-arc oxidation, *Mater. Res. Bull.* 43 (2008) 45–53, <https://doi.org/10.1016/j.matresbull.2007.02.019>.
- [42] X. Zhang, Y. Wu, Y. Lv, Y. Yu, Z. Dong, Formation mechanism, corrosion behaviour and biological property of hydroxyapatite/TiO2 coatings fabricated by plasma electrolytic oxidation, *Surf. Coat. Technol.* 386 (2020) 125483, <https://doi.org/10.1016/j.surfcoat.2020.125483>.
- [43] M. Kumar Yadav, R. Hiren Shukla, K.G. Prashanth, A Comprehensive Review on Development of Waste Derived Hydroxyapatite (HAP) For Tissue Engineering Application, *Mater Today Proc.* 2023, <https://doi.org/10.1016/j.matpr.2023.04.669>.
- [44] M.K. Yadav, V. Pandey, K. Mohanta, V.K. Singh, A low-cost approach to develop silica doped Tricalcium phosphate (TCP) scaffold by valorizing animal bone waste and rice husk for tissue engineering applications, *Ceram. Int.* 48 (2022) 25335–25345, <https://doi.org/10.1016/j.ceramint.2022.05.207>.
- [45] P.A.B. Kuroda, T.H. Montes, M.C. Rossi, C.R. Grandini, C.R.M. Afonso, Unraveling crystalline phases, morphology, hardness, and adhesion of PEO anodic coatings on Ti-15Nb alloy surface, *Mater. Lett.* 356 (2024) 135607, <https://doi.org/10.1016/j.matlet.2023.135607>.
- [46] M. Yan, S.D. Luo, G.B. Schaffer, M. Qian, TEM and XRD characterisation of commercially pure α -Ti made by powder metallurgy and casting, *Mater. Lett.* 72 (2012) 64–67, <https://doi.org/10.1016/j.matlet.2011.12.072>.
- [47] S. Eiumtadanai, S. Mahathanabodee, R. Tongrsi, B. Vetyanungul, P. Wiman, Deformation and corrosion resistance of sintered AISI 303 austenitic stainless steel after hot forging, *J. Mater. Eng. Perform.* (2025) 1–14, <https://doi.org/10.1007/s11665-025-11276-5>.
- [48] R. Ummethala, P.S. Karamched, S. Rathinavelu, N. Singh, A. Aggarwal, K. Sun, E. Ivanov, L. Kollo, I. Okulov, J. Eckert, K.G. Prashanth, Selective laser melting of high-strength, low-modulus Ti–35Nb–7Zr–5Ta alloy, *Materials* 14 (2020) 100941, <https://doi.org/10.1016/j.mta.2020.100941>.
- [49] R. Rahmani, M. Brojan, M. Antonov, K.G. Prashanth, Perspectives of metal-diamond composites additive manufacturing using SLM-SPS and other techniques for increased wear-impact resistance, *Int. J. Refract. Met. Hard Mater.* 88 (2020) 105192, <https://doi.org/10.1016/j.ijrmhm.2020.105192>.
- [50] H.S. Maurya, K. Kosiba, K. Juhani, F. Sergejev, K.G. Prashanth, Effect of powder bed preheating on the crack formation and microstructure in ceramic matrix composites fabricated by laser powder-bed fusion process, *Addit. Manuf.* 58 (2022) 103013, <https://doi.org/10.1016/j.addma.2022.103013>.
- [51] A. Sagidugumar, D. Dogadkin, A. Turlybekuly, D. Kaliyev, Calcium phosphate coatings deposited on 3D-printed Ti–6Al–4V alloy by plasma electrolytic oxidation, *Coatings* 2024 14 (2024) 69614, <https://doi.org/10.3390/COATINGS14060696>, Page696.
- [52] J. Yao, Y. Wang, G. Wu, M. Sun, M. Wang, Q. Zhang, Growth characteristics and properties of micro-arc oxidation coating on SLM-produced TC4 alloy for biomedical applications, *Appl. Surf. Sci.* 479 (2019) 727–737, <https://doi.org/10.1016/j.apsusc.2019.02.142>.
- [53] G. Wu, L. Li, M. Sun, Y. Wang, F. Luo, Q. Zhang, R. Liu, Z. Chen, J. Yao, Microstructural evolution and biological properties of PEO coating on SLM-prepared NiTi alloy, *Surf. Coat. Technol.* 452 (2023) 129065, <https://doi.org/10.1016/j.surfcoat.2022.129065>.
- [54] I. Vonavkova, D. Vojtech, D. Palousek, Characterization of β -Ti alloy prepared by SLM method, *Manuf. Technol.* 20 (2020) 690–696, <https://doi.org/10.21062/mft.2020.091>.
- [55] G. Wu, Y. Wang, M. Sun, Q. Zhang, J. Yao, Influence of microstructure of TC4 substrate on the MAO coating, *Surf. Eng.* 36 (2020) 827–836, <https://doi.org/10.1080/02670844.2019.1693732>.
- [56] L. Pezzato, M. Dabala, S. Gross, K. Brunelli, Effect of microstructure and porosity of AlSi10Mg alloy produced by selective laser melting on the corrosion properties of plasma electrolytic oxidation coatings, *Surf. Coat. Technol.* 404 (2020) 126477, <https://doi.org/10.1016/j.surfcoat.2020.126477>.
- [57] H. Wang, D. Zhai, K. Feng, Effect of the microstructure of a titanium alloy fabricated using selective laser melting on microarc oxidation film, *Met. Mater. Trans Phys. Met. Mater. Sci.* 52 (2021) 4691–4702, <https://doi.org/10.1007/s11661-021-06421-3>.
- [58] J. Karimi, C. Suryanarayana, I. Okulov, K.G. Prashanth, Selective laser melting of Ti6Al4V: effect of laser re-melting, *Mater. Sci. Eng. A* 805 (2020) 140558, <https://doi.org/10.1016/j.msea.2020.140558>.
- [59] J. Karimi, C. Zhao, K.G. Prashanth, Massive transformation in dual-laser powder bed fusion of Ti6Al4V alloys, *J. Manuf. Process.* 119 (2024) 282–292, <https://doi.org/10.1016/j.jmapro.2024.03.083>.
- [60] K.G. Prashanth, R. Damodaram, T. Maity, P. Wang, J. Eckert, Friction welding of selective laser melted Ti6Al4V parts, *Mater. Sci. Eng. A* 704 (2017) 66–71, <https://doi.org/10.1016/j.msea.2017.08.004>.
- [61] N. Rameshbabu, K.P. Rao, T.S.S. Kumar, Accelerated microwave processing of nanocrystalline hydroxyapatite, *J. Mater. Sci.* 40 (2005) 6319–6323, <https://doi.org/10.1007/s10853-005-2957-9>.
- [62] S.S. Nisar, H.-C. Choe, Mechanical hydroxyapatite coatings on PEO-treated Ti–6Al–4V alloy for enhancing implant’s surface bioactivity, *Ceram. Int.* 50 (2024) 17703–17719, <https://doi.org/10.1016/j.ceramint.2024.02.259>.
- [63] T. Kokubo, H. Takadama, How useful is SBF in predicting in vivo bone bioactivity? *Biomaterials* 27 (2006) 2907–2915, <https://doi.org/10.1016/j.biomaterials.2006.01.017>.
- [64] W.-H. Song, Y.-K. Jun, Y. Han, S.-H. Hong, Biomimetic apatite coatings on micro-arc oxidized titania, *Biomaterials* 25 (2004) 3341–3349, <https://doi.org/10.1016/j.biomaterials.2003.09.103>.
- [65] S. Arun, B.S. Lim, S.G. Ahn, H.-C. Choe, Osteoconductive element-doped, porous, and low-elastic-modulus duplex coatings on a Ti-6Al-4 V alloy: a hybrid coating system for accelerating cell growth, *J. Alloys Compd.* 943 (2023) 169131, <https://doi.org/10.1016/j.jallcom.2023.169131>.
- [66] S. Ikonopisov, Theory of electrical breakdown during formation of barrier anodic films, *Electrochim. Acta* 22 (1977) 1077–1082, [https://doi.org/10.1016/0013-4686\(77\)80042-X](https://doi.org/10.1016/0013-4686(77)80042-X).
- [67] H. Mozafarnia, A. Fattah-Alhosseini, R. Chaharmahali, M. Nouri, M.K. Keshavarz, M. Kaseem, Corrosion, wear, and antibacterial behaviors of hydroxyapatite/MgO composite PEO coatings on AZ31 Mg alloy by incorporation of TiO2 nanoparticles, *Coatings* 12 (2022), <https://doi.org/10.3390/coatings12121967>.
- [68] M. Echeverry-Rendón, O. Galvis, D. Quintero Giraldo, J. Pavón, J.L. López-Lacomba, E. Jiménez-Piqué, M. Anglada, S.M. Robledo, J.G. Castaño, F. Echeverría, Osseointegration improvement by plasma electrolytic oxidation of modified titanium alloys surfaces, *J. Mater. Sci. Mater. Med.* 26 (2015) 1–18, <https://doi.org/10.1007/s10856-015-5408-4>.
- [69] T. Ahmed, H.J. Rack, Martensitic transformations in Ti–(16–26 at%) Nb alloys, *J. Mater. Sci.* 31 (1996) 4267–4276, <https://doi.org/10.1007/BF00356449>.
- [70] L. Zhou, T. Yuan, J. Tang, J. He, R. Li, Mechanical and corrosion behavior of titanium alloys additively manufactured by selective laser melting –A comparison

- between nearly β titanium, α titanium and $\alpha + \beta$ titanium, *Opt. Laser. Technol.* (2019) 119, <https://doi.org/10.1016/j.optlastec.2019.105625>.
- [71] C. Zhao, Z. Wang, D. Li, L. Kollo, Z. Luo, W. Zhang, K.G. Prashanth, Cu-Ni-Sn alloy fabricated by melt spinning and selective laser melting: a comparative study on the microstructure and formation kinetics, *J. Mater. Res. Technol.* 9 (2020) 13097–13105, <https://doi.org/10.1016/j.jmrt.2020.09.047>.
- [72] Z. Wang, M. Xie, Y. Li, W. Zhang, C. Yang, L. Kollo, J. Eckert, K.G. Prashanth, Premature failure of an additively manufactured material, *NPG Asia Mater.* 12 (2020) 1–10, <https://doi.org/10.1038/s41427-020-0212-0>.
- [73] N.P. Ferraz, F.C.F. Marcos, A.E. Nogueira, A.S. Martins, M.R.V. Lanza, E.M. Assaf, Y.J.O. Asencios, Hexagonal-Nb2O5/anatase-TiO2 mixtures and their applications in the removal of Methylene blue dye under various conditions, *Mater. Chem. Phys.* 198 (2017) 331–340, <https://doi.org/10.1016/j.mchemphys.2017.06.029>.
- [74] D.A.H. Hanoor, C.C. Sorrell, Review of the anatase to rutile phase transformation, *J. Mater. Sci.* 46 (2011) 855–874, <https://doi.org/10.1007/s10853-010-5113-0>.
- [75] A.E.R. Friedemann, T.M. Gesing, P. Plegemann, Electrochemical rutile and anatase formation on PEO surfaces, *Surf. Coat. Technol.* 315 (2017) 139–149, <https://doi.org/10.1016/j.surfcoat.2017.01.042>.
- [76] S. Subramanian, M.K. Yadav, J. Jayaraj, F. Yangyang, L. Xi, K.G. Prashanth, Microstructural homogenization through laser remelting in an additively manufactured Ti-40Nb sample from elemental feedstock powders, *J. Mater. Res. Technol.* 38 (2025) 4305–4320, <https://doi.org/10.1016/j.jmrt.2025.08.203>.
- [77] J. Karimi, L. Kollo, K.G. Prashanth, Tailoring anisotropy and heterogeneity of selective laser melted Ti6Al4V alloys, *Trans. Indian Natl. Acad. Eng.* 2023 (2023) 1–7, <https://doi.org/10.1007/s41403-023-00393-z>.
- [78] J. Karimi, M. Antonov, L. Kollo, K.G. Prashanth, Role of laser remelting and heat treatment in mechanical and tribological properties of selective laser melted Ti6Al4V alloy, *J. Alloys Compd.* 897 (2022) 163207, <https://doi.org/10.1016/j.jallcom.2021.163207>.
- [79] J. Karimi, M.S. Xie, Z. Wang, K.G. Prashanth, Influence of substructures on the selective laser melted Ti-6Al-4V alloy as a function of laser re-melting, *J. Manuf. Process.* 68 (2021) 1387–1394, <https://doi.org/10.1016/j.jmapro.2021.06.059>.
- [80] N. Valizade, A. Sabour Rouh Aghdam, G. Jarjoura, Corrosion and biological study on biofunctionalized porous coating on titanium produced by plasma electrolytic oxidation, *Colloids Surf. Physicochem. Eng. Asp.* 688 (2024) 133567, <https://doi.org/10.1016/j.colsurfa.2024.133567>.
- [81] S. Arun, S.G. Ahn, H.C. Choe, Surface characteristics of HA-coated and PEO-treated Ti-6Al-4V alloy in solution containing Ag nanoparticles, *Surf. Interfaces* 39 (2023) 102932, <https://doi.org/10.1016/j.surfint.2023.102932>.
- [82] X.Q. Wu, F.Q. Xie, Z.C. Hu, L. Wang, Effects of additives on corrosion and wear resistance of micro-arc oxidation coatings on TiAl alloy, *Trans. Nonferrous Met. Soc. China* 20 (2010) 1032–1036, [https://doi.org/10.1016/S1003-6326\(09\)60253-3](https://doi.org/10.1016/S1003-6326(09)60253-3).
- [83] N.A. Sukrey, M. Rizwan, A.R. Bushroa, S.Z. Salleh, W.J. Basirun, Development and characterization of bioglass incorporated plasma electrolytic oxidation layer on titanium substrate for biomedical application, *Rev. Adv. Mater. Sci.* 60 (2021) 678–690, https://doi.org/10.1515/RAMS-2021-0052/ASSET/GRAPHIC/JRAMS-2021-0052_FIG_011.JPG.
- [84] M. Kulkarni, Y. Patil-Sen, I. Junkar, V. Kulkarni, M. Lorenzetti, A. Iglıc, Wettability studies of topologically distinct titanium surfaces, *Colloids. Surf. B Biointerfaces* 129 (2015) 47–53, <https://doi.org/10.1016/j.colsurfb.2015.03.024>.
- [85] W. Zhu, N. Tang, C. Jia, Y. Zhang, A superwetting rough structured nanofibrous membrane with enhancing anti-fouling performance for oil–water separation, *Sep. Purif. Technol.* 359 (2025) 130800, <https://doi.org/10.1016/j.seppur.2024.130800>.
- [86] S.S. Farhadi, M. Aliofkhaezai, G. Barati Darband, A. Abolhasani, A. Sabour Rouhaghdam, Corrosion and wettability of PEO coatings on magnesium by addition of potassium stearate, *J. Magnes. Alloys* 5 (2017) 210–216, <https://doi.org/10.1016/j.jma.2017.06.002>.
- [87] J. Xiang Han, Y. Lin Cheng, W. bin Tu, T.Y. Zhan, Y. liang Cheng, The black and white coatings on Ti-6Al-4V alloy or pure titanium by plasma electrolytic oxidation in concentrated silicate electrolyte, *Appl. Surf. Sci.* 428 (2018) 684–697, <https://doi.org/10.1016/j.apsusc.2017.09.109>.
- [88] Y. Li, W. Wang, F. Yu, D. Wang, S. Guan, Y. Li, M. Qi, Characterization and cytocompatibility of hierarchical porous TiO2 coatings incorporated with calcium and strontium by one-step micro-arc oxidation, *Mater. Sci. Eng. C* 109 (2020) 110610, <https://doi.org/10.1016/j.msec.2019.110610>.
- [89] M. Molaei, A. Fattah-alhosseini, M. Nouri, P. Mahmoodi, A. Nourian, Incorporating TiO2 nanoparticles to enhance corrosion resistance, cytocompatibility, and antibacterial properties of PEO ceramic coatings on titanium, *Ceram. Int.* 48 (2022) 21005–21024, <https://doi.org/10.1016/j.ceramint.2022.04.096>.
- [90] M. Fazel, H.R. Salimijazi, M. Shamanian, I. Apachitei, A.A. Zadpoor, Influence of hydrothermal treatment on the surface characteristics and electrochemical behavior of Ti-6Al-4V bio-functionalized through plasma electrolytic oxidation, *Surf. Coat. Technol.* 374 (2019) 222–231, <https://doi.org/10.1016/j.surfcoat.2019.05.088>.
- [91] S.S. Malheiros, M.H.R. Borges, E.C. Rangel, C.A. Fortulan, N.C. da Cruz, V.A. R. Barao, B.E. Nagay, Zinc-doped antibacterial coating as a single approach to unlock multifunctional and highly resistant titanium implant surfaces, *ACS Appl. Mater. Interfaces* (2025), <https://doi.org/10.1021/acsami.4c21875>.
- [92] R.C. Costa, J.G.S. Souza, J.M. Cordeiro, M. Bertolini, E.D. de Avila, R. Landers, E. C. Rangel, C.A. Fortulan, B. Retamal-Valdes, N.C. da Cruz, M. Feres, V.A.R. Barão, Synthesis of bioactive glass-based coating by plasma electrolytic oxidation: untangling a new deposition pathway toward titanium implant surfaces, *J. Colloid. Interface Sci.* 579 (2020) 680–698, <https://doi.org/10.1016/j.jcis.2020.06.102>.
- [93] H.S. Maurya, R. Kumar, S.A. Kumar, M. Tarraste, A. Hussain, R. Rahmani, K. Juhani, F. Sergejev, K.G. Prashanth, Sliding wear and debris evolution in LPBFed ceramic-reinforced steel composites under variable loads and temperatures, *Mater. Chem. Phys.* 345 (2025) 131195, <https://doi.org/10.1016/j.mchemphys.2025.131195>.
- [94] K. Praveenkumar, J. Vishnu, C. Samuel S, V. Gopal, M. Arivarasu, J.M. Lackner, B. Meier, D. Karthik, S. Suwas, S. Swaroop, K.G. Prashanth, M.K. Yadav, G. Manivasagam, High temperature dry sliding wear behaviour of selective laser melted Ti-6Al-4V alloy surfaces, *J. Mater. Process. Technol.* 329 (2024) 118439, <https://doi.org/10.1016/j.jmatprotec.2024.118439>.
- [95] B. Yavuzegit, K. Karali, E. Avcu, A. De Mori, D. Quizon, M. Haciosmanoglu, P. Hekimoglu, N. Smith, S. Usov, P. Shashkov, R. Bonithon, G. Blunn, Corrosion and mechanical performance of novel electrochemical oxidation coatings on AZ31 magnesium alloys for biomedical applications, *Surf. Coat. Technol.* 507 (2025) 132151, <https://doi.org/10.1016/j.surfcoat.2025.132151>.
- [96] K. Praveenkumar, J. Vishnu, A. Raheem, V. Gopal, S. Swaroop, S. Suwas, B. Shankar, G. Manivasagam, In-vitro fretting tribo-corrosion and biocompatibility aspects of laser shock peened Ti-6Al-4V surfaces, *Appl. Surf. Sci.* 665 (2024) 160334, <https://doi.org/10.1016/j.apsusc.2024.160334>.
- [97] M.K. Yadav, R.H. Shukla, K. Praveenkumar, S. Nilavar, C.S. Perugu, P. Sellamuthu, K. Chatterjee, S. Suwas, J. Jayaraj, K.G. Prashanth, Microstructural, mechanical, corrosion, and Biological Behavior of Spark Plasma Sintered Commercially Pure Zinc For Biomedical Applications, *Mater Adv.* 2025, <https://doi.org/10.1039/D5MA00092K>.
- [98] M.C. Rossi, P.A.B. Kuroda, A.V. Escuder, V. Amigó, C.R.M. Afonso, Nanostructured oxide composites in PEO coating of β Ti alloys with low elastic modulus for biomedical applications, *Tribol. Int.* 209 (2025) 110677, <https://doi.org/10.1016/j.triboint.2025.110677>.
- [99] F. Songur, B. Dikici, M. Niinomi, E. Arslan, The plasma electrolytic oxidation (PEO) coatings to enhance in-vitro corrosion resistance of Ti-29Nb-13Ta-4.6Zr alloys: the combined effect of duty cycle and the deposition frequency, *Surf. Coat. Technol.* 374 (2019) 345–354, <https://doi.org/10.1016/j.surfcoat.2019.06.025>.
- [100] M. Kaseem, H.C. Choe, Electrochemical and bioactive characteristics of the porous surface formed on Ti-Nb alloys via plasma electrolytic oxidation, *Surf. Coat. Technol.* 378 (2019) 125027, <https://doi.org/10.1016/j.surfcoat.2019.125027>.
- [101] L. Chen, K. Wei, Y. Qu, T. Li, B. Chang, B. Liao, W. Xue, Characterization of plasma electrolytic oxidation film on biomedical high niobium-containing β titanium alloy, *Surf. Coat. Technol.* 352 (2018) 295–301, <https://doi.org/10.1016/j.surfcoat.2018.08.025>.
- [102] S.R. Shechtman, R.G. Farrakhov, I.A. Ramazanov, V.A. Sheremetyev, E. V. Parfenov, Protective PEO-coatings on titanium shape memory alloy for medical implants, *IOP Conf Ser Mater Sci. Eng. IOP Publishing Ltd.* 2020, <https://doi.org/10.1088/1757-899X/1008/1/012016>.
- [103] M.T. Woldemedhin, D. Raabe, A.W. Hassel, Anodic oxides on a beta type Nb-Ti alloy and their characterization by electrochemical impedance spectroscopy, *Phys. Status Solidi (A) Appl. Mater. Sci.* 207 (2010) 812–816, <https://doi.org/10.1002/pssa.200983324>.
- [104] B.L. Pereira, C.M. Lepiński, V. Seba, M.J.D. Nugent, R. Torres, P.A.B. Kuroda, C. R. Grandini, P. Soares, Plasma electrolytic oxidation up to four steps performed on niobium and Nb-Ti alloys, *Surf. Coat. Technol.* 438 (2022) 128369, <https://doi.org/10.1016/j.surfcoat.2022.128369>.
- [105] J.E. Arce, A.E. Arce, Y. Aguilar, L. Yate, S. Moya, C. Rincón, O. Gutiérrez, Calcium phosphate-calcium titanate composite coatings for orthopedic applications, *Ceram. Int.* 42 (2016) 10322–10331, <https://doi.org/10.1016/j.ceramint.2016.02.177>.
- [106] L. Zhu, R.S. Petrova, J.P. Gashinski, Z. Yang, The effect of surface roughness on PEO-treated Ti-6Al-4V alloy and corrosion resistance, *Surf. Coat. Technol.* 325 (2017) 22–29, <https://doi.org/10.1016/j.surfcoat.2017.05.044>.
- [107] X. Zhu, J. Chen, L. Scheideler, R. Reichl, J. Geis-Gerstorfer, Effects of topography and composition of titanium surface oxides on osteoblast responses, *Biomaterials* 25 (2004) 4087–4103, <https://doi.org/10.1016/j.biomaterials.2003.11.011>.
- [108] K.-T. Kim, S. Sadaf Nisar, H.-C. Choe, Mechanically synthesized TCP/OCF composite coatings on the plasma electrolytic oxidized cold-worked pure titanium for bio-implant use, *Appl. Surf. Sci.* 680 (2025) 161370, <https://doi.org/10.1016/j.apsusc.2024.161370>.
- [109] S. Bauer, J. Park, K. von der Mark, P. Schmuki, Improved attachment of mesenchymal stem cells on super-hydrophobic TiO2 nanotubes, *Acta Biomater.* 4 (2008) 1576–1582, <https://doi.org/10.1016/j.actbio.2008.04.004>.
- [110] A.A. Raheem, P. Hameed, R. Whenish, R.S. Elsen, A.G. A.K. Jaiswal, K. G. Prashanth, G. Manivasagam, A review on development of bio-inspired implants using 3D printing, *Biomimetics* 6 (2021) 65, <https://doi.org/10.3390/biomimetics6040065>.

Publication IV

Subramanian, S., Manivasagam, G., Jayaraj, J., & Prashanth, K. G. (2026). Microstructural refinement, mechanical enhancement, and superior passivation of SLM Ti-Nb-Fe fabricated through insitu alloying. *Journal of Alloys and Compounds*, 187930. <https://doi.org/10.1016/j.jallcom.2026.187930>



Microstructural refinement, mechanical enhancement, and superior passivation of SLM Ti-Nb-Fe fabricated through insitu alloying

Shangavi Subramanian^a, Geetha Manivasagam^{b,c}, Jayamani Jayaraj^{d,e},
Konda Gokuldoss Prashanth^{a,b,f,*}

^a Department of Mechanical and Industrial Engineering, Tallinn University of Technology, Ehitajate tee 5, Tallinn 19086, Estonia

^b Centre for Biomaterials, Cellular and Molecular Theranostics (CBCMT), Vellore Institute of Technology, School of Mechanical Engineering, Tamil Nadu 632014, India

^c School of Healthcare Science and Engineering (SHINE), Vellore Institute of Technology, Vellore 632014, India

^d Materials Technology, Dalarna University, Falun SE-79188, Sweden

^e Department of Mechanical and Materials Engineering, Karlstad University, Karlstad SE-65188, Sweden

^f National Engineering Research Center of Near-Net-Shape Forming for Metallic Materials, South China University of Technology, Guangzhou 510640, China

ARTICLE INFO

Keywords:

Selective laser melting
Ti-35Nb-5Fe alloy
Elemental powder
Insitu Alloying

ABSTRACT

This study examines the microstructural, mechanical, and electrochemical passivation characteristics of a Ti-35 Nb-5Fe alloy fabricated by selective laser melting (SLM) using elemental powders, with Ti-40 Nb serving as a reference β -type alloy. Fe addition effectively stabilizes the β phase, increasing its fraction from $\sim 85\%$ in Ti-40 Nb to $\sim 99\%$ in Ti-35 Nb-5Fe, and promotes substantial grain refinement (from $\sim 48 \mu\text{m}$ to $\sim 11 \mu\text{m}$). These microstructural modifications enhance hardness, compressive strength, and plasticity while maintaining a low elastic modulus suitable for biomedical applications. Electrochemical impedance spectroscopy in phosphate-buffered saline at 37°C reveals the formation of a stable, protective passive film on Ti-35 Nb-5Fe, characterized by higher polarization resistance and lower capacitance during immersion. Mott-Schottky analysis confirms n-type semiconducting behavior with reduced donor density, consistent with Fe^{3+} -mediated oxygen-vacancy compensation predicted by the point defect model. X-ray photoelectron spectroscopy depth profiling identifies an $\sim 3 \text{ nm}$ thick mixed-oxide layer composed predominantly of TiO_2 , Nb_2O_5 , and Fe_2O_3 . The combined effects of β -phase stabilization, grain refinement, and modified passive-film chemistry demonstrate that SLM-fabricated Ti-35 Nb-5Fe possesses superior passivation stability and mechanical performance, highlighting its potential for load-bearing biomedical implant applications.

1. Introduction

The selection of materials for load-bearing orthopedic implants demands excellent biocompatibility, high mechanical strength, superior corrosion resistance, and an elastic modulus close to that of cortical bone [1,2]. Among available metallic biomaterials, titanium (Ti) and its alloys are widely favored because of their outstanding biocompatibility, inherent corrosion resistance, low density, and favorable mechanical performance [3,4]. Their exceptional corrosion resistance in physiological environments arises from the spontaneous formation of a stable, adherent TiO_2 passive film on the surface, which acts as an effective barrier to ionic dissolution and ensures long-term chemical stability [5,6]. Based on phase stability, Ti alloys are generally categorized into α -type, $\alpha + \beta$ -type, and β -type systems [7–9]. Early orthopedic implants

made from the $\alpha + \beta$ alloy Ti-6Al-4 V raised concerns due to the potential cytotoxicity of Al and V, as well as their relatively high elastic modulus ($\sim 110\text{--}120 \text{ GPa}$) [10–12]. Consequently, metastable β -type Ti alloys characterized by a significantly lower elastic modulus ($60\text{--}80 \text{ GPa}$) combined with high mechanical strength have emerged as promising alternatives for load-bearing orthopedic applications [13–15]. The phase stability of β -type Ti alloys is commonly designed using parameters such as the molybdenum equivalence (Mo_{eq}) and the electron-to-atom (e/a) ratio [16]. The most recent Mo_{eq} relationship for predicting the β -phase stability is proposed in Eq. (1) [17],

$$\begin{aligned} \text{Mo}_{\text{eq}} = & \text{Mo} + 1.25 \text{ V} + 0.59 \text{ W} + 0.28\text{Nb} + 0.22\text{Ta} + 1.93\text{Fe} \\ & + 1.84\text{Cr} + 1.51\text{Cu} + 2.46\text{Ni} + 2.67\text{Co} + 2.26\text{Mn} + 0.35\text{Sn} \\ & + 0.47\text{Zr} + 3.01\text{Si} + 1.47\text{Al}(\text{wt}\%) \end{aligned} \quad (1)$$

* Corresponding author at: Department of Mechanical and Industrial Engineering, Tallinn University of Technology, Ehitajate tee 5, Tallinn 19086, Estonia.
E-mail addresses: kgprashanth@gmail.com, prashanth.konda@taltech.ee (K.G. Prashanth).

<https://doi.org/10.1016/j.jalcom.2026.187930>

Received 24 February 2026; Received in revised form 6 April 2026; Accepted 8 April 2026

Available online 9 April 2026

0925-8388/© 2026 Elsevier B.V. All rights are reserved, including those for text and data mining, AI training, and similar technologies.

Elements that act as β -stabilizers in Ti alloys include Nb, Ta, Mo, Zr, Sn, and Fe [18,19]. However, alloying additions such as Ta and Mo significantly increase material cost, limiting the economic feasibility of these systems for large-scale biomedical implant production [20]. Although β -type Ti alloys offer superior mechanical and corrosion properties compared to conventional Ti-based alloys, their high cost remains a major constraint [21]. In this context, Fe has emerged as an effective and economically attractive β -stabilizing element for developing biomedical Ti alloys [22]. It is widely regarded as biocompatible for implant applications [23], and its addition strongly influences phase stability in the Ti–Nb system [24]. Dobromyslov et al. reported that Fe additions reduce the martensite start temperature in Ti–Nb alloys, promoting β -phase retention at room temperature [25]. Similarly, Lin et al. demonstrated that alloying with high-valence-electron elements such as Fe suppresses martensitic transformation in Ti–Nb alloys [26]. Moreover, Fe offers substantial cost advantages over β -stabilizers like Zr, Mo, and Ta, further enhancing the economic viability of Ti-based biomedical implants [21].

Conventional processing routes for Ti-based alloys used in biomedical implants include vacuum arc remelting, ingot casting, forging, rolling, powder metallurgy, and hot isostatic pressing [27–30]. In recent years, additive manufacturing (AM) techniques, particularly selective laser melting (SLM), have gained significant attention as advanced fabrication methods for Ti-based alloys [9,31–33]. SLM enables the development of novel alloy compositions with complex geometries and patient-specific implant designs [34–36]. Its layer-by-layer fabrication approach allows precise control over structural architecture and porosity, while the rapid cooling rates can suppress the formation of undesirable ω or α' martensitic phases and promote stabilization of the metastable β -phase [37]. Moreover, rapid solidification enhances solute retention and minimizes elemental segregation, contributing to an improved balance between strength and ductility [38,39]. Consequently, the use of SLM for fabricating β -type Ti alloys presents a promising pathway for achieving enhanced mechanical and electrochemical performance. Several studies have examined Fe-containing β -Ti alloy systems produced through various processing routes. Yasser et al. reported that Fe addition in rolled Ti–Mo–Fe alloys enhanced both mechanical and biological performance while reducing overall material cost [40]. Investigations on cast and quenched Ti–Nb–Fe alloys [41], hot isostatic pressed Ti–Mo–Fe [42] and the cast Ti–(Nb,Ta)–Fe [43] consistently demonstrated that Fe promotes β -phase stability, lowers the elastic modulus, and improves mechanical strength and hardness. Despite the growing interest in Fe-alloyed β -Ti systems, comprehensive studies evaluating the combined mechanical response and long-term corrosion and passivation behavior of SLM-fabricated alloys under physiological conditions remain limited.

Therefore, the present study investigates the SLM fabrication of a Ti–35 Nb–5Fe alloy using elemental powders. The use of elemental powders provides greater flexibility in alloy design, reduces material cost, and enables the exploration of non-equilibrium compositions achievable through SLM's rapid solidification behavior [44]. The objective of this work is to evaluate the influence of Fe addition on phase stability, microstructure, mechanical properties, and electrochemical behavior in a physiological environment, and to compare these results with our previous study on SLM-fabricated Ti–40 Nb alloy. Overall, the findings demonstrate that Fe-modified Ti–Nb alloys produced via SLM constitute a promising material system and fabrication route for next-generation biomedical implants.

2. Materials and methods

2.1. Feedstock preparation

Commercially pure titanium (CP-Ti) (>99.9%, 25 μ m, Nanoshell, UK), niobium (Nb) (>99.9%, 27 μ m, Pacific Particulate Materials Ltd., Canada), and iron (Fe) powders (>99.9%, 25 μ m, Materials Ltd.,

Canada) were used as the starting materials for preparing the feedstock. The elemental powders were blended in the required weight percentages (wt%) using a mechanical mixer operated at 10 rpm for 24 h. The Ti–40 Nb feedstock was prepared by mixing 60 wt% Ti and 40 wt% Nb, while the Ti–35 Nb–5Fe feedstock was produced by mixing 60 wt% Ti, 35 wt% Nb, and 5 wt% Fe.

2.2. Sample preparation

The Ti–40 Nb and Ti–35 Nb–5Fe bulk samples were fabricated using an SLM 280 2.0 system (SLM Solutions) equipped with an IPG 1064 nm fiber laser with a spot size of \sim 110 μ m and a maximum power of 700 W. Cuboidal specimens (10 \times 10 \times 10 mm³) were produced using a laser power of 650 W, a scanning speed of 650 mm/s, a hatch spacing of 35 μ m, a layer thickness of 30 μ m, and a hatch rotation angle of 67°. Following previously reported procedures [45], a triple-melting strategy was employed to enhance compositional uniformity and microstructural homogeneity. After fabrication, the samples were detached from the Ti build platform using wire electrical discharge machining (WEDM). Densities measured via Archimedes' principle (Mettler Toledo ME204, Germany) indicated a relative density of approximately 99%.

2.3. Material characterization

Phase analysis of the mixed powders and SLM-fabricated samples was carried out using a Bruker AXS X-ray diffractometer (XRD) equipped with Cu K α radiation ($\lambda = 1.54$ Å). Diffraction patterns were collected over a 2θ range of 30°–90° with a step size of 0.02°. Lattice parameters of the printed samples were determined using Rietveld refinement. Morphological characterization of the mixed powders and microstructural analysis of the fabricated samples were performed using a Zeiss Gemini SEM 450 equipped with an electron backscatter diffraction (EBSD) detector. Average particle size of the mixed powders was quantified from SEM micrographs using ImageJ software. Prior to microstructural examination, samples were mechanically ground using SiC papers from P600 to P4000, followed by electropolishing according to standard metallographic procedures. Electropolishing was performed using a M/s. Struers system (Model: LectroPol 5) with Electrolyte A3 (consisting of 58.82% methanol, 35.29% 2n-butoxyethanol, and 5.89% perchloric acid). The process was conducted at an applied voltage of 32 V with a resulting current density of 0.2 A/cm² for a duration of 12 s at a controlled temperature of 25 °C. The polished samples were subsequently examined using SEM and EBSD for detailed microstructural characterization. The grain size of the SLM-fabricated samples was measured from EBSD data using the area fraction method. A scan area of approximately 450 μ m \times 335 μ m was considered for the EBSD analysis. The Vickers microhardness of the samples was measured using a Buehler Micromet hardness tester under an applied load of 1000 g and a dwell time of 10 s. For each sample, the reported hardness value represents the average of ten indentations. Compressive mechanical behavior was evaluated at room temperature using an Instron 5967 universal testing machine equipped with a 30 kN load cell. Tests were conducted at a constant strain rate of 1×10^{-3} s⁻¹ to obtain the stress–strain response. Cylindrical specimens measuring 6 mm in height and 3 mm in diameter were prepared in accordance with ASTM E9 [46], with the loading axis aligned parallel to the build direction. For each condition, three independent specimens were tested to ensure reproducibility and consistency of the mechanical results.

The electrochemical behavior of the Ti–35 Nb–5Fe and Ti–40 Nb samples was evaluated at 37 ± 1 °C using an Autolab PGSTAT302N-FRA32 electrochemical workstation in phosphate-buffered saline (PBS), simulating physiological conditions. Measurements were conducted in a three-electrode configuration, with the samples serving as the working electrode, a platinum sheet as the counter electrode, and an Ag/AgCl electrode as the reference. Prior to testing, samples were immersed for 0.5 h to stabilize the open-circuit potential (OCP) and

ensure steady state surface conditions. Potentiodynamic polarization tests were performed on an exposed area of 0.5 cm^2 at a scan rate of 0.01 V/s over a potential range of -0.5 to $+2.0 \text{ V}_{\text{Ag}/\text{AgCl}}$. Electrochemical impedance spectroscopy (EIS) measurements were carried out at the OCP over a frequency range of 0.01 Hz to 10^4 Hz using a 10 mV (rms) sinusoidal perturbation. Equivalent circuit fitting was applied to the impedance spectra to extract polarization resistance and passive-film capacitive parameters. Long-term EIS measurements were additionally performed on Ti-35 Nb-5Fe after immersion periods of 1, 24, 48, and 72 h to assess passive-film stability. Mott–Schottky analysis was conducted at 1 kHz to evaluate the semiconducting characteristics of the passive film. All measurements were repeated three times to ensure reproducibility. Surface analysis of the Ti-35 Nb-5Fe sample was performed in both the as-polished condition (air-formed native oxide) and after 72 h immersion in PBS at 37°C to evaluate passive-film characteristics. X-ray photoelectron spectroscopy (XPS) measurements were conducted using a Thermo Scientific Nexsa system equipped with a monochromatic Al $K\alpha$ source ($E = 1486.68 \text{ eV}$). Depth profiling of the 72 h-immersed sample was carried out by sputtering the surface with an Ar-ion beam. Sputtering was performed as a function of time (for 0, 10, 20, 30, 40, 50, 60, 70, 80, and 90 s) to obtain time-resolved chemical depth profiles. The resulting spectra were used to determine the passive-film composition and estimate its thickness.

3. Results and discussion

Fig. 1(a-a3,b-b3) presents SEM images of the mixed Ti-35Nb-5Fe and Ti-40Nb powders along with their corresponding elemental compositions (wt%). The SEM analysis confirms homogeneous mixing of Ti, Nb, and Fe powders without visible agglomeration. The Ti-35 Nb-5Fe mixture contains spherical Ti and Fe particles together with irregularly shaped Nb particles, whereas the Ti-40 Nb mixture consists of spherical

Ti particles and irregular Nb particles, consistent with previous reports [45]. ImageJ analysis of the SEM micrographs indicates average particle sizes of $25 \pm 5 \mu\text{m}$ for Ti-35 Nb-5Fe and $24 \pm 3 \mu\text{m}$ for Ti-40 Nb, both within the suitable range for SLM processing. Fig. 1(c) presents the XRD patterns of the mixed powders and the SLM-fabricated Ti-35 Nb-5Fe and Ti-40 Nb samples. The mixed-powder patterns show peaks corresponding to hexagonal close-packed (hcp) CP-Ti and body-centered cubic (bcc) Nb and Fe in the Ti-35 Nb-5Fe blend, and hcp CP-Ti and bcc Nb in the Ti-40 Nb blend, with no additional phases detected within the sensitivity of the technique. After SLM processing, the Ti-35 Nb-5Fe alloy exhibits diffraction peaks corresponding to metastable β -TiNb with a bcc structure (space group $\text{Im-}3 \text{ m}$), indicating suppression of the α' -martensitic phase. In contrast, the SLM-fabricated Ti-40 Nb alloy shows the coexistence of metastable β -TiNb and α' -martensite with an hcp structure (space group $\text{P}6_3/\text{mmc}$) [47,48] This $\alpha' + \beta$ dual-phase structure is consistent with previous findings and is attributed to insufficient β -phase stabilization, which promotes martensitic transformation during solidification [45]. Quantitative Rietveld refinement further confirms that Fe addition increases the β -phase fraction from $\sim 85.4\%$ in Ti-40 Nb to $\sim 99.7\%$ in Ti-35 Nb-5Fe.

The stabilization of the β -phase in the Ti-35 Nb-5Fe alloy can be attributed to the dual influence of Fe addition: (i) an increase in the overall Mo_{eq} value, which reflects the relative β -stabilizing potency of alloying elements, and (ii) an increase in the electron-to-atom (e/a) ratio, which governs the electronic stability of the bcc lattice [49]. For metastable β -phase retention at room temperature, the Mo_{eq} should exceed $10 \text{ wt}\%$ and the e/a ratio should be greater than 4.2 [50,51]. Based on Eq. (1), the calculated values show that Ti-35 Nb-5Fe exhibits marginal increase in the Mo_{eq} (11.8) and e/a (4.43) values as compared to Ti-40 Nb ($\text{Mo}_{\text{eq}} = 11.2$; $e/a = 4.26$). The increase in both parameters with Fe addition confirms its role in enhancing β -phase stability at room temperature by suppressing the $\beta \rightarrow \alpha'$ martensitic transformation [52,

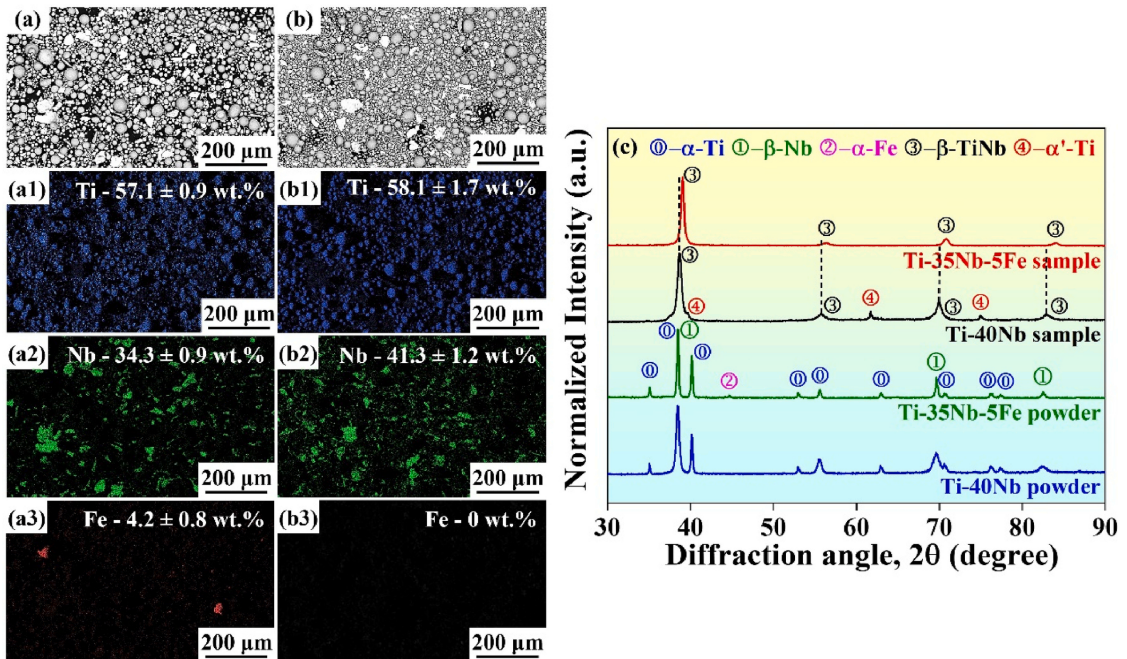


Fig. 1. (a) Scanning electron microscopy images and corresponding energy-dispersive spectroscopy area mapping of mixed (a-a3) Ti-35Nb-5Fe and (b-b3) Ti-40Nb powders, showing the powder morphology and elemental composition. (c) X-ray diffraction patterns of Ti-40Nb and Ti-35Nb-5Fe powder and selective laser melted samples. The black dotted lines in the selective laser-melted samples indicate a shift in the peak towards a higher diffraction angle (2θ).

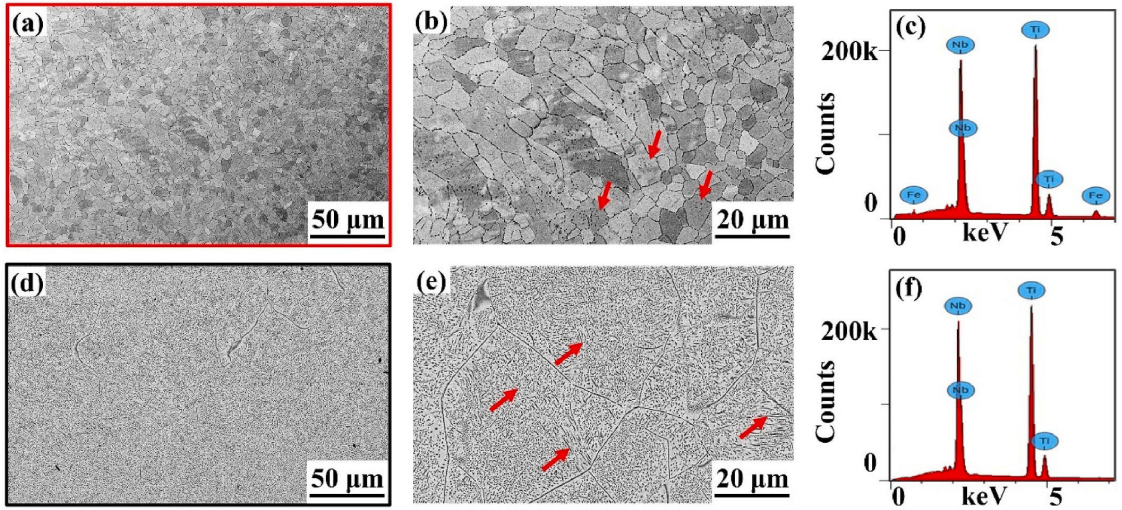


Fig. 2. Scanning electron microscopy images of the selective laser-melted (a,b) Ti-35 Nb-5Fe and (d,e) Ti-40 Nb samples acquired in backscattered mode, along with the corresponding (c,f) energy-dispersive spectroscopy maps showing elemental distributions. The red arrow indicates the presence of α -phase matrix.

53]. SEM images of the SLM-fabricated Ti-35 Nb-5Fe alloy (Fig. 2(a,b)) reveal a predominantly β -phase matrix with a trace amount of α -martensite visible at higher magnification (Fig. 2(b)). Although α -martensite is detected in SEM, its absence in the XRD patterns is likely due to its volume fraction being below the XRD detection limit (~ 3 –5%). In contrast, the Ti-40 Nb alloy (Fig. 2(d,e)) exhibits a lamellar

α -martensitic structure distributed within a β -phase matrix. The markedly reduced α -martensite fraction in Ti-35 Nb-5Fe indicates enhanced β -phase stability resulting from Fe addition [54,55]. EDS analysis (Fig. 2 (c,f)) confirms compositional homogeneity, yielding average compositions of 59.7 ± 0.3 wt% Ti, 36.7 ± 0.2 wt% Nb, and 4.5 ± 0.1 wt% Fe for Ti-35 Nb-5Fe, and 58.5 ± 0.3 wt% Ti and 41.5 ± 0.2 wt% Nb for

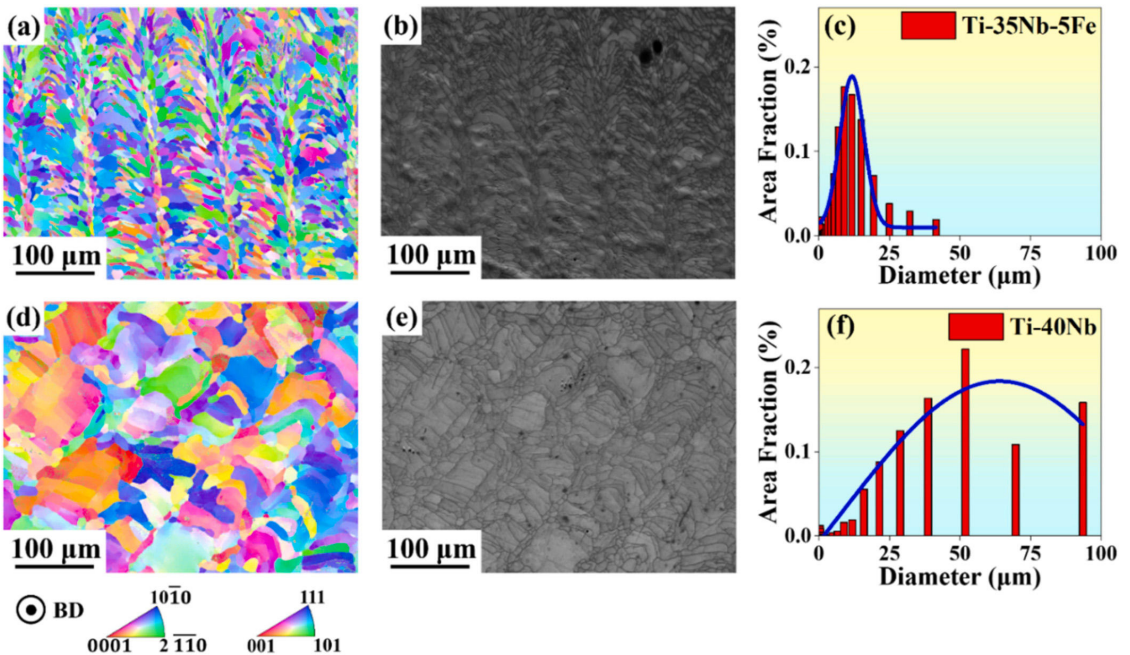


Fig. 3. Electron backscattered diffraction results highlighting the inverse pole figure maps, image quality maps, and the grain size distribution plot of the selective laser melted (a-c) Ti-35Nb-5Fe and (d-f) Ti-40Nb samples. BD represents the build direction.

Ti-40 Nb.

To further examine grain morphology and crystallographic orientation, EBSD analysis was performed on surfaces perpendicular to the build direction. Fig. 3 presents the inverse pole figure (IPF) maps, grayscale image-quality (IQ) maps, and grain-size distribution histograms for the Ti-35 Nb-5Fe and Ti-40 Nb samples. The IPF maps show that both alloys exhibit randomly oriented grains with no pronounced texture, indicating uniform solidification and the absence of directional grain growth, behavior commonly observed in rapidly cooled SLM-processed materials [56]. The IQ maps clearly delineate well-defined β -grains and grain boundaries, revealing a more refined microstructure in Ti-35 Nb-5Fe compared to Ti-40 Nb. Quantitatively, Ti-35 Nb-5Fe displays a narrow grain-size distribution ranging from $\sim 1 \mu\text{m}$ to $50 \mu\text{m}$, with an average grain size of $11 \pm 8 \mu\text{m}$, representing nearly a fivefold reduction relative to Ti-40 Nb. In contrast, Ti-40 Nb exhibits a broader distribution from $\sim 1 \mu\text{m}$ to $100 \mu\text{m}$, with an average grain size of $48 \pm 29 \mu\text{m}$. The relatively large standard deviation observed for Ti-40Nb indicates a significant variation in grain size distribution due to the coexistence of β -phase and α' -martensite, as observed in the SEM images (Fig. 2(d,e)). The presence of these phases results in a bimodal grain structure consisting of both fine and coarse grains, thereby contributing to the increased standard deviation.

The pronounced grain refinement in Ti-35Nb-5Fe arises from the combined effects of enhanced nucleation and restricted grain growth during solidification. As a β -stabilizer with high diffusivity, Fe increases the number of heterogeneous nucleation sites and contributes to grain-boundary pinning, thereby promoting the formation of finer grains [57,58]. In parallel, Fe addition increases constitutional undercooling, which further accelerates nucleation during rapid solidification [59]. The influence of solute elements on constitutional undercooling can be quantified using the growth-restriction factor Q_f , expressed in Eq. (2) [60],

$$Q_f = m_l C_0 (k - 1) \quad (2)$$

where m_l is the slope of the liquidus line, C_0 is the solute concentration, and k is the equilibrium partition coefficient. Solute elements with larger Q_f values promote greater constitutional undercooling and increase the density of heterogeneous nucleation sites, ultimately leading to finer grain structures [61]. The m_l values for Nb and Fe are 10 and -18 , respectively, while the k values for Nb and Fe are 1.25 and 0.38, respectively [61,62]. Using these parameters, the calculated Q_f is higher for Ti-35Nb-5Fe (143.3) than for Ti-40Nb (100). This increase in Q_f demonstrates that Fe incorporation provides stronger growth restriction during solidification, suppressing grain coarsening and resulting in significantly finer β -grains.

The influence of Fe addition on the mechanical behavior of the SLM-fabricated alloys was assessed through Vickers microhardness and compression testing. As shown in Fig. 4(a), the Ti-35 Nb-5Fe alloy

exhibits a significantly higher hardness ($494 \pm 11 \text{ HV}_1$) compared to Ti-40 Nb ($374 \pm 12 \text{ HV}_1$). This enhancement is attributed to the refined β -grain structure in Ti-35 Nb-5Fe, which reduces the effective dislocation mean free path and increases resistance to dislocation motion, thereby improving hardness [63–65]. The true stress–true strain curves in Fig. 4(b) further illustrate the compressive response of the alloys. Ti-35 Nb-5Fe demonstrates a higher yield strength ($908 \pm 33 \text{ MPa}$) and ultimate compressive strength ($1945 \pm 17 \text{ MPa}$) than Ti-40 Nb, which exhibits a yield strength of $845 \pm 24 \text{ MPa}$ and an ultimate compressive strength of $1490 \pm 20 \text{ MPa}$. The plastic strain also increases from $\sim 33\%$ in Ti-40 Nb to $\sim 48\%$ in Ti-35 Nb-5Fe. Additionally, the elastic modulus decreases from 34 GPa in Ti-40 Nb to 30 GPa in Ti-35 Nb-5Fe, consistent with the suppression of the stiffer α' -martensitic phase and stabilization of the more compliant β -phase [66]. Fig. 4(c) presents the strain-hardening behavior of both alloys, revealing three distinct regions: Region I shows a rapid decrease in strain-hardening rate immediately after yielding; Region II exhibits a relatively stable hardening rate; and Region III is characterized by a further decline in hardening rate. While both alloys display similar behavior in Region I, the Ti-35 Nb-5Fe alloy maintains a higher and more sustained strain-hardening rate in Region II, indicating superior compressive deformability and work-hardening capability compared to Ti-40 Nb. [67–69].

The transition from a dual-phase ($\alpha' + \beta$) microstructure in Ti-40 Nb to a predominantly single β -phase in Ti-35 Nb-5Fe reduces the contribution of α' -martensite, whose hcp structure offers limited slip systems. In contrast, the bcc β -phase provides multiple slip systems, enabling more uniform plastic deformation [70,71]. The primary strengthening mechanisms responsible for the enhanced yield strength of Ti-35 Nb-5Fe are solid-solution strengthening and grain-boundary strengthening [56, 67]. Solid-solution strengthening arises from the substitutional incorporation of Fe and Nb atoms into the β -Ti lattice, replacing Ti atoms. The resulting atomic size mismatch generates local lattice distortions that interact with dislocations and increase resistance to dislocation glide. The magnitude of solid-solution strengthening ($\Delta\sigma_{ss}$) was estimated using the empirical relation provided in Eq. (3) [16],

$$\Delta\sigma_{ss} = (\sum_i B_i^{3/2} X_i)^{2/3} \quad (3)$$

where B_i is the strengthening coefficient ($71 \text{ MPa}\cdot\text{at}^{-2/3}$ for Nb and $1715 \text{ MPa}\cdot\text{at}^{-2/3}$ for Fe) [67,72]. X_i is the atomic fraction of the solute element. The calculated $\Delta\sigma_{ss}$ values are $\sim 50 \text{ MPa}$ for Ti-35Nb-5Fe and $\sim 36.7 \text{ MPa}$ for Ti-40Nb, confirming the stronger contribution of Fe to solid solution strengthening due to its smaller atomic radius and higher strengthening coefficient. The contribution of grain boundary strengthening to the enhanced strength of Ti-35Nb-5Fe can be evaluated using the Hall-Petch relationship, as expressed in Eq. (4) [59,60]

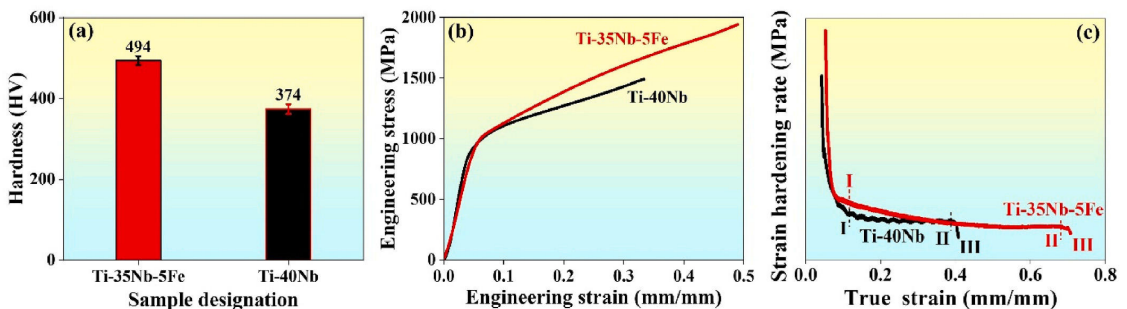


Fig. 4. Plot demonstrates the (a) Vickers hardness values, (b) compressive stress-strain curve, and (c) strain hardening behavior of the selective laser-melted Ti-35Nb-5Fe and Ti-40Nb samples.

$$\Delta\sigma_g = kD^{-1/2} \quad (4)$$

where k is the Hall-Petch constant [61] and D is the average grain size. The estimated grain boundary strengthening contributions are ~ 135 MPa for Ti-35Nb-5Fe and ~ 65 MPa for Ti-40Nb. The higher grain-boundary density in Ti-35 Nb-5Fe more effectively impedes dislocation motion, contributing to the observed increase in yield strength. Overall, the enhanced yield strength, compressive strength, and plastic strain in Ti-35 Nb-5Fe highlight the significant role of Fe addition in strengthening the alloy. The simultaneous achievement of high strength, improved ductility, and a reduced elastic modulus demonstrates mitigation of the conventional strength-ductility trade-off and results in a high strength-to-modulus ratio—an essential attribute for load-bearing biomedical applications [73,74].

The passivation behavior of the SLM-fabricated Ti-35 Nb-5Fe and Ti-40 Nb samples was evaluated using PDP, EIS, and Mott-Schottky analyses in PBS at 37 °C to simulate physiological conditions. The anodic region of the PDP curves (Fig. 5) shows characteristic active-passive transitions for both alloys. The corrosion potential (E_{corr}), corrosion current density (I_{corr}), passivation potential (E_{pp}), and passive current density (I_p) were extracted from the polarization curves and are summarized in Table 1. From the E_{corr} to E_{pp} , the increase in current density reflects active dissolution, while the nearly constant current density beyond E_{pp} up to 1.5 V_{Ag/AgCl} confirms stable passivation. The slightly more noble E_{corr} and lower I_{corr} values observed for Ti-35Nb-5Fe improved corrosion resistance relative to Ti-40 Nb. The similar I_p values for both alloys suggest comparable passive-film stability under the tested conditions.

To evaluate the polarization resistance of the alloys under open-circuit potential (OCP) conditions, EIS measurements were performed after 0.5 h of immersion in PBS at 37 °C, and the corresponding Nyquist plots are shown in Fig. 6(a). Both Ti-35 Nb-5Fe and Ti-40 Nb exhibit a single, incomplete semicircular arc, indicating the presence of one dominant time constant associated with the passive-film response of these passivating alloys [75–77]. The experimental impedance spectra were fitted using a modified Randles equivalent circuit, represented as $[R_s(QR_p)]$, where R_s is the electrolyte resistance, R_p is the polarization resistance of the passive film, and Q is the constant phase accounting for non-ideal capacitive behavior arising from surface heterogeneity. Circuit elements enclosed in square brackets are connected in series, whereas those within parentheses are connected in parallel. The impedance response is described as [78]:

$$Z = [Q(j\omega)^n]^{-1} \quad (5)$$

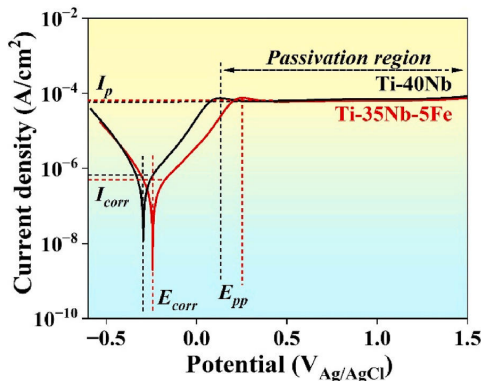


Fig. 5. Potentiodynamic polarization curves of the selective laser-melted Ti-35Nb-5Fe and Ti-40Nb samples in phosphate-buffer saline (PBS) solution at 37°C.

Table 1

Table summarizing the potentiodynamic polarization parameters of the selective laser-melted Ti-40Nb and Ti-35Nb-5Fe samples in phosphate-buffered saline (PBS) solution at 37°C. E_{corr} denotes the corrosion potential, I_{corr} the current density, E_{pp} the passivation potential, and I_p the passivation current density.

| Sample | E_{corr} (V _{Ag/AgCl}) | I_{corr} (μA/cm ²) | E_{pp} (V _{Ag/AgCl}) | I_p (μA/cm ²) |
|-------------|------------------------------------|----------------------------------|----------------------------------|-----------------------------|
| Ti-40Nb | -0.29 ± 0.03 | 1.57 ± 0.03 | 0.13 ± 0.01 | 73.02 ± 0.02 |
| Ti-35Nb-5Fe | -0.24 ± 0.04 | 1.06 ± 0.09 | 0.25 ± 0.02 | 73.01 ± 0.01 |

where Q is a proportionality constant with units of $\Omega^{-1} \cdot s^n$, n is the exponent of Q (constant phase element) with values ranging from -1 to 1 (-1 represents inductance, 0 represents resistance, and 1 represents capacitance), and j is the imaginary unit that equals $\sqrt{-1}$ and ω is the angular frequency. The fitted parameters are summarized in Table 2. The Chi-square (χ^2) value in the order of 10^{-3} indicate excellent agreement between the experimental and simulated spectra. The n values of both Ti-35Nb-5Fe (0.95) and Ti-40Nb (0.95) samples after 0.5 h of immersion reflect near-ideal capacitive behavior, suggesting the formation of uniform passive films. The R_s values are comparable for both alloys, indicating similar electrolyte resistance. The slightly higher R_p value for Ti-35 Nb-5Fe suggests a more resistive and protective passive film, consistent with the behavior expected for passivating alloys [79–81]. The capacitance of the passive film was calculated using Brug's Eq. (6) [78],

$$C = [Q(R_s^{-1} + R_p^{-1})^{n-1}]^{1/n} \quad (6)$$

The calculated capacitance values were found to be similar for both samples (Table 2). These capacitance values were subsequently substituted into Eq. (7) [82], which relates the capacitance of the passive film to its thickness,

$$C = \frac{\epsilon\epsilon_0 A}{d} \quad (7)$$

where ϵ_0 is the vacuum permittivity (8.854×10^{-14} F/cm), ϵ is the dielectric constant of the passive oxide film, and d is the passive film thickness. The dielectric constants of TiO₂, Nb₂O₅, and Fe₂O₃ are 80, 28, and 26, respectively [82–84]. The passive films formed on Ti-35 Nb-5Fe and Ti-40 Nb are expected to consist of mixed oxides of Ti, Nb, and Fe. Reliable dielectric-constant data for mixed oxides in the Ti-Nb-Fe system are not available in the literature. As the passive film composition in both alloys is predominantly Ti-Nb-based oxides, an effective ϵ value of 51 was adopted based on reported literature on Ti-40Nb alloys [85]. Accordingly, the passive-film thickness values were estimated using this effective dielectric constant and provided in Table 2. Several studies on Ti-Nb alloys processed through various routes have shown that passive films formed in aqueous environments are predominantly composed of TiO₂ and Nb₂O₅, as confirmed by XPS analyses [85–88]. However, despite extensive research on Ti-Nb alloys, information regarding the long-term stability of the passive films formed on Ti-35 Nb-5Fe remains limited. To address this gap, EIS measurements were performed on the Ti-35 Nb-5Fe alloy at OCP in PBS at 37 °C for immersion durations ranging from 1 h to 72 h.

The Nyquist plots obtained at different immersion times are presented in Fig. 6(b). Similar to the response at 0.5 h, long-term immersion reveals a single semicircular arc, confirming the persistence of a single dominant time constant throughout the exposure period. A pronounced increase in R_p is observed from 1 h to 72 h, accompanied by a slight decrease in capacitance. This reduction in capacitance corresponds to a modest increase in passive-film thickness, from 1.59 nm to 1.68 nm. Despite the relatively small change in thickness, the substantial rise in R_p indicates a progressive reduction in charge-carrier mobility and an improvement in barrier integrity with immersion time [12]. The continuous increase in R_p and the concurrent decrease in capacitance suggest that passive-film growth follows a logarithmic rate law,

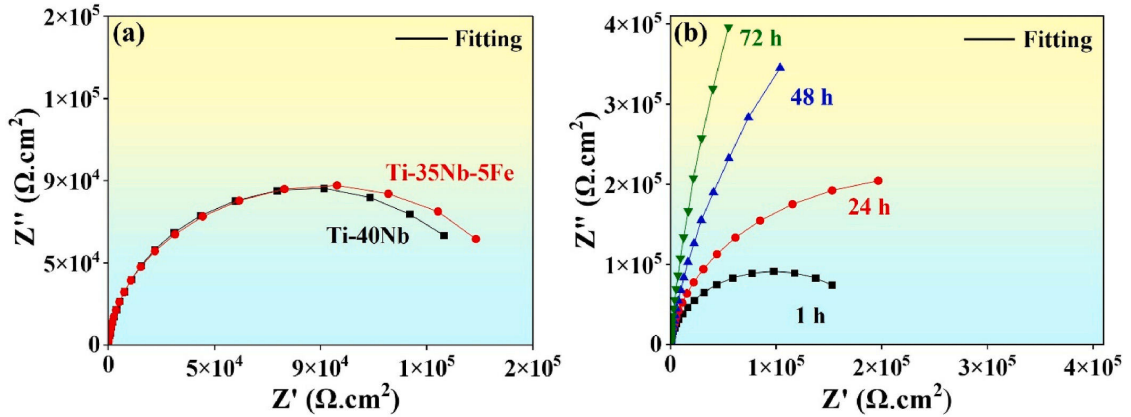


Fig. 6. (a) Nyquist plots showing the electrochemical impedance spectroscopy response of the selective laser-melted Ti-35 Nb-5Fe and Ti-40 Nb samples after 0.5 h of immersion, and (b) Nyquist plots of the Ti-35 Nb-5Fe sample after long-term immersion at various exposure times in phosphate-buffered saline (PBS) at 37 °C.

Table 2

Equivalent electric circuit fitted values of selective laser-melted Ti-40Nb and Ti-35Nb-5Fe samples with respect to different immersion times in phosphate-buffer saline solution at 37°C.

| Sample | Immersion time (h) | R_s ($\Omega.cm^2$) | Y_o ($\mu\Omega^{-1}.s^0.cm^{-2}$) | n (no unit) | R_p ($M\Omega.cm^2$) | C ($\mu F/cm^2$) | d (nm) |
|-------------|--------------------|-------------------------|--|-------------|--------------------------|--------------------|-------------|
| Ti-40Nb | 0.5 | 14.47 ± 0.94 | 41.32 ± 0.76 | 0.95 ± 0.01 | 0.15 ± 0.19 | 28.11 ± 0.60 | 1.59 ± 0.01 |
| Ti-35Nb-5Fe | 0.5 | 14.52 ± 0.71 | 40.66 ± 0.56 | 0.95 ± 0.01 | 0.17 ± 0.24 | 27.79 ± 0.50 | 1.68 ± 0.02 |
| | 1 | 15.49 ± 0.54 | 39.05 ± 0.48 | 0.94 ± 0.02 | 0.18 ± 0.12 | 24.47 ± 0.37 | 1.84 ± 0.02 |
| | 24 | 16.56 ± 0.50 | 35.83 ± 0.36 | 0.94 ± 0.01 | 0.44 ± 0.16 | 22.75 ± 0.37 | 1.98 ± 0.01 |
| | 48 | 12.51 ± 0.44 | 30.46 ± 0.31 | 0.94 ± 0.07 | 2.33 ± 1.42 | 17.89 ± 0.72 | 2.45 ± 0.02 |
| | 72 | 11.57 ± 1.24 | 35.29 ± 0.78 | 0.92 ± 0.01 | 9.06 ± 5.93 | 17.48 ± 2.63 | 2.65 ± 0.01 |

characteristic of diffusion-controlled thickening under constant-potential conditions [85]. After 72 h, the high R_p value and reduced capacitance confirm the formation of a dense and stable passive film on the Ti-35 Nb-5Fe alloy (Fig.7).

To further elucidate the electronic properties of the passive films formed on both alloys in PBS at 37 °C, Mott-Schottky analysis was performed at a frequency of 1 kHz, and the corresponding results are shown in Fig. 8. The $1/C^2$ versus potential plots exhibit linear regions with positive slopes in the potential ranges of -0.2 – 0.8 $V_{Ag/AgCl}$ for Ti-35 Nb-5Fe and -1.1 – 0.3 $V_{Ag/AgCl}$ for Ti-40 Nb, indicating n-type semiconducting behavior of the passive films on both alloys. This behavior

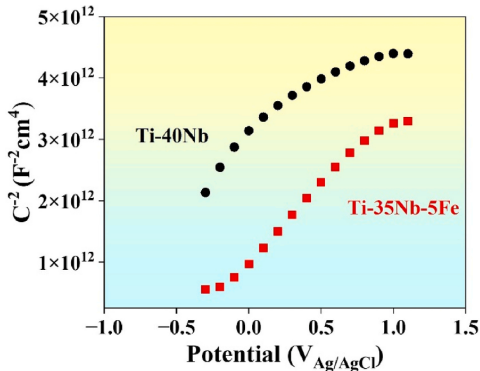


Fig. 7. Mott-Schottky measurements of the selective laser-melted Ti-35Nb-5Fe and Ti-40Nb samples in phosphate-buffer saline (PBS) solution at 37°C.

confirms that oxygen vacancies and metal interstitials act as dominant donor defects governing electronic transport through the passive layer. The donor density (N_D) was calculated from the slope of the linear region of the Mott-Schottky plot using Eq. (8) [82],

$$C^{-2} = \frac{2}{\epsilon\epsilon_0 e N_D} \left(E - E_{fb} - \frac{kT}{e} \right) \quad (8)$$

where ϵ and ϵ_0 are the dielectric constants of the passive film and vacuum, respectively, e is the electronic charge, and E_{fb} is the flat-band potential, measured as -1.05 $V_{Ag/AgCl}$ for Ti-35 Nb-5Fe and -0.26 $V_{Ag/AgCl}$ for Ti-40 Nb. The N_D values calculated using Eq. (8) were 3.1×10^{21} cm^{-3} for Ti-35 Nb-5Fe and 4.7×10^{21} cm^{-3} for Ti-40 Nb, both falling within the typical range reported for passive Ti-based alloys [89]. The lower N_D value of Ti-35 Nb-5Fe indicates a reduced defect concentration, consistent with its higher R_p , whereas the higher N_D of Ti-40 Nb suggests the formation of a more defect-rich passive layer.

Based on the point defect model (PDM), passive-film formation and growth occur through the generation, migration, and annihilation of point defects within the oxide layer [90]. The sequence of interfacial reactions governing these processes at the metal/film and film/solution interfaces is described by reactions (9–13) occurring at the metal/film and the film/solution interfaces [90]. A schematic representation of the PDM framework is shown in Fig. 8. The defect notation follows Kröger-Vink conventions, where m represents the metal atoms (Ti, Nb, and Fe) in the sample, and M_M^x represents the metal ions. V_M^x represents the cation vacancy site in the passive film, V_O^- and O_o denotes the oxygen vacancy and oxygen ions, and e^- denotes the electrons.



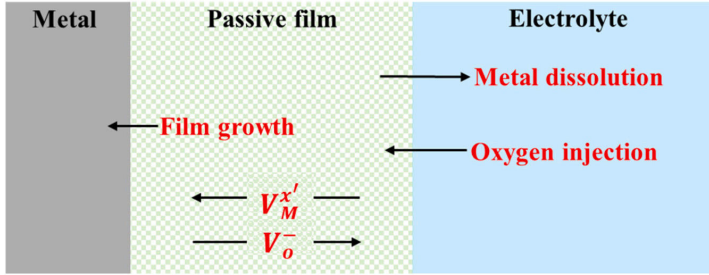
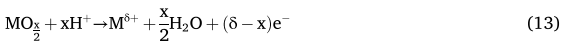


Fig. 8. Schematic representation of the point defect model illustrating passive-film growth on the selective laser-melted Ti-35 Nb-5Fe and Ti-40 Nb samples in phosphate-buffered saline (PBS) at 37 °C.



At the onset of anodic polarization, metal atoms from the substrate oxidize and migrate into the passive film (reaction 9). Each oxidation event generates oxygen vacancies (V_O^-), producing some oxygen-deficient Ti-Nb-based passive layer that exhibits n-type semiconducting behavior due to donor-type defects [88]. Simultaneously, portions of the lattice reorganize as metal atoms occupy pre-existing cation vacancies (reaction 10), reinforcing the metal/film interface and initiating film densification. Under higher anodic potentials, partial dissolution of metal cations occurs at the film/solution interface (reaction 11), generating additional cation vacancies and establishing the steady state film thickness. Concurrently, water molecules react with oxygen vacancies (reaction 12), contributing to vacancy annihilation and promoting self-healing of the passive layer [91]. The overall dissolution process is represented by reaction 13, which becomes significant only under extreme anodic conditions. In the Ti-40 Nb alloy, passive-film growth is primarily governed by defect generation and cation transport as described by reactions (9) and (10), leading to the formation of oxygen vacancies and cation interstitials. These donor-type defects enhance electronic conductivity, consistent with the higher N_D value ($4.7 \times 10^{21} \text{ cm}^{-3}$) obtained from the Mott-Schottky analysis. During oxidation, Nb forms Nb^{5+} and incorporates into the Ti^{4+} lattice, modifying the oxide structure and dielectric response but not fully suppressing oxygen-vacancy formation. In contrast, the addition of Fe to the Ti-Nb system significantly alters the defect chemistry [89]. Fe oxidizes to Fe^{3+} species and substitutes for Ti^{4+} sites in the oxide lattice, which it interacts with oxygen vacancies according to reaction (14), resulting in charge compensation.



This substitution effectively neutralizes oxygen vacancies and reduces the concentration of donor-type defects, resulting in a lower N_D value ($3.1 \times 10^{21} \text{ cm}^{-3}$) and enhanced passive-film resistivity. The incorporation of Fe^{3+} also promotes the formation of a mixed Ti-Nb-Fe oxide layer that is richer in oxygen and structurally more compact. Consequently, the combined effects of Nb^{5+} , which strengthens the oxide framework and Fe^{3+} , which compensates donor defects lead to the development of a dense and stable passive film. To further verify the role of Fe in the passive layer, XPS analysis was performed on the Ti-35 Nb-5Fe sample.

The passivation behavior of the Ti-35 Nb-5Fe alloy was examined by analyzing the surface in the as-polished condition (air-formed native

film) and after 72 h of immersion in PBS at 37 °C (electrochemically formed passive film). The XPS high-resolution spectra of Ti 2p, Nb 3d, and Fe 2p for both the native and passive films at different sputtering depths are presented in Fig. 9(a-f). The Ti 2p spectra for both conditions display the characteristic Ti 2p_{3/2} and Ti 2p_{1/2} doublet. Metallic Ti appears at ~454.6 eV, while oxide states corresponding to TiO, Ti₂O₃, and TiO₂ occur at higher binding energies, with TiO₂ identified near 459 eV and 465 eV. The native film contains both metallic and oxidized Ti, Nb, and Fe species, with oxides being predominant. After 72 h of immersion, the passive film shows a strong dominance of TiO₂, and metallic Ti is absent at the outermost surface (0 s sputtering). The Nb 3d spectra exhibit Nb 3d_{5/2} and Nb 3d_{3/2} peaks corresponding to metallic Nb at ~202 eV and 205 eV. Oxidized Nb species NbO, NbO₂, and Nb₂O₅ appear at progressively higher binding energies, with Nb₂O₅ observed near 207 eV and 210 eV. In the native film, both metallic and oxidized Nb are present, whereas the passive film after 72 h shows a pronounced enrichment of Nb₂O₅ at the surface. With increasing sputtering time, the oxide signal decreases and the metallic Nb contribution increases, indicating the transition from the oxide layer to the oxide/metal interface. The Fe 2p spectra show metallic Fe at ~706 eV and oxide states corresponding to FeO and Fe₂O₃ at higher binding energies, with Fe₂O₃ identified near 710 eV and satellite features above 718 eV. In both the native and passive films, Fe is predominantly present in its oxidized form at the surface.

The presence of Fe₂O₃ across all sputtering depths in the passive film confirms the participation of Fe into the oxide layer. Further, the Ti 2p and Nb 3d spectra show metallic species appear only at the sputtering time of 60 s, indicating the oxide/metal interface of the passive film. Using a sputtering rate of 0.05 nm/s, the passive film thickness is estimated to be ~3 nm. Previous studies on the passivation behavior of Ti-based alloys in various electrolytes like NaCl, SBF, and PBS have reported a similar passive film thicknesses (in the range of ~1–6 nm) [92–97]. As described by the PDM, passive-film formation results from the inward diffusion of oxygen anions and the outward migration of Ti^{4+} , Nb^{5+} , and Fe^{3+} cations. The compositional distribution within the film is governed by the migration kinetics of these cations, their thermodynamic affinity for oxygen, and the stability of the corresponding oxides under physiological conditions. The enrichment of TiO₂ and Nb₂O₅, together with the incorporation of Fe₂O₃, contributes to the enhanced protective characteristics of the passive film formed on the Ti-35 Nb-5Fe alloy.

4. Conclusion

The following conclusions can be drawn from the present study:

1. Selective laser melting of Ti-35 Nb-5Fe from elemental powders produced a fully β -phase microstructure, demonstrating that the addition of 5 wt% Fe is highly effective in stabilizing the β phase. In addition, Fe enhances the solute-driven undercooling offering

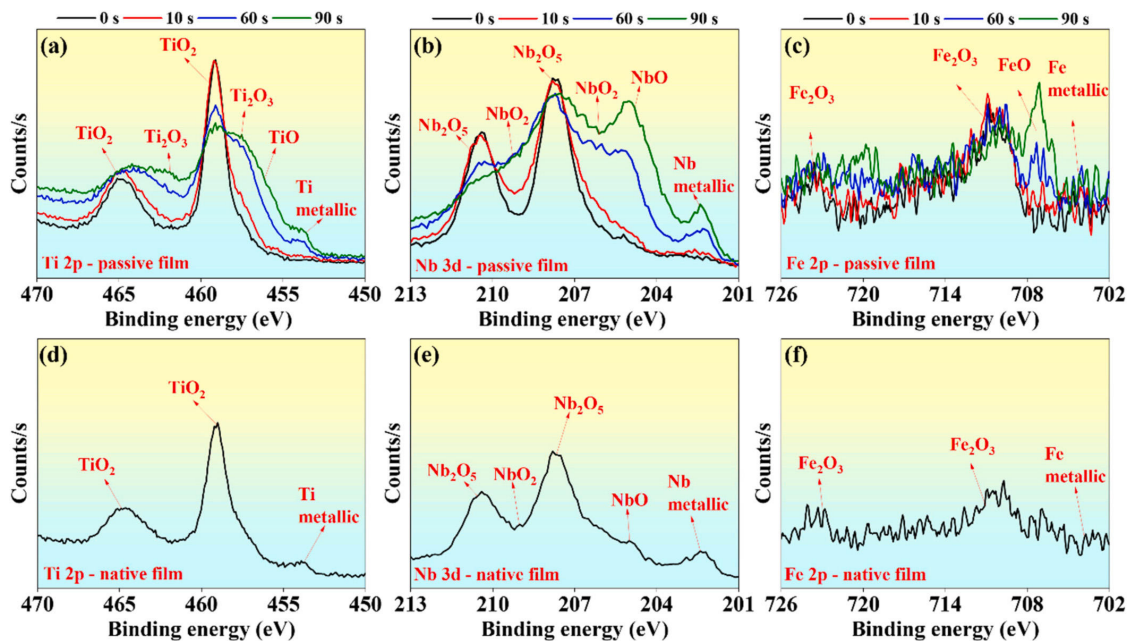


Fig. 9. High-resolution X-ray photoelectron spectroscopy spectra of the selective laser-melted Ti-35 Nb-5Fe sample showing (a-c) the passive film measured at different sputtering times after 72 h of immersion and (d-f) the native film, both in phosphate-buffered saline (PBS) at 37 °C.

heterogeneous nucleation sites, promoting significant grain refinement to $\sim 11 \mu\text{m}$.

- The combined effects of Fe-induced grain refinement, suppression of α -martensite, and lattice strain arising from atomic-size mismatch resulted in improved hardness, compressive strength, and plasticity, while maintaining a reduced elastic modulus.
- The SLM Ti-35 Nb-5Fe alloy exhibits superior passivation behavior compared to Ti-40 Nb, as evidenced by its higher polarization resistance, lower capacitance, and thicker passive film during long-term immersion in PBS at 37 °C. Mott-Schottky analysis confirms n-type semiconducting behavior for both alloys, with donor densities falling within the expected range for passive Ti-based oxides. The significantly lower donor density of Ti-35 Nb-5Fe ($1.9 \times 10^{21} \text{ cm}^{-3}$) indicates a reduced defect concentration and enhanced electronic resistance of its passive layer.
- Point defect model interpretation reveals that Fe incorporation fundamentally alters defect chemistry, where Fe^{3+} substitution for Ti^{4+} compensates oxygen vacancies and suppresses donor-type defects. This mechanism contributes directly to the improved barrier properties of the Ti-35 Nb-5Fe passive film.
- XPS depth profiling demonstrates that the passive film on Ti-35 Nb-5Fe is enriched in TiO_2 and Nb_2O_5 , with Fe_2O_3 uniformly incorporated throughout the oxide, forming a compact, oxygen-rich mixed-oxide layer. The measured passive-film thickness ($\sim 3 \text{ nm}$) aligns closely with EIS-derived values, validating the electrochemical analysis. The combined effects of Nb^{5+} -induced structural stabilization and Fe^{3+} -mediated defect compensation produce a dense, stable, and protective passive film, positioning Ti-35 Nb-5Fe as a promising candidate for biomedical applications requiring long-term corrosion resistance in physiological environments.

Overall, the findings establish SLM-fabricated Ti-35 Nb-5Fe exhibits promising grain refinement and enhanced electrochemical stability. In the present study, our primary focus is on mechanical properties,

microstructural characterization, and corrosion behavior. In future work, we plan to extend this investigation to *in vitro* studies, such as biocompatibility and cell-material interactions, to further evaluate its potential for biomedical applications.

CRedit authorship contribution statement

Prashanth Konda Gokuldoss: Writing – review & editing, Validation, Supervision, Resources, Project administration, Investigation, Funding acquisition, Conceptualization. **Jayamani Jayaraj:** Writing – review & editing, Validation, Resources, Investigation, Data curation, Conceptualization. **Geetha Manivasagam:** Writing – review & editing, Validation, Methodology. **Shangavi Subramanian:** Writing – original draft, Methodology, Investigation, Formal analysis, Data curation, Conceptualization.

Declaration of Competing Interest

The authors declare that they have no known competing financial interests or personal relationships that could have appeared to influence the work reported in this paper.

Acknowledgments

The authors thank Mayank Kumar Yadav for his assistance in carrying out experiments. The funding from the European Union's Horizon 2020 Research and Innovation programme under Grant Agreement No 101004730 is acknowledged.

References

- [1] E. Marin, A. Lanzutti, History of metallic orthopedic materials, *Metals* 15 (2025) 378, <https://doi.org/10.3390/met15040378>.

- [2] S. Choi, J. Kwon, K. Suk, H. Kim, S. Moon, S. Park, B.H. Lee, The clinical use of osteobiologic and metallic biomaterials in orthopedic surgery: the present and the future, *Materials* 16 (2023) 3633, <https://doi.org/10.3390/ma16103633>.
- [3] M. Geetha, A.K. Singh, R. Asokamani, A.K. Gogia, Ti based biomaterials, the ultimate choice for orthopaedic implants – A review, *Prog. Mater. Sci.* 54 (2009) 397–425, <https://doi.org/10.1016/j.pmatsci.2008.06.004>.
- [4] L. Kunická, R. Kocich, T.C. Lowe, Advances in metals and alloys for joint replacement, *Prog. Mater. Sci.* 88 (2017) 232–280, <https://doi.org/10.1016/j.pmatsci.2017.04.002>.
- [5] W. Abd-Elazimi, M.A. Darwish, A. Hamada, W.M. Daoush, Titanium-Based alloys and composites for orthopedic implants applications: a comprehensive review, *Mater. Des.* 241 (2024), <https://doi.org/10.1016/j.matdes.2024.112850>.
- [6] L. Zhou, T. Yuan, J. Tang, J. He, R. Li, Mechanical and corrosion behavior of titanium alloys additively manufactured by selective laser melting – A comparison between nearly β titanium, α titanium and $\alpha + \beta$ titanium, *Opt. Laser Technol.* 119 (2019), <https://doi.org/10.1016/j.optlastec.2019.105625>.
- [7] T.B. Sercombe, L.-C. Zhang, S. Li, Y. Hao, Additive manufacturing of cp-Ti, Ti-6Al-4V and Ti2448, in: *Titanium in Medical and Dental Applications*, Elsevier, 2018, pp. 303–324, <https://doi.org/10.1016/b978-0-12-812456-7.00014-7>.
- [8] Q. Tao, Z. Wang, G. Chen, W. Cai, P. Cao, C. Zhang, W. Ding, X. Lu, T. Luo, X. Qu, M. Qin, Selective laser melting of Cp-Ti to overcome the low cost and high performance trade-off, *Addit. Manuf.* 34 (2020), <https://doi.org/10.1016/j.addma.2020.101198>.
- [9] N. Singh, P. Hameed, R. Ummethala, G. Manivasagam, K.G. Prashanth, J. Eckert, Selective laser manufacturing of Ti-based alloys and composites: impact of process parameters, application trends, and future prospects, *Mater. Today Adv.* 8 (2020) 100097, <https://doi.org/10.1016/j.mtadv.2020.100097>.
- [10] S. Guo, J. Zhang, X. Cheng, X. Zhao, A metastable β -type Ti-Nb binary alloy with low modulus and high strength, *J. Alloy. Compd.* 644 (2015) 411–415, <https://doi.org/10.1016/j.jallcom.2015.05.071>.
- [11] X. Luo, Y. Li, C. Yang, C. Zhao, H. Ma, T. Song, M. Sun, X. Liu, D. Li, N. Li, Insights into laser powder bed fused β -type titanium alloy: Investigating corrosion behavior and wear properties after post-hot treatment, *J. Mater. Res. Technol.* 37 (2025) 1596–1605, <https://doi.org/10.1016/j.jmrt.2025.06.120>.
- [12] F. Brumbauer, P. Brunner, L. Poitevin, M. Sterrer, H. Wilsche, S. Arneitz, M. P. Kainz, N.L. Okamoto, T. Ichitsuho, W. Sprengel, M. Luckbauer, Long-term corrosion behaviour of an ω -resistant, β -type Ti-12Cr-3Sn alloy: Effect of Sn addition on surface passivation and metal ion release in simulated physiological environment, *J. Alloy. Compd.* 1032 (2025) 180750, <https://doi.org/10.1016/j.jallcom.2025.180750>.
- [13] X. Zhao, M. Niinomi, M. Nakai, J. Hieda, Beta type Ti-Mo alloys with changeable Young's modulus for spinal fixation applications, *Acta Biomater.* 8 (2012) 1990–1997, <https://doi.org/10.1016/j.actbio.2012.02.004>.
- [14] R. Chen, D.G. Lee, Y. Lee, S. Hui, W. Ye, X.J. Mi, Grain growth characteristics of low cost beta Ti-2Al-9.2Mo-2Fe alloys with various boron contents, *Sci. Adv. Mater.* 8 (2016) 1951–1957, <https://doi.org/10.1166/sam.2016.2831>.
- [15] H. Schwab, K.G. Prashanth, L. Löber, U. Kühn, J. Eckert, Selective laser melting of Ti-45Nb alloy, *Met. (Basel)* 5 (2015) 686–694, <https://doi.org/10.3390/met5020686>.
- [16] S.F. Jawed, C.D. Rabadiya, Y.J. Liu, L.Q. Wang, P. Qin, Y.H. Li, X.H. Zhang, L. C. Zhang, Strengthening mechanism and corrosion resistance of beta-type Ti-Nb-Zr-Mn alloys, *Mater. Sci. Eng. C* 110 (2020) 110728, <https://doi.org/10.1016/j.msec.2020.110728>.
- [17] L. Zhou, T. Yuan, R. Li, J. Tang, M. Wang, F. Mei, Anisotropic mechanical behavior of biomedical Ti-13Nb-13Zr alloy manufactured by selective laser melting, *J. Alloy. Compd.* 762 (2018) 289–300, <https://doi.org/10.1016/j.jallcom.2018.05.179>.
- [18] T. Nagase, T. Hori, M. Todai, S.-H. Sun, T. Nakano, Additive manufacturing of dense components in beta-titanium alloys with crystallographic texture from a mixture of pure metallic element powders, *Mater. Des.* 173 (2019) 107771, <https://doi.org/10.1016/j.matdes.2019.107771>.
- [19] T. Ozaki, H. Matsumoto, S. Watanabe, S. Hanada, Beta Ti alloys with low Young's modulus, *Mater. Trans.* 45 (2004) 2776–2779, <https://doi.org/10.2320/matertrans.45.2776>.
- [20] L. Bolzoni, F. Yang, M. Paul, Development and characterisation of low-cost powder metallurgy Ti-Cu-Fe alloys, *J. Mater. Res. Technol.* 24 (2023) 2678–2687, <https://doi.org/10.1016/j.jmrt.2023.03.178>.
- [21] G. Senopati, R.A. Rahman Rashid, I. Kartika, S. Palanisamy, Recent development of low-cost β -Ti alloys for biomedical applications: a review, *Metals* 13 (2023) 194, <https://doi.org/10.3390/met13020194>.
- [22] C. Guo, J. Xia, G. Dai, Y. Guo, Z. Sun, H. Chang, Q. Zhang, Enhanced mechanical properties and refined microstructure induced by micron Fe for additive manufactured Ti-Fe alloys, *J. Alloy. Compd.* 1033 (2025) 181144, <https://doi.org/10.1016/j.jallcom.2025.181144>.
- [23] J. Niu, Y. Guo, K. Li, W. Liu, Z. Dan, Z. Sun, H. Chang, L. Zhou, Improved mechanical, bio-corrosion properties and in vitro cell responses of Ti-Fe alloys as candidate dental implants, *Mater. Sci. Eng. C* 122 (2021) 111917, <https://doi.org/10.1016/j.msec.2021.111917>.
- [24] X.T. Li, R. Liu, J.P. Hou, Z.J. Zhang, Z.F. Zhang, Trade-off model for strength-ductility relationship of metallic materials, *Acta Mater.* 289 (2025) 120942, <https://doi.org/10.1016/j.actamat.2025.120942>.
- [25] A.V. Dobromyslov, V.A. Elkin, Martensitic transformation and metastable β -phase in binary titanium alloys with d-intervals of 4–6 periods, *Sov. Mater.* 44 (2001) 905–910, [https://doi.org/10.1016/s1359-6462\(00\)00694-1](https://doi.org/10.1016/s1359-6462(00)00694-1).
- [26] C. Lin, G. Yin, Y. Zhao, P. Ge, Z. Liu, Analysis of the effect of alloy elements on martensitic transformation in titanium alloy with the use of valence electron structure parameters, *Mater. Chem. Phys.* 125 (2011) 411–417, <https://doi.org/10.1016/j.matchemphys.2010.10.039>.
- [27] R. Rahmani, N. Kamboj, M. Brojan, M. Antonov, K.G. Prashanth, Hybrid metal-ceramic biomaterials fabricated through powder bed fusion and powder metallurgy for improved impact resistance of craniofacial implants, *Mater. (Oxf.)* 24 (2022) 101465, <https://doi.org/10.1016/j.mta.2022.101465>.
- [28] H. Attar, K.G. Prashanth, A.K. Chaubey, M. Calin, L.C. Zhang, S. Scudino, J. Eckert, Comparison of wear properties of commercially pure titanium prepared by selective laser melting and casting processes, *Mater. Lett.* 142 (2015) 38–41, <https://doi.org/10.1016/j.matlet.2014.11.156>.
- [29] W. Kong, E.M. Francis, Q. Shi, S.C. Cox, F. Wang, M. Kuang, M.M. Attallah, The influence of advanced hot isostatic pressing on phase transformations, mechanical properties of Ti-34Nb-13Ta-5Zr-0.2O alloy manufactured by In-situ alloying via selective laser melting, *J. Alloy. Compd.* 903 (2022) 163974, <https://doi.org/10.1016/j.jallcom.2022.163974>.
- [30] R. Ummethala, P.S. Karamched, S. Rathinavelu, N. Singh, A. Aggarwal, K. Sun, E. Ivanov, L. Kollo, I. Okulov, J. Eckert, K.G. Prashanth, Selective laser melting of high-strength, low-modulus Ti-35Nb-7Zr-5Ta alloy, *Mater. (Oxf.)* 14 (2020) 100941, <https://doi.org/10.1016/j.mta.2020.100941>.
- [31] I. Novakova, D. Vojtech, D. Paloušek, Characterization of β -Ti alloy prepared by SLM method, *Manuf. Technol.* 20 (2020) 690–696, <https://doi.org/10.21062/mf.2020.091>.
- [32] H. Attar, L. Löber, A. Funk, M. Calin, L.C. Zhang, K.G. Prashanth, S. Scudino, Y. S. Zhang, J. Eckert, Mechanical behavior of porous commercially pure Ti and Ti-TiB composite materials manufactured by selective laser melting, *Mater. Sci. Eng. A* 625 (2015) 350–356, <https://doi.org/10.1016/j.msea.2014.12.036>.
- [33] R. Ummethala, J. Jayaraj, P.S. Karamched, S. Rathinavelu, N. Singh, K.B. Surreddi, K.G. Prashanth, Vitro Corrosion Behavior of Selective Laser Melted Ti-35Nb-7Zr-5Ta, *J. Mater. Eng. Perform.* (2021) 1–12, <https://doi.org/10.1007/s11665-021-05940-9>.
- [34] C.Y. Yap, C.K. Chua, Z.L. Dong, Z.H. Liu, D.Q. Zhang, L.E. Loh, S.L. Sing, Review of selective laser melting: Materials and applications, *Appl. Phys. Rev.* 2 (2015) 041101, <https://doi.org/10.1063/1.4935926>.
- [35] P. Hameed, C.F. Liu, R. Ummethala, N. Singh, H.H. Huang, G. Manivasagam, K. G. Prashanth, Biomimetic porous Ti6Al4V gyroid scaffolds for bone implant applications fabricated by selective laser melting, *Prog. Addit. Manuf.* 6 (2021) 455–469, <https://doi.org/10.1007/s40964-021-00210-5>.
- [36] A.A. Raheem, P. Hameed, R. Whemish, R.S. Elsen, G. Aswin, A.K. Jaiswal, K. G. Prashanth, G. Manivasagam, A review on development of bio-inspired implants using 3d printing, *Biomimetics* 6 (2021) 65, <https://doi.org/10.3390/biomimetics6040065>.
- [37] H. Attar, S. Ehtemam-Haghighi, D. Kent, M.S. Dargusch, Recent developments and opportunities in additive manufacturing of titanium-based matrix composites: a review, *Int. J. Mach. Tools Manuf.* 133 (2018) 85–102, <https://doi.org/10.1016/j.ijmactools.2018.06.003>.
- [38] J.B. Jin, S. Zhou, H. Yang, J. Yang, Z. Zhang, B. Guo, L.C. Zhang, Breaking through the strength-ductility trade-off of LPBF-produced Ti-xNb alloys from mixed powders via ω -phase induced ferrostructure, *Int. J. Extrem. Manuf.* 7 (2025), <https://doi.org/10.1088/2631-7990/aded4e>.
- [39] C. Zhao, Z. Wang, D. Li, L. Kollo, Z. Luo, W. Zhang, K.G. Prashanth, Cu-Ni-Sn alloy fabricated by melt spinning and selective laser melting: a comparative study on the microstructure and formation kinetics, *J. Mater. Res. Technol.* 9 (2020) 13097–13105, <https://doi.org/10.1016/j.jmrt.2020.09.047>.
- [40] Y. Abdelrhman, M.A.-H. Gepreel, S. Kobayashi, S. Okano, T. Okamoto, Biocompatibility of new low-cost ($\alpha + \beta$)-type Ti-Mo-Fe alloys for long-term implantation, *Mater. Sci. Eng. C* 99 (2019) 552–562, <https://doi.org/10.1016/j.msec.2019.01.133>.
- [41] C.A.F. Salvador, M.R. Dal Bó, F.H. Costa, M.O. Taipina, E.S.N. Lopes, R. Caram, Solute lean Ti-Nb-Fe alloys: an exploratory study, *J. Mech. Behav. Biomed. Mater.* 65 (2017) 761–769, <https://doi.org/10.1016/j.jmbm.2016.09.024>.
- [42] C. Catanio Bortolan, L. Contri Campanelli, P. Mengucci, G. Barucca, N. Giguère, N. Brodusch, C. Paternoster, C. Bolfarini, R. Gauvin, D. Mantovani, Development of Ti-Mo-Fe alloys combining different plastic deformation mechanisms for improved strength-ductility trade-off and high work hardening rate, *J. Alloy. Compd.* 925 (2022) 166757, <https://doi.org/10.1016/j.jallcom.2022.166757>.
- [43] A. Biesiekierski, J. Lin, Y. Li, D. Ping, Y. Yamabe-Mitarai, C. Wen, Investigations into Ti-(Nb,Ta)-Fe alloys for biomedical applications, *Acta Biomater.* 32 (2016) 336–347, <https://doi.org/10.1016/j.actbio.2015.12.010>.
- [44] Y. Chen, X. Zhang, M.M. Parvez, F. Liou, A review on metallic alloys fabrication using elemental powder blends by laser powder directed energy deposition process, *Page 3562* 13, *Materials* 2020 13 (2020) 3562, <https://doi.org/10.3390/MA13163562>.
- [45] S. Subramanian, M.K. Yadav, J. Jayaraj, F. Yangyang, L. Xi, K.G. Prashanth, Microstructural homogenization through laser remelting in an additively manufactured Ti-40Nb sample from elemental feedstock powders, *J. Mater. Res. Technol.* 38 (2025) 4305–4320, <https://doi.org/10.1016/j.jmrt.2025.08.203>.
- [46] C. Affolter, U. Müller, C. Leinenbach, B. Weisse, Compressive testing of ductile high-strength alloys, *J. Test. Eval.* 43 (2015) 1554–1562, <https://doi.org/10.1520/jte20140301>.
- [47] R. Karre, B.K. Kodli, A. Rajendran, N. J. D.K. Pattanayak, K. Ameyama, S.R. Dey, Comparative study on Ti-Nb binary alloys fabricated through spark plasma sintering and conventional P/M routes for biomedical application, *Mater. Sci. Eng. C* 94 (2019) 619–627, <https://doi.org/10.1016/j.msec.2018.10.006>.
- [48] J. Karimi, C. Suryanarayana, I. Okulov, K.G. Prashanth, Selective laser melting of Ti6Al4V: Effect of laser re-melting, *Mater. Sci. Eng. A* 805 (2020) 140558, <https://doi.org/10.1016/j.msea.2020.140558>.

- [49] L.A. Alberta, Y. Fortouna, J. Vishnu, S. Pilz, A. Gebert, C. Lekka, K. Nielsch, M. Calin, Effects of Ga on the structural, mechanical and electronic properties of β -Ti-45Nb alloy by experiments and ab initio calculations, *J. Mech. Behav. Biomed. Mater.* 140 (2023) 105728, <https://doi.org/10.1016/j.jmbmm.2023.105728>.
- [50] L. Ren, W. Xiao, C. Ma, R. Zheng, L. Zhou, Development of a high strength and high ductility near β -Ti alloy with twinning induced plasticity effect, *Scr. Mater.* 156 (2018) 47–50, <https://doi.org/10.1016/j.scriptamat.2018.07.012>.
- [51] Y.P. Hou, S. Guo, X.L. Qiao, T. Tian, Q.K. Meng, X.N. Cheng, X.Q. Zhao, Origin of ultralow Young's modulus in a metastable β -type Ti-33Nb-4Sn alloy, *J. Mech. Behav. Biomed. Mater.* 59 (2016) 220–225, <https://doi.org/10.1016/j.jmbmm.2015.12.037>.
- [52] M. Bönisch, M. Calin, L. Giebele, A. Helth, A. Gebert, W. Skrotzki, J. Eckert, Composition-dependent magnitude of atomic shuffles in Ti-Nb martensites, *J. Appl. Crystallogr.* 47 (2014) 1374–1379, <https://doi.org/10.1107/S1600576714012576>.
- [53] O.N. Senkov, S.I. Rao, T.M. Butler, T.I. Daboiko, K.J. Chaput, Effect of Fe additions on the microstructure and properties of Nb-Mo-Ti alloys, *Int. J. Refract. Met. Hard Mater.* 89 (2020) 105221, <https://doi.org/10.1016/j.jmrhm.2020.105221>.
- [54] S.E. Haghghi, H.B. Lu, G.Y. Jian, G.H. Cao, D. Habibi, L.C. Zhang, Effect of α' martensite on the microstructural and mechanical properties of beta-type Ti-Fe-Ti alloys, *Mater. Des.* 76 (2015) 47–54, <https://doi.org/10.1016/j.matdes.2015.03.028>.
- [55] M. Abdel-Hady, K. Hinoshita, M. Morinaga, General approach to phase stability and elastic properties of β -type Ti-alloys using electronic parameters, *Scr. Mater.* 55 (2006) 477–480, <https://doi.org/10.1016/j.scriptamat.2006.04.022>.
- [56] C. Guo, G. Dai, J. Niu, Y. Guo, Z. Sun, H. Chang, Q. Zhang, Fe nanoparticles modified pure Ti alloy on microstructure evolution and fine crystallization mechanism fabricated by additive manufacturing, *J. Mater. Res. Technol.* 26 (2023) 5860–5872, <https://doi.org/10.1016/j.jmrt.2023.08.221>.
- [57] M.A. Haq, I. Ali, Y. Song, B.S. Kim, Insights into the development of Fe modified Ti-Nb alloy: A powder metallurgy perspective, *Mater. Today Commun.* 38 (2024) 107743, <https://doi.org/10.1016/j.mtcomm.2023.107743>.
- [58] W. Huang, G. Chen, X. Huang, Z. Zeng, Y. Du, S. Qin, Effect of Fe content on the microstructure and mechanical properties of Al-Cu-Ni-Ti-Fe alloy fabricated by selective laser melting, *Vacuum* 242 (2025) 114746, <https://doi.org/10.1016/j.vacuum.2025.114746>.
- [59] C. Guo, B. Yuan, P. Du, H. Chen, Y. Zhou, H. Zhang, R. Song, L. Zhang, Laser beam powder bed fusion of NiTiFe shape memory alloys by in-situ alloying: microstructural evolution and generation of strain glass, *Virtual Phys. Prototyp.* 20 (2025), <https://doi.org/10.1080/17452759.2024.2438896>.
- [60] R. Schmid-Fetzer, A. Kozlov, Thermodynamic aspects of grain growth restriction in multicomponent alloy solidification, *Acta Mater.* 59 (2011) 6133–6144, <https://doi.org/10.1016/j.actamat.2011.06.026>.
- [61] M.J. Bermingham, S.D. McDonald, M.S. Dargusch, D.H. St.John, Grain-refinement mechanisms in titanium alloys, *J. Mater. Res.* 23 (2008) 97–104, <https://doi.org/10.1557/jmr.2008.0002>.
- [62] M.Y. Mendoza, P. Samimi, D.A. Brice, B.W. Martin, M.R. Rolchigo, R. LeSar, P. C. Collins, Microstructures and Grain Refinement of Additive-Manufactured Ti-xW Alloys, *Metall. Mater. Trans. A* 48 (2017) 3594–3605, <https://doi.org/10.1007/s11661-017-4117-7>.
- [63] A. Issariyapat, J. Huang, S. Kariya, B. Chen, S. Li, J. Umeda, K. Yamanaka, A. Chiba, K. Kondoh, Sustainable alloy design: Fe-enhanced Ti alloys for superior mechanical performance in additive manufacturing, *J. Alloy. Compd.* 1010 (2025) 177767, <https://doi.org/10.1016/j.jallcom.2024.177767>.
- [64] S. Scudino, G. Liu, K.G. Prashanth, B. Bartusch, K.B. Surreddi, B.S. Murty, J. Eckert, Mechanical properties of Al-based metal matrix composites reinforced with Zr-based glassy particles produced by powder metallurgy, *Acta Mater.* 57 (2009) 2029–2039, <https://doi.org/10.1016/j.actamat.2009.01.010>.
- [65] F. Ali, S. Scudino, G. Liu, V.C. Srivastava, N.K. Mukhopadhyay, M. Samadi Khoshkhou, K.G. Prashanth, V. Uhlenwinkel, M. Calin, J. Eckert, Modeling the strengthening effect of Al-Cu-Fe quasicrystalline particles in Al-based metal matrix composites, *J. Alloy. Compd.* 536 (2012) S130–S133, <https://doi.org/10.1016/j.jallcom.2011.12.022>.
- [66] É.S.N. Lopes, C.A.F. Salvador, D.R. Andrade, A. Cremasco, K.N. Campo, R. Caram, Microstructure, mechanical properties, and electrochemical behavior of Ti-Nb-Fe alloys applied as biomaterials, *Metall. Mater. Trans. A* 47 (2016) 3213–3226, <https://doi.org/10.1007/s11661-016-3411-0>.
- [67] G.-H. Zhao, X.Z. Liang, B. Kim, P.E.J. Rivera-Díaz-del-Castillo, Modelling strengthening mechanisms in beta-type Ti alloys, *Mater. Sci. Eng. A* 756 (2019) 156–160, <https://doi.org/10.1016/j.msea.2019.04.027>.
- [68] M.K. Yadav, R.H. Shukla, K. Praveenkumar, S. Nilwar, C.S. Perugu, P. Sellamuthu, K. Chatterjee, S. Suwas, J. Jayaraj, K.G. Prashanth, Microstructural, mechanical, corrosion, and biological behavior of spark plasma sintered commercially pure zinc for biomedical applications, *Mater. Adv.* 6 (2025) 3546–3560, <https://doi.org/10.1039/D5MA00092K>.
- [69] L.A. Alberta, J. Vishnu, A. Hariharan, S. Pilz, A. Gebert, M. Calin, Novel low modulus beta-type Ti-Nb alloys by gallium and copper minor additions for antibacterial implant applications, *J. Mater. Res. Technol.* 20 (2022) 3306–3322, <https://doi.org/10.1016/j.jmrt.2022.08.111>.
- [70] A. Ismaeel, X. Li, D. Xu, J. Zhang, L. Weining, C. Wang, R. Yang, Effect of slip and twinning on texture evolution mechanisms in dual-phase titanium alloys, *J. Mater. Res. Technol.* 35 (2025) 4882–4894, <https://doi.org/10.1016/j.jmrt.2025.02.102>.
- [71] D. Kent, G. Wang, M. Dargusch, Effects of phase stability and processing on the mechanical properties of Ti-Nb based β Ti alloys, *J. Mech. Behav. Biomed. Mater.* 28 (2013) 15–25, <https://doi.org/10.1016/j.jmbmm.2013.07.007>.
- [72] S.F. Jawed, C.D. Rabadia, Y.J. Liu, L.Q. Wang, P. Qin, Y.H. Li, X.H. Zhang, L. C. Zhang, Strengthening mechanism and corrosion resistance of beta-type Ti-Nb-Zr-Mn alloys, *Mater. Sci. Eng. C* 110 (2020) 110728, <https://doi.org/10.1016/j.MSEC.2020.110728>.
- [73] H.Z. Niu, H.R. Zhang, Q.Q. Sun, D.L. Zhang, Breaking through the strength-ductility trade-off dilemma in powder metallurgy Ti-6Al-4V titanium alloy, *Mater. Sci. Eng. A* 754 (2019) 361–369, <https://doi.org/10.1016/j.msea.2019.03.089>.
- [74] H.-C. Hsu, K.-K. Wong, S.-C. Wu, Y.-X. Chen, W.-F. Ho, Metastable dual-phase Ti-Nb-Sn-Zr and Ti-Nb-Sn-Fe alloys with high strength-to-modulus ratio, *Mater. Today Commun.* 30 (2022) 103168, <https://doi.org/10.1016/j.mtcomm.2022.103168>.
- [75] J. Navarro Laboulais, A. Amigó Mata, V. Amigó Borrás, A. Igual Muñoz, Electrochemical characterization and passivation behaviour of new beta-titanium alloys (Ti35Nb10Ta-xFe), *Electrochim. Acta* 227 (2017) 410–418, <https://doi.org/10.1016/j.electacta.2016.12.125>.
- [76] X. Ou-yang, Y. Yu, W. Ye, W. Zhang, Q. Liu, S. Hui, The corrosion behavior and passive film structure of industrial pure titanium with different Fe content in hydrochloric acid, *J. Mater. Res. Technol.* 35 (2025) 599–610, <https://doi.org/10.1016/j.jmrt.2025.01.063>.
- [77] A.K. Shukla, R. Balasubramaniam, S. Bhargava, Effect of replacement of V by Fe and Nb on passive film behavior of Ti-6Al-4V in simulated body fluid conditions, *J. Alloy. Compd.* 389 (2005) 144–152, <https://doi.org/10.1016/j.jallcom.2004.08.005>.
- [78] R. Ummethala, J. Jayaraj, P.S. Karamched, S. Rathinavelu, N. Singh, K.B. Surreddi, K.G. Prashanth, Vitro corrosion behavior of selective laser melted Ti-35Nb-7Zr-5Ta, *J. Mater. Eng. Perform.* 30 (2021) 7967–7978, <https://doi.org/10.1007/s11665-021-05940-9>.
- [79] N. El-Bagoury, S.I. Ahmed, O. Ahmed Abu Ali, S. El-Hadad, A.M. Fallatah, G.A. M. Mersal, M.M. Ibrahim, J. Wysocka, R. Ryl, R. Boukherroub, M. A. Amin, The influence of microstructure on the passive layer chemistry and corrosion resistance for some titanium-based alloys, *Materials* 12 (2019) 1233, <https://doi.org/10.3390/ma12081233>.
- [80] A.N. Ribeiro, L.M. Garcia da Silva, A. de A. Mendes Filho, R.A. Antunes, S. F. Santos, Unveiling the effect of ECAP on the passive film stability, surface chemistry and corrosion resistance of the β -type Ti-29Nb-13Ta-4Mo alloy, *Appl. Surf. Sci.* 706 (2025) 163506, <https://doi.org/10.1016/j.apsusc.2025.163506>.
- [81] I. Milošević, T. Kosec, H.-H. Strehlow, XPS and EIS study of the passive film formed on orthopaedic Ti-6Al-7Nb alloy in Hank's physiological solution, *Electrochim. Acta* 53 (2008) 3547–3558, <https://doi.org/10.1016/j.electacta.2007.12.041>.
- [82] J. Jayaraj, A. Ravi Shankar, U. Kamachi Mudali, Electrochemical and passive characterization of a beta type Ti45Zr38Al17 cast rod in nitric acid medium, *Electrochim. Acta* 85 (2012) 210–219, <https://doi.org/10.1016/j.electacta.2012.08.047>.
- [83] R.A. Lunt, A.J. Jackson, A. Walsh, Dielectric response of Fe2O3 crystals and thin films, *Chem. Phys. Lett.* 586 (2013) 67–69, <https://doi.org/10.1016/j.cplett.2013.09.023>.
- [84] G. Nanda, E.W. Awin, T. Gasyak, E. Koroleva, A. Filimonov, S. Vakhrushev, R. Sujith, R. Kumar, Temperature dependent conductivity and broadband dielectric response of precursor-derived Nb2O5, *Ceram. Int.* 46 (2020) 9512–9518, <https://doi.org/10.1016/j.ceramint.2019.12.213>.
- [85] I. Çaha, A.C. Alves, C. Chirico, A. Maria Pinto, S. Tsipas, E. Gordo, O. Bondarchuk, F. Leonard Deepak, F. Toptan, Atomic-scale investigations of passive film formation on Ti-Nb alloys, *Appl. Surf. Sci.* 615 (2023) 156282, <https://doi.org/10.1016/j.apsusc.2022.156282>.
- [86] M.T. Woldemedhin, D. Raabe, A.W. Hassel, Characterization of thin anodic oxides of Ti-Nb alloys by electrochemical impedance spectroscopy, *Electrochim. Acta* 82 (2012) 324–332, <https://doi.org/10.1016/j.electacta.2012.06.029>.
- [87] P. Qin, L.Y. Chen, C.H. Zhao, Y.J. Liu, C.D. Cao, H. Sun, L.C. Zhang, Corrosion behavior and mechanism of selective laser melted Ti35Nb alloy produced using pre-alloyed and mixed powder in Hank's solution, *Corros. Sci.* 189 (2021) 109609, <https://doi.org/10.1016/j.corsci.2021.109609>.
- [88] H. Liu, Z.-X. Wang, J. Cheng, N. Li, S.-X. Liang, L. Zhang, F. Shang, D. Oleksandr, L.-Y. Chen, Nb-content-dependent passivation behavior of Ti-Nb alloys for biomedical applications, *J. Mater. Res. Technol.* 27 (2023) 7882–7894, <https://doi.org/10.1016/j.jmrt.2023.11.203>.
- [89] H. Liu, Y. Li, L. Shi, H. Wang, X. Ma, L. Ren, Corrosion behavior of laser powder bed fusion prepared Cu-bearing β titanium alloy under simulated inflammatory conditions, *Electrochim. Acta* 533 (2025) 146533, <https://doi.org/10.1016/j.electacta.2025.146533>.
- [90] D.D. Macdonald, The point defect model for the passive state, *J. Electrochem. Soc.* 139 (1992) 3434–3449, <https://doi.org/10.1149/1.12069096>.
- [91] M.T. Woldemedhin, D. Raabe, A.W. Hassel, Anodic oxides on a beta type Nb-Ti alloy and their characterization by electrochemical impedance spectroscopy, *Physica Status Solidi (A) Applications Materials Science* 207 (2010) 812–816, <https://doi.org/10.1002/pssa.200983324>.
- [92] H. Qin Lin, P. Ren, G. Xu Zhang, W. Min Chen, L. Jun Zhang, Microstructure, mechanical properties, and bio-corrosion behaviors of Ti-based BCC multi-principal element alloys, *Trans. Nonferrous Met. Soc. China* 35 (2025) 2632–2651, [https://doi.org/10.1016/S1003-6326\(25\)66837-3](https://doi.org/10.1016/S1003-6326(25)66837-3).
- [93] B.C. Barreto, G.R.L. Matos, J.F.Q. Rodrigues, M.C.S.S. Macedo, S.A.S. de Araujo Souza, Microstructural, mechanical and electrochemical characterization of Ti-35Nb-xY alloys for biomedical applications, *Mater. Res.* 28 (2025) e20240616, <https://doi.org/10.1590/1980-5373-MR-2024-0616>.
- [94] N. Hu, L. Xie, Q. Liao, A. Gao, Y. Zheng, H. Pan, L. Tong, D. Yang, N. Gao, M. J. Starink, P.K. Chu, H. Wang, A more defective substrate leads to a less defective passive layer: Enhancing the mechanical strength, corrosion resistance and anti-

- inflammatory response of the low-modulus Ti-45Nb alloy by grain refinement, *Acta Biomater.* 126 (2021) 524–536, <https://doi.org/10.1016/j.actbio.2021.02.045>.
- [95] Z. Zhan, Q. Zhang, S. Wang, X. Liu, H. Zhang, Z. Sun, Y. Ge, N. Du, Comparison on the electrochemical corrosion behavior of Ti6Al4V alloys fabricated by laser powder bed fusion and casting, *Materials* 17 (2024) 3322, <https://doi.org/10.3390/ma17133322>.
- [96] R. Silva, J. Silva, C.C. Viana, C.R.M. Afonso, P. Hammer, D.C.C. Magalhães, A. H. Plaine, C.A.D. Rovere, Optimizing strength and corrosion resistance of the metastable β -alloy Ti-35Nb-7Zr-5Ta alloy by equal-channel angular pressing, *J. Mater. Res. Technol.* 35 (2025) 2055–2067, <https://doi.org/10.1016/j.jmrt.2025.01.136>.
- [97] X. Lu, W. Zou, X. Zhou, J. Zhang, X. Chen, X. Pang, W.Y. Ip, C. Lai, L. Chan, Y. Wang, Effect of process parameters on mechanical properties and corrosion resistance of Ti-6Al-4V alloys prepared by selective laser melting, *J. Mater. Res. Technol.* 36 (2025) 1743–1757, <https://doi.org/10.1016/j.jmrt.2025.03.249>.

Curriculum vitae

Personal data

Name: Shangavi Subramanian
Date of birth: 05.03.1995
Place of birth: India
Citizenship: Indian

Contact data

E-mail: sangmarch@gmail.com
shangavi.subramanian@taltech.ee

Education

2022–2026 Tallinn University of Technology, PhD
2018–2022 Central University of Tamil Nadu, India, MTech
2012–2016 Government College of Engineering-Salem, India, BE

Language competence

English Fluent
Tamil Native

Professional employment

2021–2022 Materials Engineer, HCL Technologies, India
2016–2018 SAP associate, Accenture, India

Research visit

Jun 2025 Department of Materials Engineering, Dalarna University, Falun, Sweden
Dec 2024 Department of Materials Engineering, Dalarna University, Falun, Sweden
Sep 2023–Nov 2023 SMEC, Vellore Institute of Technology, Tamil Nadu, India

Elulookirjeldus

Isikuandmed

Nimi: Shangavi Subramanian
Sünniaeg: 05.03.1995
Sünnikoht: India
Kodakondsus: India

Kontaktandmed

E-post: sangmarch@gmail.com,
shangavi.subramanian@taltech.ee

Hariduskäik

2022–2026 Tallinna Tehnikaülikool, PhD
2018–2022 Tamil Nadu keskülikool, India, MTech
2012–2016 India Riiklik Inseneriteaduste Kolledž - Salem, India, BE

Keelteoskus

Inglise keel kõrgtase
Tamili emakeel

Teenistuskäik

2021–2022 Materjaliinsener, HCL Technologies, India
2016–2018 SAP partner, Accenture, India

Teadusviit

Juuni 2025 Materjalitehnika osakond, Dalarna Ülikool, Falun, Rootsi
Detsember 2024 Materjalitehnika osakond, Dalarna Ülikool, Falun, Rootsi
Sept 2023–nov 2023 SMEC, Vellore'i Tehnoloogiainstituut, Tamil Nadu, India

ISSN 2585-6901 (PDF)

ISBN 978-9916-80-506-0 (PDF)